A Study of the Relationship Between Blood Clotting Propensity and Mass Transfer Characteristics of Artificial Obstructions in a Stream of Blood.

BY

WILLIAM DONALD TAYLOR

Thesis presented for the Degree of Doctor of Philosophy.

University of Edinburgh.

July 1978.

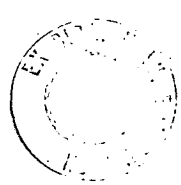

Acknowledgements.

I would like to thank Dr. Norman MacLeod for his help and encouragement throughout this project, and to all those who have aided me, in particular Mr. D.M. Wade, Prof. P. Kuypers, Mr. R. Hardie, Prof. D.E.M. Taylor, Dr. S. Shaw, Mr. D. Ketchin and his technical staff in the Chemical Engineering Department at Edinburgh University, Mr. E. Lucey, Mr. A. McEwan and Mrs. H. Carlin.

Financial support from the Science Research Council and the Wellcome Trust is gratefully acknowledged.

TABLE OF CONTENTS

LIST OF FIGURES

List of symbols.

C_s	concentration of swelling agent in polymer surface.
f	geometric factor in the equation $\frac{N'\lambda}{2} = \delta.f$
i	angle between the normal to a surface and the incident or reflected light beam.
K	mass transfer coefficient.
N	order of first fringe.
N'	fringe number.
P_s	vapour pressure.
Re.No.	Reynolds Number.
Sc.No.	Schmidt Number.
t	duration.
γ	angle between camera axis and normal to surface.
δ	recession of mass transferring surface.
η	refractive index.
λ	wavelength of He-Ne laser light.
μ	viscosity.
υ	kinematic Viscosity.
τ	shear stress.
v	distance between object and crossover point.
f'	distance between negative image and crossover point.
s'	distance between object and centre of lens.

CHAPTER 1

Introduction.

1.1 The problem of prosthesis-induced thrombosis.

The major remaining obstacle to the safe and prolonged use of prosthetic heart valves is prosthesis-induced thrombosis and subsequent peripheral embolisation, which results in death or serious injury (1-6). The problem is also significant in arterial shunts, heart patches, kidney machines, heart-lung machines, and oxygenators.

Commonly, two types of thrombus are observed on artificial surfaces; white thrombus and red thrombus. It is not clear whether these are the results of two distinct mechanisms or if they are different stages of the same basic mechanism. Salzman (33) found that red thrombus consists of homogeneous fibrin and red blood cells (RBC's), while white thrombus has a white head of platelets and a red tail of fibrin and RBC's. Turitto & Leonard (136) describe thrombus as being essentially composed of agglutinated platelets and fibrin. Hladovec & Riha (138), in experiments with thrombus formation on a nylon net in flowing blood, found that thrombus near the net consisted mainly of platelets, with increasing fibrin and erythrocyte content downstream of the net. Chandler (70) found that thrombus formed in moving blood consisted of platelets, a few RBC's, fibrin and numerous leukocytes, whereas clot formed in stagnant blood had a red tail of RBC's, few platelets, and scattered leukocytes in normal proportions. Although considerable work has been published on the behaviour of platelets and RBC's at artificial surfaces (41, 53, 68, 132, 137, 139) relatively little study has been concerned with white cell deposition, and it is not clear what the precise role of white cells is in the overall clotting mechanism.

Grabowski (135) observed that in his experiments, leukocyte deposition always accompanied platelet adhesion, but this was with heparinized blood, and the conclusion may not apply to unheparinized blood.

Madras et al (52) describes the wedge thrombi forming behind supporting struts as platelet aggregates and white cells. The symmetric thrombi which grow round the stagnation point in the low-flow chambers have the same composition as the wedge thrombi ; however in the high-flow chambers, white cells can be permanently deposited on the surface with no subsequent thrombus formation.

Dutton et al (141), in their T-chamber experiments, found that thrombus consisted of a fibrin-RBC mesh between platelet aggregates, with white cells sometimes observed.

Baier (142), making microscopic observations of blood element behaviour at interfaces, states that white cell deposition always occurs in thrombus formation.

The question as to what extent white cell deposition is an indicator of blood clotting propensity is not yet resolved. All that can be asserted is that in some cases white cell deposition is associated with thrombus formation. It may be that there are not just two distinct types of thrombus, but a multitude of them, some requiring the deposition of white cells, some not.

Approaches to the solution of the problem.

The main approaches so far have been:

(1) through the use of anticoagulant therapy.

(2) through the use of valves made from human or animal tissue.

(3) through the development of a material of construction which is sufficiently athrombogenic.

(4) through the elimination of prosthesis-induced hydrodynamic disturbance.

It is not yet possible to design an athrombogenic valve by the application of the biochemical theory of the coagulation mechanism alone, as the understanding of this complex mechanism is not sufficiently advanced (7-11).

Anticoagulant therapy.

Although with certain types of valve in some patients the treatment eliminates thromboembolic episodes, there are severe side-effects, e.g. danger of haemorrhage, an associated morbidity, and a mortality of 1% p.a. (12-19).

Tissue valves

These are leaflet valves, either transplanted pig valves, or fabricated from human or animal pericardium, fascia lata, or dura mater tissue. Although these valves have favourable athrombogenic characteristics, they have not in the past proved durable. The leaflets suffer from fibrosis, thickening, degeneration, calcification, cracking, tearing, and bacterial attack (23-27). The Hancock porcine valve, however, is currently showing promising short-term (3½ yr.) results (20-22).

Athrombogenic materials of construction.

Much work has been done in the attempt to develop an athrombogenic construction material, having a natural or polished surface, or a surface coated with heparin or similar substance, or a surface carrying a permanent negative electric charge (28-35). Although some promising results have emerged, as yet no artificial materials of valve construction, able to guarantee freedom from clot, are known.

Prosthesis-induced hydrodynamic disturbance.

Virchow (143) first enunciated the triad of factors involved in coagulation, namely, blood chemistry, surface chemistry, and flow. It is now generally agreed that the hydrodynamic design of a valve greatly influences its thrombogenic effect. An opposed view is that of Effler (36), who believes that prosthesis-induced thrombosis is essentially a material rejection phenomenon, but no one else has affirmed this view.

In general, the hydrodynamic disturbances which have been supposed to be associated with thrombosis, consist of the following fluid mechanical effects, which are potentially damaging to blood:

(a) Shearing effects between adjacent layers of blood or between blood and a solid boundary, which give rise to velocity gradients which in turn promote tubulent momentum transport, enhancing the rate at which fresh blood elements are brought into contact with a flow obstruction. Increased shear is associated with pressure variations, flow separation, and vortex formation.

(b) Flow stagnation, found where fluid impinges at right angles to a surface, or in areas of recirculating fluid.

Some of these individual phenomena have been investigated. The results reported in Refs 37-41 show that high levels of shear stress can encourage thrombus formation on foreign surfaces in some circumstances, but the relationship is neither simple nor clear. The effect of flow separation on platelet aggregation, one of the steps in the coagulation mechanism, is described in Refs. 42 and 43. Increased thrombus formation in turbulent flow compared to laminar flow in an in vivo canine experiment is reported in Ref. 44. Some

work on the effect of stagnation and vortex formation is described in Refs. 45-47.

It seems probable from the literature that thrombus formation is not dependent on any single fluid mechanical disturbance effect, but on a combination of these effects.

Conclusion.

The most promising approach to the attainment of an athrombogenic valve seems to be the use of a highly athrombogenic material incorporated in a hydrodynamically favourable design. This thesis is concerned entirely with the question: what hydrodynamic design features conduce to athrombogenic behaviour? A complete answer to this question would allow the design of a given type of valve, made of a given suitable, relatively athrombogenic material, to be optimised with respect to its clinical performance by the application of purely physical principles.

1.2 The supposition of a correlation between mass transfer coefficients and blood clotting propensity

In general, the value of the mass transfer coefficient at a point on the surface of an obstruction in a fluid flow is closely associated with the hydrodynamic disturbances mentioned in (a) in the previous section. Since blood clotting propensity is also associated with these effects, the a priori suggestion is made that this propensity could be correlated with mass transfer coefficients. The value of establishing such a correlation would be that heart valves and other devices could be designed relatively easily by attention to their mass transfer characteristics. In the absence of such guidance, blood clotting characteristics have at present to be determined by direct trial in vivo.

The meaning of mass transfer coefficient.

Suppose an obstruction is placed in a fluid flow, and either of two circumstances exist, viz., the material constituting the surface of the obstruction is capable of being dissolved by the fluid flow, and the dissolved particles carried away by the flow, or, a component of the fluid is capable of absorption by the surface of the obstruction. Then for given materials of fluid and obstruction, the local mass transfer coefficient is a measure of the rate at which material is dissolved or deposited at any point on the surface per unit of concentration difference between solid and liquid phases. This is quantitatively expressed

$$\text{mass transfer coefficient} = \frac{\text{flux of dissolved material at the point}}{\text{overall concentration difference.}}$$

The suggestion that blood clotting propensity can be correlated with mass transfer coefficients does not imply that during the process of prosthesis-induced thrombosis any mass transfer actually takes place. The proposal is that the mass transfer coeffficient is a single measure of various hydrodynamic disturbances which themselves are associated with blood coagulation. The mass transfer coefficient is a measure of the efficiency of convective transport between fluid and surface, which transport process is presumably involved in forming surface thrombi. If such transport processes are involved in thrombus formation at a foreign surface exposed to flowing blood, it must however be noticed that the transported matter may well be particulate, not dissolved species in a homogeneous medium. But if the particles concerned are sufficiently small, their transport will not entirely disobey the laws of convective and diffusive transfer in single phase media.

1.3 Preliminary indications supporting the proposed correlation.

(1) Knight et al (49).

In a series of canine in vivo experiments in the development of the Edinburgh Heart Value, blood clot was found on the unfaired edge of the annulus and on that part of the upstream face of the occluder from which the jet of blood leaving the sharp-edged orifice would impinge (Fig. 1.)

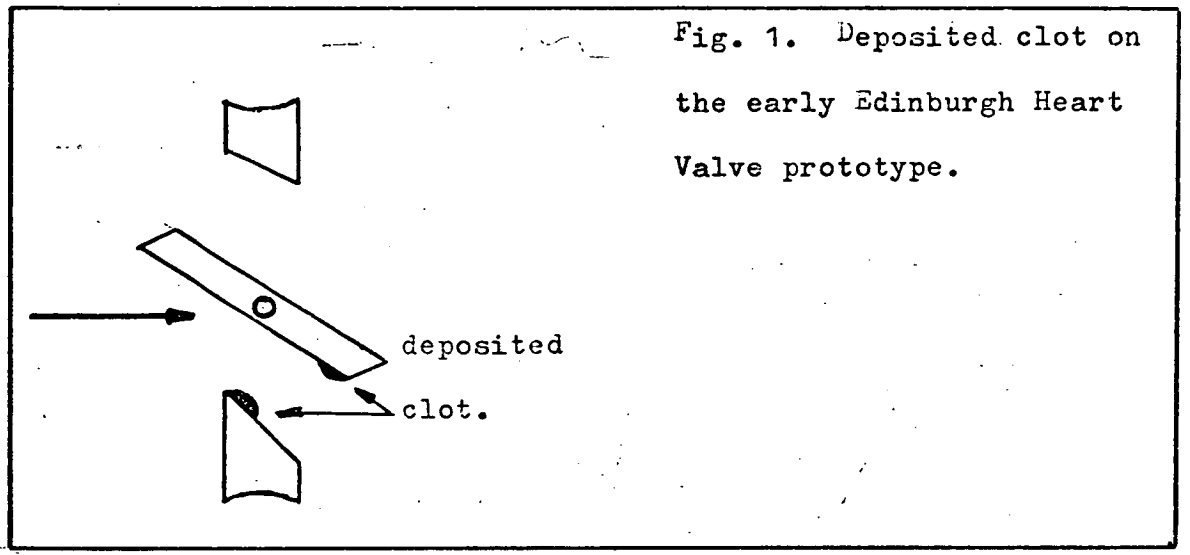

Fig. 1. Deposited clot on the early Edinburgh Heart Valve prototype.

At these points, the flow is known to be highly disturbed, and mass transfer rates are high. In subsequent prototypes (50) the annulus was faired, and there was no longer locally deposited clot on this edge or on the occluder face.

(2) Vorhauer (51).

A variety of bluff and faired bodies (Fig. 2) were implanted in the canine descending aorta. A cylindrical container downstream caught any shed thrombus, which was subsequently weighed. The ranking of the bodies by degree of thrombogenity was found to be: disc, ball upstream-apex cone, tear-drop. In terms of the transfer rate to the surface of the shapes, the ranking would be disc, ball, tear-drop, cone. In terms of the degree of disturbed wake behind the shapes, the ranking would be cone, disc, ball, tear-drop.

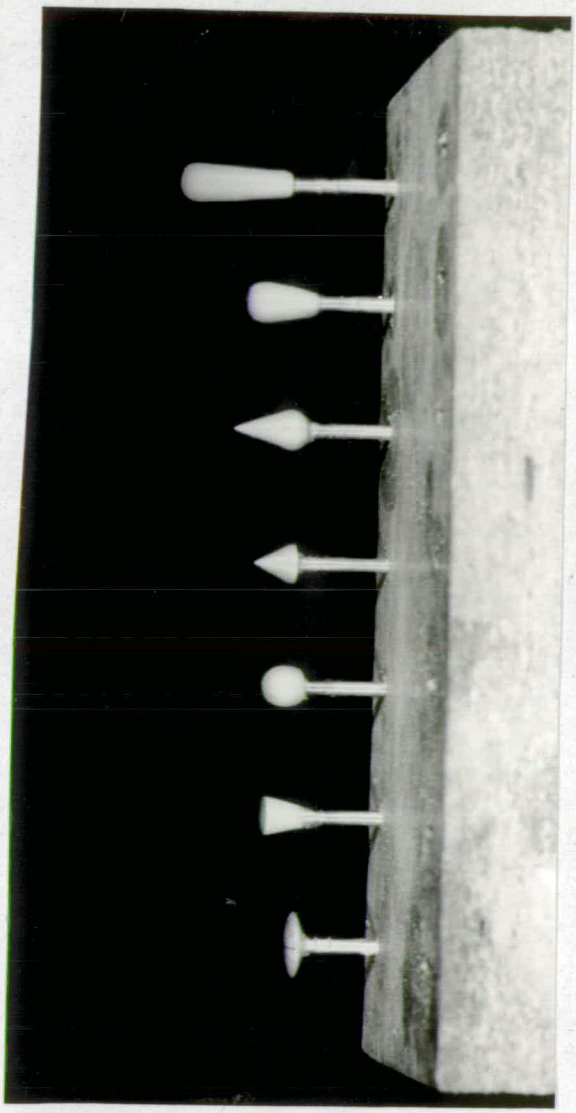

Fig. 2. Vorhauer's implantable probes.

And so, with the exception of the cone, the experiment provides confirmation of the hypothesis that thrombogenity can be linked to mass transfer coefficients.

(3) Gott and Furuse (31).

During an investigation into the thromboresistance of a variety of materials, using 9m.m. x 7 m.m. i.d. rigid tubes implanted in dogs, it was observed that tubes with blunt edges caused considerably more deposited thrombus than tubes with streamlined leading and trailing edges. Further experiments using tubes with a step projecting into the bloodstream showed clot formation on the leading edge of the step. These observations agree very well qualitatively with what would be expected from the mass transfer characteristics of such flow-obstructing objects on the hypothesis under consideration.

(4) Dutton et al (141).

The authors describe a stagnation point T-chamber (Fig. 3) through which canine blood is passed. They observed thrombus formation in the wake of surface imperfections on the slide, and a diminution in the amount of deposited thrombus with increasing distance downstream of the centre, like that to be expected for the mass transfer coefficient. The experiment is similar to Petschek's (see part (6)), but the observers were here concerned rather with the time required for various phenomena of thrombus formation to make their appearance, than with white cell deposition.

(5) Lederman et al (140).

The authors describe the development of the intravascular magnetic suspension of a torpedo-shaped test device, which is coated with an athrombogenic material. Any thrombus which forms on the

torpedo increases its drag coefficient, which effect can be measured by noting the additional current required to hold the torpedo in its suspended position. The device looks promising, because the torpedo can be suspended upstream of the vascular incisions, eliminating any effect which such damage might have on the thrombus deposited on the torpedo surface. Also, there are no supporting struts to interface with the results obtained on the torpedo. Unfortunately, comprehensive data showing the distribution of clot on the surface has not yet been obtained; such data would be extremely valuable.

(6) Madras, Morton, and Petschek (52).

This is the most promising work to lend weight to the proposed correlation. Other papers (43, 48, 134) by Petschek's co-workers describe similar experiments.

In these experiments, blood from the carotid artery of a dog is made to impinge on a glass slide and the resultant thrombus formation is observed through a microscope (Fig. 4). The glass slide is generally coated with a test substance whose blood clotting propensity is required to be known, for the technique is used by its inventors primarily to assess the relative thrombogenicity of different materials under defined flow conditions. A flow regulator on the downstream apparatus evens out pulse fluctuations in the flow. The flow is kept at a constant 2 ml./min, and the depth between the plates and the jet diameter are varied to provide different flow conditions.

The flow rate is kept low to avoid the need to return blood to the animal, so that all blood impinging on the plate has never before contacted a non-biological surface.

A variety of events are observed in the experiments; initially a

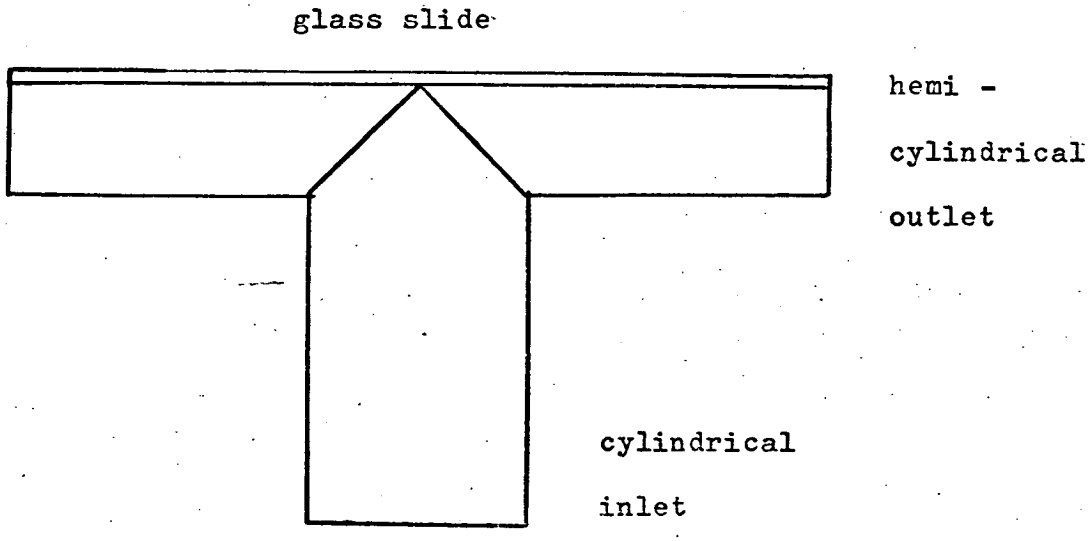

Fig. 3. Dutton's stagnation point T-chamber.

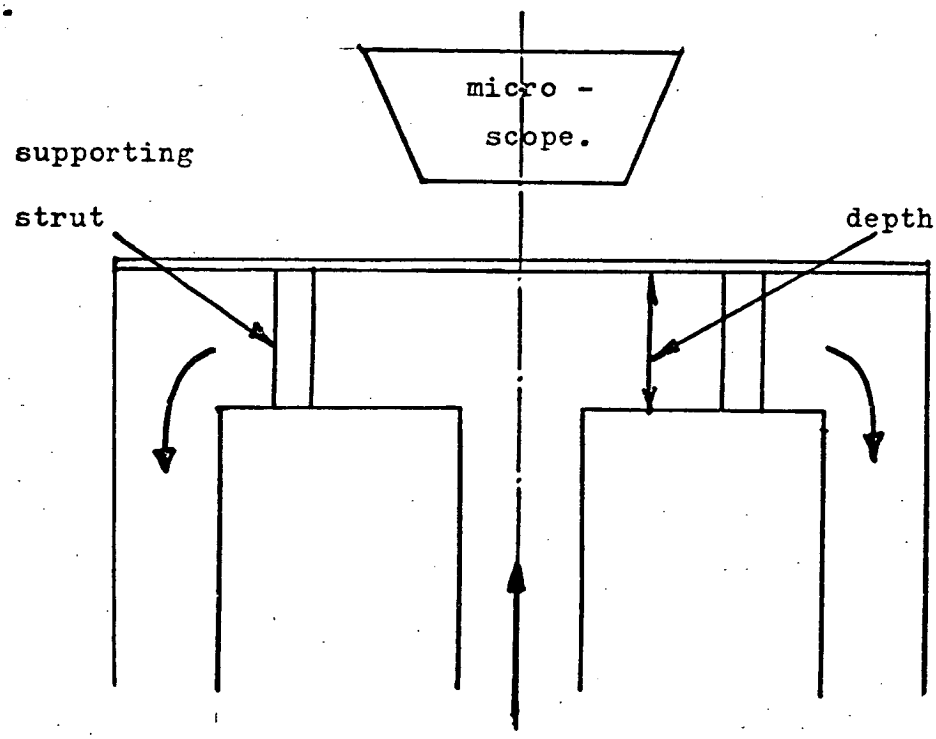

Fig. 4. Petschek's stagnation point flow chamber.

monolayer of platelets is deposited, later a circle of deposited white cells, centred round the stagnation point, can be seen. Symmetric thrombus or wedge-shaped thrombus, consisting of platelet aggregates and white cells, can be seen.

A build-up of thrombus behind the supporting struts can sometimes be observed. The particular athrombogenic surface used does not seem to affect the general character of the results. The authors describe the mechanism of thrombus formation thus:

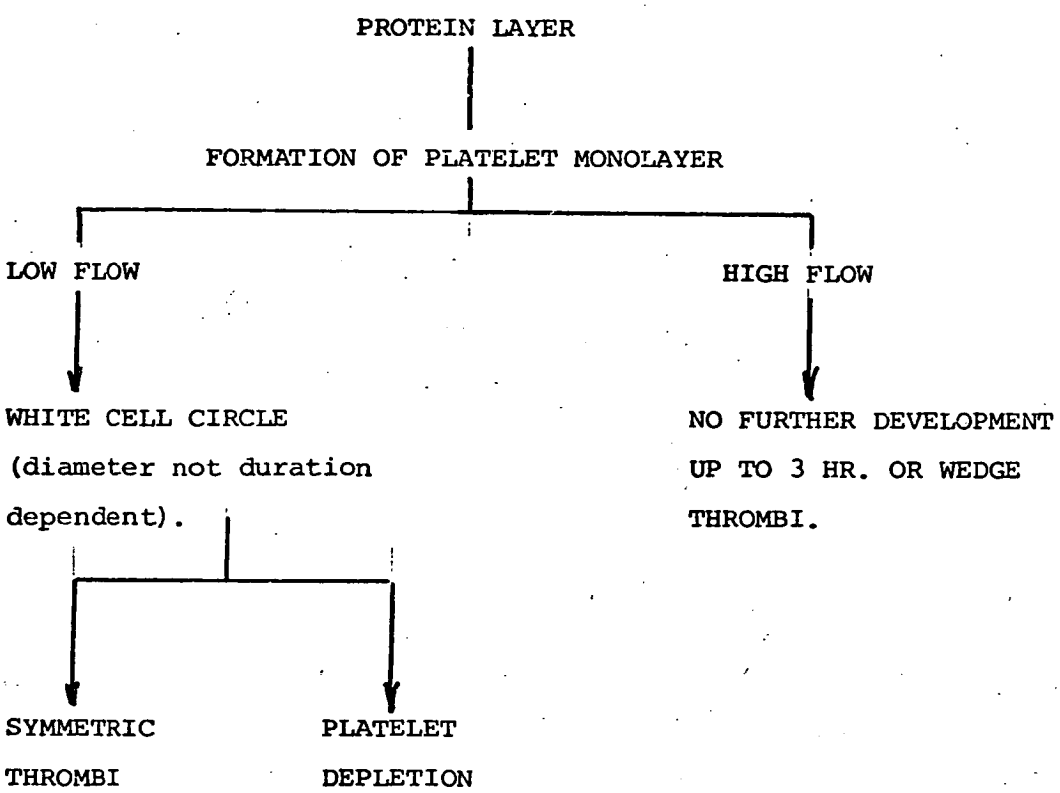

Thrombus formation behind struts.

The authors suggest this is associated with the distrubed flow which exists in such a region.

Wedge thrombi.

The authors suggest that these are initiated by small surface imperfections which are sometimes large enough to be seen under the microscope. If a wedge thrombus was shed from the surface, another reformed in the same place.

Both of these suggestions are apparently consistent with the view that wake regions of high mass transfer are also regions where

thrombus appears.

White cell circle formation.

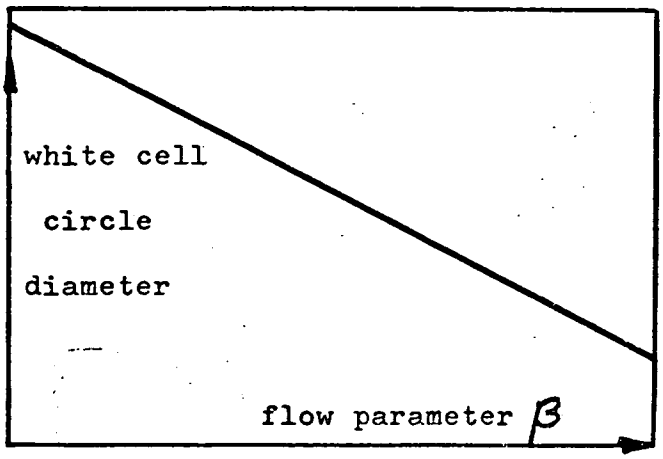

Superficially, the radial distribution of deposited white cells about the stagnation point of the jet suggests a relation with the distribution of convective mass transfer coefficient obtained in the rather similar wall-jet system investigated theoretically by Scholtz and Trass (144) and experimentally by Kapur and MacLeod (98). For a normal wall jet it is known that the mass transfer coefficient at a given jet flow rate diminishes with increasing radial distance from the stagnation point. It might appear that the white cell cirle of limited radius observed in the impinging blood jet experiments corresponds to the limited zone over which the convective jet/wall mass transfer coefficient equals or exceeds some threshold value necessary for white cell deposition. However the issue is clouded by the fact that fluid behaves differently within and without the jet area.

The authors only considered an area of glass plate equal in area to the impinging jet, and although mass transfer rates decrease with distance from the stagnation point at radii greater than that of the jet, the shape of the mass transfer rate distribution in the immediate vicinity of the stagnation point is not known with certainty.

Two possible shapes are shown in Fig. 5. The results obtained by Kapur and MacLeod (98) could be interpreted to yield either of these curves. If a "bumped" crater of the general type (b) reflects the true situation, then Petschek et al's findings constitute evidence to support the hypothesis; if curve (a) is the correct one, then the findings constitute contrary evidence.

Since the white cell circle diameter decreases with increasing flow parameter, the authors conclude, on the basis of a theoretical fluid mechanical relation between shear stress and radial distance from the central stagnation point, that the white cell deposition is shear limited. Outside the circle, the shear stress is supposed to exceed the adhesive force immobilising the deposit on the surface.

Based on an analysis by Schlichting (145), Petschek et al develop the relation for the radial variation of shear stress at the wall

$\tau = \rho.\upsilon.\beta.r$ where τ = shear stress.

ρ = fluid density.

ν = fluid kinematic viscosity.

r = radial distance from central stagnation point.

β = flow parameter.

This indicates that, for a given jet velocity, τ increases monotonically with distance from the jet axis. He then postulates a limited shear stress for white cell deposition and fits the relation $5.5 = \rho.\nu.\beta.r.$ to his data for β and white cell circle diameter.

There are two shortcomings in his conclusion; firstly, the straight line he draws through his data points is not a good fit; and secondly he erroneously extends his line to a region outside the jet area, for which Schlichting's analysis is not applicable. This

latter defect in the "shear limit" theory of white cell circle formation will now be examined.

The relation between shear stress and radial distance outside the jet area.

Consider the control volume shown in the streamline pattern of an ideal frictionless fluid impinging on a flat plate (Fig. 6).

Volume of fluid entering control volume/unit time

= volume of fluid leaving control volume/unit time.

To a first approximation,

Volume entering = πr^2 x jet velocity. (providing r is within the jet radius).

volume leaving = $2\pi rd$ x outward radial velocity.

outward radial velocity = $\frac{r \times \text{jet velocity}}{2d}$

i.e. radial velocity increases linearly with distance from centre since the jet velocity is constant.

However, if r is outside the jet radius, the volume entering is not a function of r, but equals $\frac{\pi}{4}$ (jet diameter)^2. (jet velocity), and so the outward radial velocity α 1/r. This analysis can be approximately applied to the case of a real fluid having viscosity, in which case the shear stress at the surface, being proportional to velocity, increases with radius as far as the jet radius, and decreases outside the jet radius. Glauert (146) gives an analysis of the flow behaviour of an infinitesimally narrow jet impinging on a flat plate, and arrives at the relation

$$\tau = \frac{\text{const.}\rho}{\nu^{\frac{1}{4}} \cdot r^{\frac{11}{4}}}$$

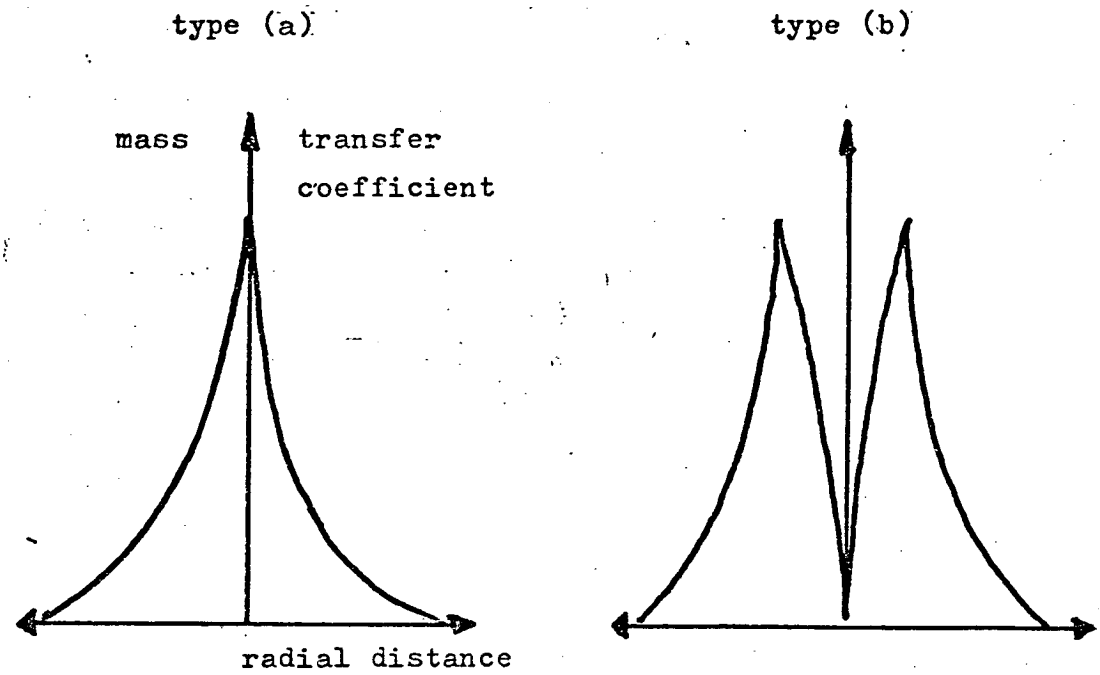

Fig. 5. Distribution of mass transfer coefficient about the stagnation point.

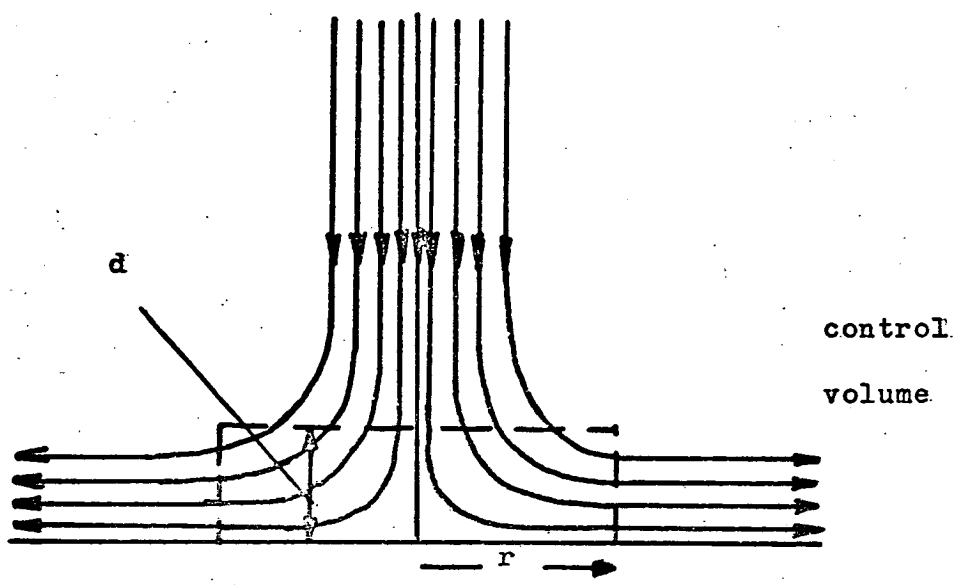

Fig. 6. Streamline pattern of ideal fluid flow perpendicular to a flat plate.

which result supports the approximate result obtained by considering the control volume, i.e. shear stress decreasing with radius outside the jet radius. Thus, the relation $\tau \alpha r$ derived by Petschek only applies over a region of impingement of radius comparable with that of the jet orifice. The formation of white cell deposits of larger radius cannot, therefore, be explained by the shear limit hypothesis.

Further tentative evidence to support the hypothesis.

A great deal of work has been published concerning the association of hydrodynamic disturbance, especially shear stress levels, with blood damage, particularly hemolysis. Although there is as yet no proof that hemolysis is assocated with thrombosis, the supposition is plausible on the grounds that both phenomena occur as a result of trauma to the circulatory system.

The effects of a variety of hydrodynamic disturbance on blood damage are reported in Refs. 53-62; and in Refs. 63-66, it is shown that when the blood is in contact with non-biological surfaces the shear stress level necessary to cause blood damage is substantially reduced. The mass transfer coefficient is closely linked to the shear stress at the surface. In Refs. 67 and 68, it is shown that adhesion of blood elements to a surface, one of the initial steps in thrombosis, is influenced by the rate of diffusion of the elements toward the surface, perpendicular to the main flow. Mass transfer is similar in that diffusion toward the surface enhances the process. An association between hemolysis and thrombosis is suggested in Refs. 53 and 69 from a theoretical biochemical standpoint, and in Ref 67 as part of a proposed model which attempts to account for blood cell tethering to a surface.

This tentative evidence is included to support the hypothesis by

the chain of association:

mass transfer ~ hydrodynamic disturbance ~ hemolysis ~ thrombosis.

1.4 The strategy adopted for establishing the proposed correlation.

Of the evidence cited in Section 1.3 associating mass transfer coefficient with hydrodynamical factors in thrombus formation, the most significant were deemed to be: the formation of clot on the early Edinburgh valve; the formation of thromboemboli downstream of Vorhauer's implantable probes, and the formation of white cell circles and wedge thrombi in Petschek's blood flow chamber.

The thesis contains an account of three separate investigations. The first describes the attempt to obtain blood clot data from animal studies with the Edinburgh valve. This attempt involved the parallel objective of determining the vane opening angle in vivo so that the configurations of the opened valve could be accurately simulated for mass transfer experiments. The second part of the project consisted of the development of a method for the experimental measurement of mass transfer coefficients on small curved surfaces, viz., Vorhauer's disc probe - a method intended ultimately to be applied to the surfaces of valves. The third part of the project was a direct attempt to test the hypothesis of the correlation between mass transfer and clotting by the measurement of mass transfer coefficients on Petschek's blood flow chamber.

Ultimately, it was intended to compare the distribution of blood clot on the curved surface of the Edinburgh valve with the mass transfer coefficient distribution, and to compare the dimensions and other characteristics of the white cell circles in the stagnation point flow chamber with the mass transfer coefficient variation on the chamber surface.

CHAPTER 2

The determination of the vane opening angle of the Edinburgh valve.

2.1 Introduction

In the course of a series of canine experiments, conducted by M. Turina in Switzerland, the Edinburgh valve was found to be stenotic at the elevated heart rates obtaining postoperatively. (50). The excised valves were subsequently found to be encased in clot. Although the elevated heart rates obtain for a short time, vane malfunction or high pressure drop across the valve due to its relatively small orifice would be sufficient to initiate the clotting process which would continue even when the valve was operating satisfactorily at lower heart rates.

It was necessary, therefore, to determine whether the stenosis was caused by inadequate opening of the vane or by insufficient orifice size, for the multiple purpose of:

(a) developing further the Edinburgh valve.

(b) determining the orientation of the valve in vivo so that this position could be simulated in the mass transfer measurement experiments.

(c) obtaining blood clot data.

The importance of purpose (b) for the present work is that the mass transfer coefficient variation over the surface of the valve would be greatly influenced by the angle which the vane assumed in the blood flow. In particular, if the valve was failing to open fully, the in vitro experiments would have to investigate effects of impinging and separated flow.

2.2 The in vitro determination of the vane opening angle.

A mock circulatory loop, of the Wind-kessel, or lumped parameter type, was constructed in which to observe the valve

operations.

In general, a loop of this type represents the cardiovascular system by the following components.

1. A pulsatile fluid flow representing the cardiac output.
2. A valve operating chamber.
3. A load-impedance, consisting of relatively few resistive, capacitative, and inductive components representing the sum of all of these effects in the vascular system. For a detailed account of the model requirements see (62).

The main design decision in this form of testing is the degree of authenticity, and hence complexity, which is required. Huckaba and Hahn (71) comments "Arterial blood flow is the almost-periodic, unsteady-state flow of a non-Newtonion fluid through a flexible-walled, tapered, branching conduit". This paper, along with Ref. (72,73) illustrate the theoretical complexity of the topic, in terms of analagous A.C. electric circuits. Mrava (74) and Klain (75) suggest general hydrodynamic approaches, and Westerhof et al (76) provide an adjustable design which is reported to correlate well with the available data on man, dog, cat and rat.

The question arises: what degree of authenticity of representation is

(a) possible.

(b) required.

(a) The description of the dynamic characteristics of the cardiac output and the load impedance of the vascular system is at best very complex, even when many simplifying assumptions are made. The available physiological data (77,78,79) suggest that only a very

approximate model could even be constructed.

(b) Since the required degree of authenticity for the purpose of determining vane opening angle was unknown, it was decided to utilise existing equipment at Edinburgh, as a starting point.

EQUIPMENT (Fig. 7)

The mock circulatory loop was based on the design described by Alami & MacLeod (80). The pulsatile flow was provided by MacLeod's positive displacement diaphragm pump, which has independently variable frequency, stroke volume, and systolic/diastolic ratio. (81).

The working fluid was water; the intention was to replace this with a glycerine/water mixture of the same viscosity as blood when the model had been successfully adjusted.

The valve operating chamber was a cylindrical perspex housing of the same diameter as the valve.

The lumped capacitance of the circuit consisted of an expansible silicone rubber tube. The valve could be altered by using different gauges of rubber, or by enclosing the tube in an airtight container.

The lumped resistance consisted of a screw clamp on one of the connecting tubes, and could be varied further by using different diameters of tube.

The immediate shortcomings of this model are that:

The values of the capacitance and resistance can only be grossly estimated and controlled;

The screw clamp is not a pure resistor as its effect alters

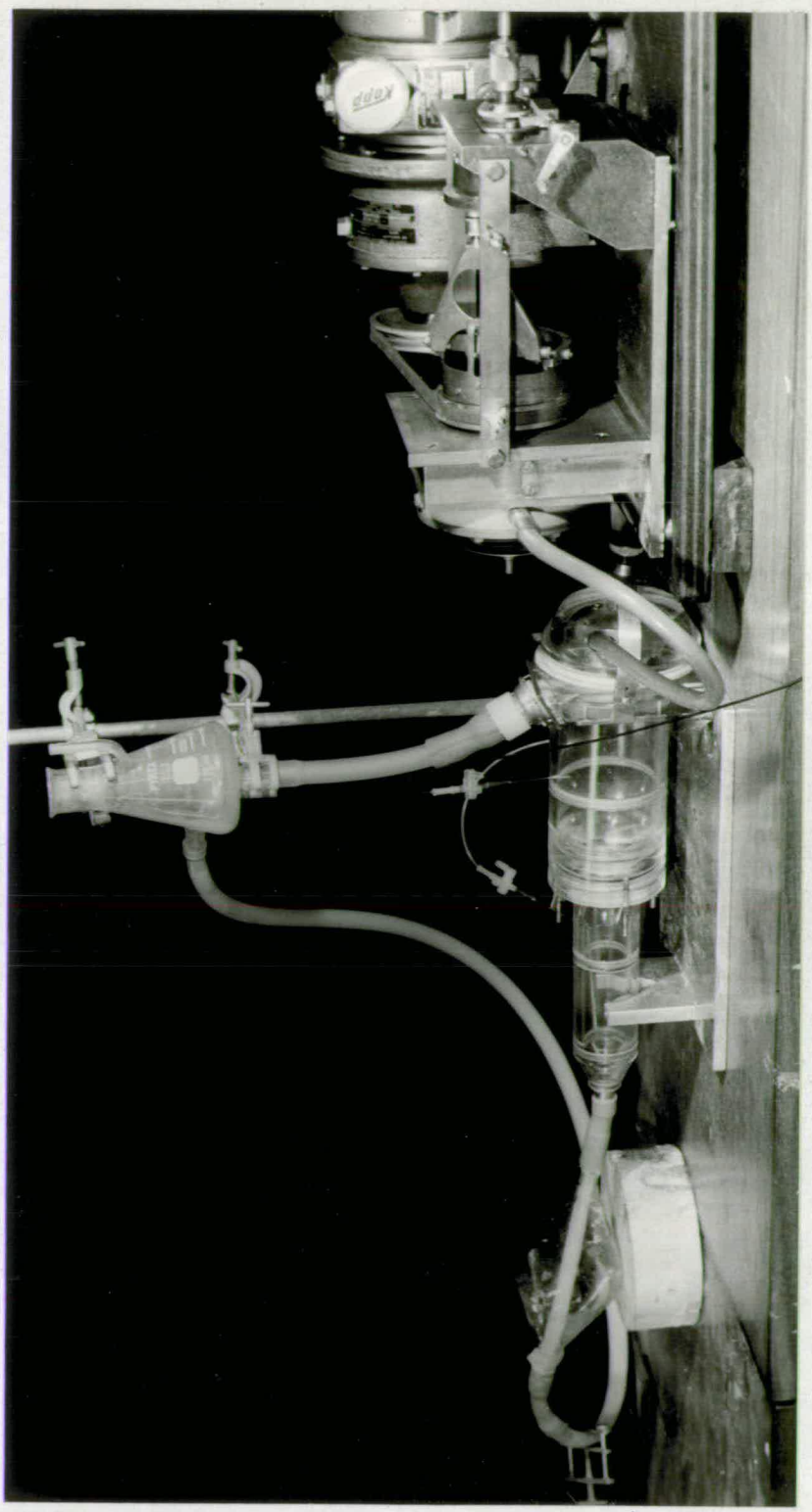

Fig.7. The mock circulatory loop.

with pressure fluctuations during the cycle;

There is an additional unknown capacitance effect due to the flexible nature of the rubber or P.V.C. connecting tubes;

The inductive effect of this circuit is necessarily too great, due to the large working fluid mass;

The physiological phenomenon of wave reflection from arterial bifurcations is not taken into account.

Initial Experiments with the loop.

The valve was tested under a variety of pulsatile conditions, to determine its limits of operation.

At first, results were not reproducible because:

(a) certain examples of the valve had slightly sticky pivots, severely affecting the performance. (those were subsequently screened out).

(b) The flexibility of the compliant tube material diminished with increased total immersion time and total number of operational cycles (subsequently the tube was frequently renewed).

However, it quickly became apparent that very slight changes in the parameter specification crucially affected the valve's performance; the valve could be made to operate satisfactorily under almost any cardiac output conditions by altering the downstream distance of the capacitance, or by altering the atrial head.

Furthermore, intermittent operation of the vane was observed, i.e. an occasional flutter every several cycles. No explanation for this effect was found.

Therefore, no valid results were obtained, and it was decided to improve the design of the model.

Modifications.

Since the valve was so sensitive to the particular flow conditions, it seemed sensible to firstly attend to the immediate vicinity of the valve. The cylindrical valve housing was replaced with a more realistic chamber.

The requirements of the chamber were considered to be:

1. Realistic cross sectional areas immediately upstream and downstream of the valve.
2. Longer inlet approach length to minimise the effect of the severely disturbed flow emanating from the pump diaphragm.

A cylindrically symmetical perspex housing was built to simulate the variation in flow area of the approaches to the valve in the human heart (Fig. 8). This equivalent diameter cross-sectional flow area was obtained from Weiting (82) who injected silicone rubber into human hearts during necropsy, subsequently slicing the silicone impression every 2.5 mm. parallel to the valve annulus for 30 mm. either side of the valve, and expressing the area of each slice as an equivalent circular diameter.

Additional cylindrical sections could be added to lengthen the inlet and outlet approaches to the valve.

Effect of the Modification.

Different values of the range of operation of the valve were obtained with the new chamber, but the sensitivity to small manipulations of the circuit parameter valves remained high. The greatly increased diameter of the inlet section increased the

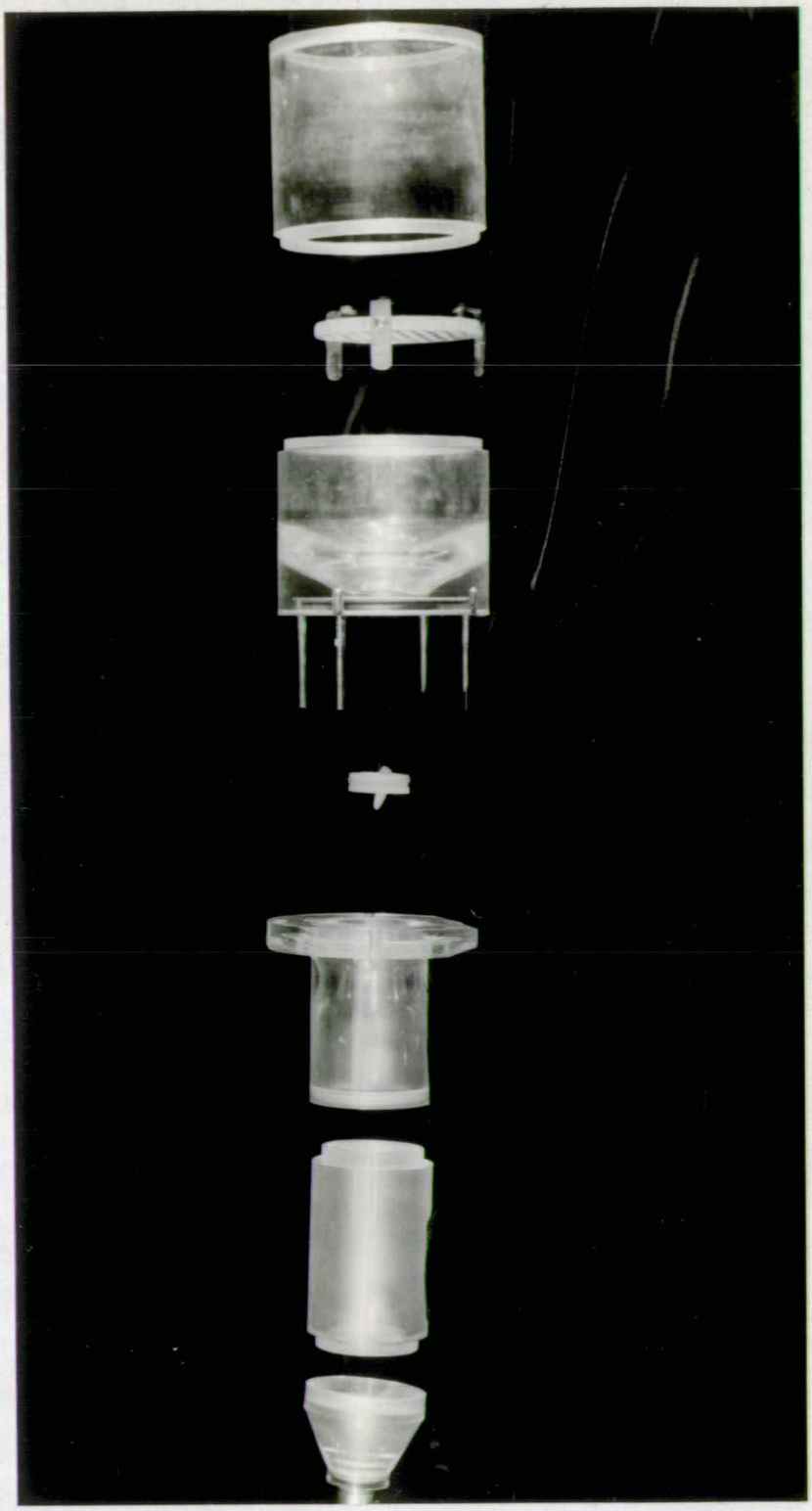

Fig.8. Exploded view of heart valve test chamber.

inductive component of the circuit, but the effect of this could not be interpreted. Also, using potassium permanganate dye, it was observed that considerable swirling of the fluid was occurring in the large inlet section, and so a sieve flow straightener was devised (Fig. 9). Although a comprehensive series of tests were undertaken, no meaningful pattern emerged to indicate the specific effect of any one of the circuit parameters.

Conclusion.

It was now clear that it would be virtually impossible to achieve the accuracy required to give entirely reliable test information, therefore it was decided to abandon the loop and divert attention to possible in vivo methods of settling the vane opening angle question.

2.3 The in vivo determination of the vane opening angle.

2.3.1 Echocardiography.

The use of a V.H.F. (2×10^6 HZ) sound echo beam to give a radar picture of internal organs is a well-established non-invasive diagnostic technique in medicine, in particular to diagnose human heart complaints (83-86) by comparing echo patterns with known characteristic reference patterns.

With the help of Dr. S. Shaw (Western General Hospital, Edinburgh), calibration echo patterns of the Edinburgh valve in the mock circulatory loop in various opening angles were made, and compared with in vivo patterns obtained from two dogs with valves implanted under the direction of Mr. D.M. Wade (Royal Infirmary, Edinburgh), to try to ascertain whether the valve was indeed opening fully.

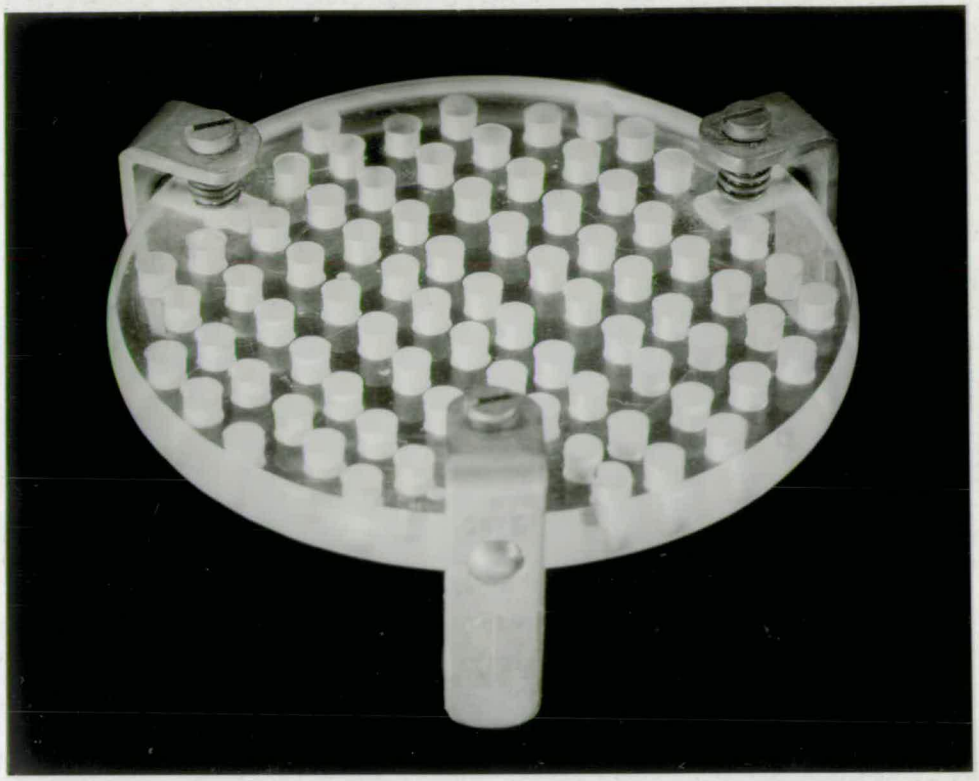

Fig.9. The flow straightener.

The ultra-sonic transmitter/receiver probe was aimed in a direction which maximised the displacement signal obtained (Fig. 10). This direction is easily found by trial and error in the in vitro calibrations; but in vivo this direction can only be estimated because the exact orientation of the valve in the animal is unknown.

Fig. 11 shows a typical trace of the valve opening fully in vitro. The horizontal axis measures time, the vertical axis measures displacement in the direction of the sound beam.

The horizontal line at the bottom of the photograph is the signal from the fixed valve housing.

Figs. 12 and 13 show typical traces obtained from the valve in each of the two dogs. In Fig. 12, the white wavy boundary at the top of the photo, and the speckled wavy band at the bottom of the photo represent the pulsations of the surrounding heart tissue.

In all three photographs the lowest point on the trace represents the closed position of the valve.

The ultra sonic technique measures the movement of the valve occluder relative to a fixed external source of ultrasound (i.e. the transmitter/receiver probe), rather than the motion of direct hydraulic importance, viz. that relative to the valve housing. The two motions are quite dissimilar because the valve housing moves grossly with the pulsations of the surrounding heart tissue.

The traces in Figs. 12 and 13 could therefore only be interpreted meaningfully if a datum line for the movement of the valve housing could be distinguished, against which the trace of the occluder could be compared. However this datum line is in some unknown position within the speckled wavy band; that is the

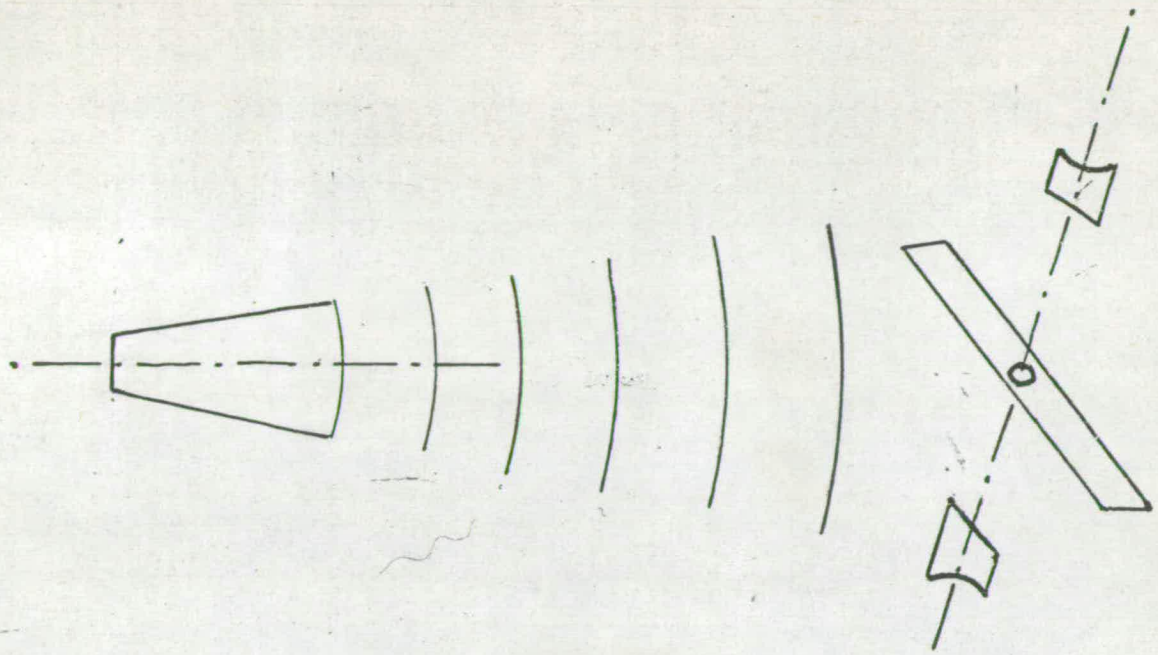

Fig. 10. Optimum direction of echo probe.

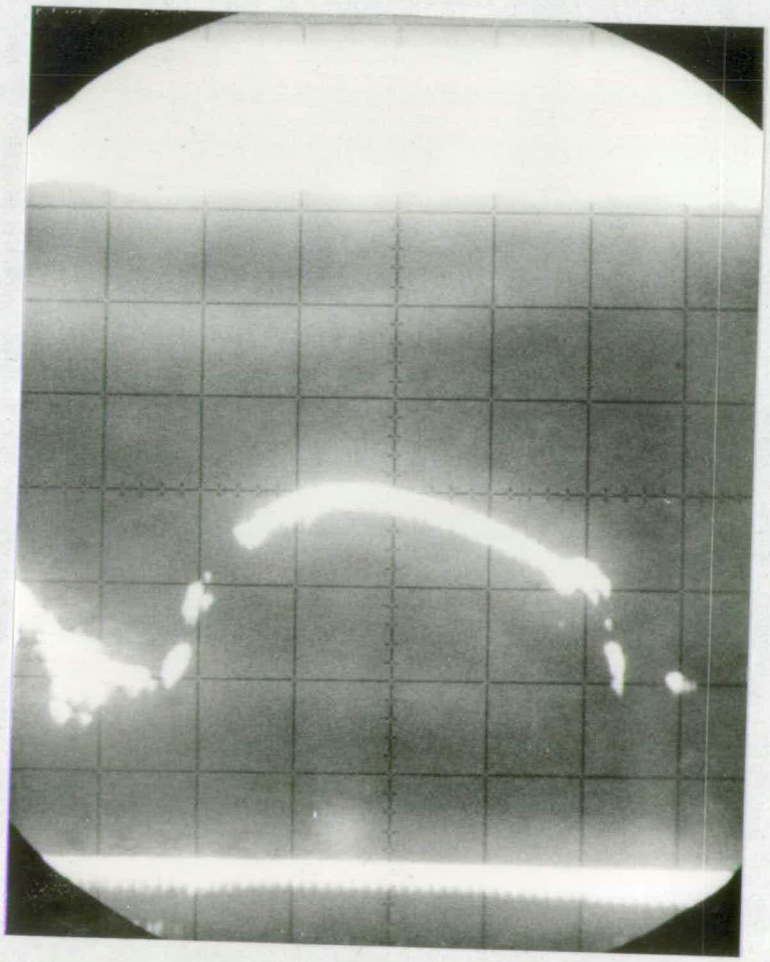

Fig. 11. In vitro echo trace.

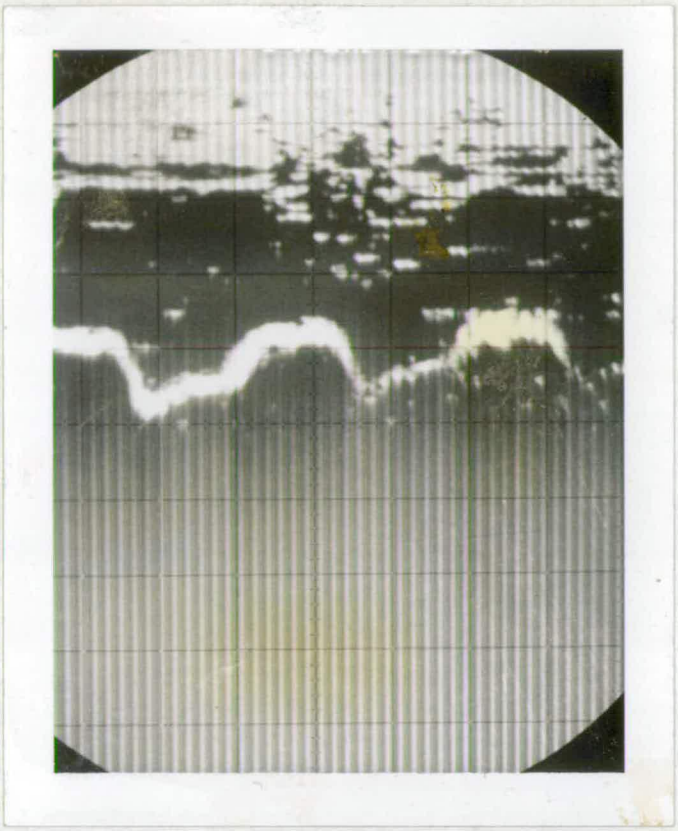

Fig. 12. In vivo echo trace.

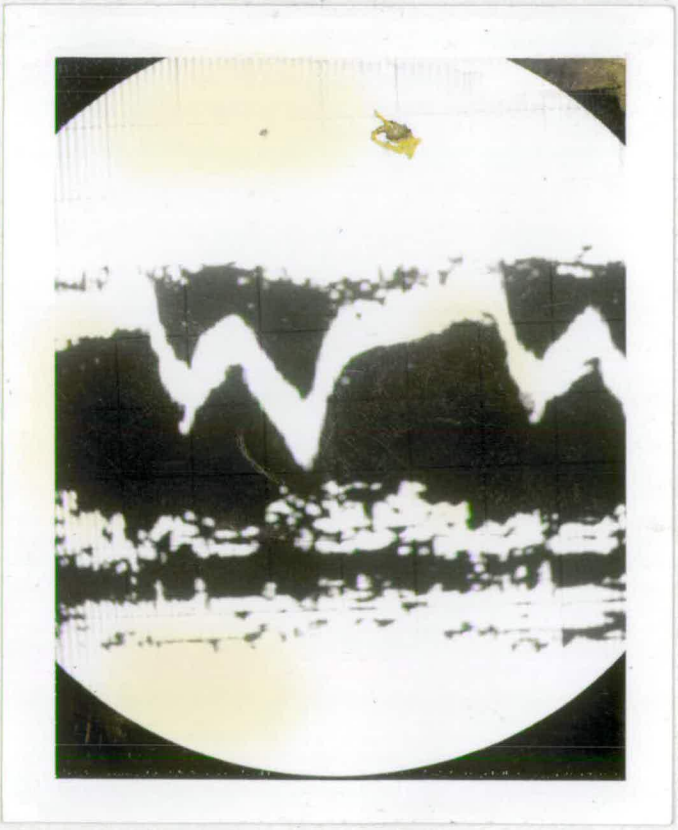

Fig. 13. In vivo echo trace.

technique is not capable of resolving the signals obtained from the valve housing and tissue.

This method of determining valve opening angle was therefore abandoned.

2.3.2 Cineradiography.

It was felt that cineradiography (i.e. the making of cine film of the image obtained from an X-ray machine) (87) could provide the required opening angle information which echocardiography had failed to give.

A delrin model of the valve was fitted with X-ray opaque register marks made of silver wire (Fig. 14) and implanted in a dog under the direction of Mr. D.E.M. Taylor (Royal Infirmary, Edinburgh, now Royal College of Surgeons).

The register marks were required because a valve made in either delrin or carbon would not be detected by X-ray. The principle of the method is to geometically analyse the X-ray film frame by frame, calculating the angular displacement between the register marks on the occluder and housing, to determine whether this displacement ever reaches its possible maximum i.e. the value opening fully. Three register marks, the minimum number to prevent ambiguity in the film analysis, were embedded in the vane, and one on the ring.

However, during the experiment, the cine equipment failed, and no results were obtained. Plans for a subsequent attempt were abandoned when it became clear that an alternative method of detecting valve opening angle, Telemetry, looked more promising.

2.3.3 Telemetry.

For the determination of valve opening angle, a valve with an

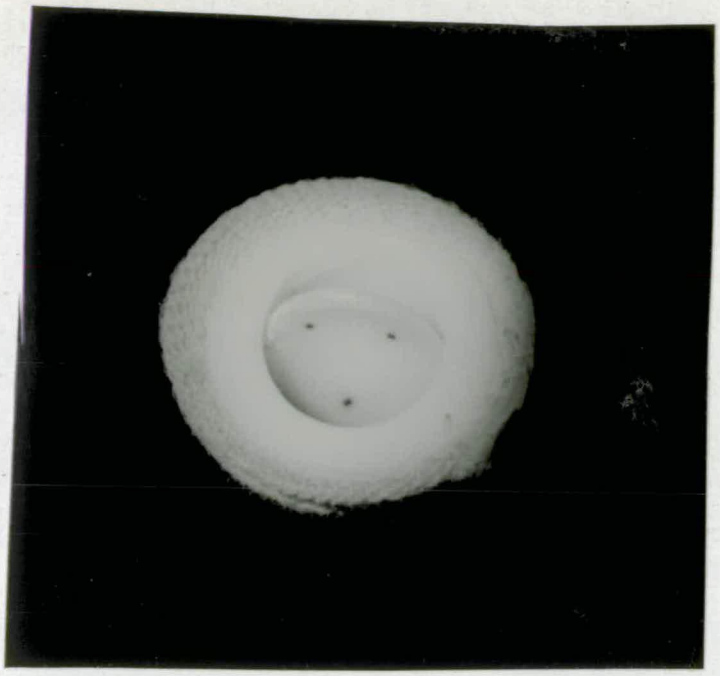

Fig.14. The X-ray Valve.

attached radio-transmitting device was built (Fig. 15). The system was based on the change of inductance of a coil wound on the non-conducting delrin valve annulus as the conducting carbon vane changed its position. The coil was connected to a tuned resonant circuit, transmitter, and battery power pack situated just outside the myocardium of the experimental animal. The transmitter gave a continuous vane opening angle signal which was monitored on an oscilliscope via a receiver.

The electronics of the system were devised by J. Filshie and J. McGee (Poultry Research Unit, Edinburgh) as an extension of their telemetry devices developed for implantation in poultry (88). The implantations of the radio-valve were supervised by Mr. D.M. Wade.

Initially, although the system gave a clear signal, it suffered from the same limitation as the echocardiography technique, that is, the calibration of the signal in vitro could not be reliably extended to the results obtained in vivo, because of the presence of moving conducting tissue and fluids, which severely affected the response of the inductance coil.

The method showed great promise, and a separate development program was undertaken by The Wolfson Electronics Unit (Edinburgh University), to devise a more advanced electronics system to solve the calibration problem. The principle of the advanced system was to tilt the axis of the coil slightly on the valve annulus, so that as the vane reached its maximum possible opening angle, a distinct turning point appeared on the transmitted signal, which provided a definite internal calibration. Typical traces are shown in Fig. 16.

This project, described by MacLeod (50) was entirely successful; the results showed that even at very high post-operative heart rates

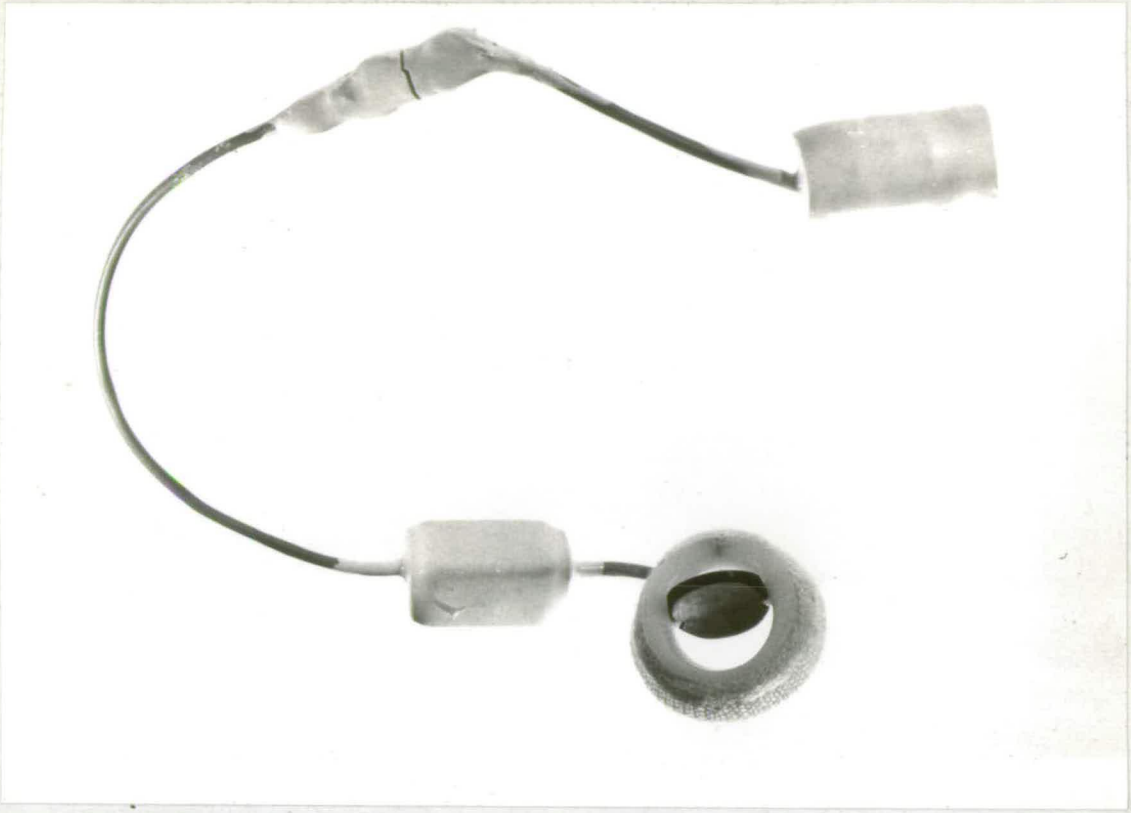

Fig. 15. The telemetry valve.

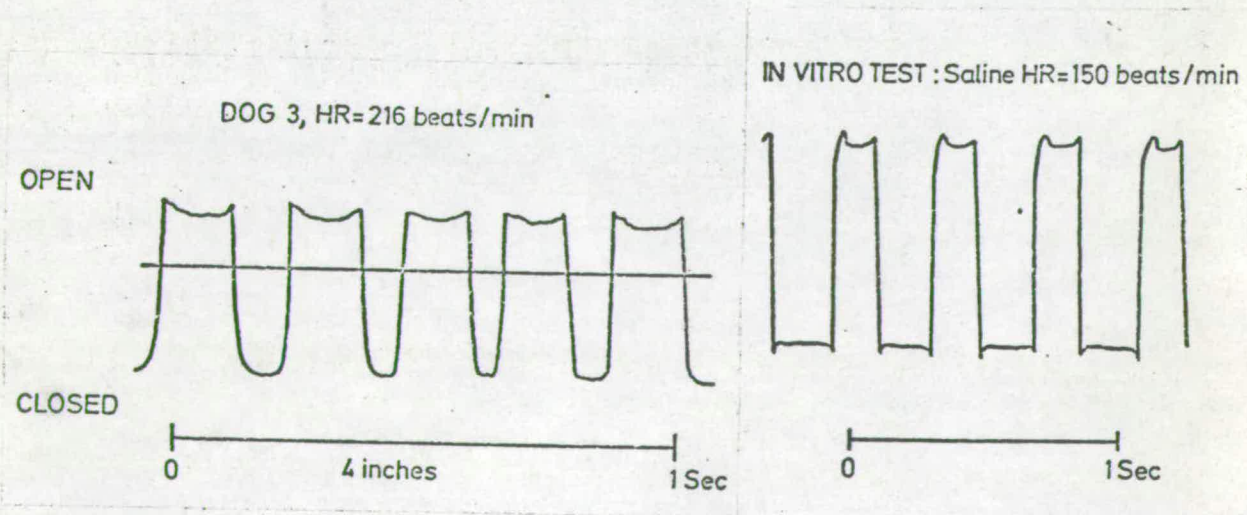

Fig. 16. Traces obtained with the telemetry valve.

of 220 beats/min, the valve opened fully.

2.3.4 Valve occlusion by massive clot formation

During the series of animal experiments, many implanted valves were found on post mortem to be completely covered in clot. Shorter term experiments indicated that this clot, resembling tissue, originated at the suture line on the endothelium, and gradually grew inwards. This type of clotting is distinct from thrombus formed on the working parts of the valve primarily exposed to the blood flow, and the problem is apparently peculiar to dogs, and not to humans or calves (89). In an attempt to inhibit the clot from spreading over the valve, a variety of silicone shields were constructed, based on a design described in (89), and attached to the implanted valves (Fig. 17).

However, none of the silicone shields were successful; subsequently calves were used instead of dogs during the further development of the Edinburgh valve (90).

2.4 Conclusion.

The success of the telemetry device in proving that the valve opened fully eliminated the possibility that clotting was caused by occluder malfunction, therefore it was concluded that some aspect of the shape of valve was to blame, subsequently found to be the relatively small orifice size.

Since the exact position of the vane in vivo had now been established, both the measurement of the mass transfer coefficients and the further development of the Edinburgh valve (described in 50 and 90) could proceed. Although no blood clotting data was obtained, it was decided to go ahead with the acquisition of mass

transfer data, in the hope that blood clot data would in the meantime be forthcoming from another source.

The failure of the attempt to obtain blood clotting data was due to the fact that later prototypes of the Edinburgh valve did not form clot on the valve surface in short term experiments as the first, flat-vaned prototype had done. Experiments long enough to allow clot to form were not possible because of the massive clot occlusion phenomenon particular to dogs.

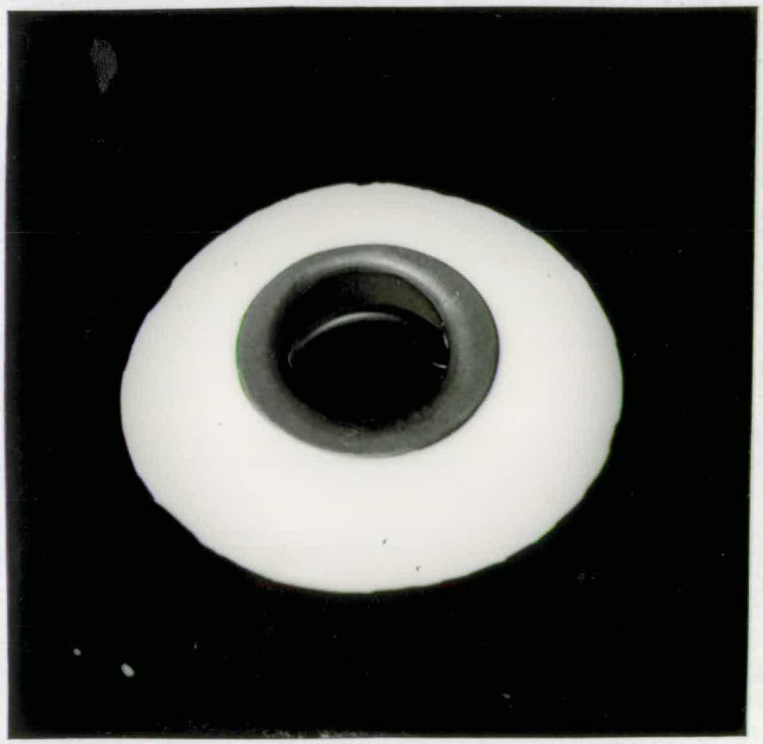

Fig. 17. The silicone rubber shielded valve.

CHAPTER 3

The determination of mass transfer coefficients on small curved surfaces.

3.1 Introduction

Ultimately, it is desired to ascertain the local mass transfer coefficients over the surface of a heart valve which is operating in an oscillating flow.

In order to develop the technique of holographic interferometry to such an extent, it was necessary to proceed stepwise because of the considerable experimental difficulty with this method, even if simplified mass transfer experiments are undertaken.

The developmental steps envisaged from the current level of development of this technique, i.e. large flat plates, exposed to a steady stream of air, at a great distance from the holographic viewpoint, were thus:

1) Gain experimental expertise with the large plates already investigated.
2) Extend method to small objects, having simply-described curvatures, exposed to a steady flow.
3) Extend method to a heart valve, of complex shape, in a variety of fixed partially and fully open positions, exposed to a steady flow.
4) Extend method to a heart valve in a variety of fixed positions in an oscillating flow.
5) Extend method to a heart valve allowed to operate freely in an oscillating flow.

To begin with, the small curved object chosen was the disc probe described by Vorhauer (51) since limited blood clot data existed for this shape. It was anticipated that more detailed data would become available for the disc and the rest of Vorhauer's probes.

The disc (Fig. 18) was chosen in favour of the other probe shapes because:

(a) it has the largest diameter of the probes, facilitating the miniaturisation of the available experimental technique.

(b) its two spherical faces constitute an approximation to a continuous surface, thus facilitating the mathematical analysis of the fringes, as opposed to the discontinuities present in the cone and frustrum, and the change of curvature in the tear drop shapes.

3.2 General Principles of the holographic technique

Techniques based on holographic interferometry have been widely used to measure surface displacements and deformations of solid objects (91-97).

In holographic interferometry, the wave front from the studied object in its original position is first recorded on a hologram, and the reconstructed image is subsequently superimposed on the perturbed object or its reconstruction, resulting in interference fringes from which the extent of the surface displacement can be calculated in terms of the wavelength of light and the geometry of the optical system.

A beam of coherent light is split into two beams, one illuminating the holographic plate (the reference beam), the other illuminating the object (the object beam) (Fig. 19). The light scattered from the object interferes with the reference beam at the holographic plate forming a density pattern on the photographic emulsion. The hologram thus records the amplitude and phase of the light reflected from the object. When the plate is developed and re-illuminated with the reference beam, the plate acts as a diffraction

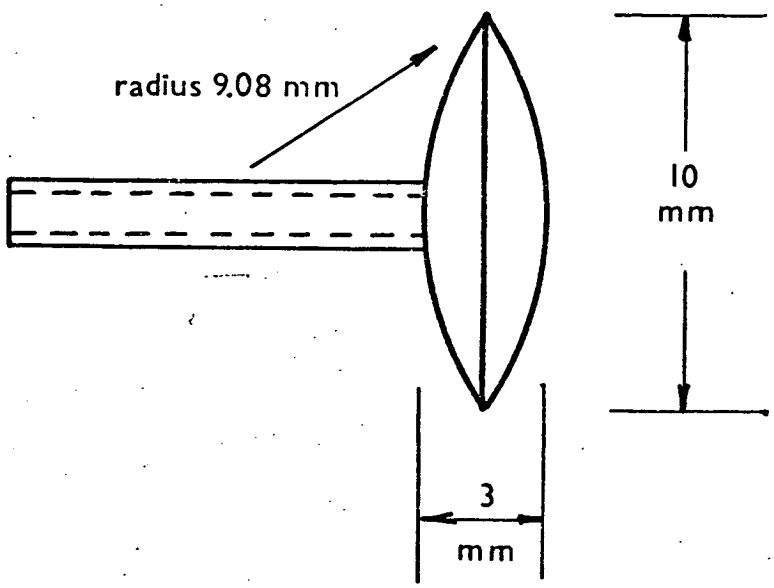

Fig. 18. The convex disc.

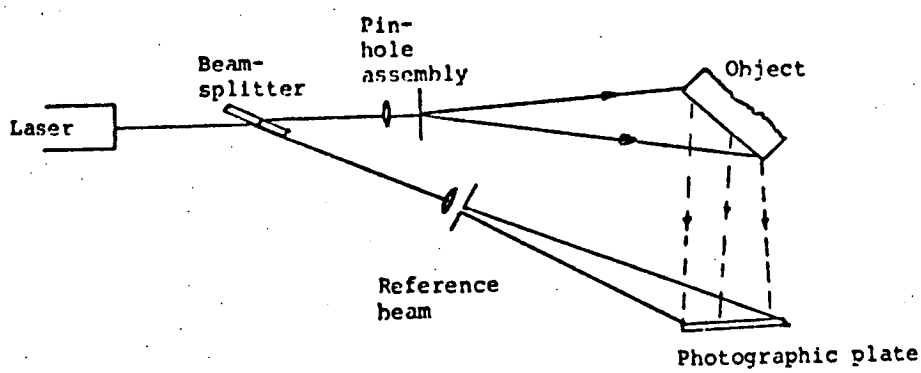

Fig. 19. Optical arrangement for recording a hologram.

grating and reconstructs a three-dimensional virtual image of the object.

Providing the holographic plate is returned to exactly the same position after developing, the reconstructed image is exactly superimposed on the real object, and any movement or deformation of the object results in interference fringes across the object surface.

This technique has been applied by Kapur and MacLeod (98-100) to measure mass transfer coefficients, where the deformation of the object consists of a surface recession brought about by mass transferred from a swollen polymer coating on the surface.

Their technique is superior to conventional methods, summarised by MacLeod et al (101 and 103), where the surface recession of a subliming-solid model of the test object is measured mechanically or pneumatically. This holographic method is more accurate as a means of measuring surface recession by an order of magnitude, consequently the actual recessions used can be made small enough not to affect the hydraulic characteristics of the object itself.

The diffusely reflecting object is coated with transparent silicone rubber to a thickness of .2 m.m. approximately, and immersed in a volatile organic swelling agent until equilibrium swelling is reached (103). A variant of this technique, "front-surface reflection", uses opaque instead of transparent coatings.

A hologram is made of the object, which is then placed in a constant temperature airflow whose velocity is measured. Some of the swelling agent evaporates into the airflow, causing the polymer layer to shrink. At any point on the object surface, the rate of shrinkage of the swollen coating is proportional to the fluid-side mass-transfer coefficient, providing the initial conditions are

chosen according to charts relating vapour pressure with percentage of equilibrium swelling (103). If the total amount of swelling agent removed from the coating is kept within a certain limit, the vapour pressure remains nearly constant during the experiment, and so the rate at which the agent is evaporated is a reasonable measure of the mass transfer coefficient.

A second holographic exposure of the object is made after mass transfer, and this is exactly superimposed on the first image. The optical path length of the object illuminating beam has changed because the beam passes through a different thickness of coating, whose refractive index is different from that of air (Fig. 20).

The interference fringes formed by the difference in optical path lengths between the two exposures can be interpreted in terms of surface recession, and then in terms of local mass transfer coefficients.

3.3 Difficulties with the method.

The practical disadvantage with this method is that unusual skill and care are required to realise fringe patterns.

Since the interferometry technique is capable of detecting movements as little as half a wavelength of light i.e. 3×10^{-4} m.m., any extraneous movement of this order of magnitude can eliminate the appearance of fringes, and still smaller movements can introduce unacceptable "noise" in the optical system.

For example, the heat of the hand touching an optical component causes sufficient expansion to upset the experiment. Also, between exposures, the test object must be removed and replaced gently on its kinematic mount, each of whose three located points must be

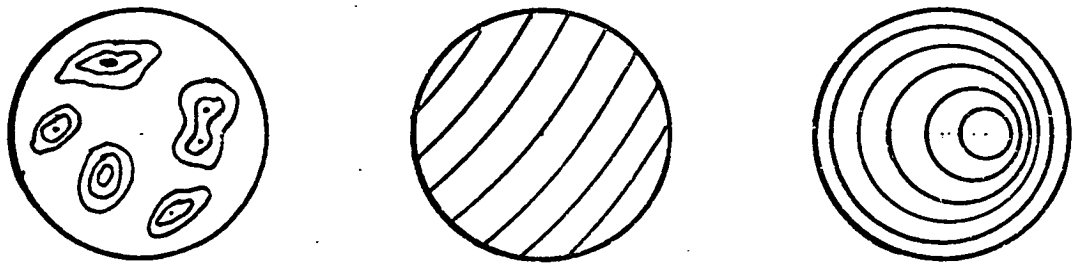

swelling agent too volatile

probe displaced

mass-transfer pattern

Fig.21. Fringe patterns.

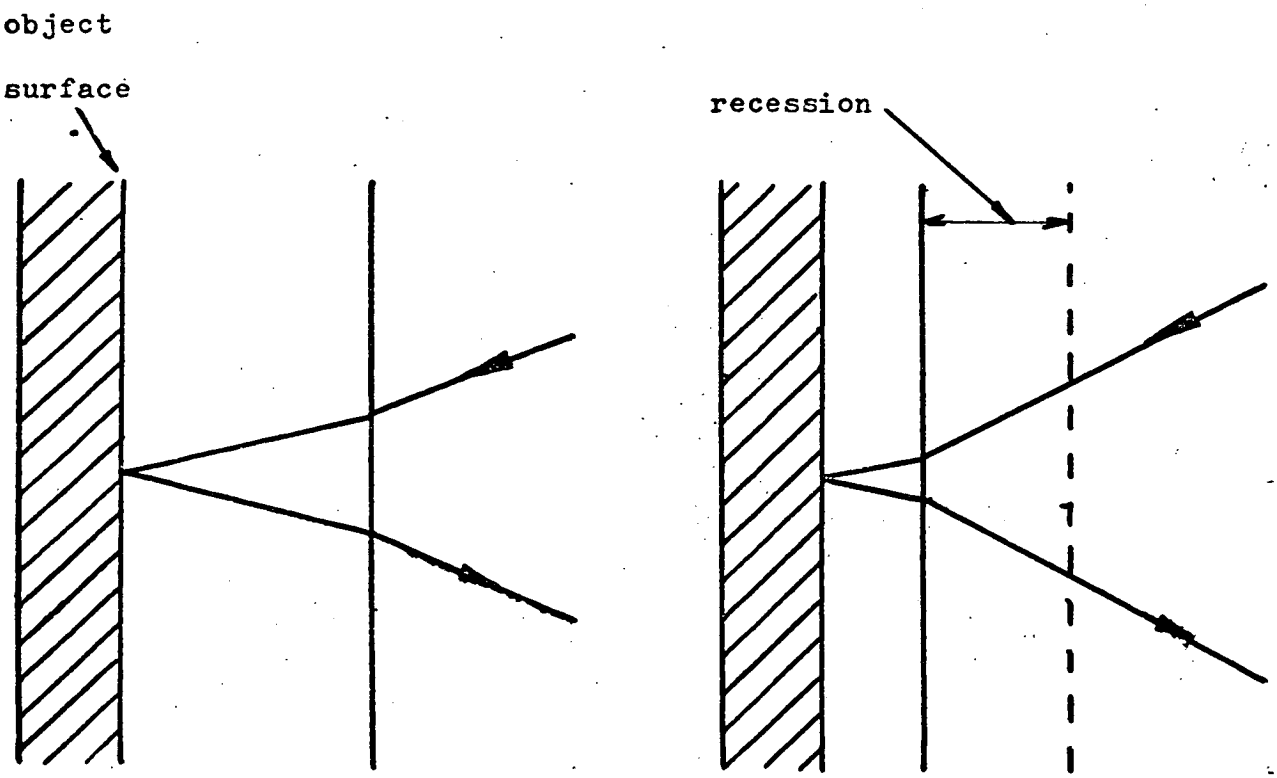

First exposure

Second exposure after mass transfer

Fig.20. Optical path through recessed polymer coating.

approached in a particular order, to minimise even such slight "impact" forces and the distortions caused by them. Moreover, in holographic interferometry it is difficult to adjust the many variables independently, because a slight discrepancy in one can mask a gross discrepancy in another e.g. fringe clarity depends on, among other things, the correct balance between beam intensity ratio, exposure time, and emulsion developing time.

3.4 Experimental Procedure.

3.4.1 Making the hologram.

The aim of the experiment is to create a photograph of a holographic fringe pattern which can then be analysed to find the local mass transfer coefficients.

The five steps in making the hologram are:

(1) Coat disc surface with polymer.

The polymer chosen was silicone rubber type General Electrics R.T.V. 602, which is the nearest currently available to that recommended by Kapur (105). The desirable properties of a coating are:

(a) significant increase in volume after immersion in the swelling agent.

(b) good adhesion to surface after repeated swellings.

(c) good optical properties.

(d) shrinkage normal to surface proportional to volume change of swollen polymer.

The aluminium probe was polished smooth then etched with conc. NaOH to make the surface diffusely reflecting. The polymer was brushed on, and cured at 150°C for four hours. The thickness of the coating must exceed the expected recession, but not be so great as to affect

the hydraulic characteristics of the probe.

Evenness of thickness is not critical because the local change, and not the absolute value, of the thickness is being measured. Difficulty was encountered initially because the swelling, evaporation, and adhesion characteristics had unsuspectedly deteriorated with age. Eventual discovery of this fact was hindered because this type of material has a limited market and therefore a long and uncertain storage time at suppliers; also, manufacturers' published data do not take account of such obscure properties as the swelling characteristics. Age-deterioration is also pronounced in developing and fixing chemicals.

(2) Swell the coating to equilibrium.

Iso-butyl benzoate was chosen as the swelling agent, according to the criteria suggested by Kapur (105). Methyl salicylate and ethyl salicylate, were found to be too volatile, resulting in natural convection to the atmosphere, thus confusing the fringe pattern (Fig. 21). Diethyl adipate and dimethyl phthalate were not volatile enough, resulting in long mass transfer times, undesirable both because of inconvenience and the possibility of any extraneous temperature or dimensional change in the optical apparatus between exposures, which might affect the fringe patterns.

(3) Make the first holographic exposure.

The probe was carefully positioned on its kinematic mount. The exposure time for maximum image clarity was determined by trial and error. Initially, a metronome was used to judge the 1-2 secs exposure time, later the cardboard pendulum was used for the short exposure times when the layout of the table was optimised.

(4) Expose probe to a rotameter-controlled filtered airflow.

The probe was removed from the kinematic mount and placed in the airflow rig. The volumetric flow rate, temperature, time of mass transfer, and pipe diameter were measured, so that the Reynold number could be found. The amount of air which had to be passed over the probe to obtain a suitable fringe pattern was determined by trial and error. Too short a time, and insufficient swelling agent is transferred to cause enough recession to produce the first fringe; too long a time and the fringes become numerous and merge into one another, and nothing is seen.

The mounting of the disc on its support had to be fortified, to prevent any movement of the disc (relative to its kinematic mount position) under the buffetting of the airflow. This malady results in a superposition of a "parallel" fringe pattern onto the "concentric" transfer pattern as shown in Fig. 21.

(5) Make second exposure of hologram.

The probe is replaced on its kinematic mount, which guarantees accuracy of relocation better than 1.67×10^{-4} m.m. (Ref. 104), and a second exposure taken. The holographic plate is developed, washed and fixed, and the fringe pattern photographed. In practice, the best fringe clarity obtains when the photographic exposure time is made double that indicated by a standard exposure meter. The reason for this is not known.

3.4.2 The optimum arrangement of the optical table.

The conventional arrangement for holographic interferometry is shown in Fig. 19 .

In this arrangement, suitable for a large object at a large

distance from the holographic plate, the components are arranged on an ellipse, as described by Abramson (106) to achieve fringe localisation (Fig. 23).

In the case of a small object, this arrangement is inadequate, because the image size, and hence fringe separation, is too small. Therefore the arrangement shown in Fig. 24 was evolved, ignoring the requirement of fringe localisation (see Section 5.5). The components are arranged to fulfill the following requirements:

(a) The total path length of all beams to be as short as possible to reduce the effects of any movement in the table.

(b) The disc and the kinematic mount must be accessible for removal and replacement in the dark.

(c) All the beams, and pinhole assemblies to be parallel to the table; the disc, plate, mirrors, and beam splitter to be perpendicular to the table, to give vertical symmetry in the fringe pattern.

(d) The ratio of the reference beam intensity to the object beam intensity to be set for maximum fringe contrast.

(e) As high a proportion as possible of the laser light output to fall on the object and plate, to minimise the exposure time and hence reduce the effects of any temperature or dimension changes in the rig.

(f) The object and refernce beams to impinge on the disc and plate as nearly perpendicularly as possible, to give as nearly a horizontally symmetrical fringe pattern as possible.

(g) The disc as near to the plate as possible, to give as large an image size as possible.

(h) The axis of symmetry of the disc to be perpendicular to the plate, to give a symmetrical image.

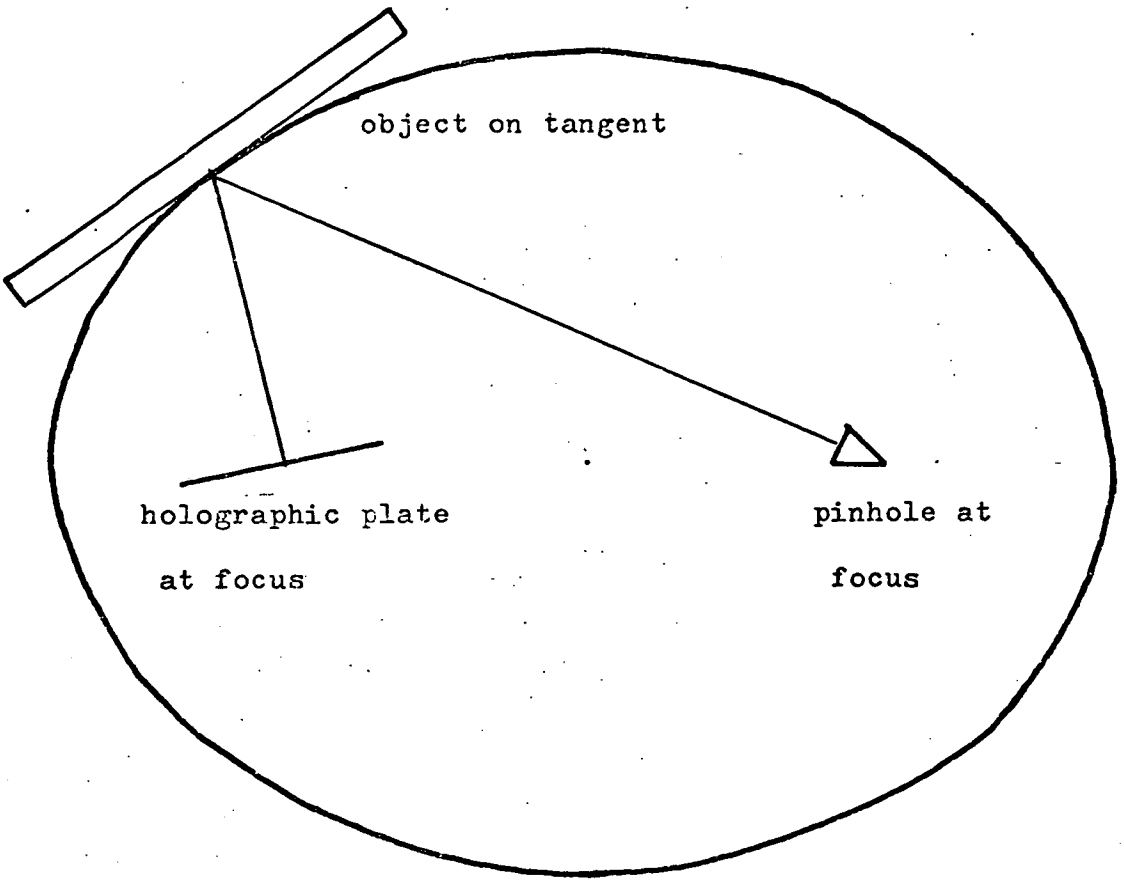

Fig. 23. Abramson's ellipse for fringe localisation.

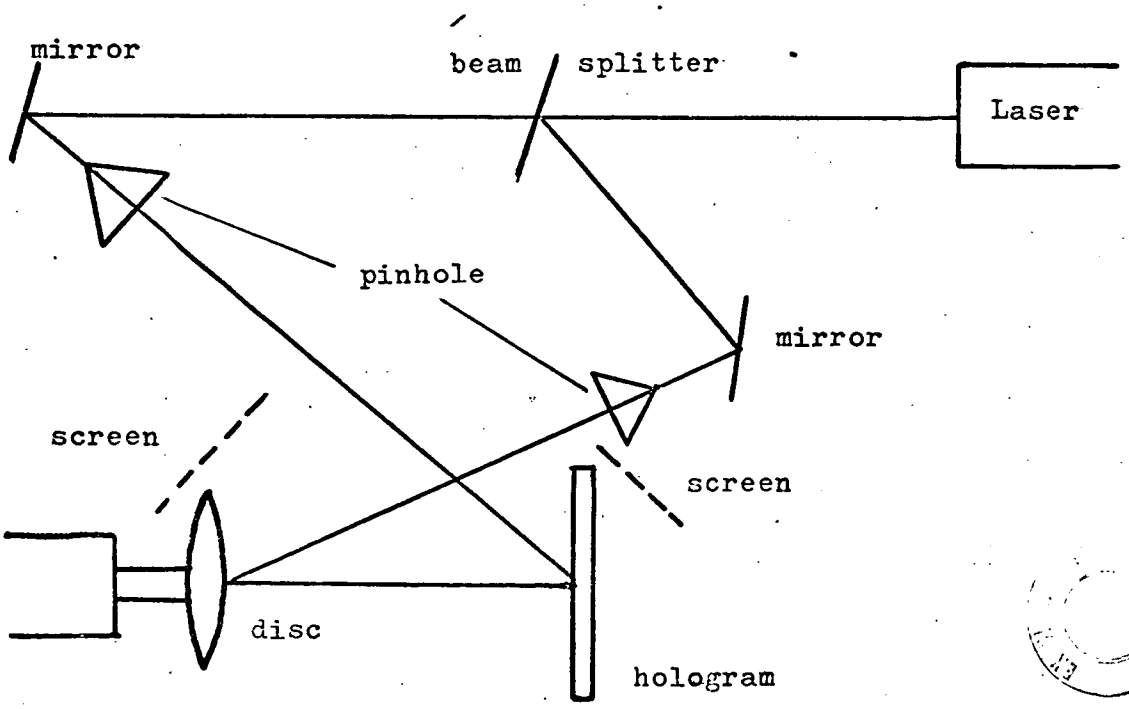

Fig. 24. Arrangement of the optical table for small objects.

(i) The optical path lengths of both beams to be as nearly equal as possible to give maximum image clarity.

The conditions (a), (b) and (c) are easily fulfilled. For condition (d), Lehman (91) recommends between 4:1 and 10:1 object: reference, according to the experimental conditions, e.g. nature of reflecting surface. The best setting of the variable-ratio beam splitter was therefore found by trial and error, in this case 60% transmission, 40% reflection. Condition (e) can be satisfied by moving the pinhole assemblies nearer or further from the disc and plate, so that the disc is just covered by the diverging beam and the area of plate illuminated is just sufficient to accommodate the image. Conditions (f), (g), (h) are strongly interacting conflicting requirements; the satisfaction of (h) was made at the expense of (f) and (g) to reduce the overall difficulty of fringe analysis. Condition (i) refers to the coherence length of the laser. If light from a laser source is split into two beams, these beams remain in phase with each other (a necessity for hologram construction) only if both beams are of nearly the same length. The greater the separation, the higher the loss of coherence. A small separation results in a clear image. For a Helium-Neon laser, the coherence length is 300 m.m. Abramson (94) gives a fuller account of coherence length.

3.4.3 Description of Equipment (Fig. 25)

The optical equipment and the hologram processing method are based on that described by Kapur (105).

Optical table: Reinforced concrete 3m. x 1m. on anti-vibration rubber mounts.

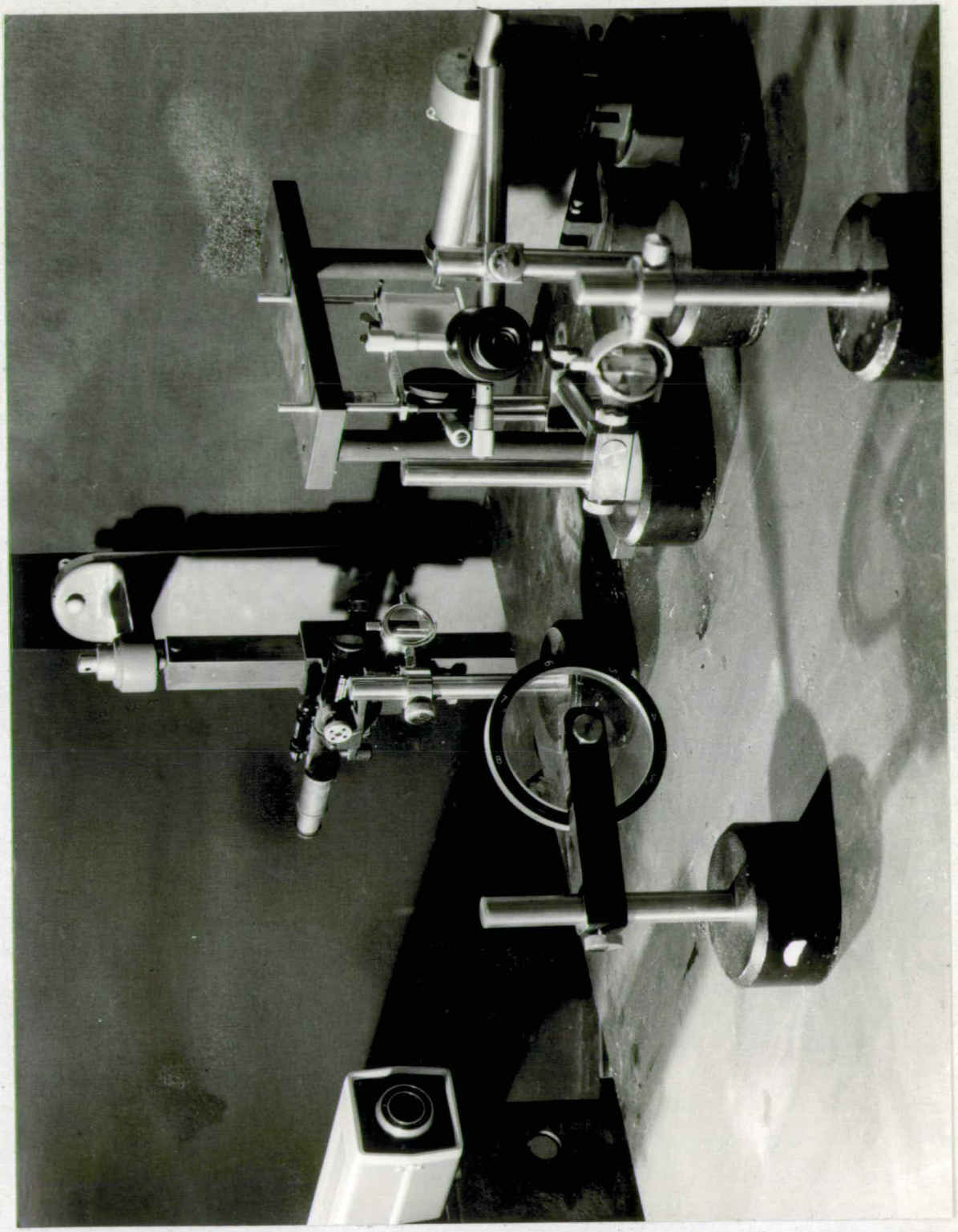

Fig.25. The arrangement of the optical table for the disc.

Laser:	Spectra-Physics 124A He-Ne 15m.w. Wavelength 6.33×10^{-4} m.m.
Beam Splitter:	Optel Variable 10/90 to 90/10 transmission/ reflection.
Steering Mirrors:	Optel.
Spatial Filters:	Optel 20 μm pinhole, focusing by microscope objective.
Holographic Plates:	Agfa-Gevaert 8E75, 90x120m.m., cut to quarter size.
Developer:	Agfa-Gevaert G280C.
Fixer:	Agfa-Gevaert G334
Plate holder:	Adjustable screw clamp type, does not accurately relocate plates, but plates can be developed in situ for real-time holography.
Kinematic mount:	See Fig. 26.
Airflow apparatus:	The disc is glued to a tube which is slid over a shaft fixed to the inside of the brass mount (Fig. 26) by three radius arms. A perspex inlet pipe is screwed onto the brass mount during mass transfer (Fig. 27). Sealing is by rubber O-ring. Tube diameter 12·7 m.m.
Exposure timer:	Initially, a matt-black block of polystyrene was suddenly gently removed and suddenly gently replaced in front of the laser, using a metronome to coarsely judge the exposure time. The metronome settings were found by trial and error. Later, the "swinging shutter" (Fig. 28) was developed, as an alternative to a conventional optical shutter which can introduce vibrations in the optical

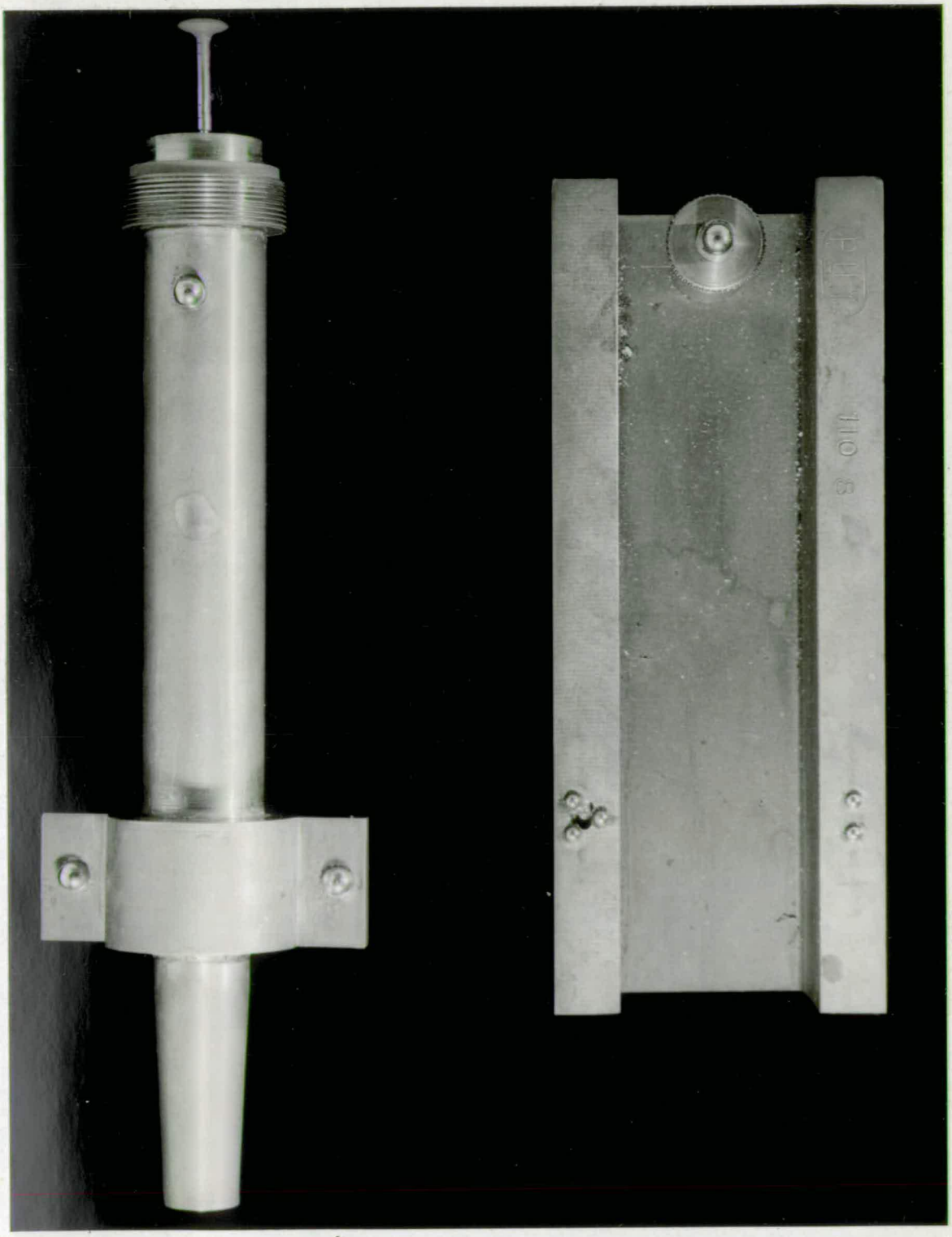

Fig. 26. The kinematic mount and disc probe.

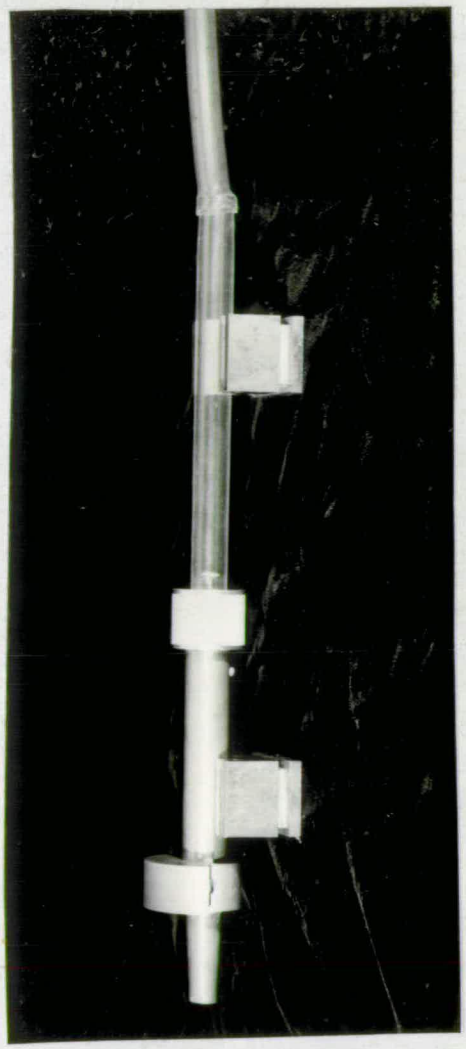

Fig.27. The mass-transferring apparatus.

table when the mechanism is activated. The cardboard pendulum is allowed to swing under gravity past the laser. The slot width setting is found by trial and error. Consistent exposure times are obtained.

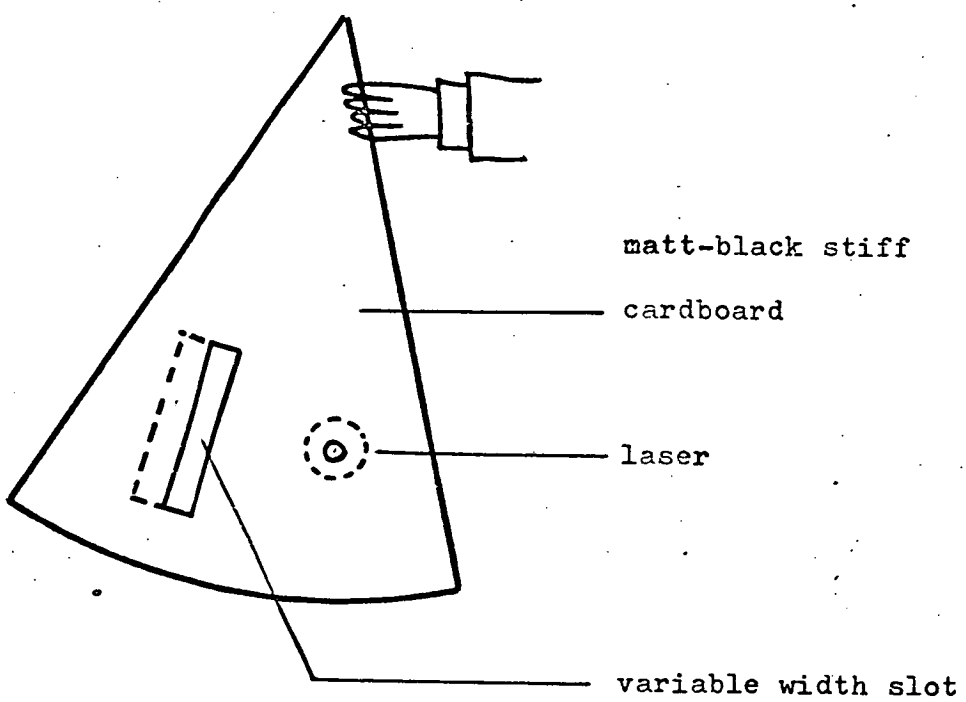

Fig.28. Pendulum exposure timer.

CHAPTER 4

The dimensional interpretation of a fringe photograph.

4.1 The dimensional authenticity of a photographic image.

This method of determining local mass transfer rates necessitates taking measurements from photographs of the fringe pattern; then relating the position of the fringes to the corresponding points on the real object.

In the case of a flat plate at a large distance from the camera, the photograph is a dimensionally accurate representation of the real object, but in the case of a non-parallel or non-planar object close to the camera, the photographic image cannot be considered to be in any simple way a "true" image of the real object. There must be some relatively complex and variable inherent mapping correspondence between a point on the real object and a point on the flat photograph.

This perspective distortion effect is quite distinct from distortion due to imperfections in the lens e.g. chromatic and spherial aberration; these are insignificant when using a good quality camera and will not be considered.

Early experiments showed that enlarging a photograph taken with the camera a great distance from the object resulted in an unacceptably low image clarity, and therefore it was decided to take photographs close-up to obtain as large a negative image as possible before enlargement.

This policy necessitates applying systematic corrections to the fringe dimensions, as measured on the photo, to take account of the inherent geometrical distortion introduced by a close-up camera.

This perspective distortion is demonstrated in Fig. 29 and 30 which show photos of a piece of graph paper, with 1/10" squares.

In Fig. 29, the camera is square onto the graph paper, and in Fig. 30 the camera is at 45° to the graph paper. In Fig. 30 the dimensions of the squares are no longer an accurate representation of the real graph paper.

The "TOP RIG" in the photos is an orientation marker so that the negatives and prints are viewed the right way up.

In the case of a curved object, a similar type of distortion occurs, because different parts of the surface of the object are "faced" at different angles by the camera.

4.2 Mathematical Models of a Camera

4.2.1 The Traditional Model

The traditional model of a camera, as described by Jenkins and White (107) is shown in Fig. 31. Consideration of the geometry yields

$$x' = \frac{xf'}{s - 2f'}, \qquad \text{Equation 1.}$$

which is the mapping correspondence of the camera, between a real dimension and an apparent image dimension. If the negative is not in the correct position, for example, this construction shows the out-of-focus effect on the point P. (Fig. 32).

That is, the mapping correspondence between object and image is no longer one to one. A similar effect occurs in a photograph of a non-planar object, where different parts of the object are at different distances from the camera. In Fig. 33, the camera is focused on P, leaving Q out of focus.

Fig. 34 shows the piece of graph paper at 45° to the camera. The centre of the grid is in focus; the distortion is most severe at

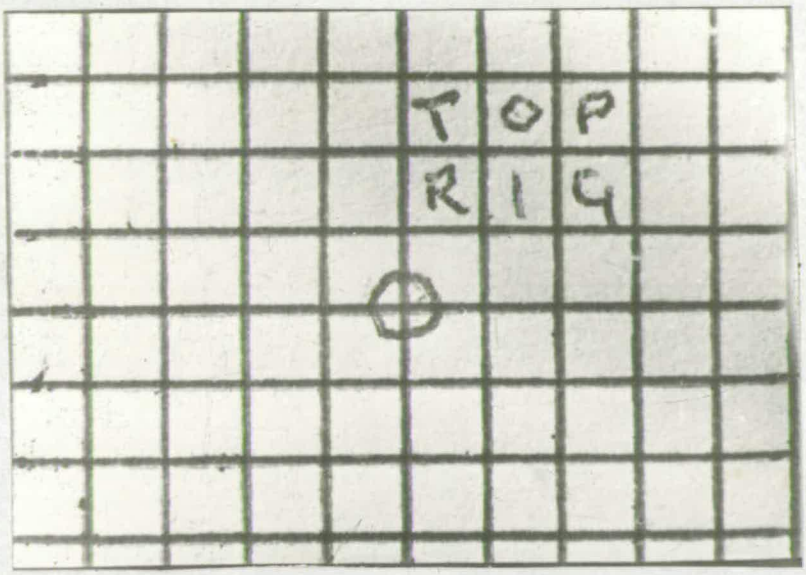

Fig. 29. Photograph of grid, camera held head-on.

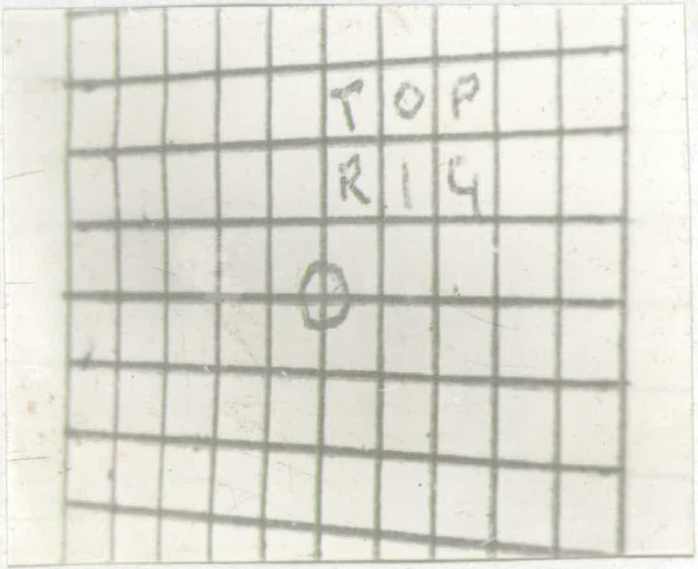

Fig. 30. Photograph of grid, camera held at 45 deg.

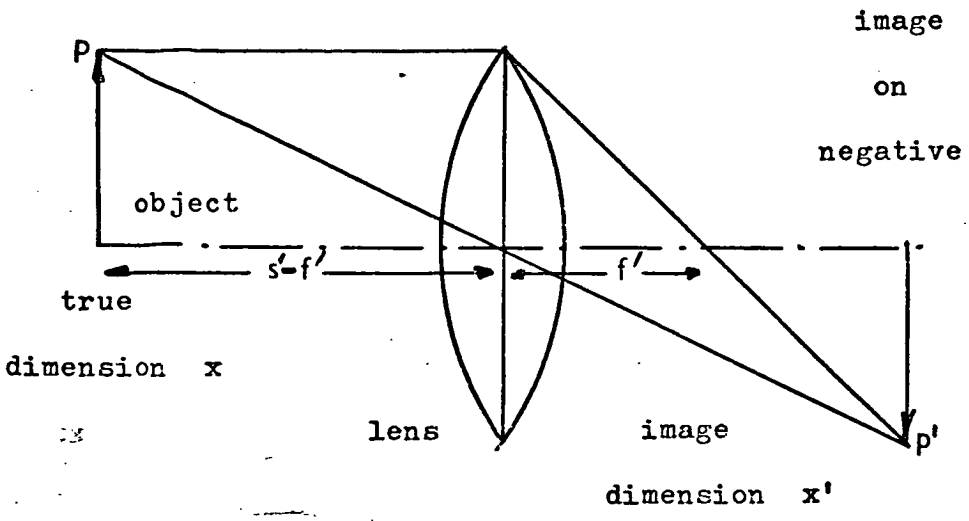

Fig.31. Geometrical construction of traditional model.

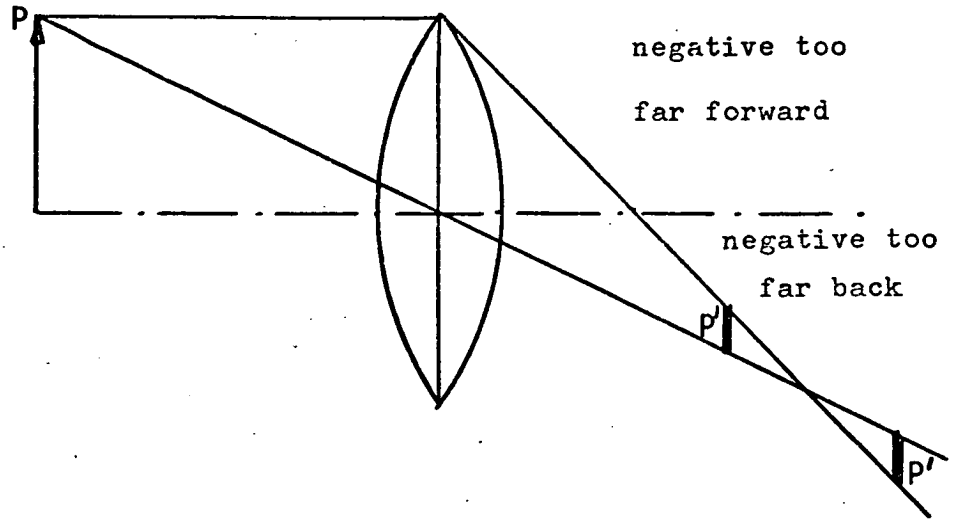

Fig.32. Out-of-focus effect in the traditional model.

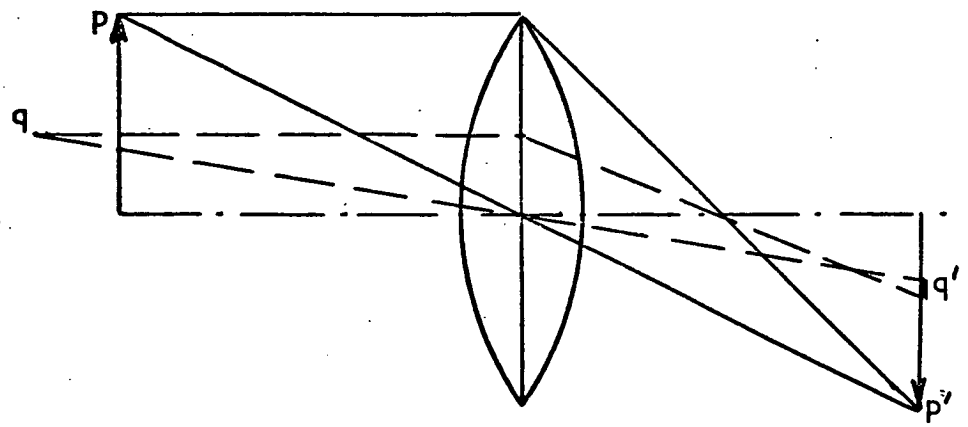

Fig.33. Depth of field in the traditional model.

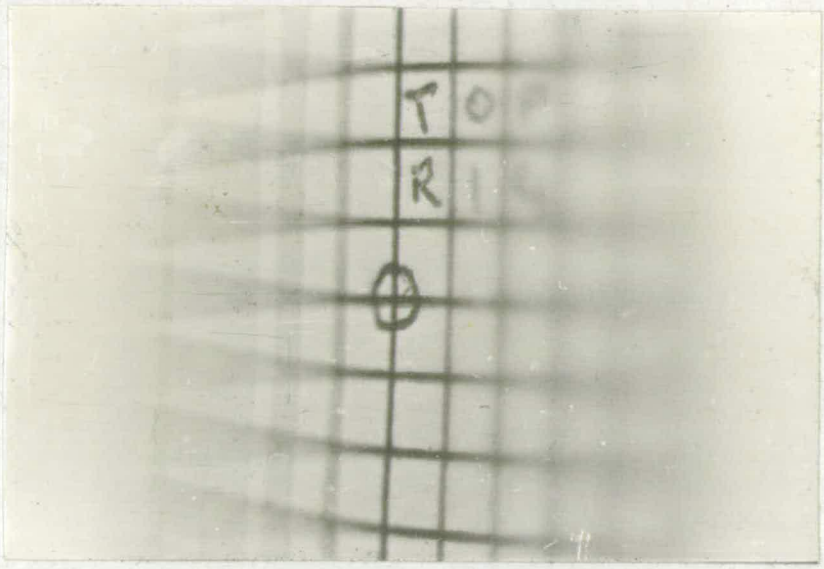

Fig. 34. Photograph of grid, camera held at 45 deg. and set at low f - No.

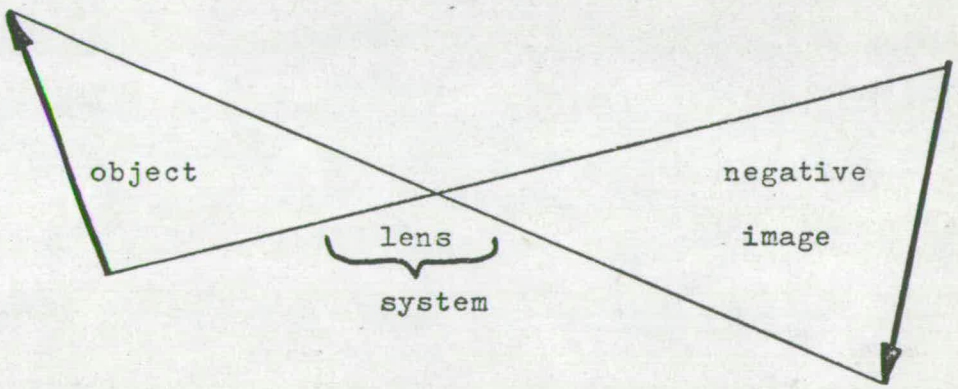

Fig. 35. The "crossover" model.

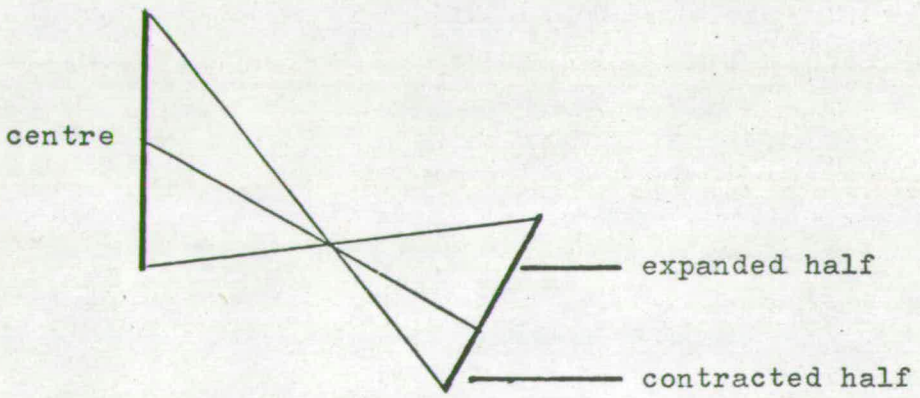

Fig. 36. Demonstration of foreshortening with the crossover model.

at the edges.

In conventional photographic practice (108) the camera lens is "stopped down", i.e. a high f-No is used, which reduces the out-of-focus effect.

In the application to the curved disc, it is desirable to have as large an aperture as possible to minimise the exposure time and hence susceptibility to movements in the optical table; while at the same time a small aperture is required to minimise out-of-focus distortion. Therefore the f-number was chosen to give negligible out-of-focus distortion at the edges of the disc.

Since the traditional model is too complicated to be of practical use, an alternative model will be developed, for this application.

4.2.2 The Crossover Model

The techniques of dimensioning real objects from photographs, known as photogrammetry, fall into three groups:- stereophotography, rectification, and grid calibration.

Stereophotography (109) is used in map-making by aerial photography, where the surface elevation is calculated using the principle of stereoscopy, and requires two sets of photographs and a wide camera separation. Although this basic principle can be used for fringe order identification (Section 5.2.3), it is unnecessarily complex for determining the true position of the recession fringes.

Rectification (110) consists of tilting the enlarger board to give the correct parallelism, and tilting the negative to give the correct proportions. This method can only be used for flat, rectangular objects such as building fronts.

Grid calibration is difficult on small curved surfaces; it was decided to use a mathematical model. It is proposed to represent any camera lens system, which is complicated in terms of the traditional optical geometry model, by the model shown in Fig. 35. A similar diagram is shown by Engel (109) to illustrate the principle of depth-of-field in practical photography.

This model automatically takes account of the non-parallel or non-planar cases. For example, in the case of a flat surface tilted to the camera, the model takes account of the foreshortening of one half of the surface in a very simple fashion. (Fig. 36). The general effect can be verified by referring to Fig. 29 and 30.

The quantitative analysis of the tilted flat plate (Fig. 37) yields the correspondence relation between the real and apparent dimensions:

$$x = \frac{vx'}{f' \cos \gamma - x' \sin \gamma} \qquad \text{(Equation 2)}$$

This extends, in two dimensions (Fig. 38), to yield the additional relation

$$y = \left(\frac{vy'}{f' \cos \gamma - x' \sin \gamma} \right) \sqrt{\frac{(f' \cos \gamma - x' \sin \gamma)^2 + x'^2}{(f'^2 + x'^2)}}$$

(Equation 3)

Measurements from Figs. 29 and 30 correspond with this analysis. The extent of the visual distortion in the case of a flat disc can be seen in Fig. 39, which compares the apparent shape with the real shape. In this case the mapping equations 2 and 3 were converted to polar coordinates. (Appendix 1). The traditional model reduces to the crossover model when the lens diameter is made infinitesimally small, i.e. a pinhole camera.

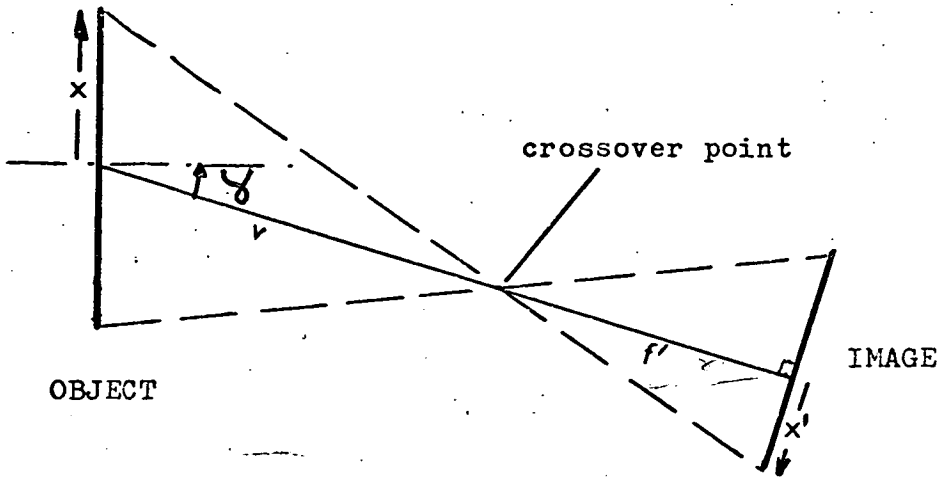

Fig.37. The crossover model in one dimension.

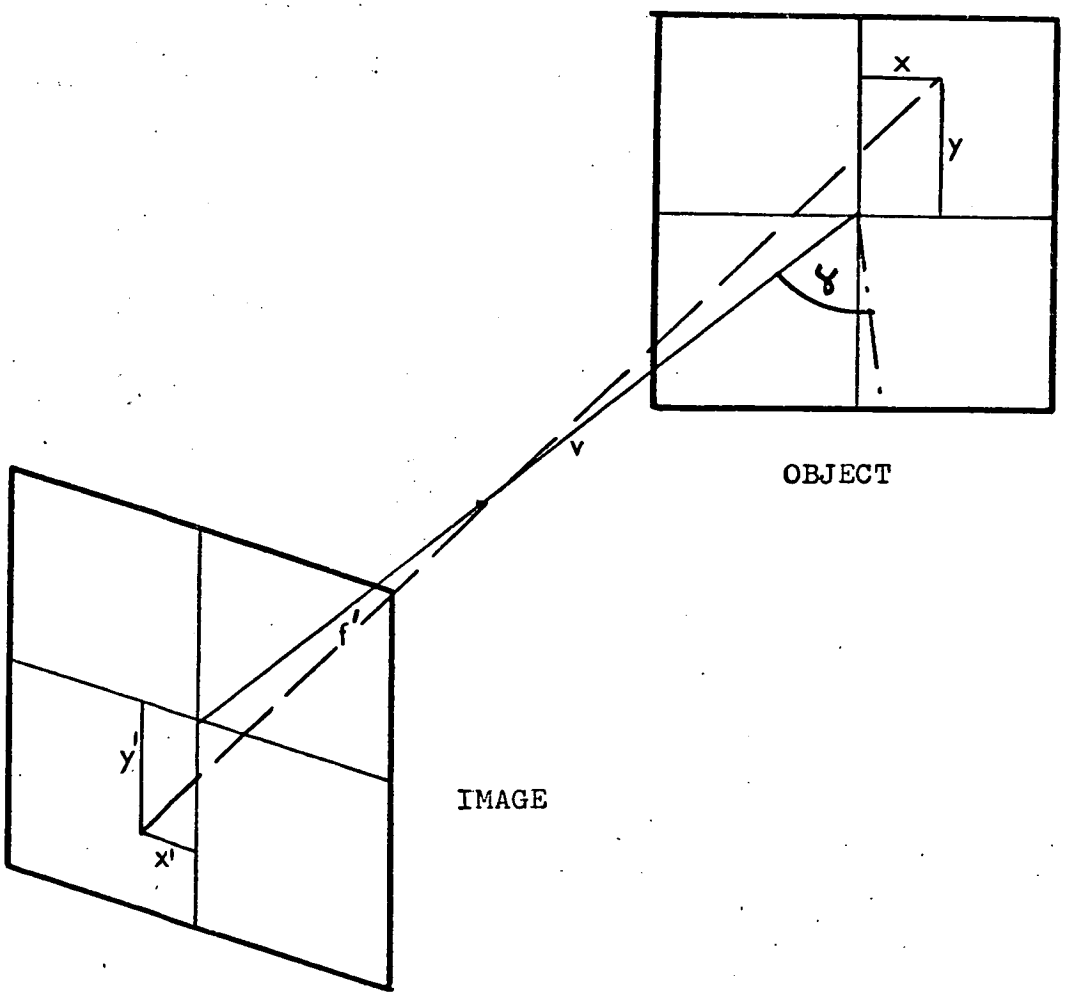

Fig.38. The crossover model in two dimensions.

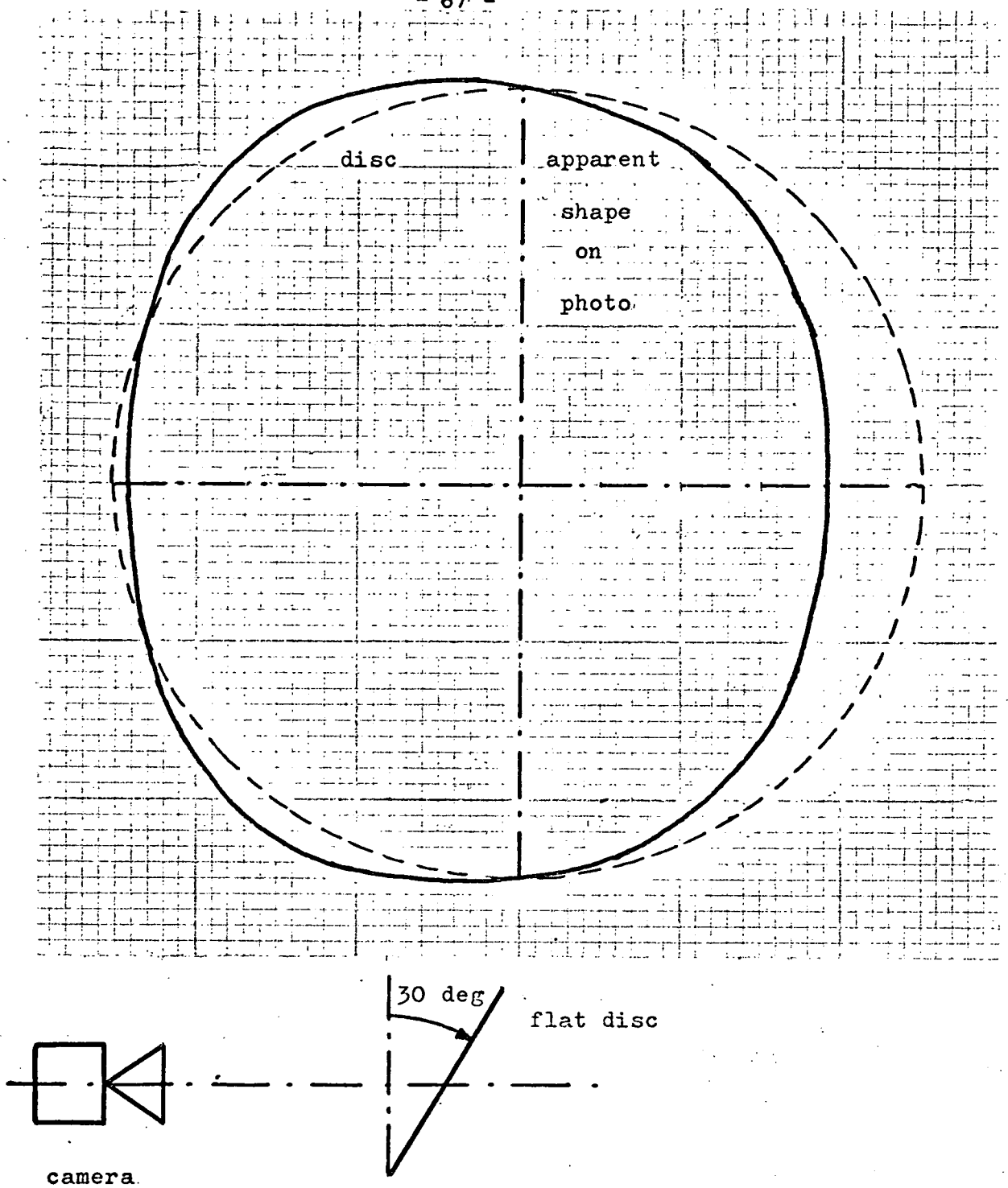

Fig. 39. Apparent shape of disc using camera tilted at 30 deg. Radius of disc = 2.5; $f' = 10$; $v = 2.5$.

4.3 Extension of the crossover model to three dimensional objects.

This section extends the analysis in 4.2.2 to take account of the curvature of the disc. The general equation connecting all points on the disc (Appendix 3) cannot be solved analytically, and so to avoid iterative methods, the points along a single horizontal equator (Fig. 40) will be considered to be representative of the disc as a whole. This is reasonable considering the symmetry of both the disc and airflow, and is verified by the actual patterns obtained, which are symmetrical about the horizontal axis. Although the recession is radially symmetrical the fringe pattern is not symmetrical about the vertical axis because the illumination source is angled to the disc (Fig. 41).

The mapping equation for the horizontal equator, with a head-on camera (Fig. 42).

$$x = x' \left[\frac{f'(v + R) + \sqrt{f'^2 (v + R)^2 - (f'^2 + x'^2)((v + R)^2 - R^2)}}{(f'^2 + x'^2)} \right]$$

(Equation 4)

is derived in Appendix 2.

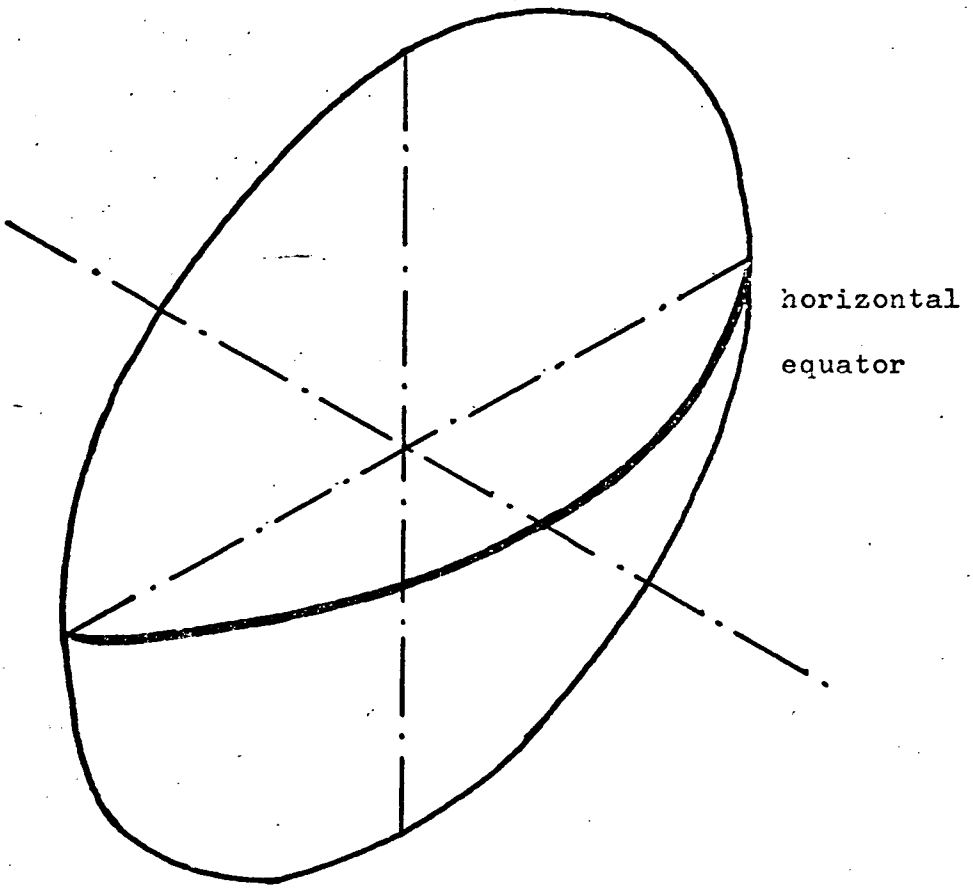

Fig. 40. The horizontal equator on the convex disc.

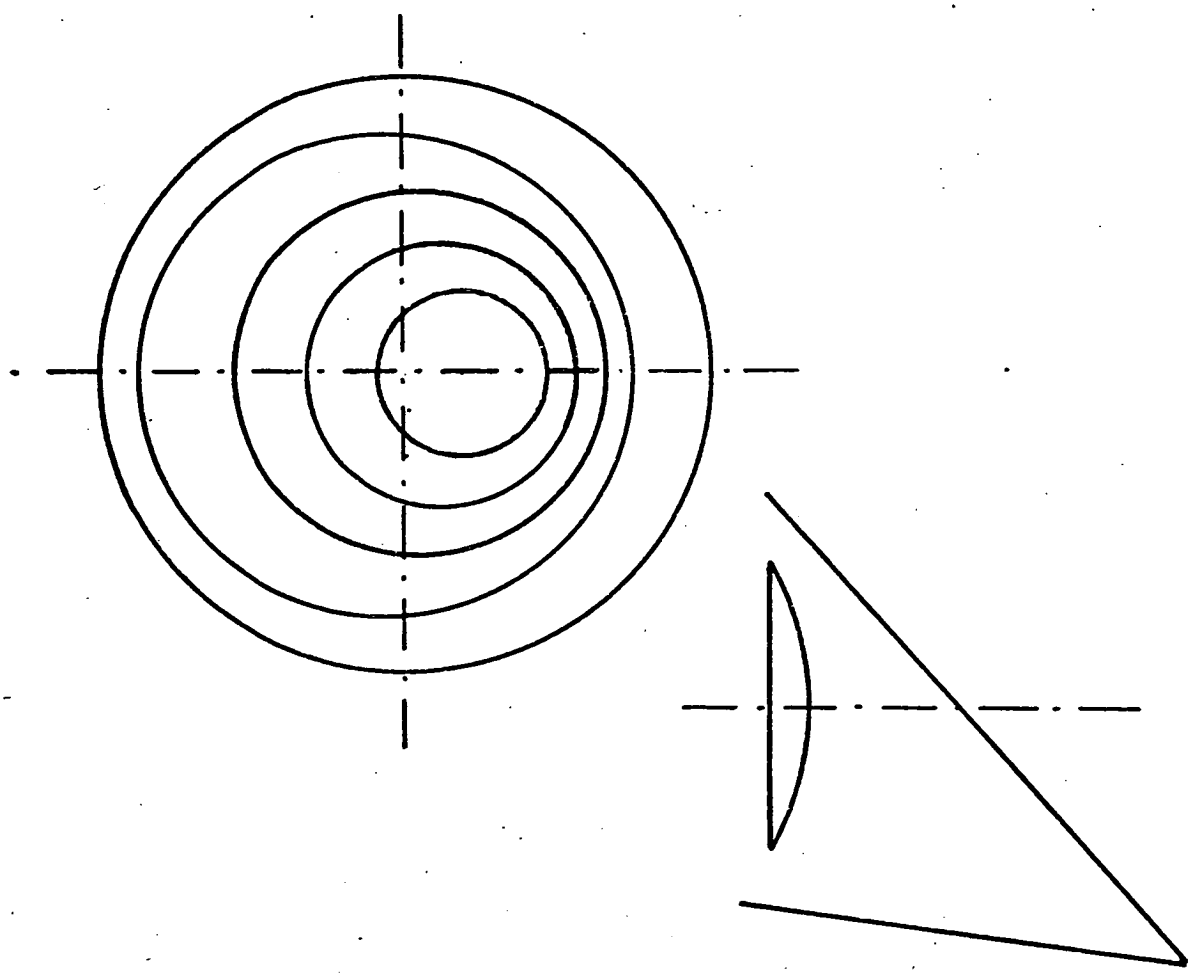

Fig.41. Asymmetric fringe pattern with angled illumination.

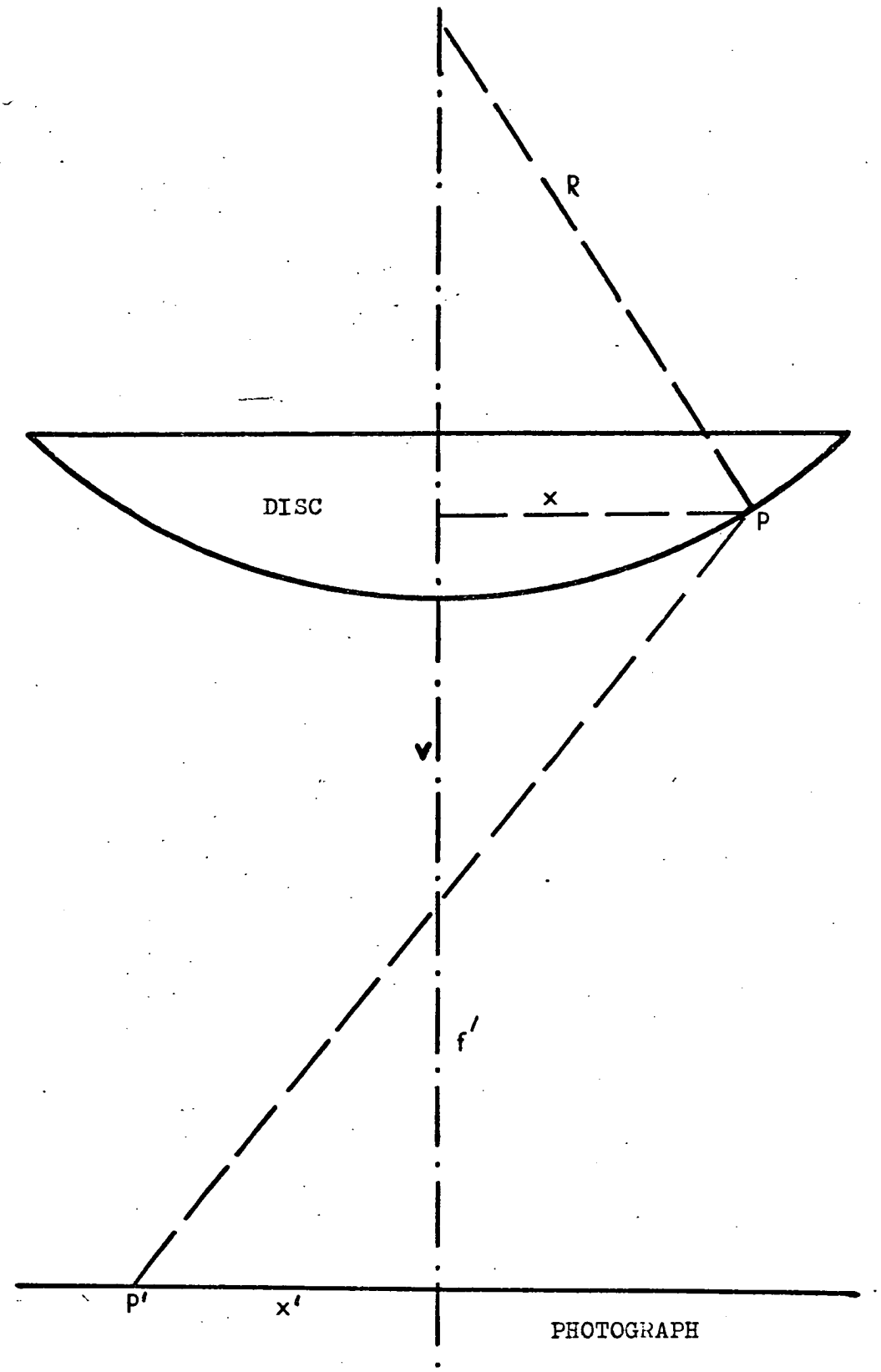

Fig.42. Plan view of disc with head-on camera. Point P on the disc maps into point P' on the photograph.

CHAPTER 5

Fringe Interpretation

5.1 Fringe Analysis.

5.1.1 Introduction.

The objective of this chapter is to devise a method of relating the position of the fringes to the surface recession. Kapur and MacLeod (111) have derived the necessary equations for a transparent-polymer-coated flat plate at a large distance from the illumination source; it remains to extend this analysis to take account of the three-dimensional nature of the disc surface, and its close proximity to the illumination source.

Considerable work has been published on the topic of 3-D fringe interpretation, falling into four categories:

(1) rigorous theoretical treatments which cannot be related to practical requirements unless strict assumptions are made or only special cases considered.

(2) practical methods requiring strict assumptions e.g. viewpoint at infinity or parallel light beams.

(3) practical methods requiring multiple views e.g. three simultaneous holograms or twin reference beams.

(4) practical methods for special cases, e.g. displacements consisting of pure translation or pure rotation.

Tsuruta (112), Stetson (113), Hildebrand (114) and Aleksandrov (115), each present a theoretical treatment of the topic. Hildebrand derives equations for two limiting cases, i.e. fringes localised at a large distance from the object (which distance must be discovered), and fringes localised on the object surface. Aleksandrov's theory requires a large distance between object and viewpoint which makes his subsequent practical application, based on

moving the eye from side to side and counting fringes, hopelessly inaccurate due to the small subtended angle of the eye. Tsuruta applies his theory to special cases only.

Abramson (106,116,117) explains how displacements may be deduced by moving the eye from side to side in each of two perpendicular directions, provided the optical components are arranged on a given series of ellipses which he calls the Holo-diagram. His method is of value where the object under study is large compared to the coherence length of the laser, or where maximum or minimum fringe sensitivity, i.e. number of fringes appearing as a result of a given displacement, is required, or where the displacements are simple translations or rotations of flat surfaces. In our application, sufficient fringe sensitivity, and thus accuracy, already ensues when the optical components are positioned according to the criteria discussed in section 3.4.2.

Boone (118), in measuring stress and strain makes the assumption that the illuminating source is at infinity. Matsumoto (119) and Shibayama (120) describe methods requiring three simultaneous holograms, and Pastor (121) specifies the use of multiple holograms. Sollid (122) uses two two holograms in certain special cases. Dandliker (97) and Abramson (123) use twin reference beams and a single hologram, Abramson requiring large viewpoint distance and almost parallel beams.

Vienot et al (124) describe a method to take account of translation and rotation of planes, and Gates (125) deals with translation perpendicular to the hologram. Hansche and Murphy (126) consider an internally pressured sphere. Lui and Kurtz (127) have devised a semi-quantitative method for 3-D motion of a flat surface.

None of the above methods are immediately applicable to our case, where the displacement is approximately radial to a spherical surface. Also, none of the proposed assumptions can legitimately be applied to our case. Therefore it was decided to derive the equations from first principles, a mathematical task no more difficult than the experimental task of using multiple beams or multiple holograms.

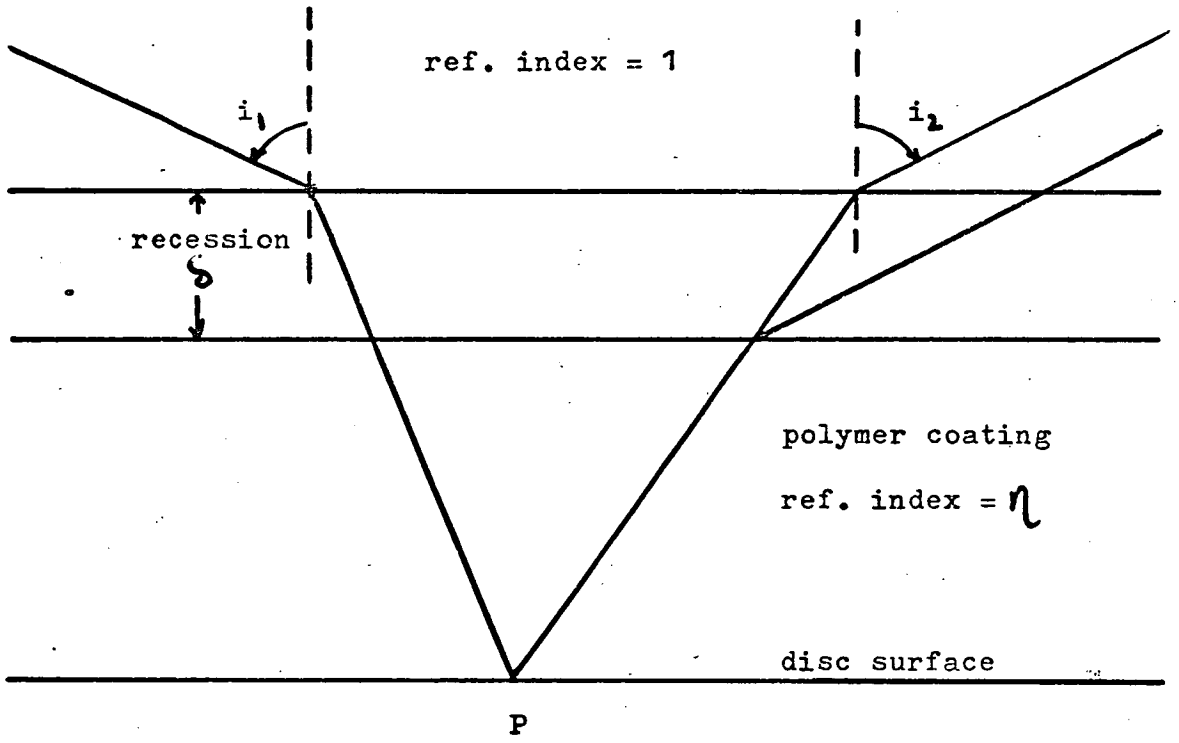

Fig. 43. The change in optical path length at a recessed surface.

5.1.2 The change in optical path length due to recession at a point on a curved polymer-coated surface.

Fig. 43, from Ref. 94, represents a very small part of the spherical disc surface, and so it is assumed to be flat to simplify the calculations. The equation relating the recession to the change in path length (derived in Appendix 4) is:

$$\frac{N\lambda}{2} = \delta\left(\sqrt{\eta^2 + \cos^2 i_1 - 1} + \sqrt{\eta^2 + \cos^2 i_2 - 1} - (\cos i_1 + \cos i_2)\right)$$

Equation 7

This equation is used to find the value of δ. When this derivation is applied to a flat plate, it is easy to measure i_1 and i_2 directly from the optical table, because the angles A and B in Fig. 44 are very small, providing the object beam source and viewing point are at a large distance from the plate compared with the plate size. That is, the geometry can be approximated to that shown in Fig. 45.

But in the spherical disc case, i_1 and i_2 vary considerably across the surface (Fig. 46) and a separate calculation of these angles is required. The variation is even more pronounced when, as in our case, the light source and the position of the eye to view are close to the disc. A further difficulty is that the value of the angle of reflection is entirely dependent on the position of the point of convergence of the reflected rays, and this point does not correspond with any physical part of the equipment, in contrast to the incident rays, whose point of divergence is, of course, the pinhole filter, i.e. the object beam source in Fig. 44. Therefore, before the derivation of an expression for the angle i_2 can proceed, it is necessary to first determine the position of the point of convergence.

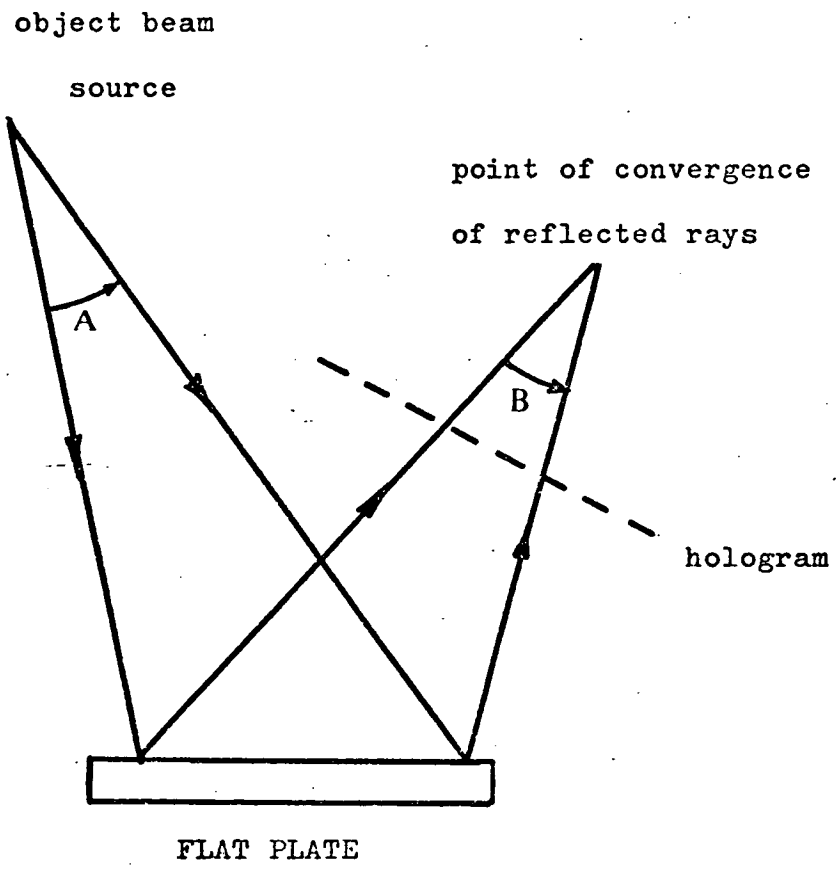

Fig.44. Reflection from a flat plate.

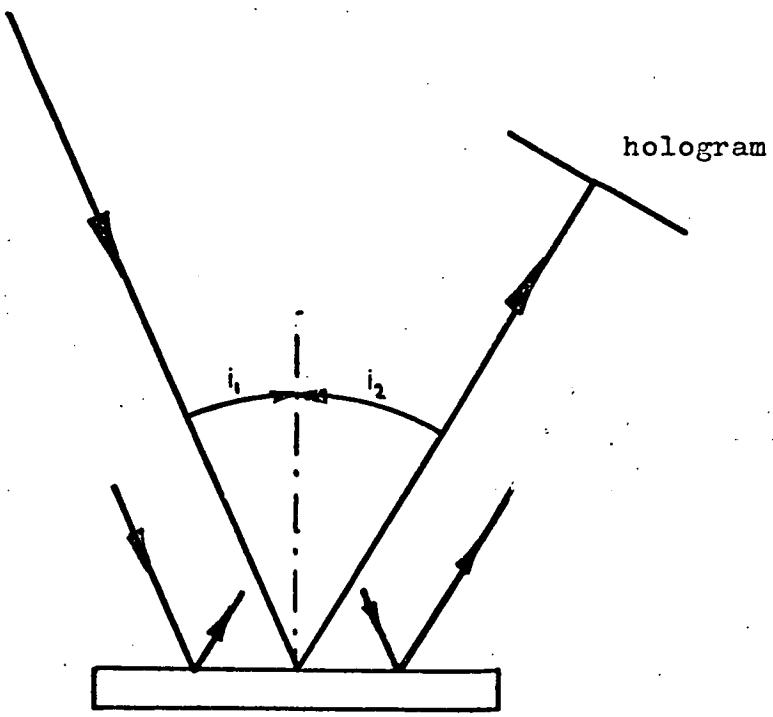

Fig.45. Reflection from a flat plate with relatively large distances between optical components.

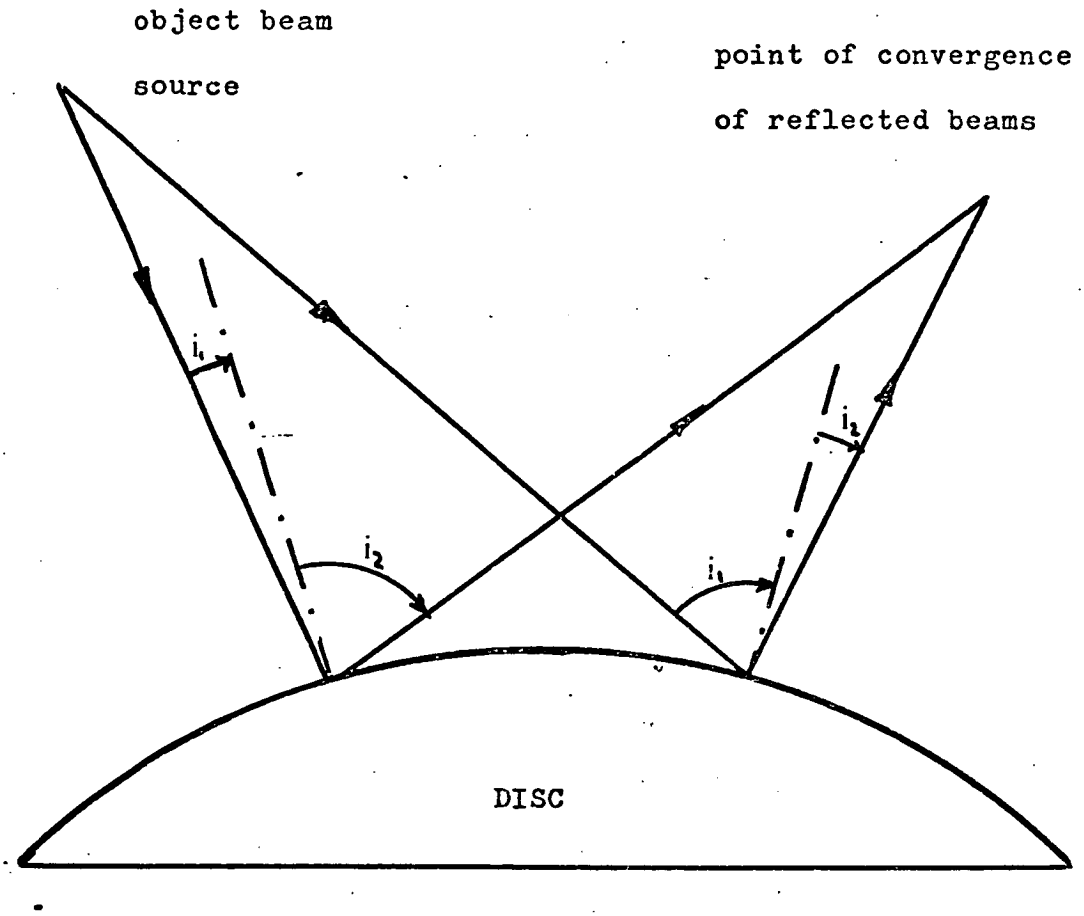

Fig.46. Reflection from the disc surface.

5.1.3 The point of convergence of the reflected rays.

In the literature, the problem of the position of the point of convergence has been neglected, since the assumptions are made that the reflected rays are parallel or the object is flat. In some cases, a parallel incident beam, instead of the usual divergent beam, has been used.

Strictly theoretical treatments of fringe analysis include a theoretical point of convergence in the derivation of generalised equations, but do not specify what the point corresponds to in physical terms.

When a hologram of an object is reconstructed by the illuminations of the original reference beam, an image of the object is seen which is geometrically identical to the real object. That is, the 3-D nature of the object can be detected through the hologram by moving the eye from side to side (the parallax effect); and the size, position and shape of the image are the same as that of the real object. Thus, for the purpose of this discussion, looking at a hologram is the same as looking at the real object. The hologram itself is a complex "black-box" whose effect is to create the apparent existence of the object in the absence of the object.

Therefore the point of convergence of the reflected beams through the hologram is identical to the point of convergence of the reflected beams from the real object, which is: a point between the lens and the retina of the eye, and in the case of a camera, a point between the lens and negative, identical to the "crossover point" in the crossover model of a camera in Section 4.2.2. To put it another way, the point of convergence is the optical centre of the imaging system.

5.1.4 The justification for considering the hologram to be a "black-box".

(a) Single exposure hologram

Consider a point P on the object surface, as shown in Fig. 47. If the light reflected from P arrives at any of the points P' on the holographic plate out of phase with the reference beam arriving at that same point, there will be a darkening of the photographic emulsion. Conversely, if the beams are in phase on arrival, a light patch will occur. And similarly for every other point on the object. The hologram itself consists of a complex pattern of light and dark lines, reminiscent of a finger-print. Thus the complete image of the object is recorded on every part of the plate. For this reason, a hologram gives a 3-D effect as it is viewed from various directions. Also, if the plate is shattered into fragments, each contains a complete image of the object.

To view the hologram, the reference beam is used to recreate the image of the object, the lines on the plate behaving as an extremely complex diffraction grating. The pattern on the holographic plate is uniquely defined without taking account of the position of the viewing eye or camera, however, the particular image which this diffraction pattern recreates is only defined by the eye position, since the multiplicity of information contained on the hologram can give rise to an almost infinite number of images.

So although for the purpose of constructing the diffraction pattern on the plate, the two light beams are represented thus:

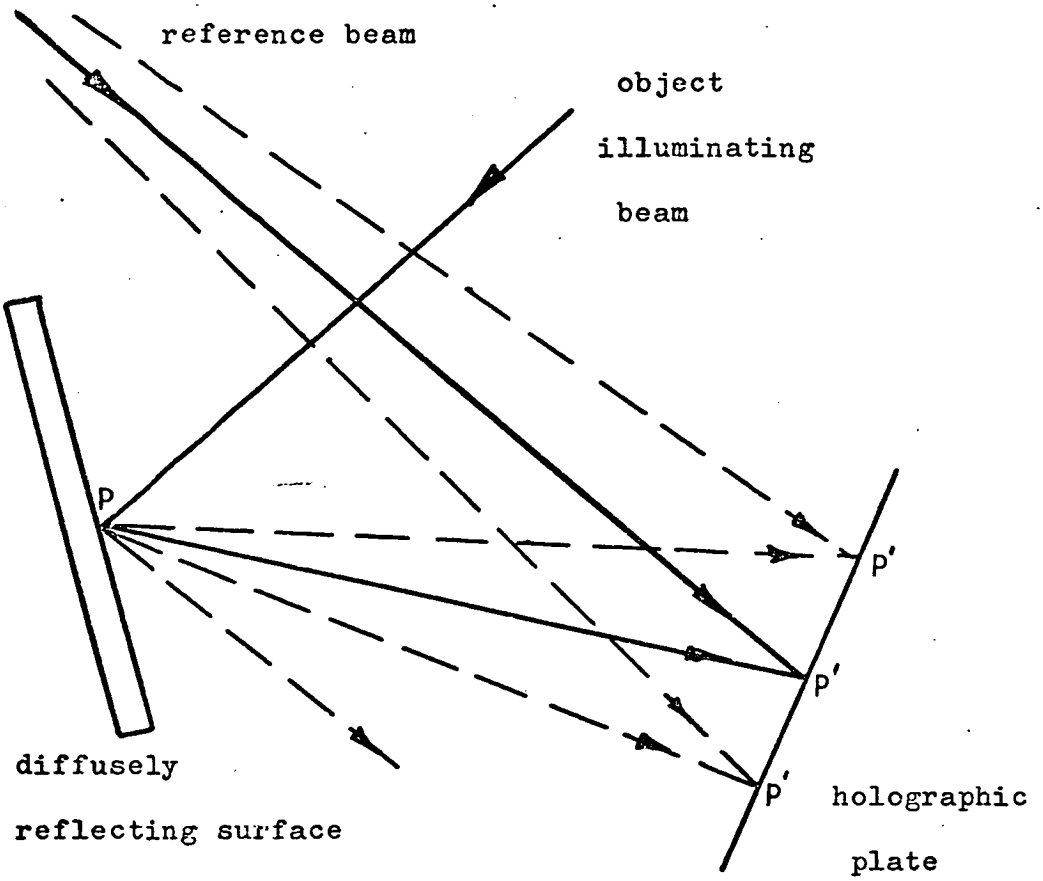

Fig.47. Formation of a single exposure hologram.

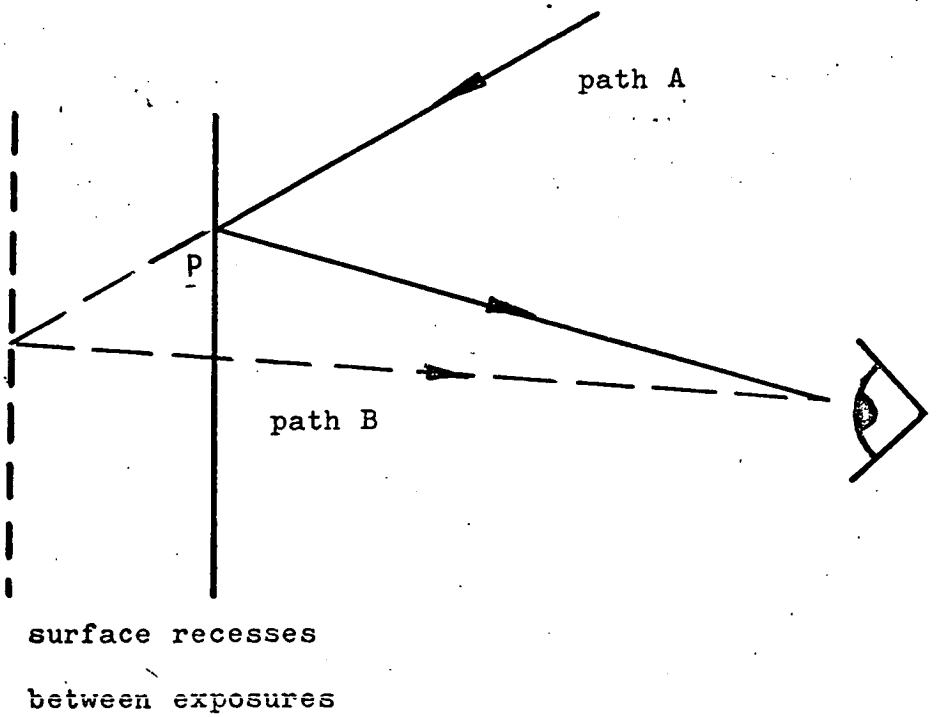

Fig.48. Reconstruction of a double exposure hologram. The paths A and B are shown only approximately.

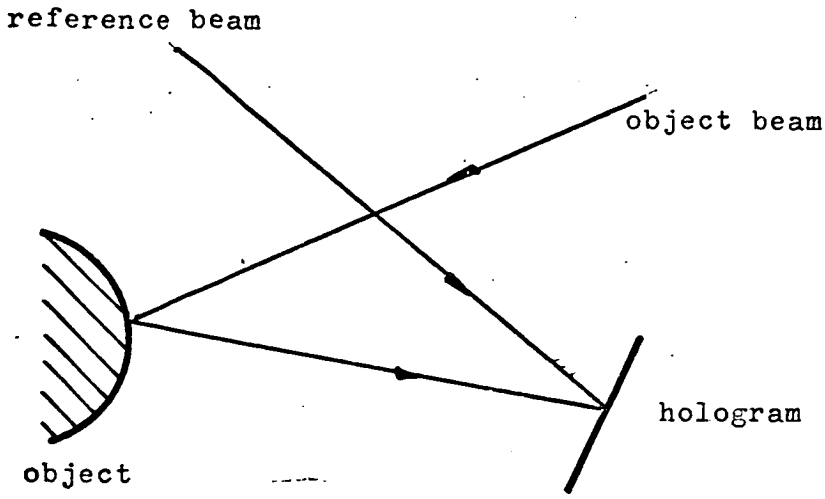

For the purpose of reconstructing the image, the single beam behaves thus:

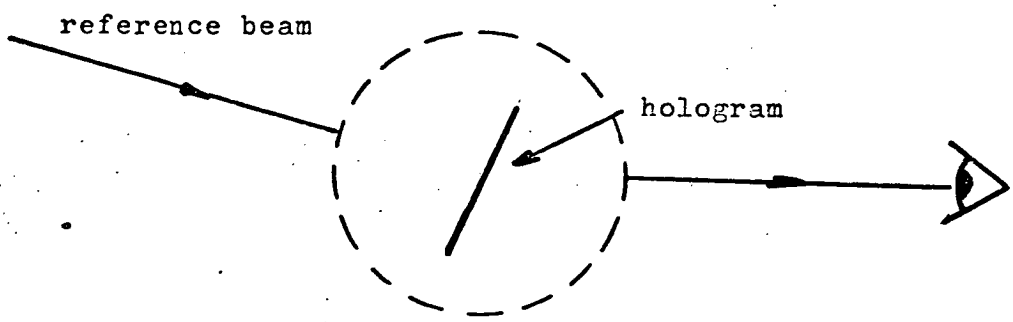

"black box" diffraction grating

And as far as the eye is concerned, the situation is identical to viewing a real object thus:

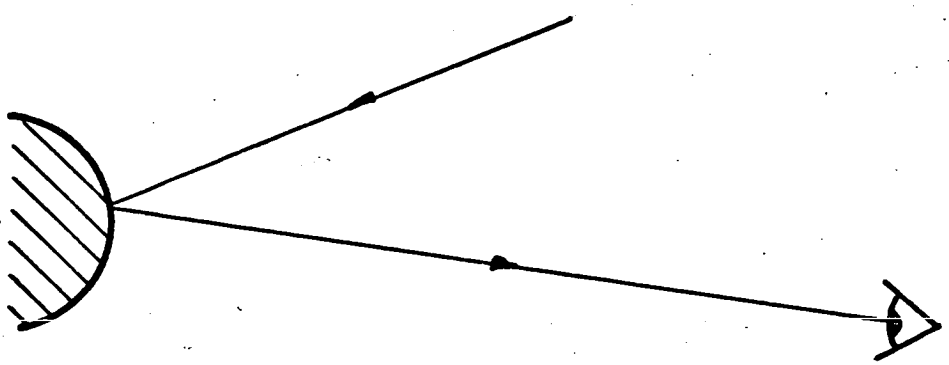

(b) Double-exposure hologram

Now consider a double-exposure hologram, where recession fringes can be seen superimposed on the image of the object (Fig. 48). The eye receives two sets of optical information from two sets of "black-box" diffraction gratings on the hologram. If the optical path lengths A and B differ by an integral number of half-wavelengths, the eye will see a dark patch obscuring P, since the beams have been "processed" by the black-box to appear to interfere destructively. For an integral number of whole wavelengths, constructive interference occurs, and the eye sees an extra-bright patch. A dark line, i.e. a recession fringe, indicates a series of recession points P where the recession is such to alter the path lengths by an equal amount. The dark line is not in any way attached to either the plate or the object, but is merely an absence of illumination along that particular sight-line.

Under certain geometrical conditions, the dark lines appear to stay in the same position relative to the object when the eye is moved around; just as dark lines painted on the surface of an object would behave, as opposed to black poles between the object and eye which would give rise to parallax effects. Fringes which appear to be on the surface of the object are often said to be "localised", although the fringes can actually be localised on any plane.

5.1.5 Fringe Localisation.

Considerable work has been devoted to the theory (112,113,128, 129,130,131) and practice (106,116,117,120,124,132) of fringe localisation, mostly with the aim of localising the fringes on a plane coinciding with the object surface. In fact, localisation is only possible or desirable in a few special cases in holographic interferometry. For example, in the case of a flat plate a great distance from the light source, the assumption can be made that the light beams impinge and reflect as two groups of parallel beams. If the equipment is arranged to localise the fringes on the surface of the object, the position of the recording camera does not need to be known, and the point of convergence question does not arise, thus simplifying the analysis.

But since in the case of a spherical disc, the position of the camera must in any case be known to calculate the reflection angles, there is no advantage in localising the fringes. In fact, the non-localisation of the fringes is put to advantage in the coincidence method of determing the fringe order number in Section 5.2.3.

5.1.6. The derivation of the incidence and reflection angles.

Consider the disc to consist of four quadrants (Fig. 49). One quadrant is shown in Fig. 50. When AP is an incident beam of light, point A represents the point of divergence of the object beam. In this case the coordinates q and s' of point A are measured directly from the optical table. When AP is a reflected beam of light, point A represents the point of convergence as defined in Section 5.1.3., and its coordinates are calculated from the measured position of the camera, by means of the mapping equations of the crossover model in Section 4.2.2. The derivation is the same in both cases. It is required to find the angle i between the ray AP and the normal to the disc PH, for any point on the disc. Taking the surface of the optical table as datum level, the axis of symmetry of the disc is set parallel to it, and the point A is set to the same height as this axis. The axis of the object illuminating beam from the pinhole (point A) and the optical axis of the recording camera are also set parallel to the table. This arrangement makes the geometry, and hence the fringe pattern, vertically symmetrical. The equation defining the angle i for any point $P(R, \alpha, \theta)$ on the disc, (derived in Appendix 5) is:

$$\cos i = \frac{\cos\alpha_o[(R + S')\cos\theta - q\sin\theta] - R}{\sqrt{R^2 + (R + S')^2 + q^2 - 2R\cos\alpha_o[(R + S')\cos\theta - q\sin\theta]}}$$

Equation 5.

which for the horizontal equator, reduces to:

$$\cos i = \frac{(R + S')\left(\sqrt{1 - \frac{x^2}{R^2}}\right) - \frac{qx}{R} - R}{\sqrt{R^2 + (R + S')^2 + q^2 - 2R\left[(R + S')\left(\sqrt{1 - \frac{x^2}{R^2}} - \frac{qx}{R}\right]\right.}}$$

Equation 6.

where x = EF in Fig. 50.

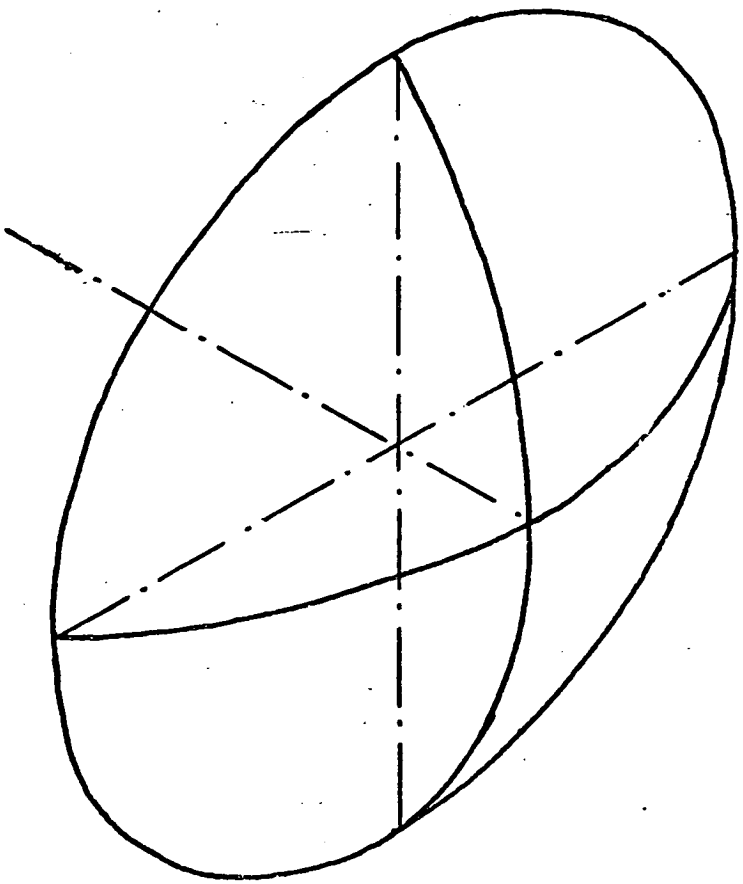

Fig.49. Division of disc into four quadrants.

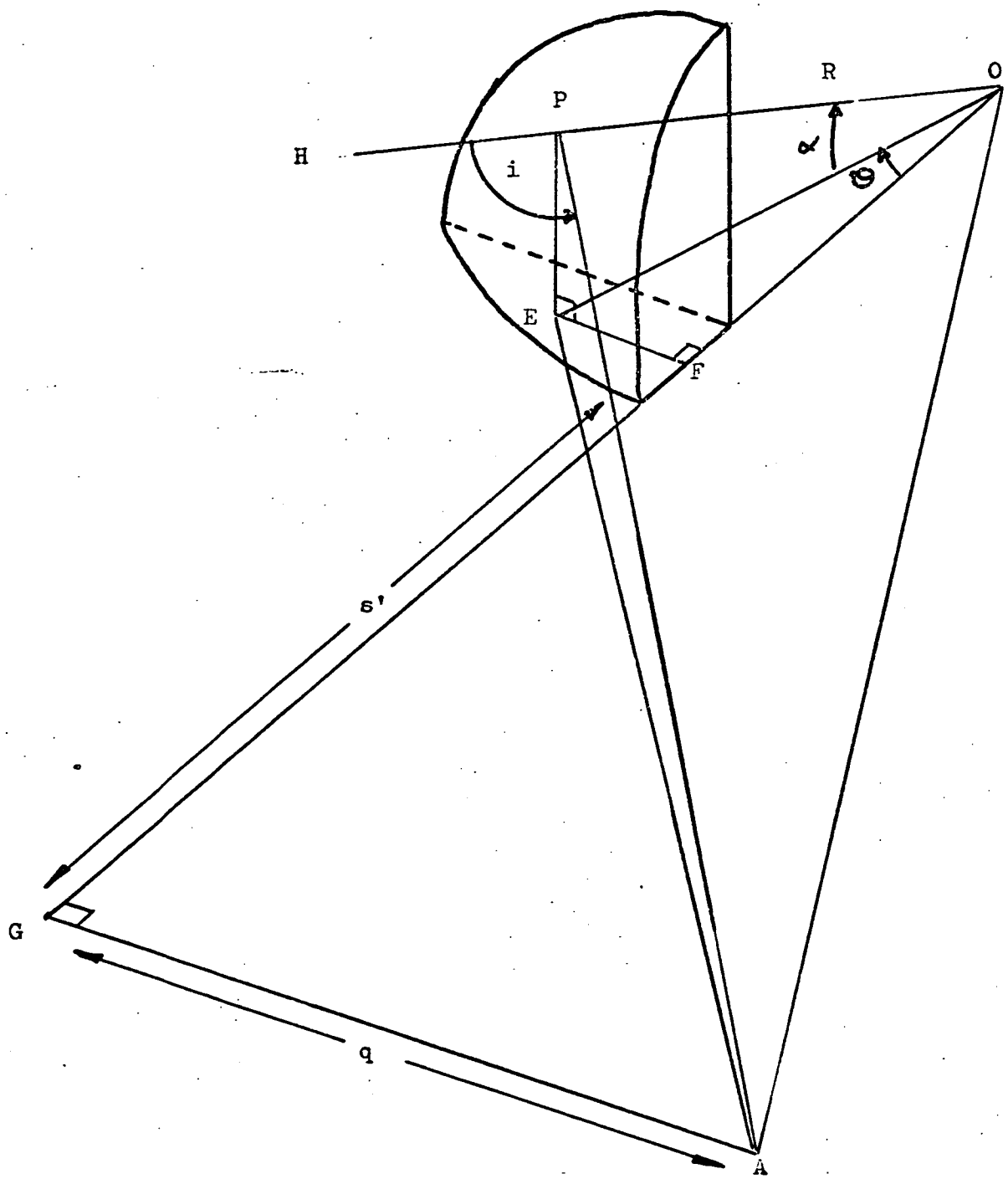

Fig. 50. Construction for finding angle i.

5.2 Fringe Order Identification.

5.2.1 Introduction.

Each interference fringe represents a change in the depth of the coating corresponding to an optical path length change proportional to an integral number (N) of half-wavelengths of light. An adjacent fringe corresponds to an optical path length change proportional to N+1 or N-1. The fringe pattern constitutes a "contour" map of the surface recession, but the contours lack a datum value. For example, in the case of a central impinging jet on a flat plate, the true surface recession deduced from the holographic fringes could be either of the patterns in Fig. 51 and Fig. 52. In these diagrams, the polymer surface need not be plane, or even smooth, because this method measures the recession and not the absolute depth of the polymer coating. In fact, both the initial and final surfaces will be quite irregular, as shown in Fig. 53. In the particular case of the impinging jet, from physical considerations, the pattern in Fig. 52 can be discarded, since the conditions prevailing indicate that the greatest mass transfer must occur in the area of jet impingement. But in more general and complicated cases the uncertainty is not easily resolved. The value of the fringe order number N determines which of a family of surface recession contours (Fig. 54) reflects the true state of the recessed surface.

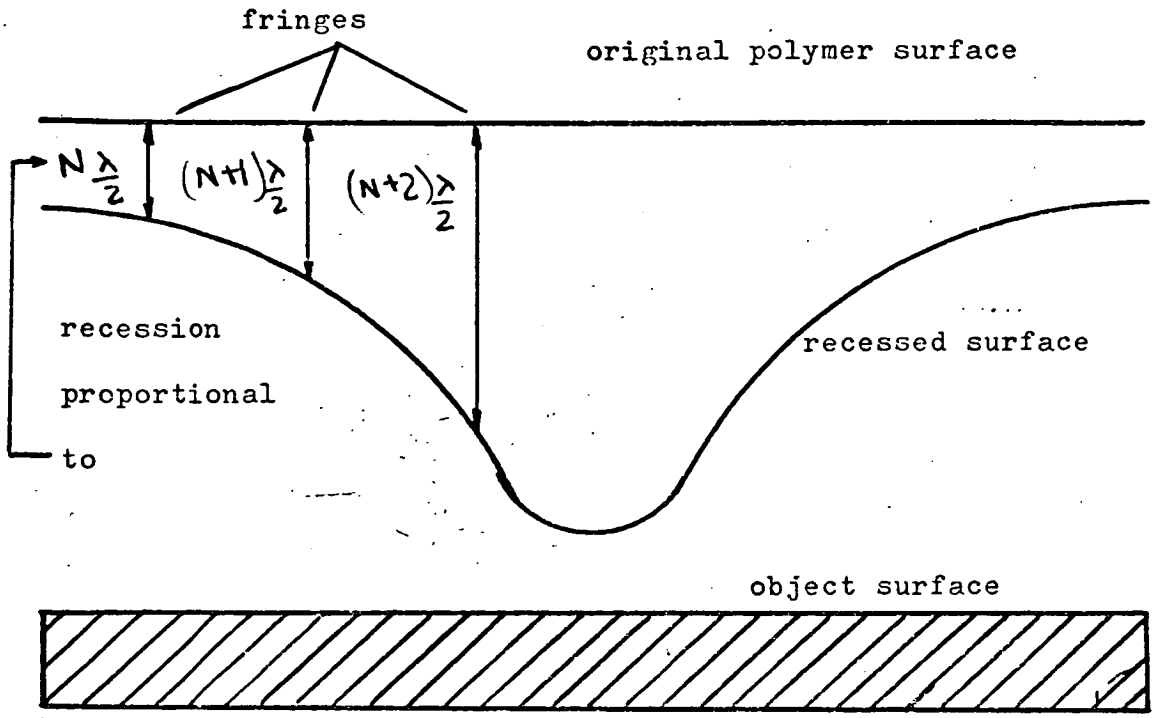

Fig. 51. Fringe position in relation to recession.

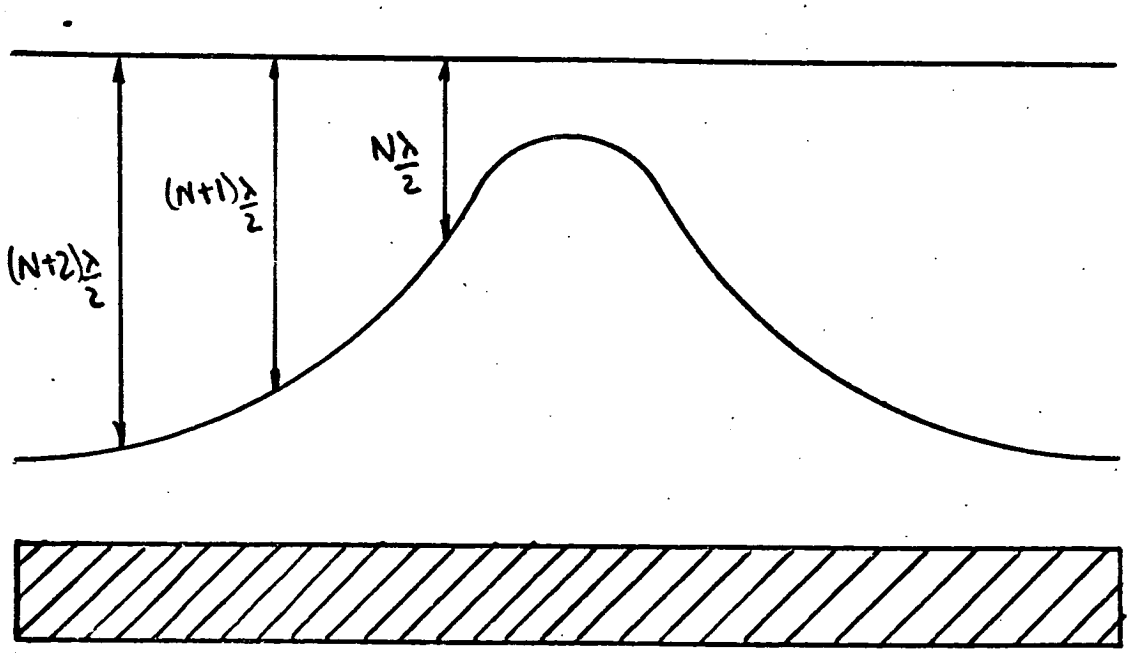

Fig. 52. Fringe position in relation to recession.

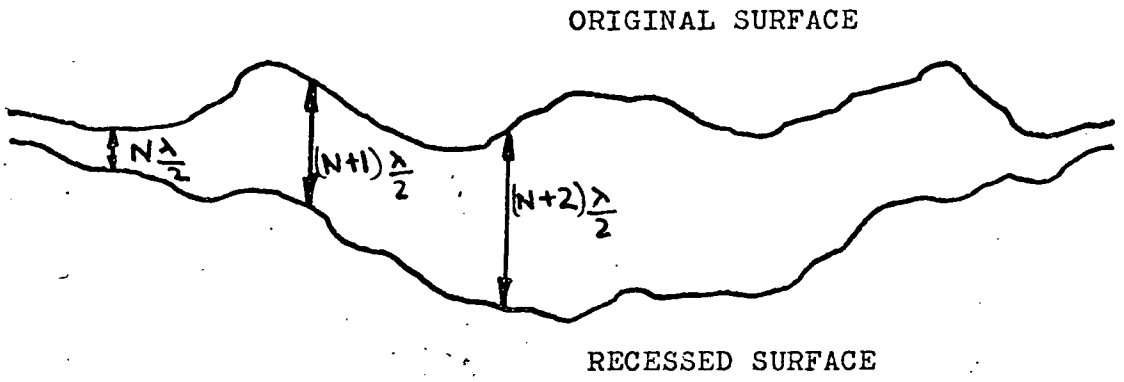

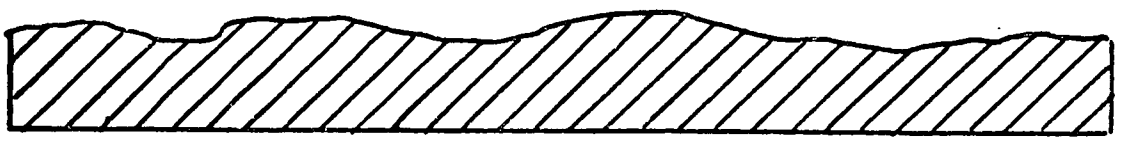

Fig.53. The irregurality of the polymer and object surfaces.

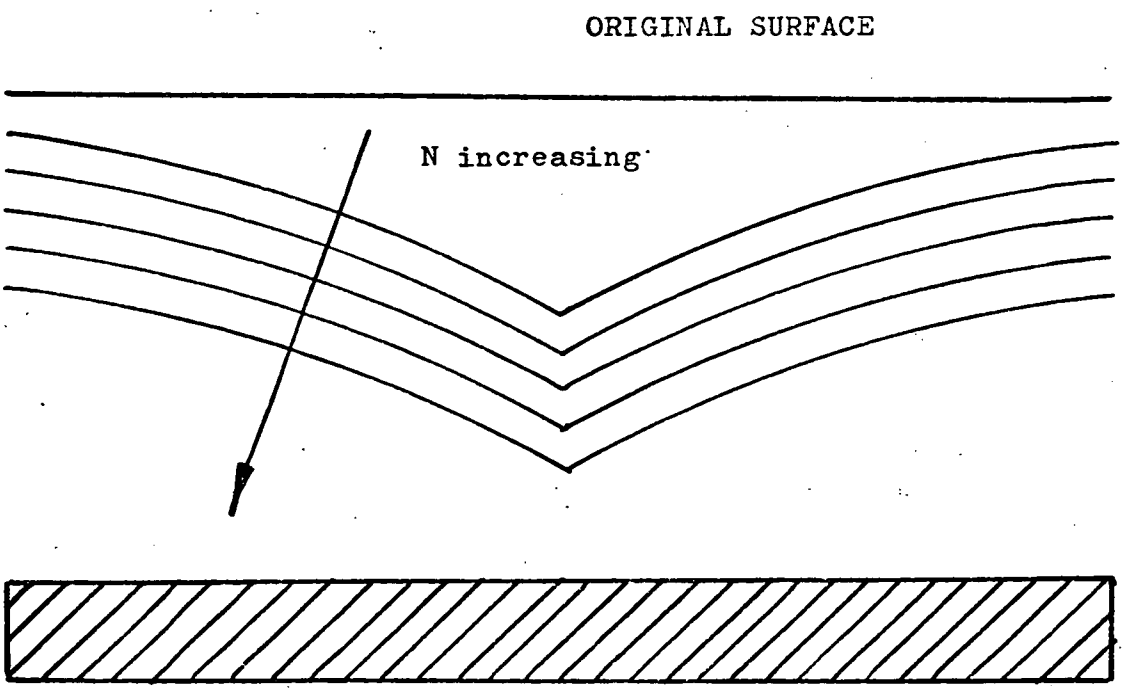

Fig.54. Variation with N of calculated recession values.

5.2.2 Methods of fringe-order determination.

One method of determing the fringe order is to conduct the mass transfer experiment in real holographic time, by viewing the recessing surface through a hologram of the original surface, and observe where and when the first fringe makes its appearance. This is not possible in the case of the disc, because the airflow distorts the observed image to such an extent that the fringes cannot be seen, due to buffetting of the disc.

The surface recession may be gauged mechanically at one particular point to determine which of the family of recession curves is correct (88). In the case of a small object, this method would be inaccurate, since a slight misalignment in the positioning of the sensor would correspond to the width occupied by several fringes. Kapur and MacLeod (98-100), in their experiments with central, normal, impinging jet on a flat plate, arrange matters so that the unchanged part of the surface (corresponding to the zeroth fringe) is in the field of view along with the recession fringes (Fig. 55). This method cannot be applied to the disc, because no part of it remains unchanged. Further, any attempt to create an artificial non-transferring surface to serve as a datum point, for example a metal stud implanted flush with the surface, would fail. This is because any non-transferring surface creates a large number of closely spaced fringes where the rate of recession is changing rapidly over a short distance (Fig. 56).

Although in the case of flat plates and spheres, there are theoretical correlations from which the mass transfer rates at certain points can be predicted, no such data exists at present for the convex disc. Although the convex disc constitutes a part of a sphere, the behaviour of the flow past the disc, as far as mass mass transfer coefficients are concerned, cannot be reliable inferred,

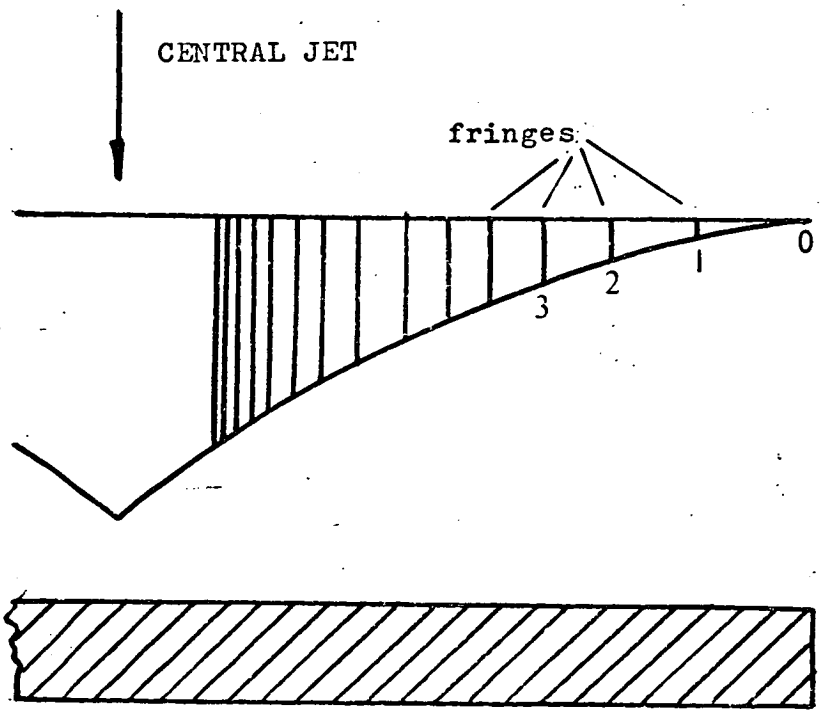

FIG.55. Zero order fringe on unchanged part of the surface distant from jet.

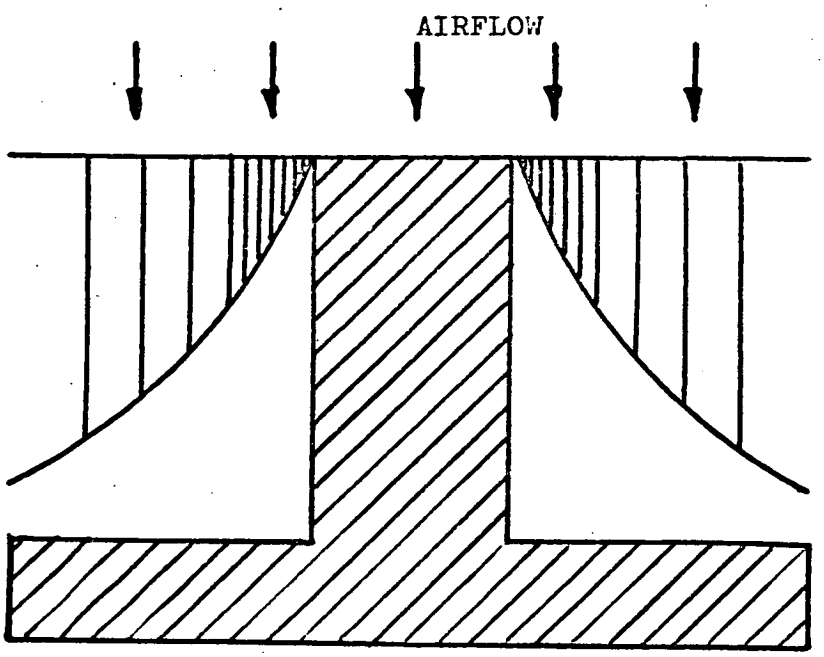

Fig.56. Closely-packed fringes on unchanged part of the surface adjacent to stud.

from the flow past a sphere, which characteristically exhibits the recession pattern shown in Fig. 57. The edge of the disc induces turbulence and flow separation which increases the mass transfer near the edge (Fig. 58).

Matsumoto (119) obtains the fringe order on a deformed cylindrical shell by fixing a taut, indexed rubber strip on the cylinder surface, and comparing the position of the index marks with the fringe positions. This method is impractical in our case, since a rubber strip on the disc would alter the hydrodynamic shape of the surface.

Abramson (116) describes an approximate method, using his Holo-diagram, relying on moving the eye from side to side and counting the fringes which appear to move past a given point. The method applies to simple displacements only. Stetson (113) proposes a method making use of localised fringes to obtain the fringe order; this method is unsuitable in our case because the fringes are not localised.

The remaining methods known collectively as "multiple view", rely on creating two or more differing fringe patterns of the object in its displaced or deformed state, from which the fringe order can be deduced from fringe coincidences. The multiple view methods use two or more of the following:

(a) directons of the reference beam.

(b) directions of the incident object beam.

(c) positions of the holographic plate (which is effectively directions of both the reference beam and the reflected object beam).

(d) viewing apertures through a single hologram.

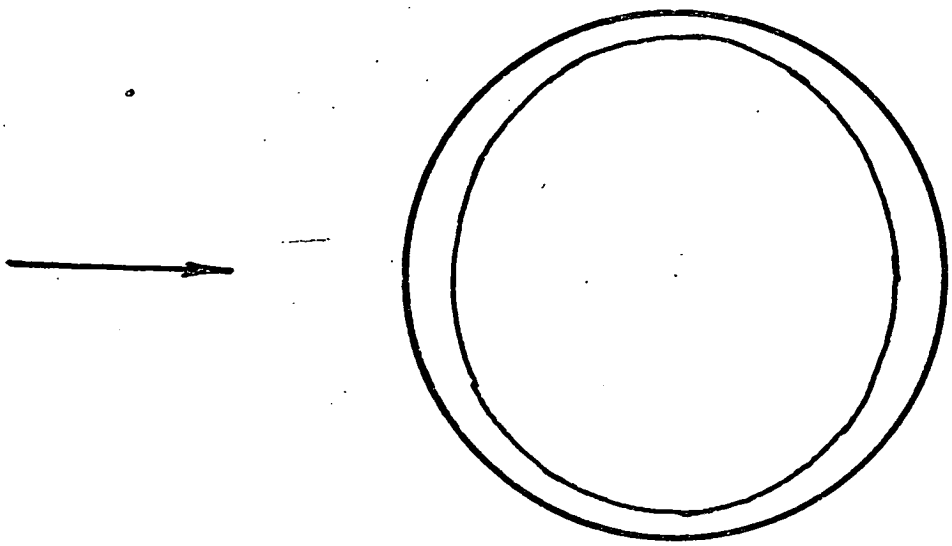

Fig.57. Characteristic recession pattern on surface of sphere.

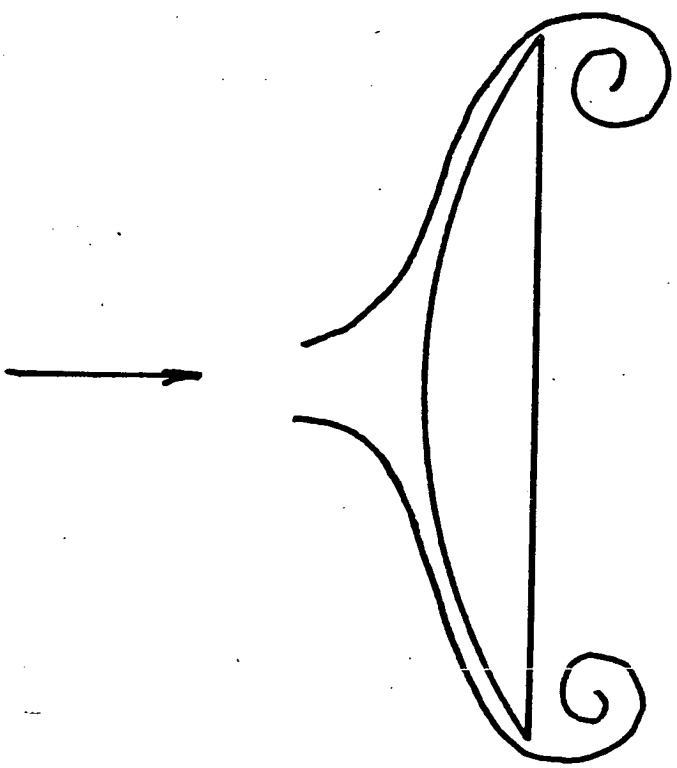

Fig.58. Flow disturbance at disc edges.

(e) positions of the reflecting surface of the object.

These methods are discussed in Section 5.1.1. There is also an extension of (a) and (b) using diffuse illumination (133) where the zero order fringe is marked by a region of high contrast surrounded by an area of low visibility.

The multiple view methods have the advantage that the required fringe order information is contained in the hologram. An application of (d), the recording camera in two viewing positions to a single hologram, was chosen as the most experimentally expedient (Fig. 59).

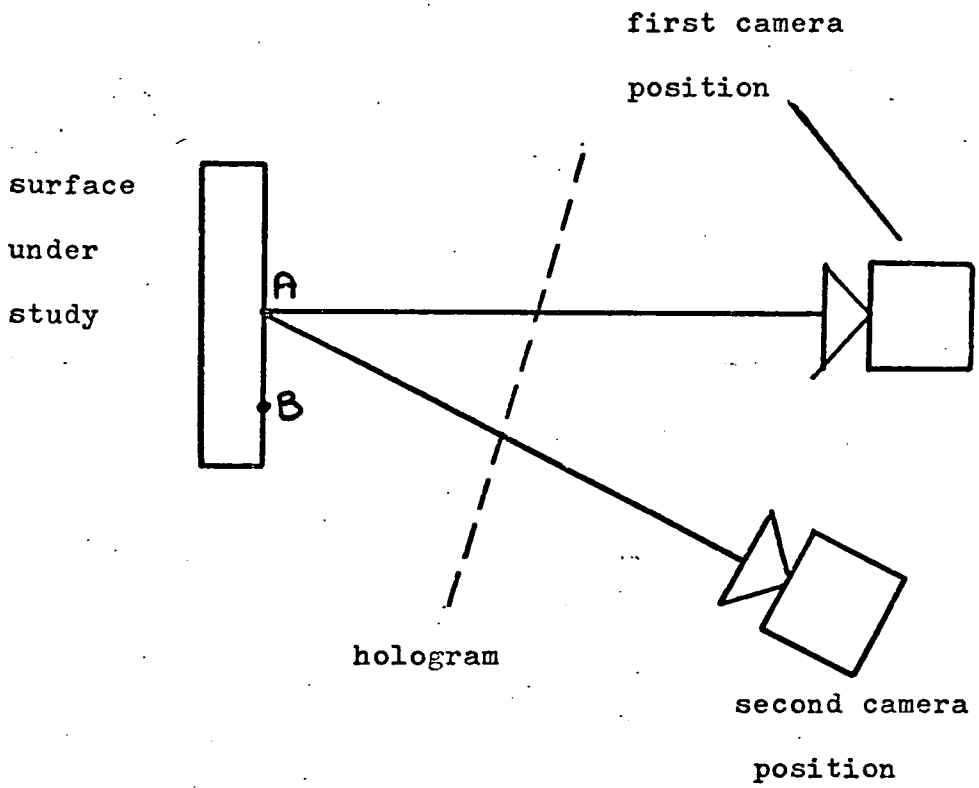

Fig.59. Two-camera method for fringe-order determination.

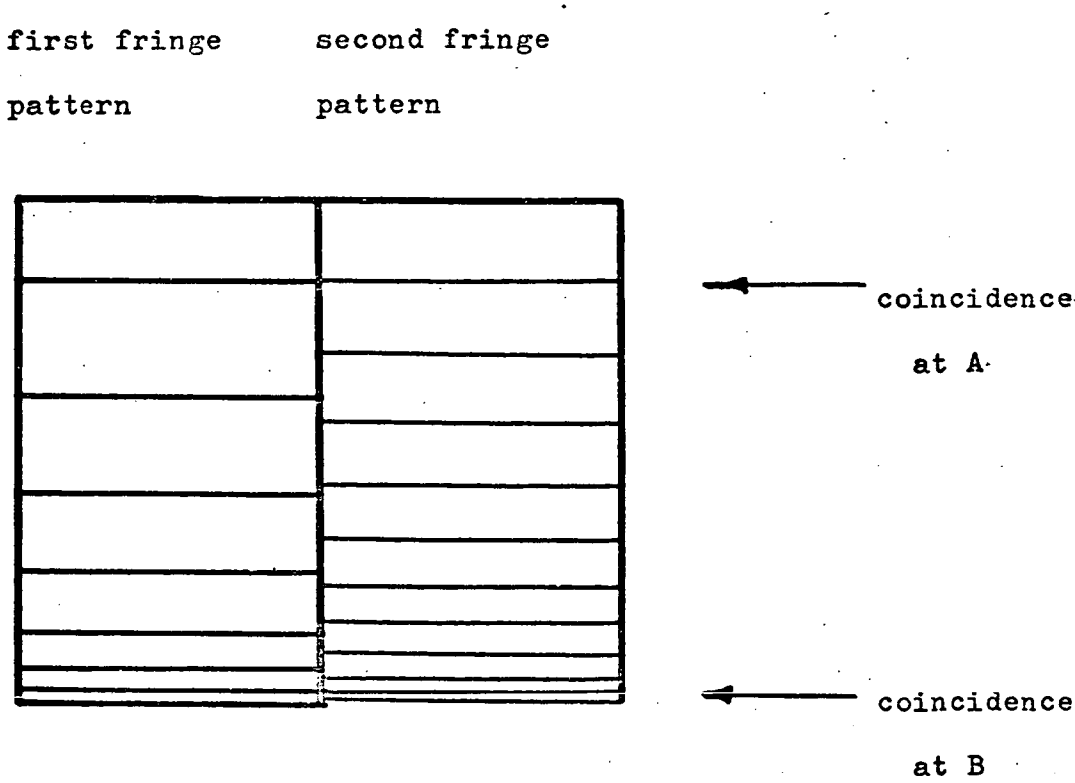

Fig.60. Fringe coincidences with the two-camera method.

5.2.3. The coincidence method for fringe order identification.

The principle of the coincidence method is that at any point on the reflecting surface, the actual recession as deduced from each of two fringe patterns must be the same. Referring to Fig. 60, the number of fringes between A and B can be counted, and the fringe order established by simultaneous equations.

The recession at point A in the first view is given by:

$$\delta = \frac{N_1 \lambda}{2f_1} \qquad \text{(from Section 5.1.2)}$$

and at point A in the second view

$$\delta' = \frac{N_2 \lambda}{2f_2}$$

Since δ must equal δ',

$$\frac{N_1}{f_1} = \frac{N_2}{f_2}$$

Similarly for a second point B where again there is a fringe coincidence

$$\frac{N_1 + a}{f_3} = \frac{N_2 + b}{f_4}$$

where a and b are the number of fringes separating A and B in each of the views. These two equations can be solved for N since f is known. The actual fringe patterns obtained in the case of the disc are not parallel lines, but are roughly circular; here the position of the fringes on an equator are considered.

It is preferable to have a wide separation between the camera

viewpoints; this results in a relatively large difference beween the f values, which reduces uncertainty in the calculated N values.

Although in the case of the disc, the fringe order was finally established by comparing the right hand and left hand halves of the disc from a single head-on photograph, the twin camera method was developed for intended use with a variety of small curved objects, and is included here for future reference. In essence, the calculations to compare the two halves of the disc are the same as the calculations to compare two views of the disc.

CHAPTER 6

The calculation of the local mass transfer coefficients on the convex disc surface.

6.1. Fringe Patterns.

Three series of photographs are shown, each series comprising the patterns obtained for various durations at one Re. No. Series 3 was chosen for analysis, since the fringes are clearest and most numerous. Series 2 includes patterns obtained with the camera held at different angles, to demonstrate the movement of fringes with this method, for the purpose of fringe order identification. For this particular shape, a greater separation of the "f" curves (Section 6.3), and thus greater accuracy, is obtained by comparing the right-hand and left-hand disc halves, instead of comparing the two camera views.

The Re. No. is based on the tube diameter (12·7 m.m.) rather than the disc diameter (10 m.m.), and is 1200, 2300 and 6100 for Series 1, 2 and 3.

SERIES 1; Flowrate 42 L/min; Re. No. 1,200;

Head-on camera except where stated.

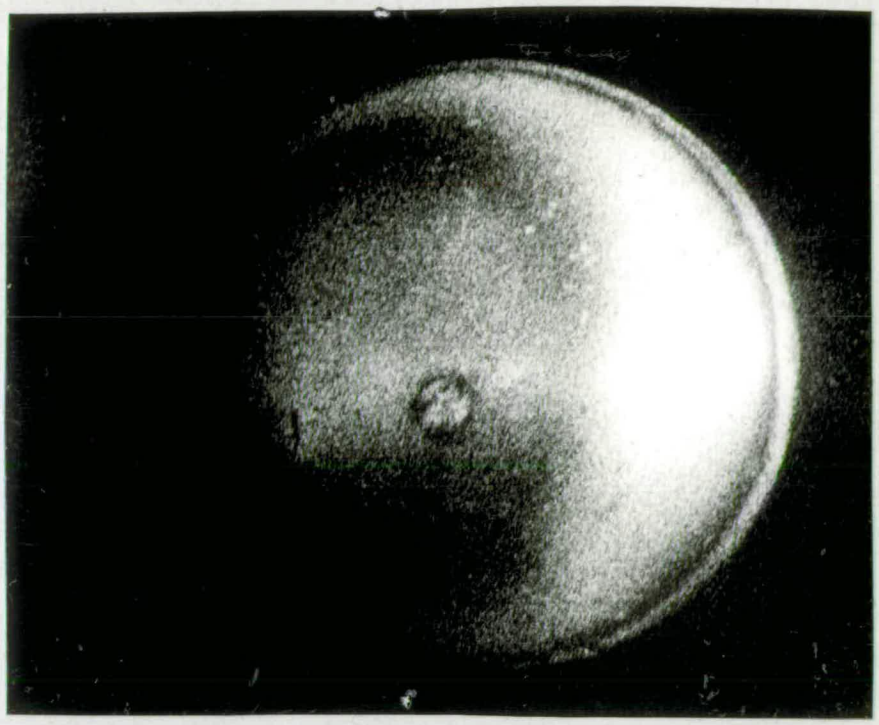

Fig. 61. Hologram 38; duration 15 secs.

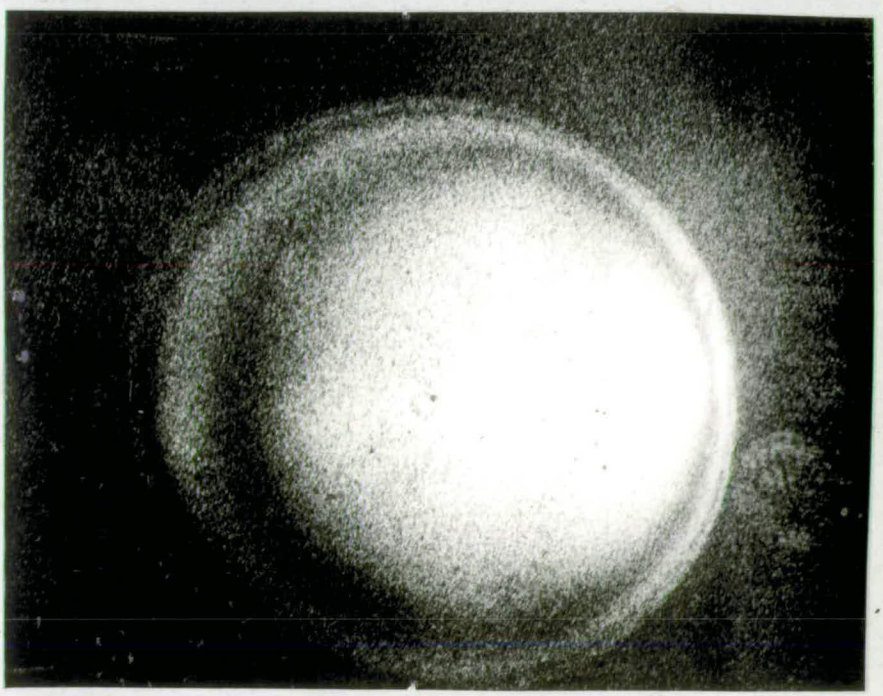

Fig.62. Hologram 36; duration 30 secs.

SERIES 1. (cont.)

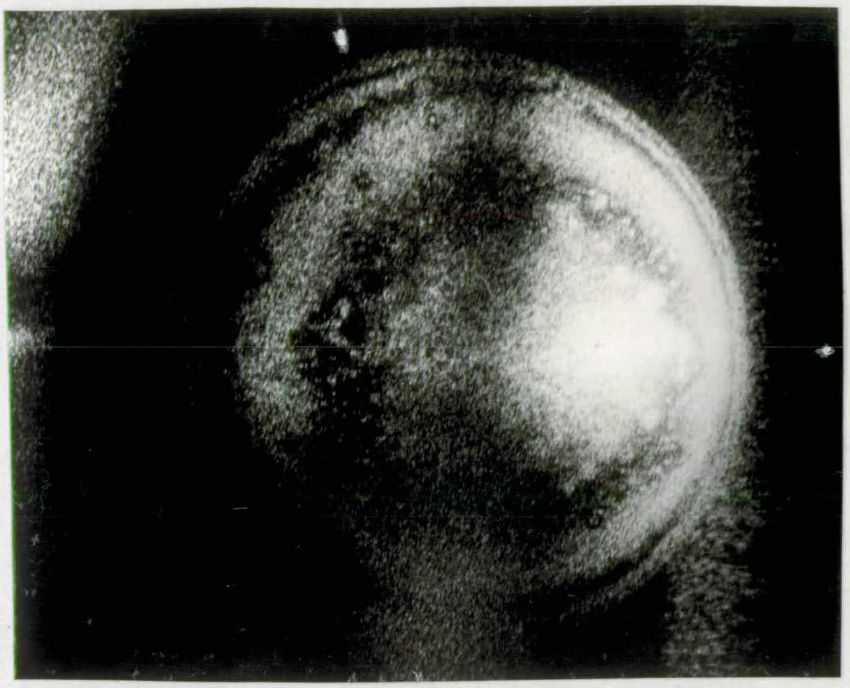

Fig. 63. Hologram 37; duration 45 secs.

SERIES 2; Flowrate 80 L/min; Re. No. 2,300.

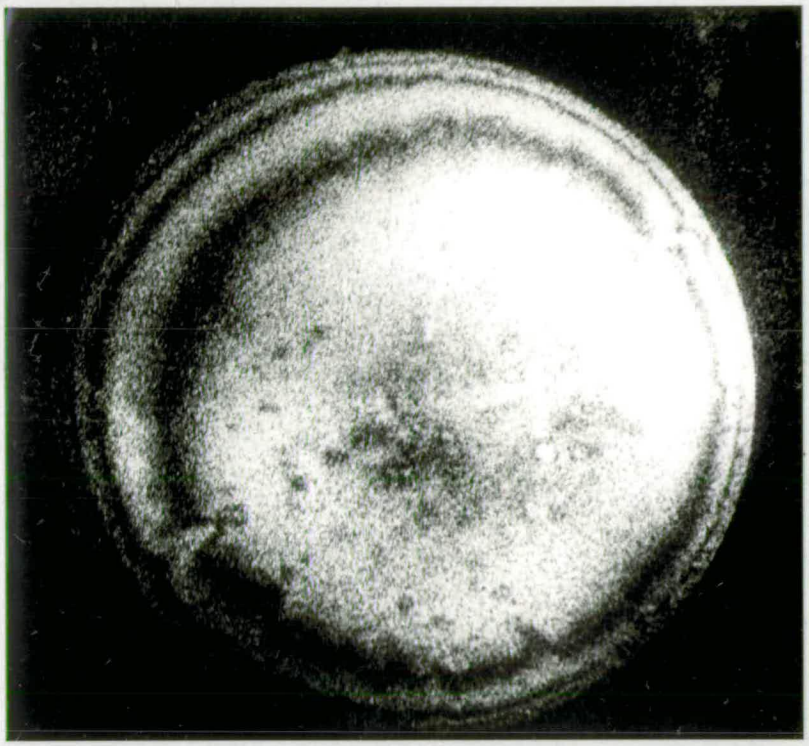

Fig. 64. Hologram 32; duration 30 secs.

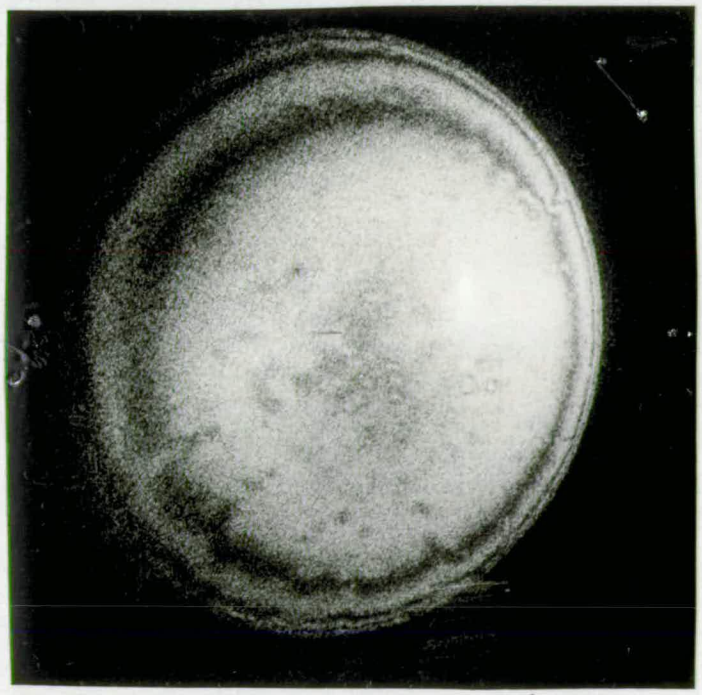

Fig. 65. Hologram 32; camera at 25 deg.

SERIES 2. (cont.)

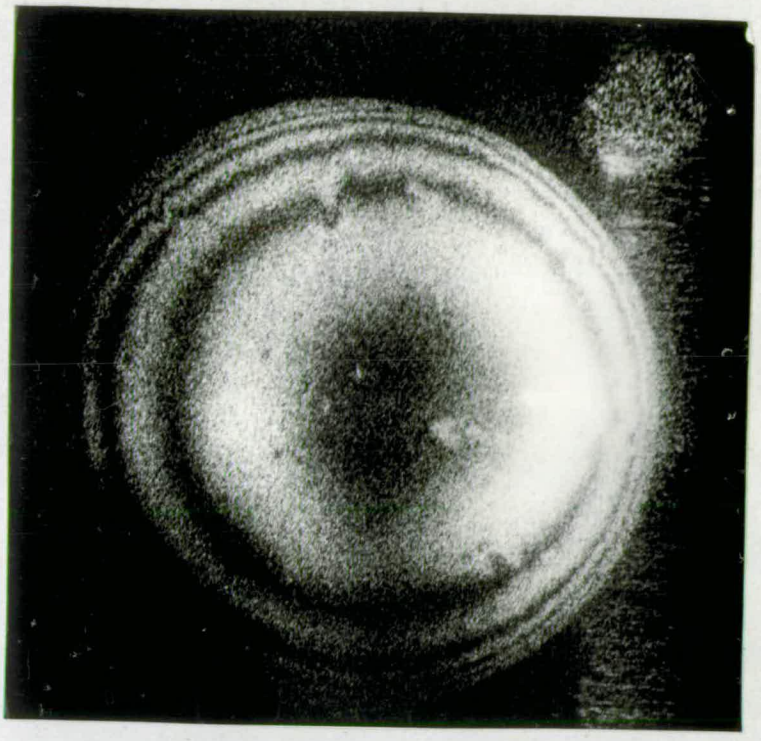

Fig. 66. Hologram 33; duration 60 secs.

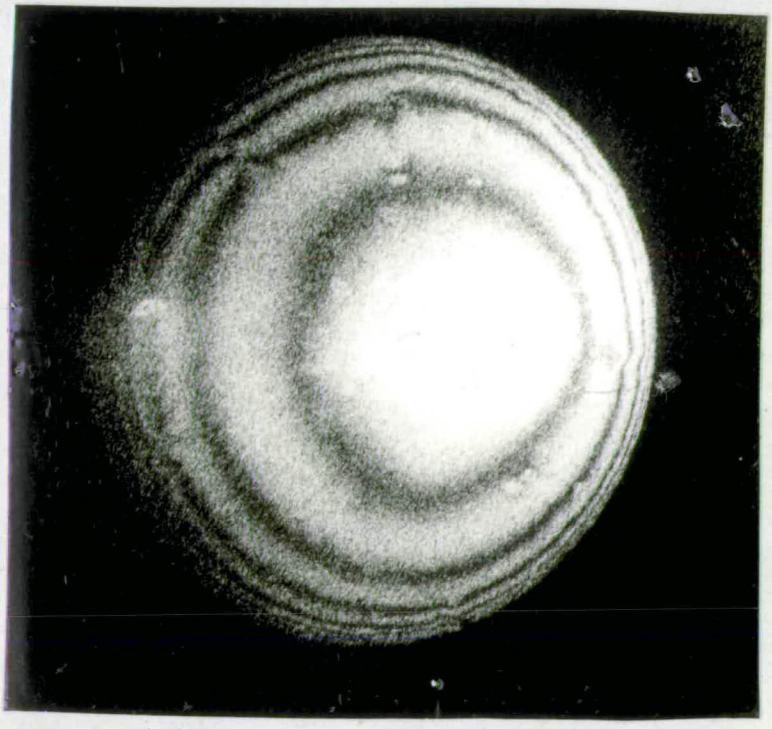

Fig. 67. Hologram 33; camera at 25 deg.

SERIES 2. (cont.)

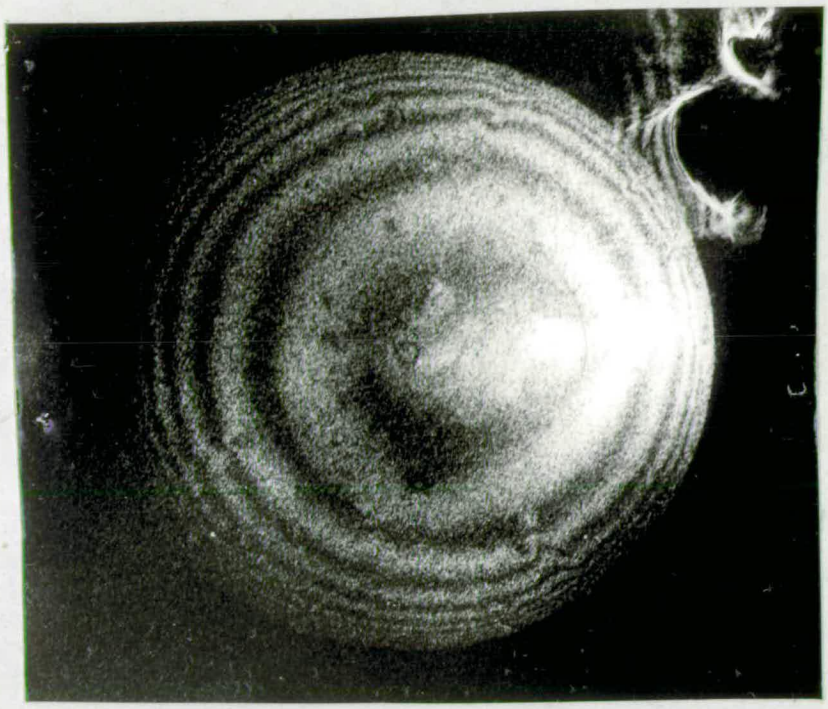

Fig. 68. Hologram 34; duration 90 secs.

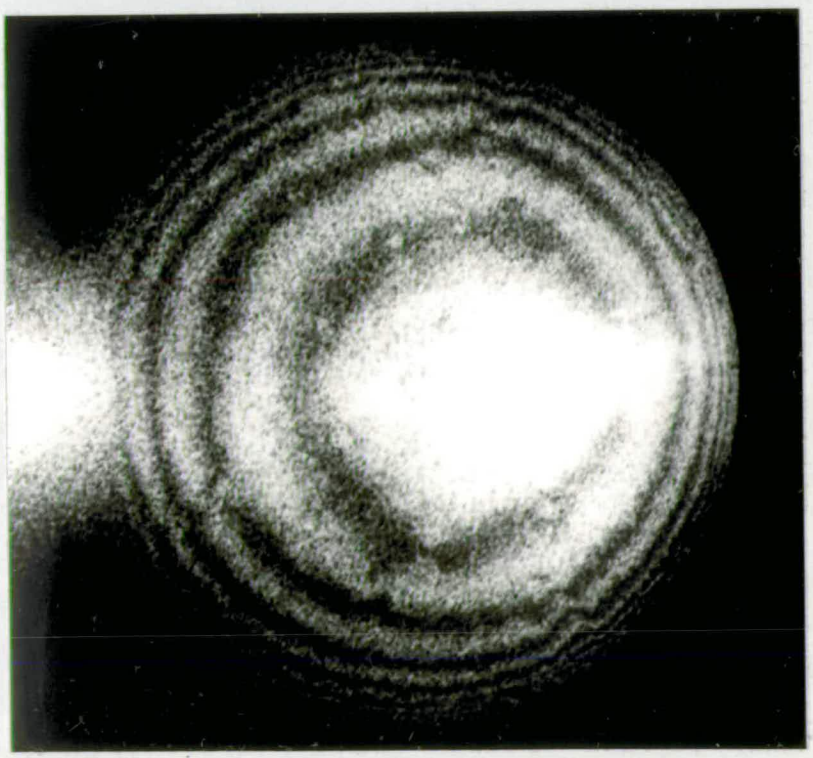

Fig. 69. Hologram 34; camera at 10 deg.

SERIES 2. (cont.)

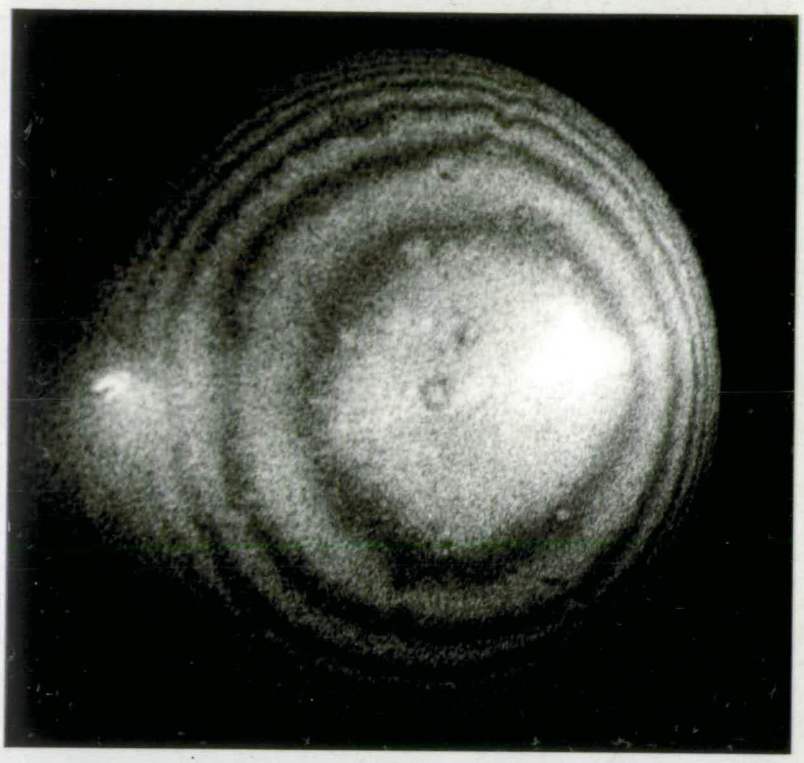

Fig. 70. Hologram 34; camera at 20 deg.

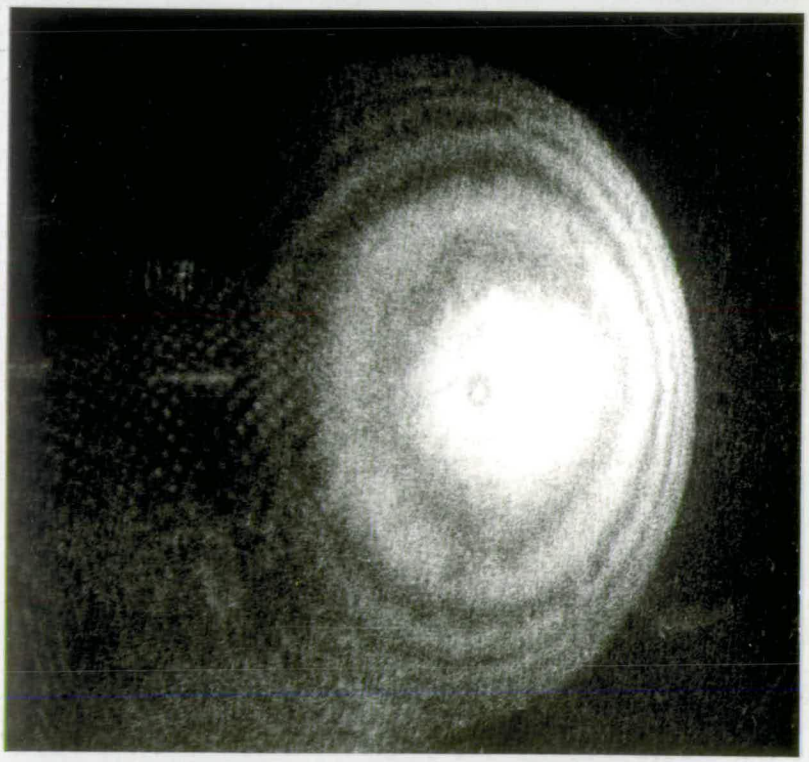

Fig. 71. Hologram 34; camera at 40 deg.

SERIES 3; Flowrate 210 L/min; Re. No. 6100.

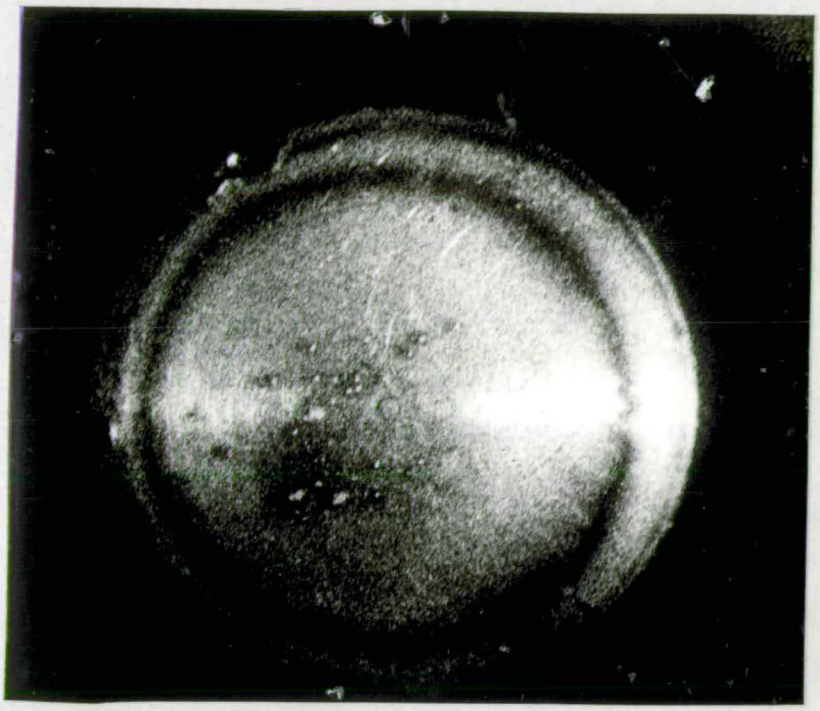

Fig. 72. Hologram 27; duration 15 secs.

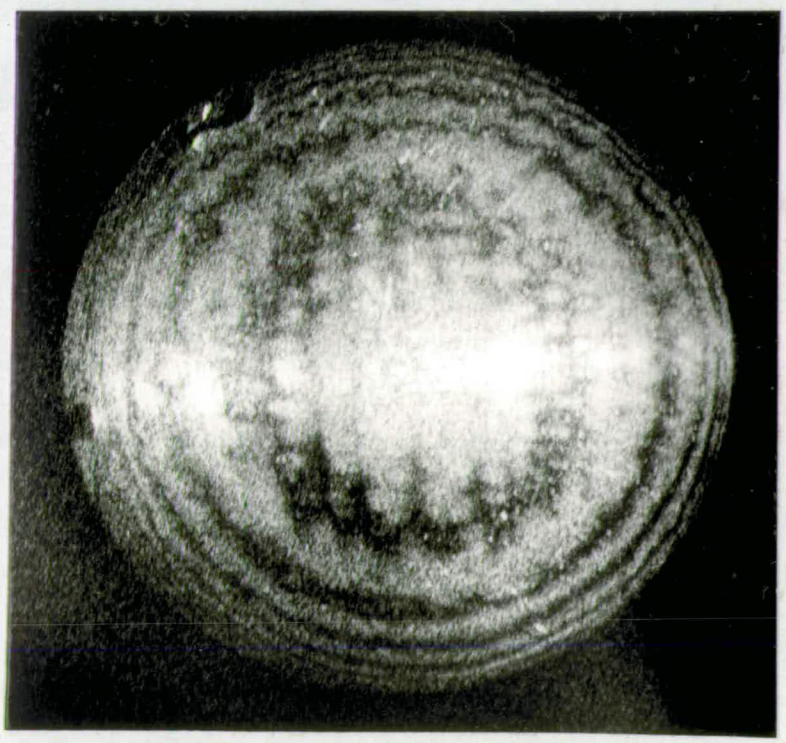

Fig. 73. Hologram 28; duration 45 secs.

SERIES 3. (cont.)

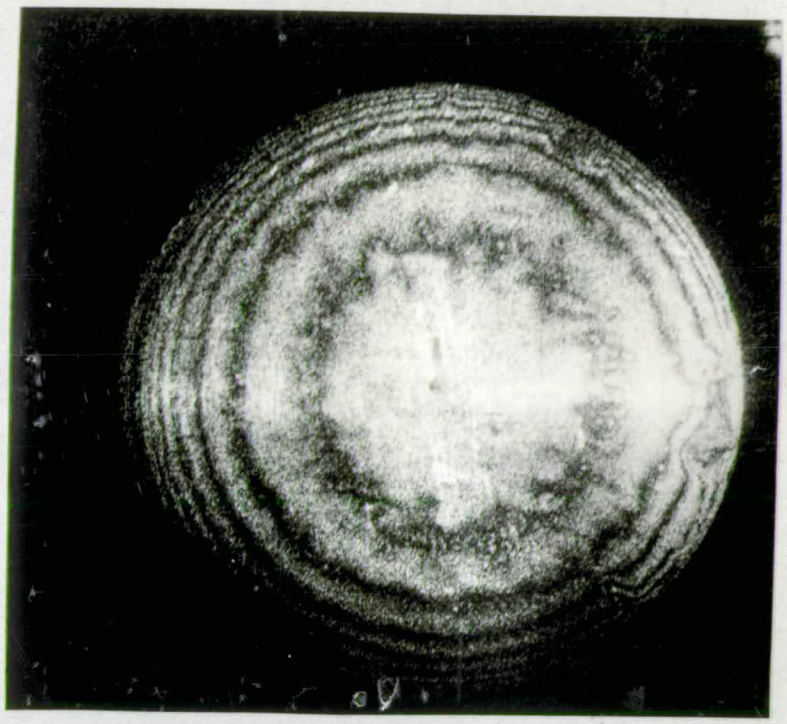

Fig. 74. Hologram 29; duration 60 secs.

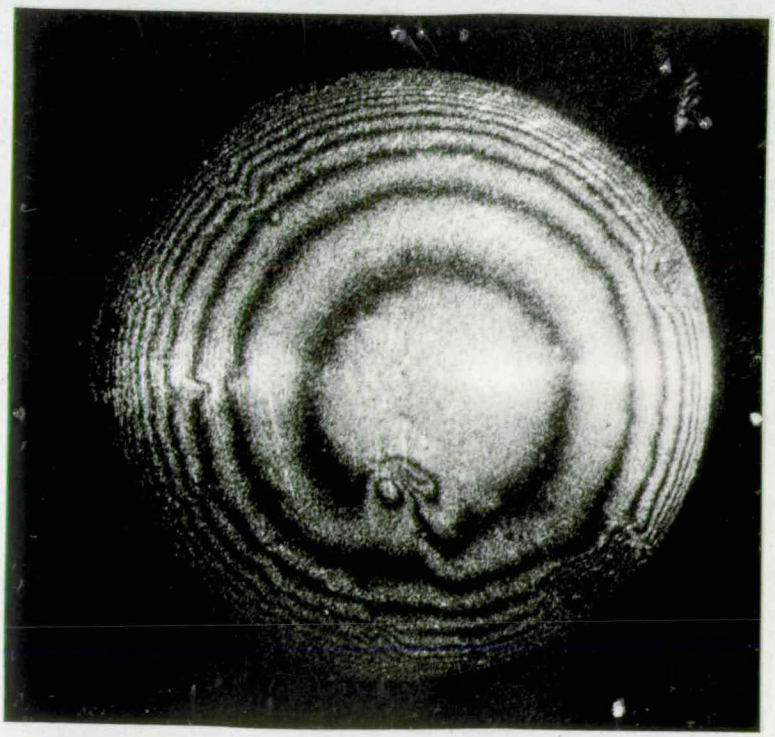

Fig. 75. Hologram 30; duration 90 secs.

SERIES. 3. (cont.)

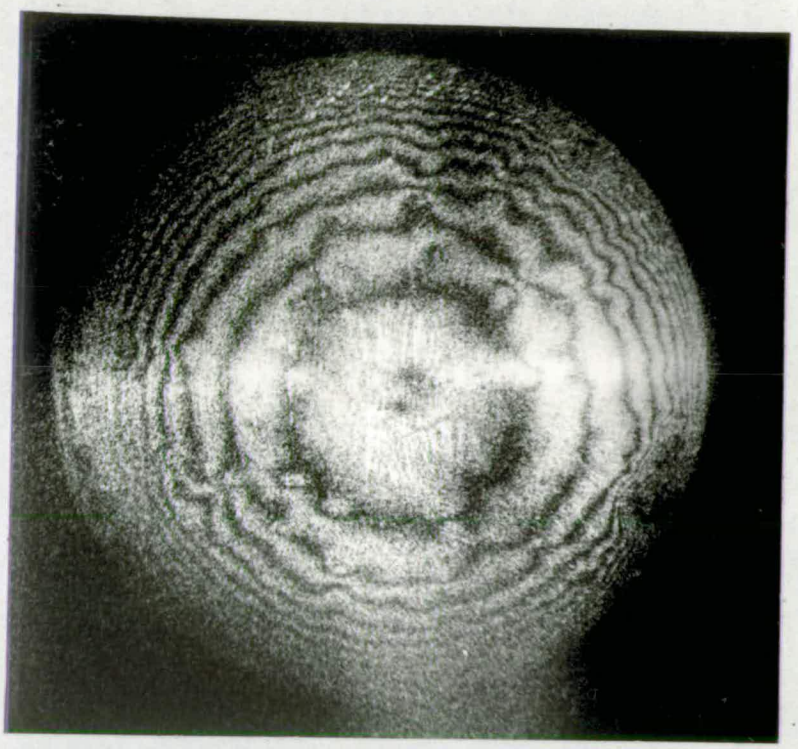

Fig. 76. Hologram 31; duration 135 secs.

6.2 The determination of direction of increasing fringe order.

The question is whether the first fringe forms at the centre (N' increasing outward) or the perimeter of the disc (N' increasing inward).

Suppose N' increases inward; the recession on the disc would be of the form shown in Fig. 77, i.e. higher mass transfer at the centre. If N' increases outward, the recession would be like that shown in Fig. 78. To clarify the distinction, imagine the disc surface flattened out (Fig. 79). Both recession patterns would consist of a series of roughly circular concentric fringes. However, since in the shortest duration experiments, fringes are seen on the outside of the disc, the recession must be greater there; and so the second recession pattern (N' increases outward) is the correct one. This was confirmed by assuming the alternative pattern in the RH-LH comparison, which resulted in negative N values. Since that is an impossible situation, the assumption is wrong.

Fringe Width

Consideration of the fringe width cannot in this case be used to determine the direction of increasing N', since the fringes increase in width toward the centre in both cases (Figs. 80 and 81). However, the variation in fringe width does indicate that the recession is of the pattern shown in Fig. 82, as opposed to that shown in Fig. 83. Width variation is also discussed in the interpretation of the parallel plate experiments (Section 9.3). The fact that fringes appear to have a finite width is because: the centre of a dark fringe represents complete destructive interference of the light beams. The centre of a bright fringe represents complete constructive interference. Moving from the centre of a dark to the centre of a bright fringe,

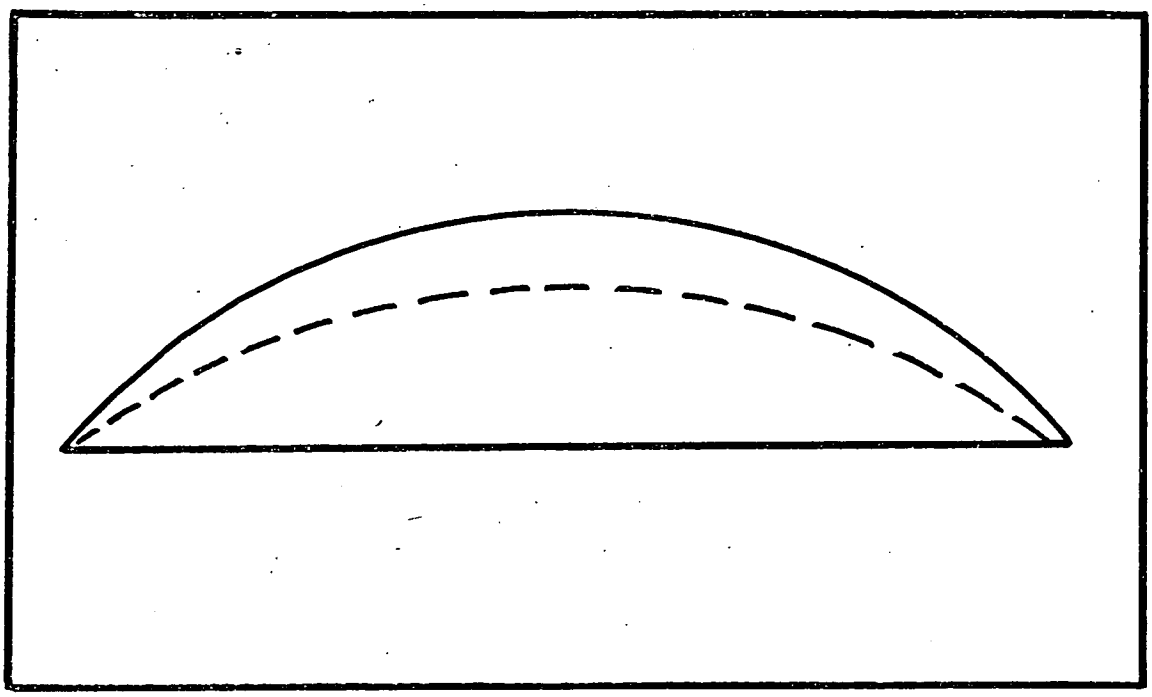

Fig.77. Recession on disc with N' increasing inward.

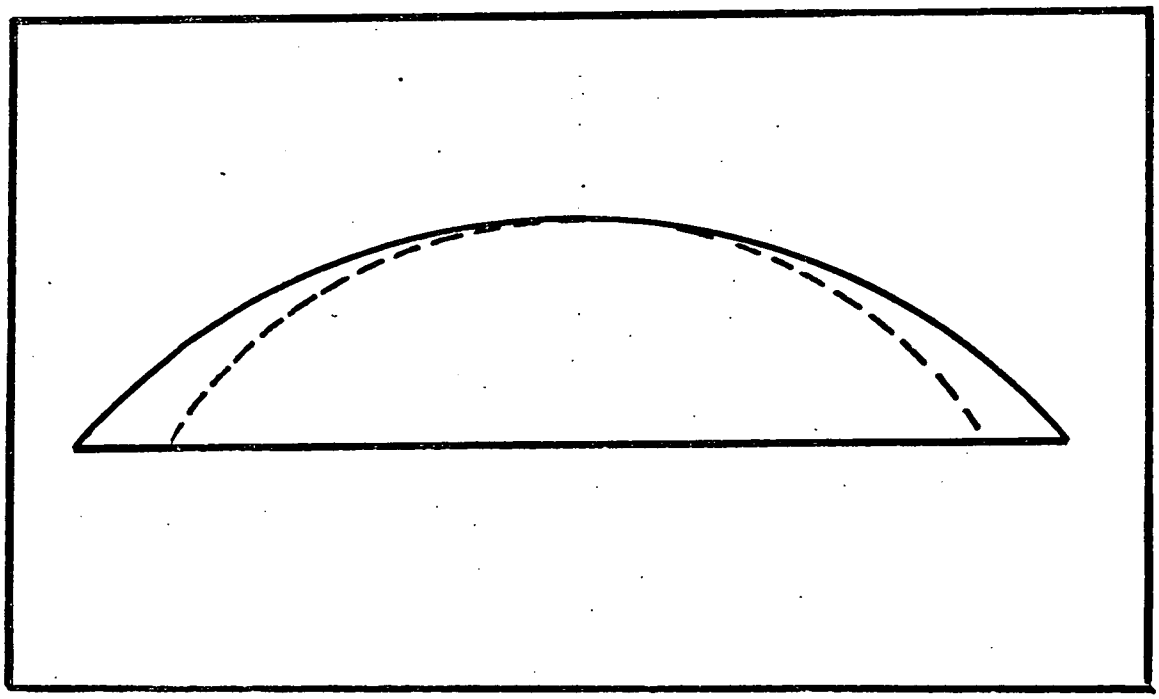

Fog.78. Recession on disc with N' increasing outward.

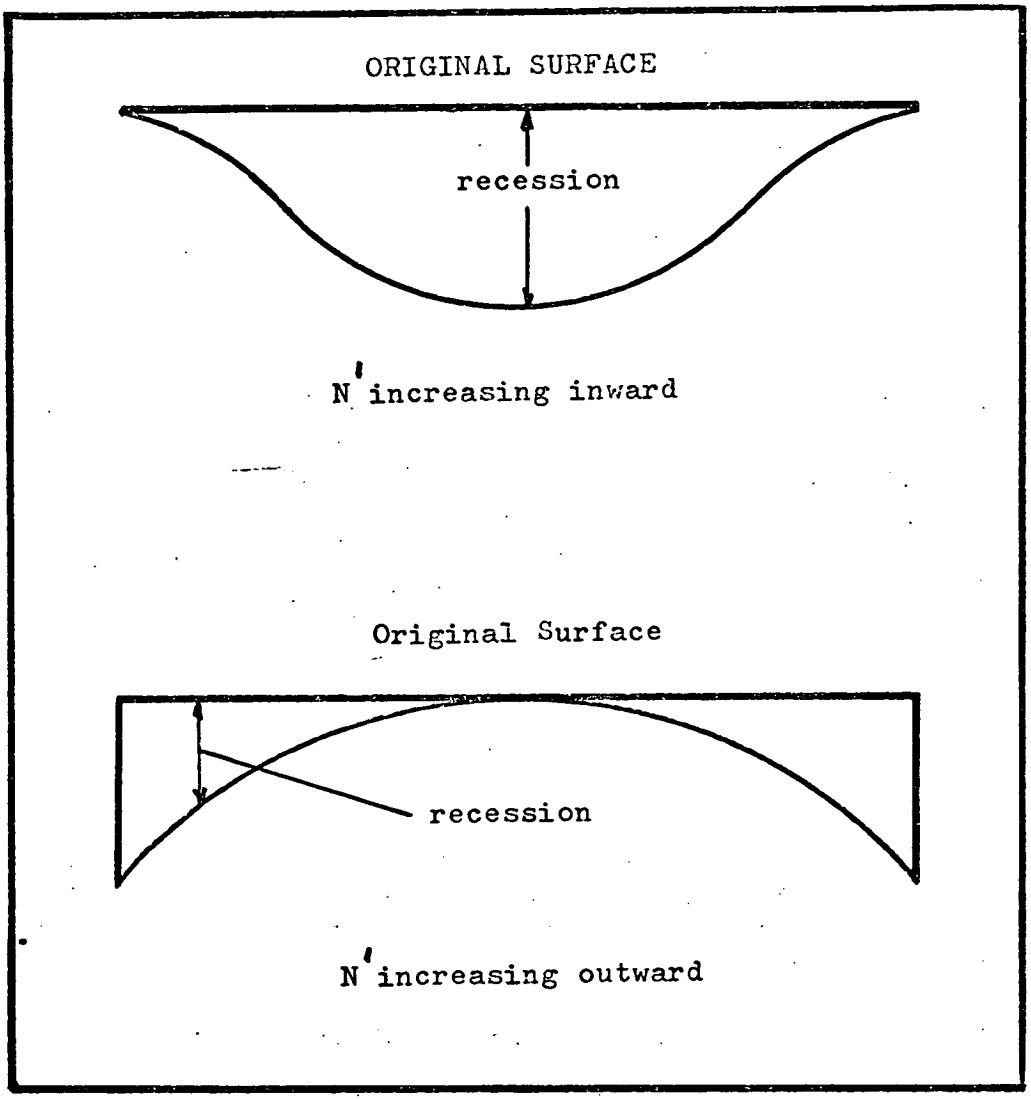

Fig.79. Recession patterns with "flattened" disc.

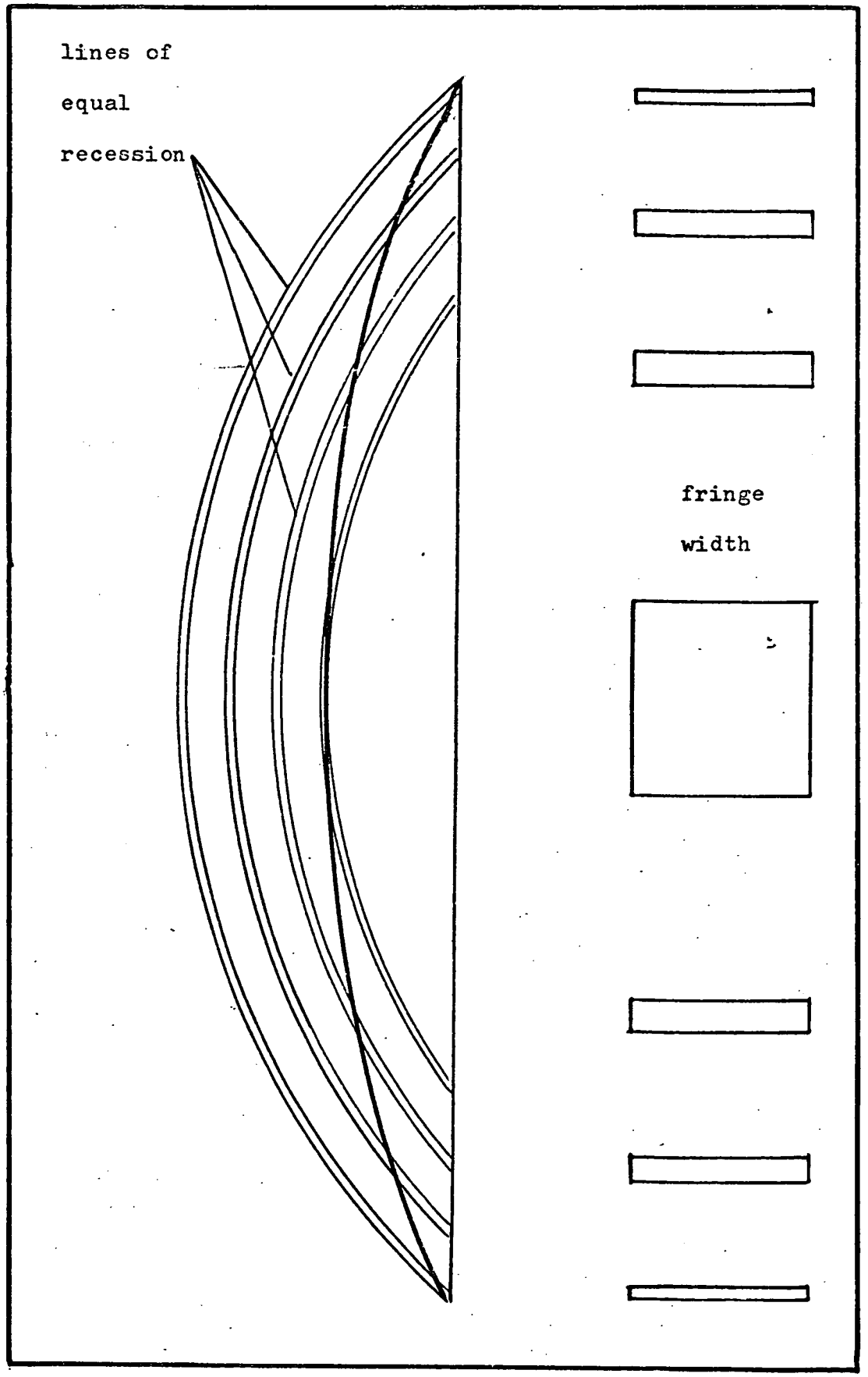

Fig.80. Fringe widths with higher mass transfer at centre.

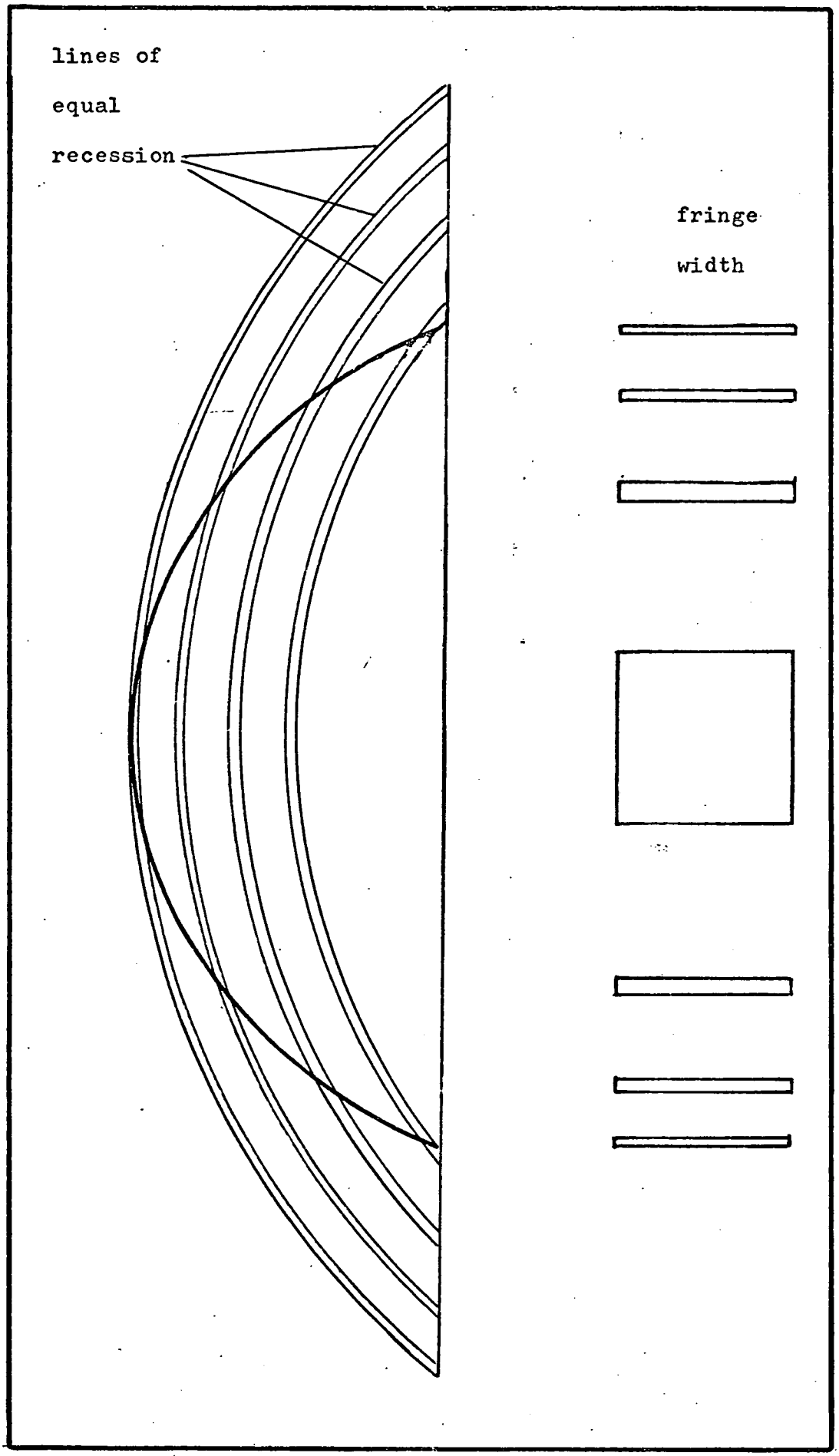

Fig.81. Fringe widths with higher mass transfer at perimeter.

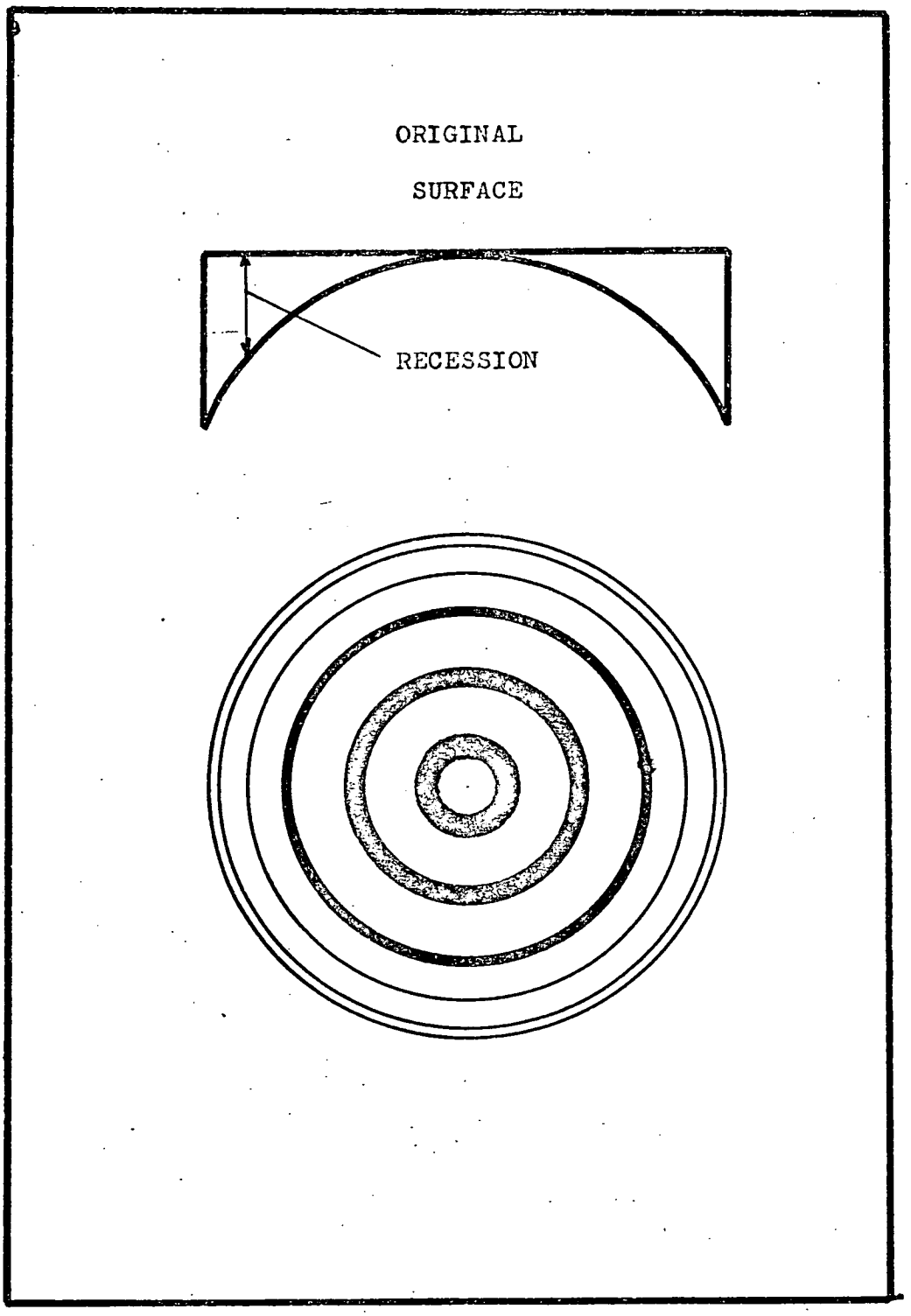

Fig.82. Recession pattern and corresponding fringe pattern.

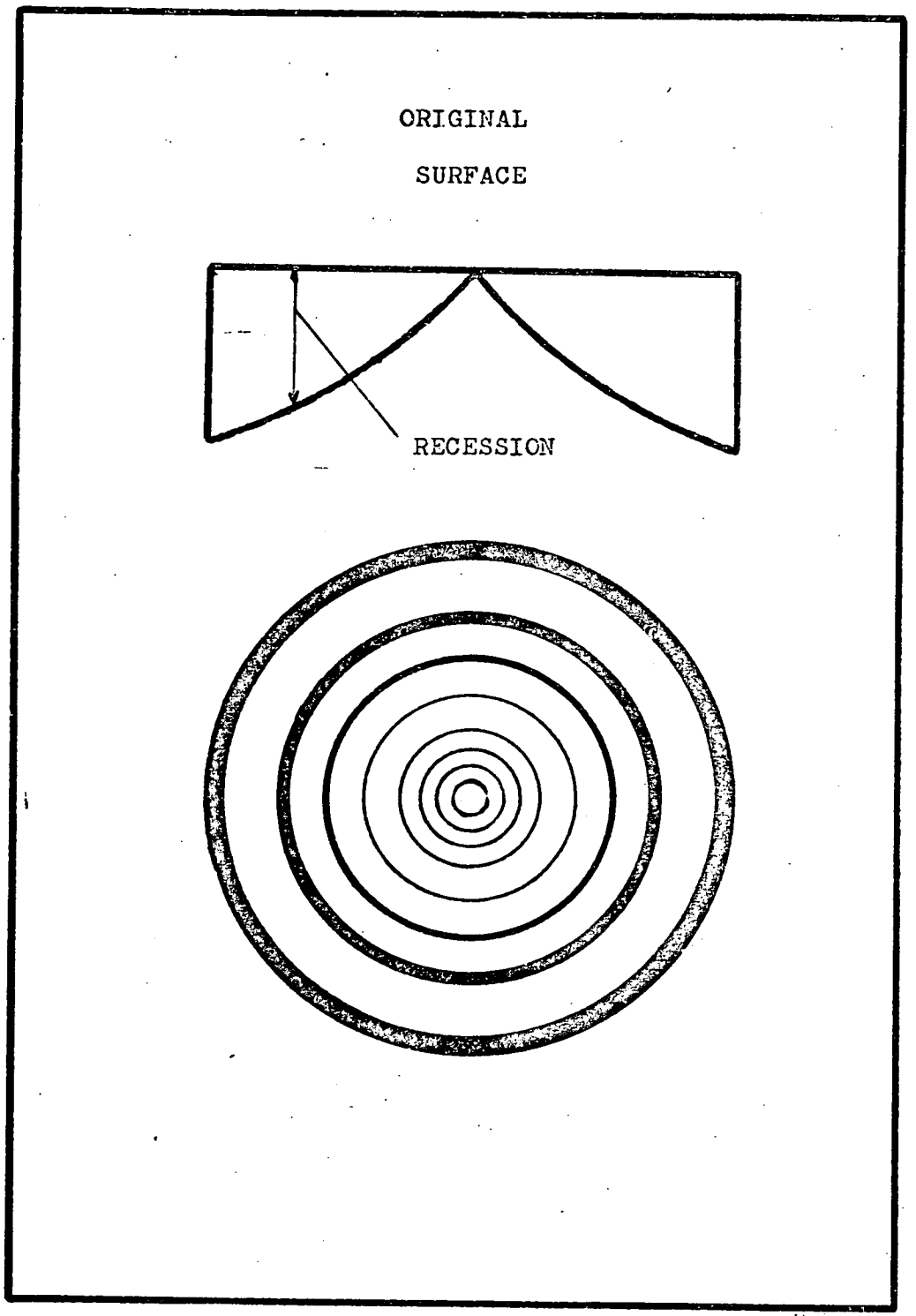

Fig.83. Recession pattern and corresponding fringe pattern.

dark gradually changes to bright, and the use of high-contrast photographic paper makes the dark fringe appear to have a distinct width.

6.3 The calculation of the mass transfer coefficients.

The first step is to adjust the measured value of the fringe position x', to the true position on the disc x, to take account of the curvature of the disc as perceived by the close-up camera. This is done using Table 1, which is calculated from equation 4, Section 4.3. Then values of the path length geometrical factor f are found for each dark fringe from the graph in Fig. 84. This graph is drawn from Table 2, which is calculated from equation 7, Section 5.1.2., i.e.

$$f = \sqrt{\eta^2 + \cos^2 i_1 - 1} + \sqrt{\eta^2 + \cos^2 i_2 - 1} - (\cos i_1 + \cos i_2)$$

where the cosine values are calculated from equation 6 Section 5.1.6. Bright fringes are ignored since they do not provide any additional information, as their position can only be gauged by considering them to be halfway between adjacent dark fringes. Thus the fringes are numbered N, N + 2, N + 4 ....etc, where each dark fringe represents a path length difference of one whole wavelength of light.

Then values of $\frac{N'}{f}$, for various values of N, are calculated for the RH and LH halves of the disc. The quantity $\frac{N'}{f}$ is proportional to the recession, and since the recession pattern on each half must be symmetrical about the vertical diameter, the $\frac{N'}{f}$ values for the RH and LH halves ought to coincide when the correct value of N is selected. That such symmetry does exist is confirmed by the symmetry of the fringes about the horizontal diameter, that is to say, the recession is constant for a given radius.

Since the $\frac{N'}{f}$ coincidence curves are ambiguous, i.e. there is a range of values of N which give equally close superposition of the curves, coincidence curves are then drawn for $\frac{N'}{f.t}$ for different mass transfer durations. The recession at any point on the disc

TABLE 1.

True x m.m.	Measured x' m.m.
0	0
.5	.5
1.0	.999
1.5	1.498
2.0	1.995
2.5	2.490
3.0	2.983
3.5	3.472
4.0	3.958
4.5	4.440
5.0	4.916

TABLE 2.

x mm	f(L.H.)	f (R.H.)
0	.882	.882
.5	.891	.876
1.0	.902	.873
1.5	.916	.871
2.0	.932	.873
2.5	.952	.876
3.0	.976	.883
3.5	1.003	.892
4.0	1.036	.905
4.5	1.074	.921
5.0	1.183	.942

where R = 9.08 m.m.; s' = 63.5 m.m. and q = 24.4 m.m. for the incident beam; s' = 88 m.m. and q = 0 for the reflected beam. Refractive index = 1.432 for RTV602 and iso-butyl benzoate.

must be proportional to the duration. Choosing the closest superposition of this second set of coincidence curves removes the ambiguity arising in the $\frac{N'}{f}$ curves.

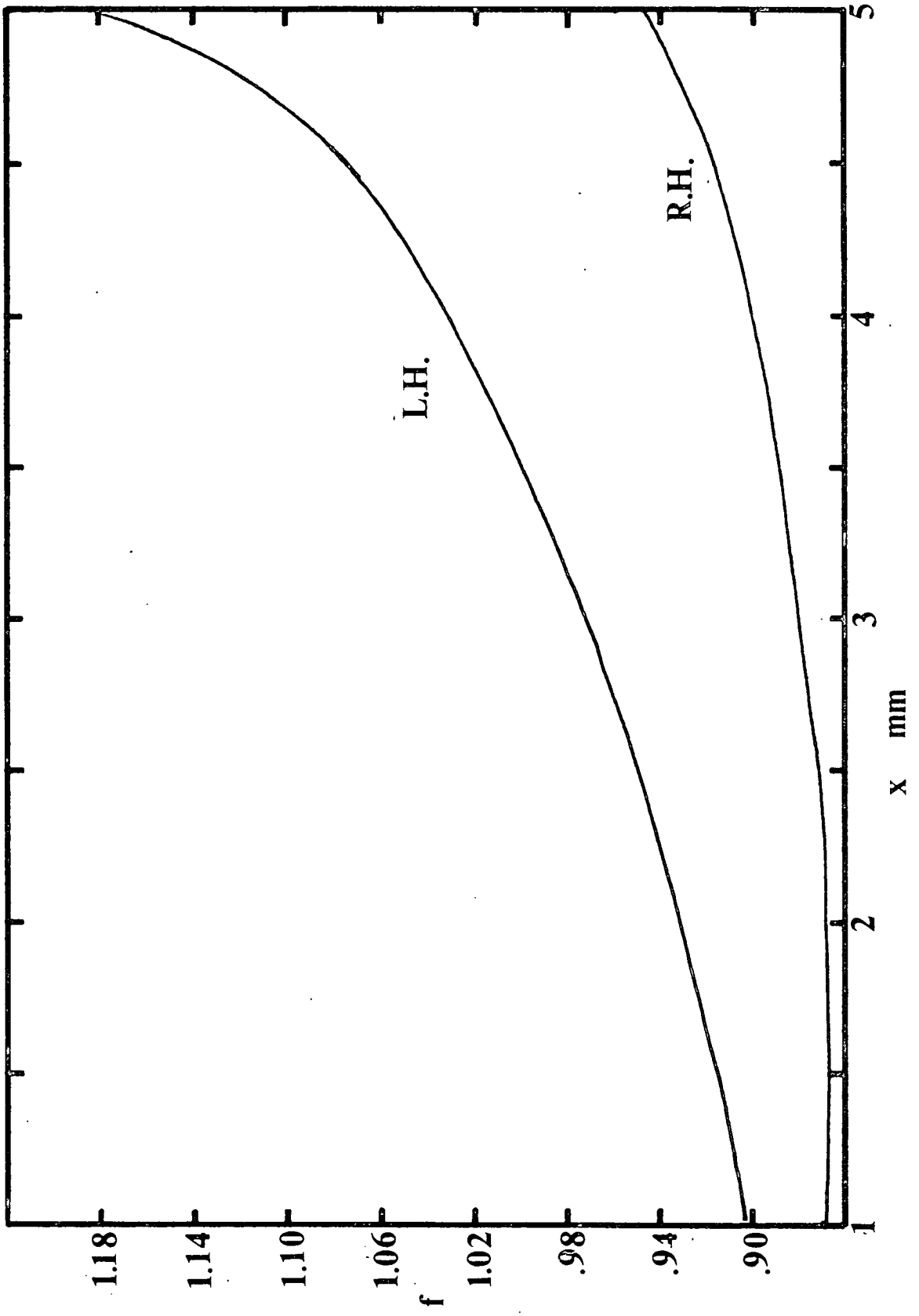

Fig.84. Geometric factor versus radius for the convex disc.

Data for K-value calculation (from Ref 105).

$\lambda = 6.33 \times 10^{-7}$ m.

Mol. wt. iso-butyl benzoate = 178.

ρ polymer RTV 602 = $.98 \times 10^{3}$ kg/m^3.

ρ iso-butyl benzoate = 1.0×10^{3} kg/m^3.

% equilibrium volume swelling = 36.3.

by proportion, ρ swollen polymer = .987 kg/m^3.

Vapour pressure iso-butyl benzoate, P_s, = .0672 m.m. Hg at 23.5°C

Concentration of swelling agent in polymer surface,

$$C_s = \frac{\text{Mol.Wt.} \times P_s \times 760}{22400 \times T_K}$$ where T_K = Abs. temp.

K.Cs.t = ρ sw.pol. $\times$ δ where t = duration, secs.

and $\delta = \frac{N'\lambda}{2f}$

$$\dot{K} = 1.609 \times 45 \times \frac{N'}{ft} \times 10^{-2} \text{ m/sec}$$ Equation 8.

Diffusivity of iso-butyl benzoate in air = $5{\cdot}00 \times 10^{-6}$ m^2/sec.

Sc. No. = 2·954.

TABLE 3. Hologram 27 (15 secs.)

	Fringe Number	Measured x'	True x	f	N'/fx3		
					N=1	N=3	N=5
LEFT HAND	N	1.67	1.69	.921	3.26	9.77	16.92
	N+2	3.97	3.99	1.032	8.72	14.53	20.35
	N+4	4.62	4.63	1.096	13.69	19.16	24.64
RIGHT HAND	N+2	3.85	3.87	.900	10.00	16.67	23.33
	N+4	4.87	4.88	.937	16.01	22.41	28.82

The recession is proportional to N'/f. The recession which would occur after 45 secs. is proportional to N'/f x 3; this figure is shown rather than N'/f, to compare with the other holograms in the series. N'/f x 3 versus radius is plotted on the graph in Fig. 85A.

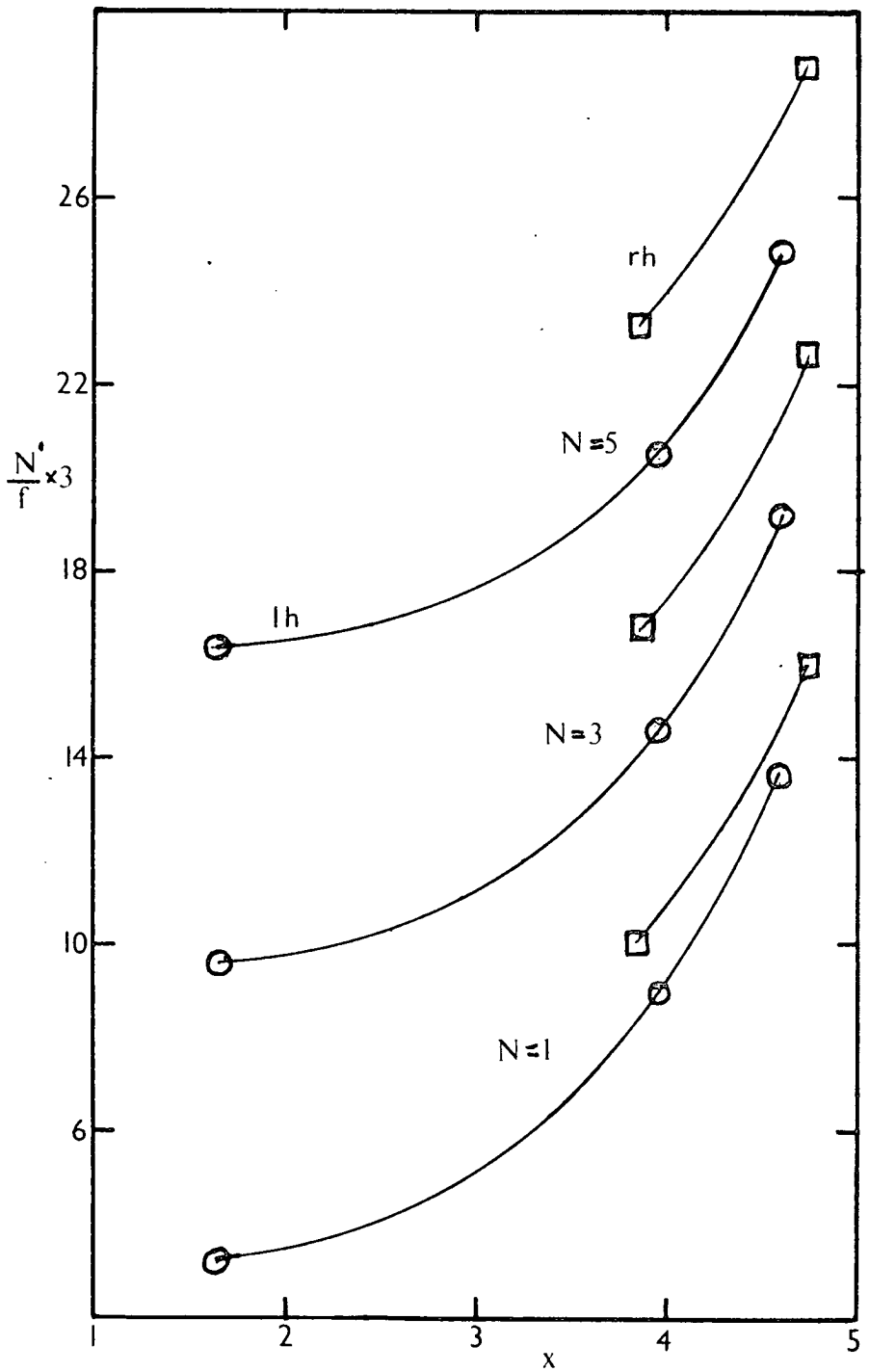

Fig 85A. Hologram 27; N'/f x 3 versus x.

TABLE 4. Hologram 28 (45 secs.)

	Fringe Number	Measured x'	True x	f	N'/f			
					N=11	N=13	N=15	N=17
	N	2.38	2.41	.948	11.60	13.71	15.82	17.93
LEFT	N+2	3.38	3.41	.999	13.01	15.02	17.02	19.02
HAND	N+4	4.00	4.03	1.034	14.51	16.44	18.38	20.31
	N+6	4.38	4.40	1.058	16.07	17.96	19.85	21.74
	N+8	4.63	4.64	1.100	17.27	19.09	20.91	22.73
	N	2.50	2.53	.878	12.53	14.81	17.08	19.36
RIGHT	N+2	4.00	4.03	.906	14.35	16.56	18.76	20.97
HAND	N+4	4.63	4.64	.928	16.16	18.32	20.47	22.63
	N+6	4.88	4.88	.937	18.14	20.28	22.41	24.55

Values of N'/f versus radius are shown on the graph in Fig. 85B

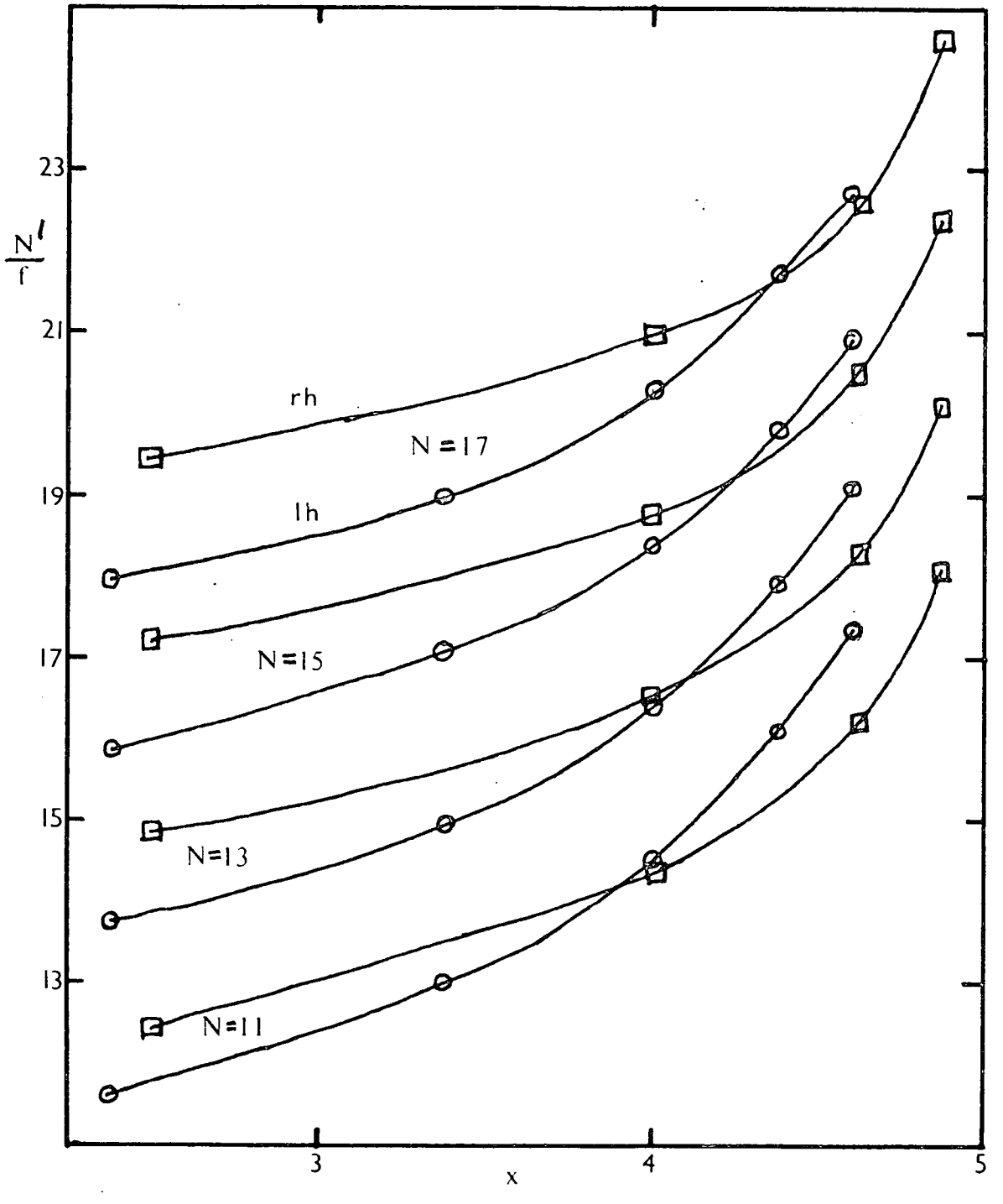

Fig. 85B. Hologram 28; N'/f versus x.

TABLE 5. Hologram 30 (90 secs.)

	Fringe Number	Measured x'	True X	f	N'/f			
					N=11	N=21	N=23	N=27
	N	1.38	1.39	.912	12.06	23.03	25.22	29.61
	N+2	2.63	2.66	.958	13.57	24.01	26.10	30.27
	N+4	3.38	3.41	.998	15.03	25.05	27.05	31.06
LEFT	N+6	3.81	3.83	1.023	16.62	26.39	28.35	32.26
HAND	N+8	4.13	4.15	1.045	18.18	17.75	29.67	33.49
	N+10	4.31	4.33	1.059	19.83	29.27	31.16	34.94
	N+12	4.44	4.45	1.07	21.50	30.41	32.71	36.45
	N+14	4.56	4.58	1.085	23.04	32.26	34.10	37.79
	N+16	4.63	4.64	1.098	24.59	33.70	35.52	39.16
	N	2.63	2.66	.878	12.53	23.92	26.20	30.75
	N+2	3.75	3.78	.899	14.46	25.58	27.81	32.26
RIGHT	N+4	4.19	4.21	.911	16.47	27.44	29.64	34.03
HAND	N+6	4.50	4.52	.922	18.44	29.28	31.45	35.79
	N+8	4.69	4.70	.930	20.43	31.18	33.33	37.63
	N+10	4.81	4.83	.934	22.48	33.19	35.33	39.61
	N+12	4.94	4.95	.939	24.49	35.14	37.27	41.53

The N'/f column is continued on the next page.

TABLE 5. (cont.)

N'/f			
N=29	N=31	N=33	N=35
31.80	33.99	36.18	38.38
32.36	34.45	36.53	38.62
33.07	35.07	37.07	39.08
34.21	36.17	38.12	40.08
35.41	37.32	39.23	41.15
36.83	38.72	40.60	42.49
38.32	40.19	42.06	43.93
39.63	41.47	43.32	45.16
40.98	42.81	44.63	46.45
33.03	35.31	37.59	39.86
34.48	36.71	38.93	41.16
36.22	38.42	40.61	42.81
37.96	40.13	42.30	44.47
39.78	41.94	44.09	46.24
41.76	43.90	46.04	48.18
43.66	45.79	47.92	50.05

Some of these values of N'/f are shown on the graphs in Fig. 85C.

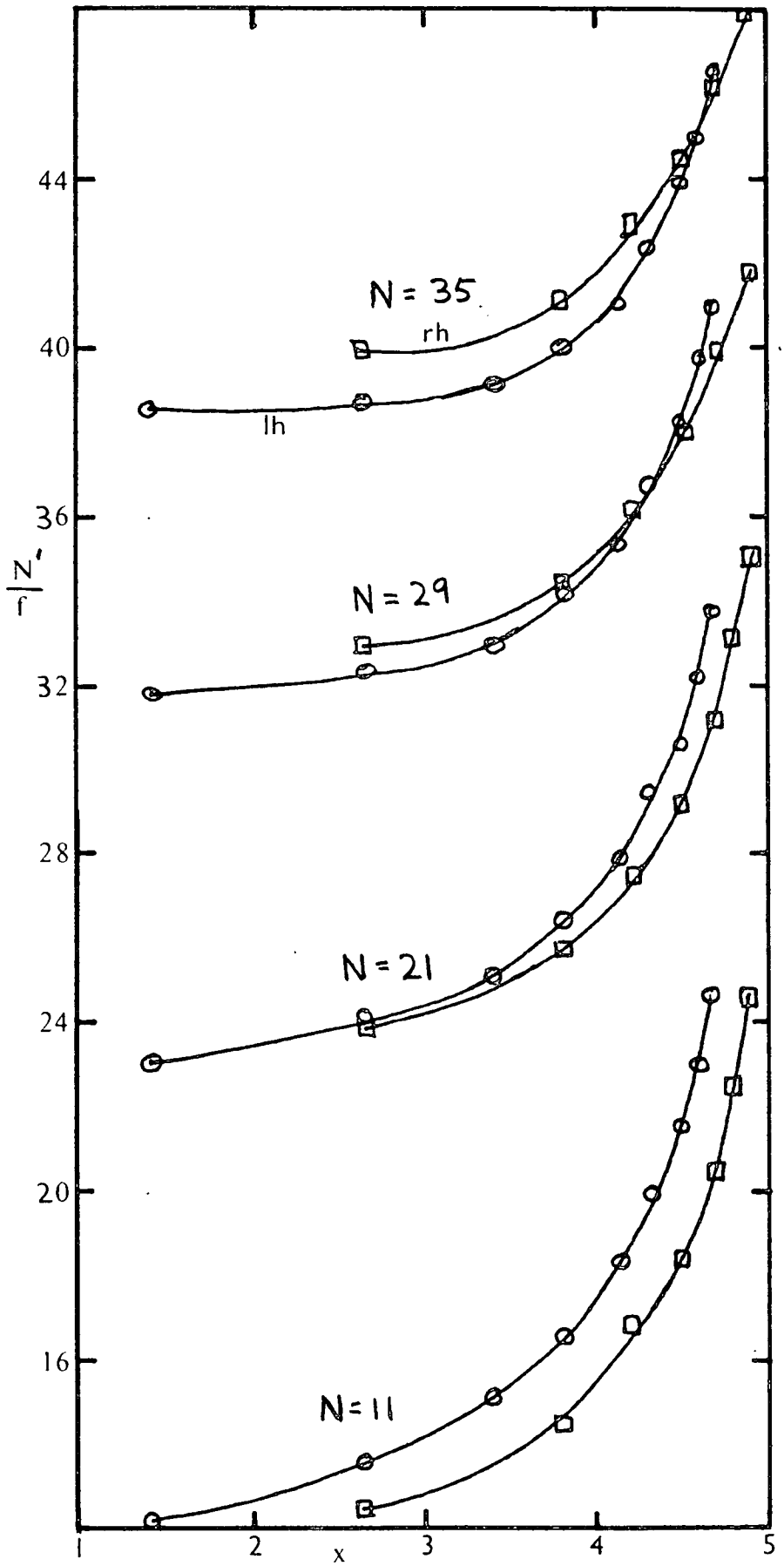

Fig. 85C. Hologram 30; N'/f versus x.

TABLE 6. Hologram 31 (135 secs.)

	Fringe Number	Measured x'	True x	f	N'/f		
					N=33	N=35	N=43
LEFT HAND	N	1.25	1.27	.908	36.34	38.55	47.36
	N+2	2.31	2.34	.945	37.04	39.15	47.62
	N+4	3.00	3.03	.978	37.83	39.88	48.06
	N+6	3.25	3.28	.989	39.43	41.46	49.54
	N+8	3.64	3.67	1.011	40.55	42.53	50.45
	N+10	3.88	3.90	1.027	41.87	43.82	51.61
	N+12	4.13	4.15	1.045	43.06	44.98	52.63
	N+14	4.25	4.27	1.053	44.63	46.53	54.13
	N+16	4.38	4.39	1.063	46.10	47.98	55.50
RIGHT HAND	N	2.00	2.03	.873	37.80	40.09	49.26
	N+2	3.13	3.16	.886	39.50	41.76	50.79
	N+4	3.75	3.78	.900	41.11	43.33	52.22
	N+6	4.13	4.15	.909	42.90	45.10	53.91
	N+8	4.38	4.39	.918	44.66	46.84	55.56
	N+10	4.50	4.52	.922	46.64	48.81	57.48
	N+12	4.63	4.64	.927	48.54	50.70	59.33
	N+14	4.75	4.76	.932			
	N+16	4.87	4.88	.937			

N'/f versus radius is plotted on the graph in Fig. 85D

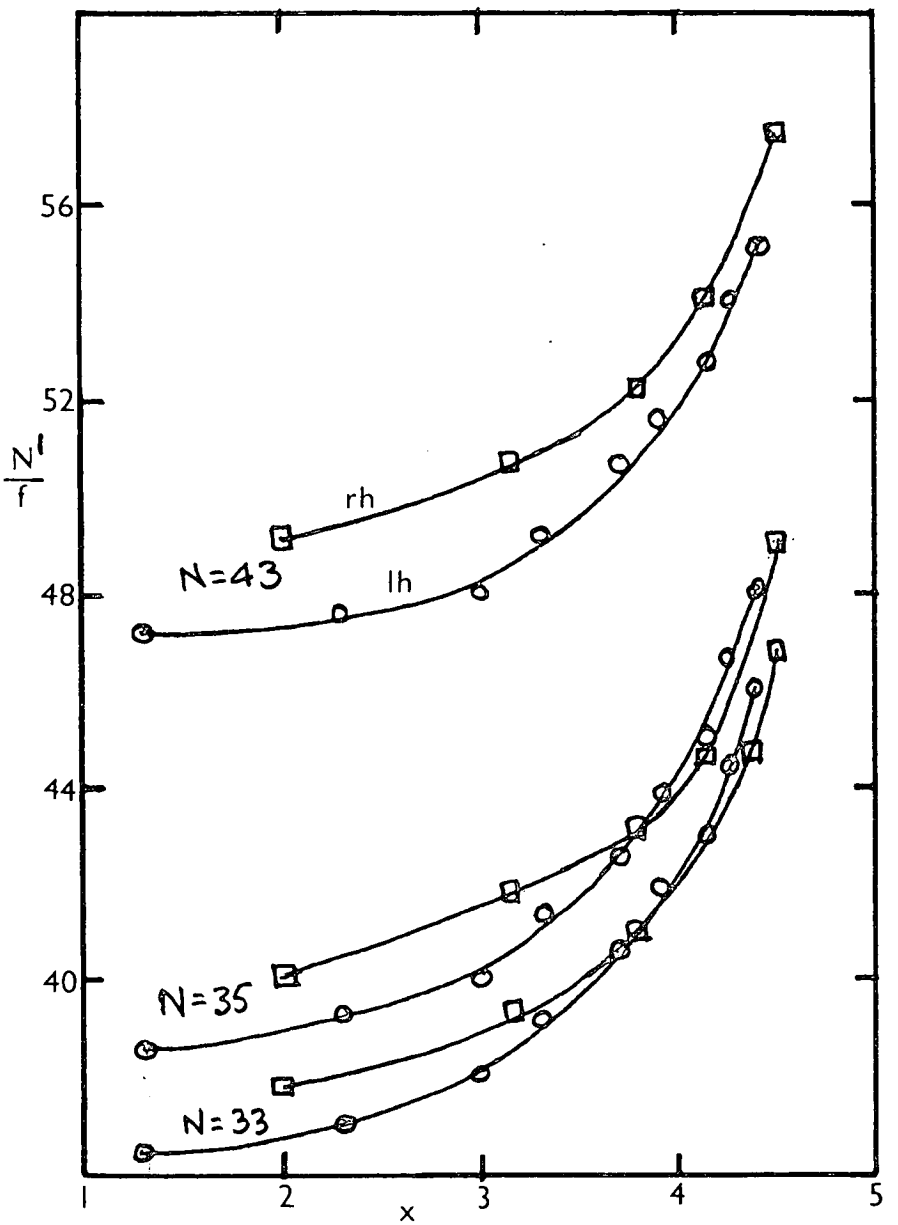

Fig. 85D. Hologram 31; N'/f versus x.

So far, we have the following information: variation of recession with radius for 4 durations, for the LH and RH disc halves, i.e. 8 sets of data. Each LH-RH pair is plotted for a variety of possible fringe order numbers. We require to match, by choosing the appropriate value of N, the LH halves with their RH halves (because of the disc's radial symmetry) and to match the short experiments with the long ones (because recession is proportional to time).

Matching of LH-RH halves

According to the N value chosen, the recession pattern is one of the characteristic patterns in Fig. 88. Unfortunately, none of the pairs of curves exactly superimpose, and in the absence of any known weighting factor which would favour, say, low order fringes (giving credence to pattern (b)), or high order fringes (giving credence to pattern (c)), the choice of N will be made on the basis of minimising the maximum percentage difference between the two halves, i.e. pattern (d). The percentage difference was noted at x values of 2.5 and 4.6 m.m. (Table 7).

Matching of short and long experiments.

As can be seen from Table 7, there is quite a large range of N values for which the discrepancy is only a few percent. Therefore, we will now consider the 4 durations to narrow the range of N. Taking Holograms 28,30,31, a good fit is obtained with N = 11,21,33 respectively, giving a maximum error between the durations, at the two x values, of 6.6%. However, an equally good fit is obtained with N = 13,25,37, with 6.9% error. In order to choose between the two sets, consider Hologram 27, which shows only a few fringes after 15 secs. mass transfer time. At such a low run-time, the start-up and shut-down errors will be considerable, and so the absolute values

of recession cannot be considered reliable. However, the ratio of the recession values at x = 2.5 and x = 4.6 is not affected by such errors. For Hologram 27, only the N values of 3 and 5 could be consistent with the other 3 holograms; the recession ratios at these values are $\frac{19.1}{10.4}$ = 1.84 and $\frac{24.6}{16.4}$ = 1.50 respectively. A recession ratio of between 1.50 and 1.84 favours the N-values of 11,21, and 33 for Holograms 28,30,31 as being a marginally better fit then N = 13,25,37. See footnote*

The three solid curves in Fig. 86 are the mean recession values of the LH and RH halves of each of Holograms 28,30, and 31 for these chosen N values. The dotted curves envelop all the individual LH and RH curves for the three holograms at these N values. The graph in Fig. 87 is drawn, using equation 8 relating the mass transfer coefficient to the recession, from the mean of the recession curves in Fig. 86 . The dotted curves in this diagram correspond to the dotted curves in Fig. 86 .

* (a) for N = 11, 21, 33 the recession ratios for holograms 28, 30, 31 are

$$\frac{16{\cdot}8}{12{\cdot}1} = 1{\cdot}39 \; ; \quad \frac{31{\cdot}4}{23{\cdot}8} = 1{\cdot}32 \; ; \quad \frac{47{\cdot}7}{37{\cdot}8} = 1{\cdot}26.$$

(b) for N = 13, 25, 37 the recession ratios for holograms 28, 30, 31 are

$$\frac{18{\cdot}6}{14{\cdot}5} = 1{\cdot}28 \; ; \quad \frac{35{\cdot}4}{28{\cdot}1} = 1{\cdot}26 \qquad \frac{34{\cdot}8}{28{\cdot}1} = 1{\cdot}24.$$

The series (a) is marginally better supported than (b) by the high ratios found for hologram 27, although this conclusion is arguable.

TABLE 7.

	N	N'/f		% max. difference
		x = 2.5	x = 4.6	
holo.27	1	4.0	13.7	20
	3	10.4	19.1	17
	5	16.4	24.6	16
holo.28	11	12.1	16.8	6.8
	13	14.5	18.6	7.2
	15	16.5	20.7	7.5
	17	18.6	22.6	7.2
holo.30	21	11.9	15.7	10.9
	23	12.9	16.7	7.3
	27	15.3	18.8	4.8
	29	16.3	19.6	2.2
	31	17.5	20.6	2.6
	33	18.5	21.8	3.0
	35	19.6	22.8	3.1
holo.31	33	12.6	15.9	3.0
	35	13.3	16.7	3.1
	43	16.3	19.5	3.8

This table shows the mean values of N'/f per 45 secs. at two radii, for various N values, for the purpose of comparing (a) the ratio of the recession at a point near the centre and the recession at a point near the perimeter, and (b) the maximum difference between the LH and RH curves. The figures are taken from Figs. 85A - 85D.

TABLE 8.

	holo. 28	holo. 30	holo. 31
x	N'/f	N'/f ÷ 2	N'/f ÷ 3
1.5		11.5	12.3
2.0		11.7	12.4
2.5	12.1	11.9	12.6
3.5	13.3	12.6	13.3
4.0	14.4	13.4	14.0
4.5	16.3	15.0	15.6
4.75	17.7	17.0	

These figures are taken from Figs. 85B, 85C, 85D, and are the mean values of N'/f per 45 seconds for the best fit RH - LH pair of curves. The graph in Fig. 86 is drawn from this table.

TABLE 9.

x	N'/f	k x 10^2 m/sec.
1.5	11.7	18.8
2.0	11.9	19.1
2.5	12.2	19.6
3.0	12.6	20.3
3.5	13.1	21.1
4.0	13.9	22.4
4.5	15.7	25.3
4.75	17.4	28.0

These figures are taken from the mean of the three curves on the graph in Fig. 86. The graph in Fig. 87 is drawn

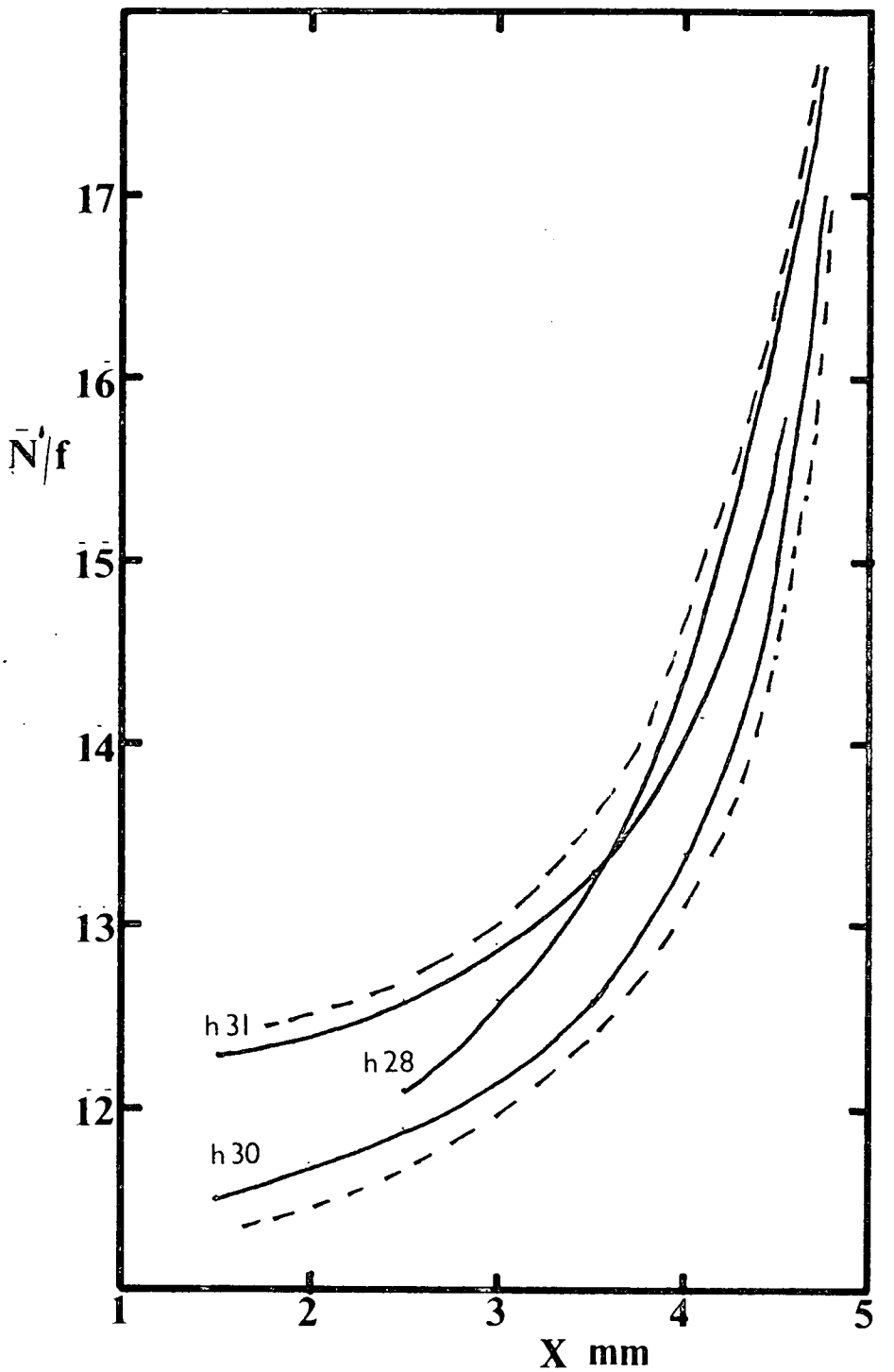

Fig.86. Comparison of recession versus radius for different mass-transfer durations.

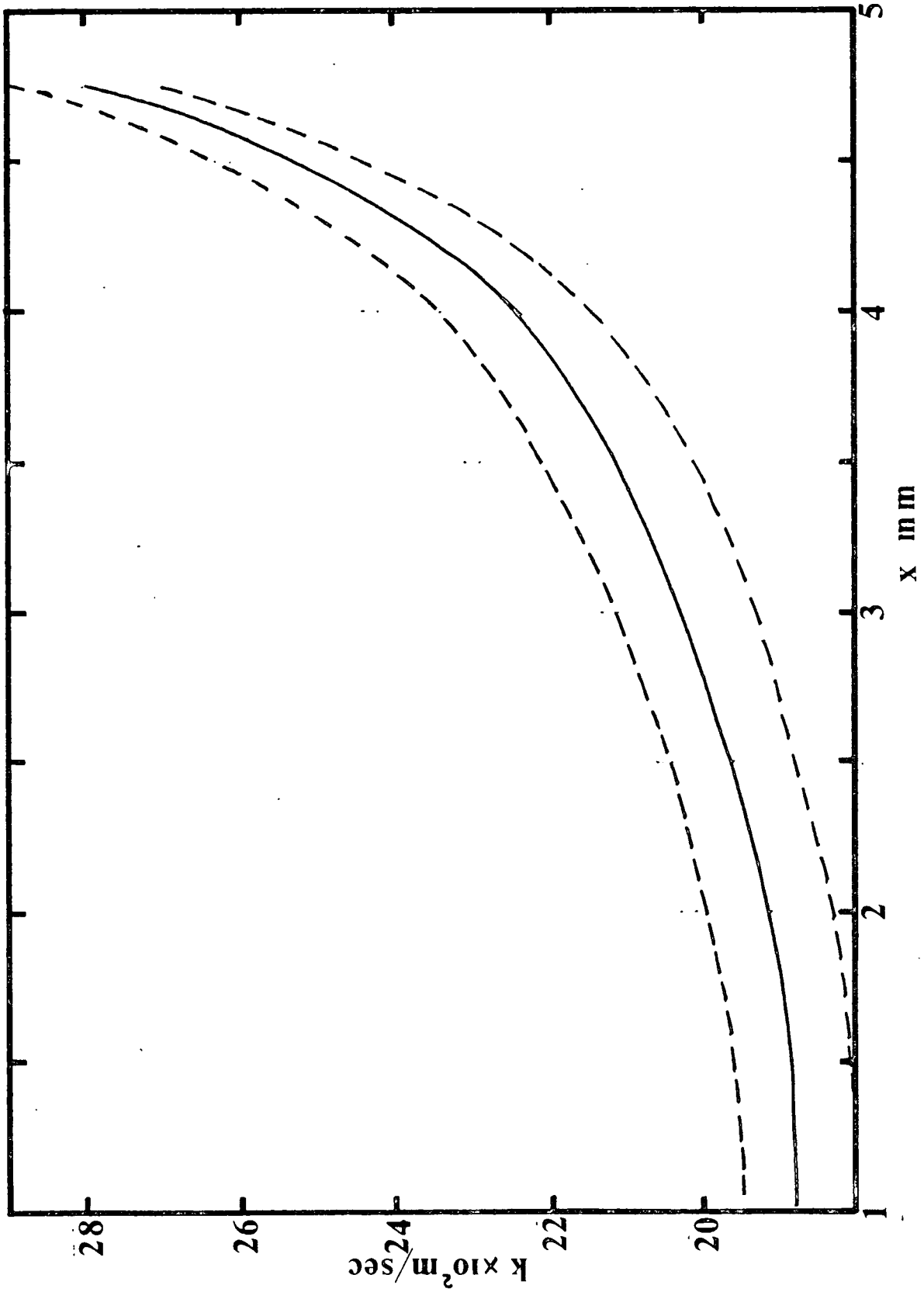

Fig.87. Mass transfer coefficient versus radius for the convex disc.
Re. No. 6100.

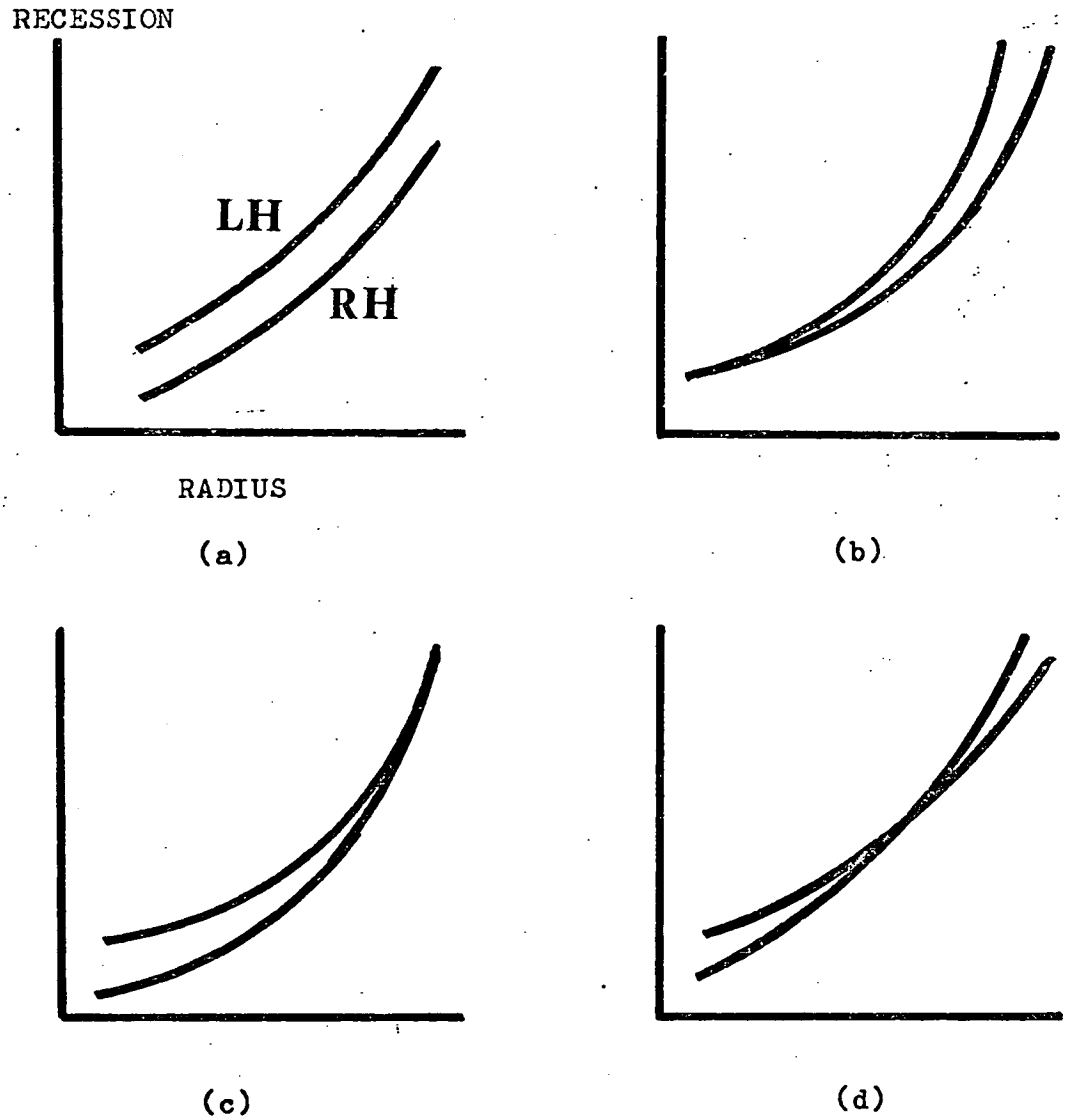

Fig.88. Characteristic recession curves.

6.4 Possible sources of error giving rise to the LH-RH symmetry.

(1) Measurement of the position of the components on the optical table.

The positions of the disc centre, the pinhole in the beam expander, and the camera film are measured to calculate values of cosi and f in equations 6 and 7. The measurements were made by projecting the disc centre, pinhole and holographic plate downwards, by eye, onto the optical table, marking with chalk, and measuring between the chalk marks. This procedure is tricky because the components are bunched closely together. The point of convergence is deduced from the film position and the developed enlargement on the negative.

The equations for cosi and f were tested for undue parameter sensitivity by increasing a variety of values of q, R, s' by 1% and noting the resulting change in cosi and f. In all cases the change was $\leq 1\%$.

(2) Measurement of the fringe position.

The position of the dark fringes was taken as the centre of the fringe band. For wide fringes near the centre, this position is sometimes not clear. For longer duration experiments, the fringes are "bumpy" curves (Fig. 76). Errors in the fringe positions would not give rise to lack of superposition of the LH-RH curves.

(3) Repositioning of holographic plates for photographing.

The plates were repositioned in the grooved holder by eye after developing; since the fringes are not localised, an error here could cause the lack of superposition in the curves.

(4) Gross variation in the polymer coating thickness.

This is unlikely as the polymer was allowed to cure on the disc while its front surface was horizontal, i.e. the gradual flow of the curing polymer under gravity would be symmetrical about the disc axis.

(5) Positioning of camera perpendicular to plate, and of plate perpendicular to disc.

This was done by eye, and errors here would give rise to the asymmetry seen in the graphs. Again because the fringes are not localised, a misalignment of the camera in either the horizontal or vertical plane alters the position of the fringes, in a systematic manner.

(6) Start-up and shut-down errors.

Such errors could not appear as LH-RH asymmetry, but would affect the comparison of the curves for different durations.

Conclusion: the most likely cause of the LH-RH asymmetry in this method is the repositioning of the plate, and the positioning of the camera, when photographing the fringes.

CHAPTER 7

The determination of mass transfer coefficients on the stagnation point flow chamber.

7.1 Design of experiments

Purpose: The experiments are to determine the mass transfer coefficients in the central area, and behind the triangular struts and surface imperfections, of Petschek's stagnation point flow chamber. The blood flow chamber is approximated by two parallel plates with a central impinging jet. The circumferential flow exit part of the apparatus is not replicated; instead the plates are made large enough to prevent the discharge of fluid to the atmosphere affecting the central area of interest.

Method: The holographic interferometric frozen-fringe method for the K-value determination is that described by Kapur (105), of which the method used for the convex disc in the preceding chapters is a development.

Scale-up: The apparatus was scaled-up to make the holographic technique easier, and air was used as the working fluid to simplify the experiments. Kapur (105) has shown that the variation of mass transfer coefficients on single flat plates subjected to a central impinging jet is not sensitive to variation in Sc. No., thus the scaling up and use of different working fluid should give reliable information, since the flow regime between the parallel plates is very similar to that over a single plate.

The dimensions are scaled up by 5.33 (chosen because of availability of entrance pipe diameter). The working fluid is air. Since the Re. No. must be preserved, the flow rate must be altered.

Petschek's flow rate is 2 ml./min blood, with a haematocrit of 39.3 ± 5.8 (43) to 43.7 ± 4.4 (48). The viscosity of blood depends on the haematocrit; Huckaba and Hahn (71) give a figure of 4-5 c.p. for haematocrit 40-45%; and they also give 1.05 x 10^3 kg/m^3 for the density. Therefore, 4.5 c.p. will be taken as the viscosity.

$$Re = \frac{4 \rho G}{\pi d \mu}$$ where G = volumetric flow rate.

ρ_{AIR} = 1.185 kg./m^3

μ_{AIR} = .0175 c.p.

Re. No. of blood flow = .33.

Air flow rate required is 36.8 ml./min, based on entrance pipe diameter. In the subsequent analyses, x represents the measured diameter of the fringes, divided by scale factor 5.33.

Equipment Petschek's five sizes of flow chambers, scaled up by 5.33, have the following dimensions:

HOLE DIAM. (m.m.)	PLATE SEPARATION (m.m.)	RE. No.	EXPT. SERIES No.
6.40	0.53	.083	1 and 'A'
8.53	1.07	.62	2
13.33	1.65	.40	3
15.47	3.68	.34	4
15.47	10.13	.34	5
Entrance pipe 16 m.m.		.33.	

Square plates were used instead of circular, due to availability. Surface imperfections were simulated by protruding steel pins. The spacing of the plates was gauged by pre-set stops fixed to the optical table, and the alignment was gauged by clamping the entrance pipe to a V-block which could be slid along a pre-set, fixed rail. After taking the first holographic exposure (Fig. 94), the second plate containing the impinging jet is placed parallel, and the rotameter-controlled airflow started (Fig. 95). The holographic plates were developed by the standard technique (105). The polymer coating is RTV602 and the swelling agent is methyl salicylate. The holes which can be seen at the corners of the second plate are incidental.

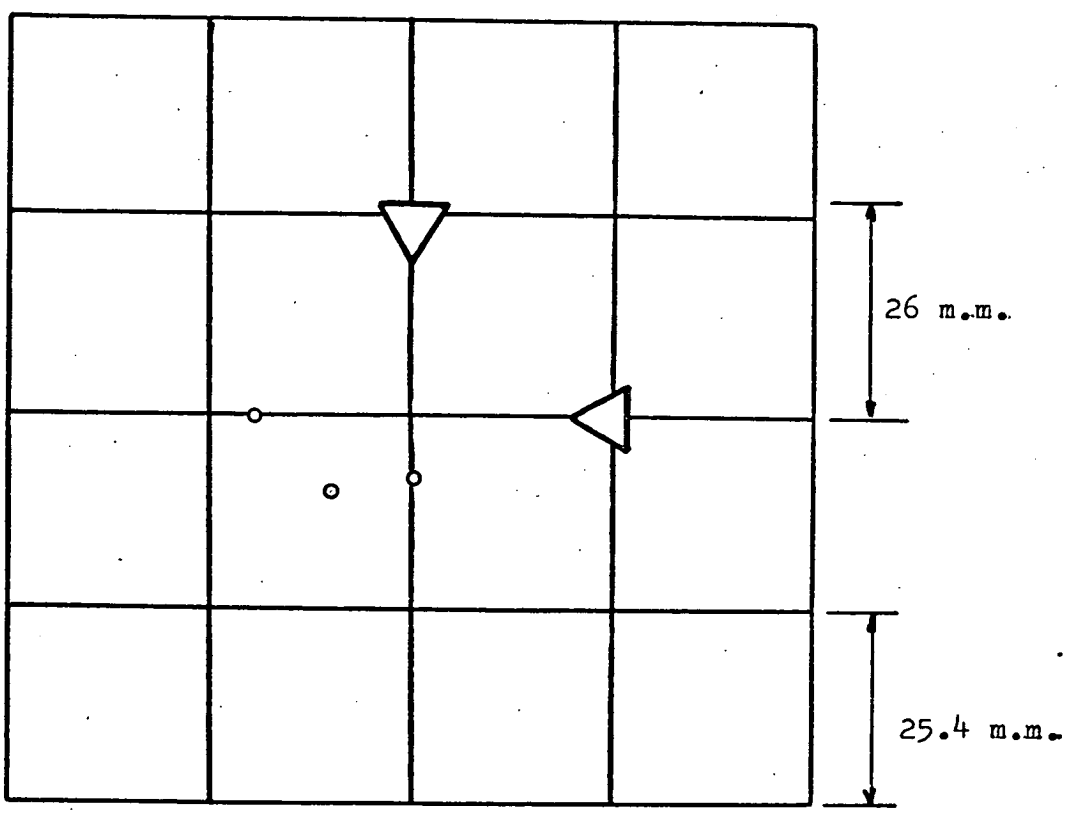

Fig. 90. Central area of mass transfer plate. Triangular struts are 8 m.m. side, simulated surface imperfections are 8, 14 and 20 m.m. from the centre.

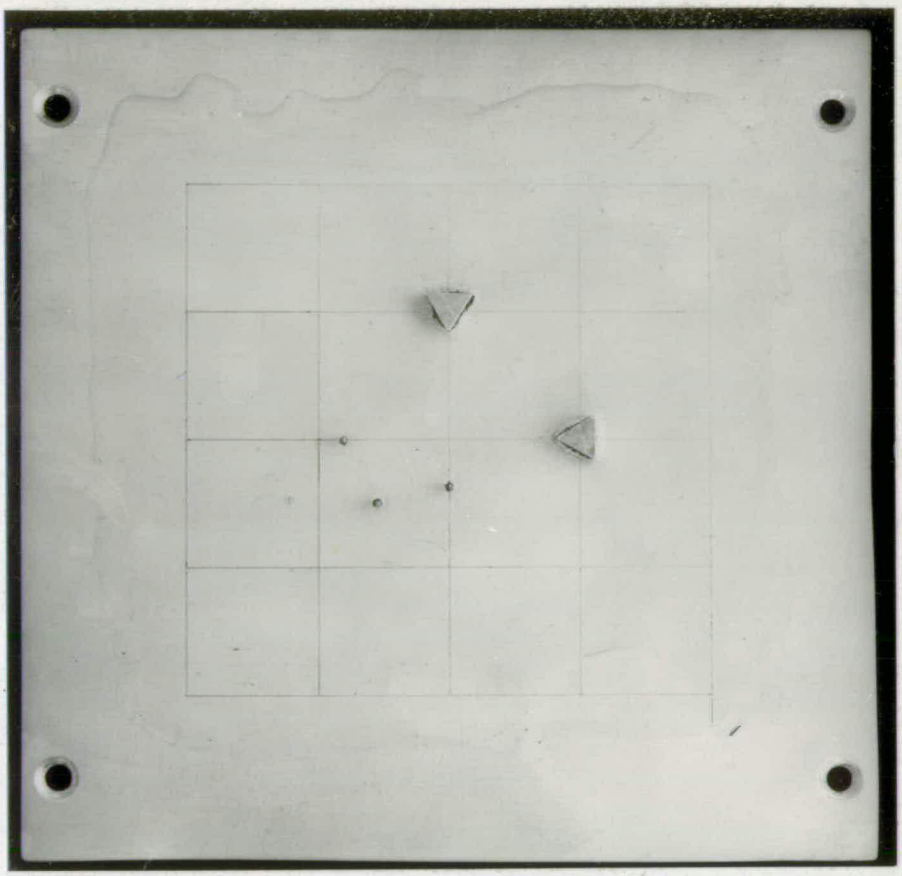

Fig.91. The polymer-coated mass transfer plate with projections added.

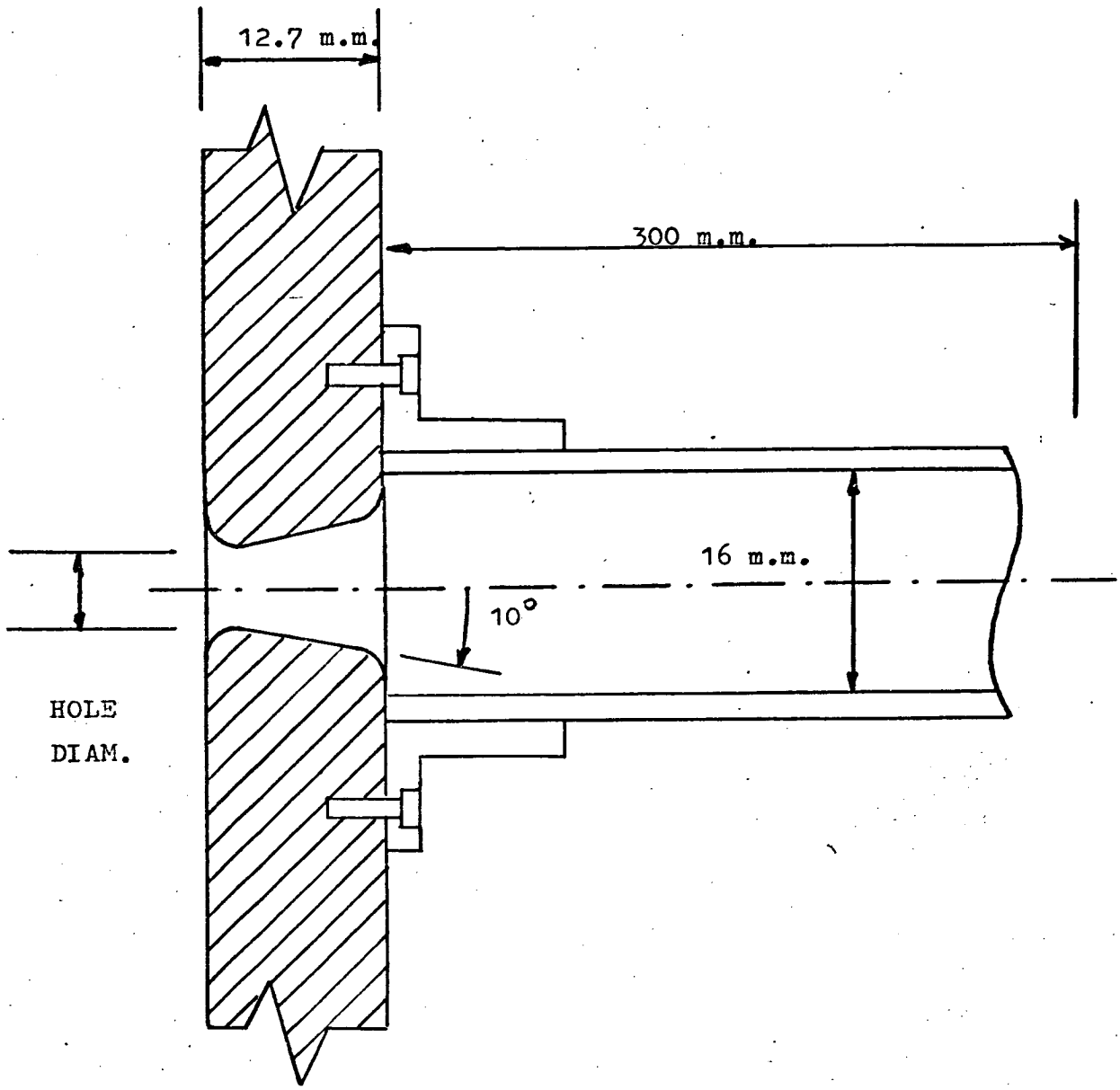

Fig. 92. Details of the central jet.

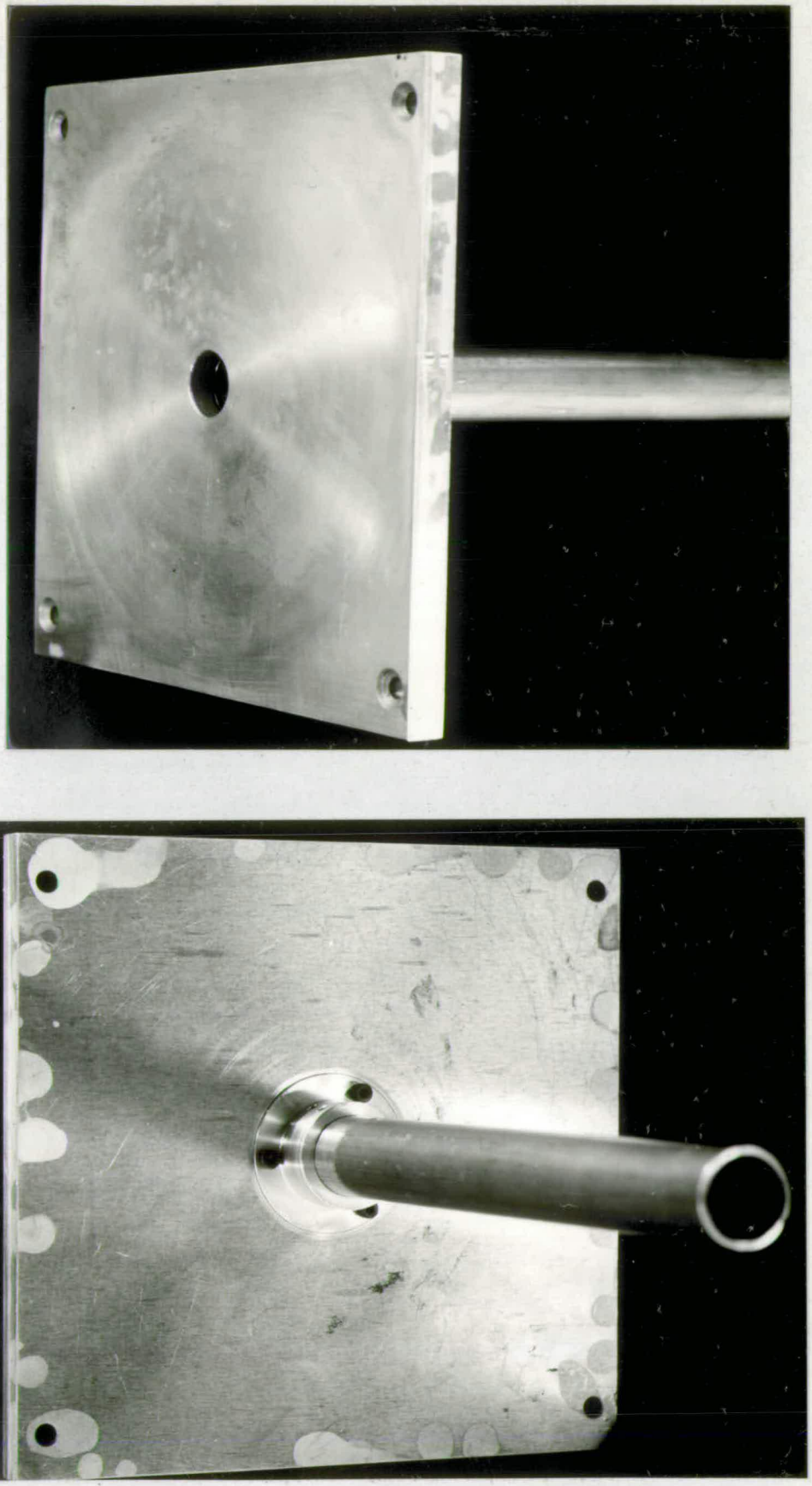

Fig.93. Two views of the parallel plate with central jet.

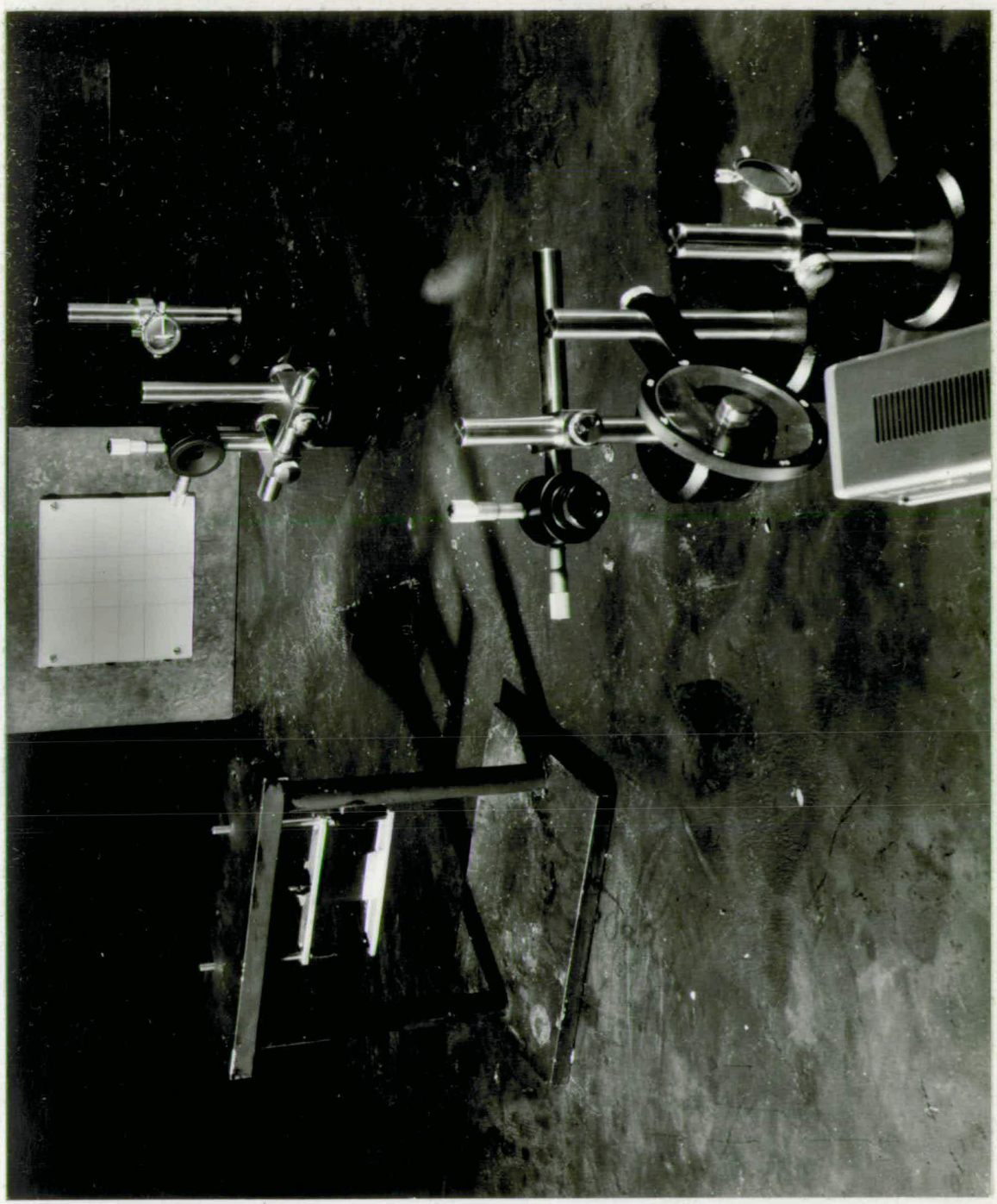

Fig.94. The arrangement of the optical table for the first exposure of the simulated blood flow chamber.

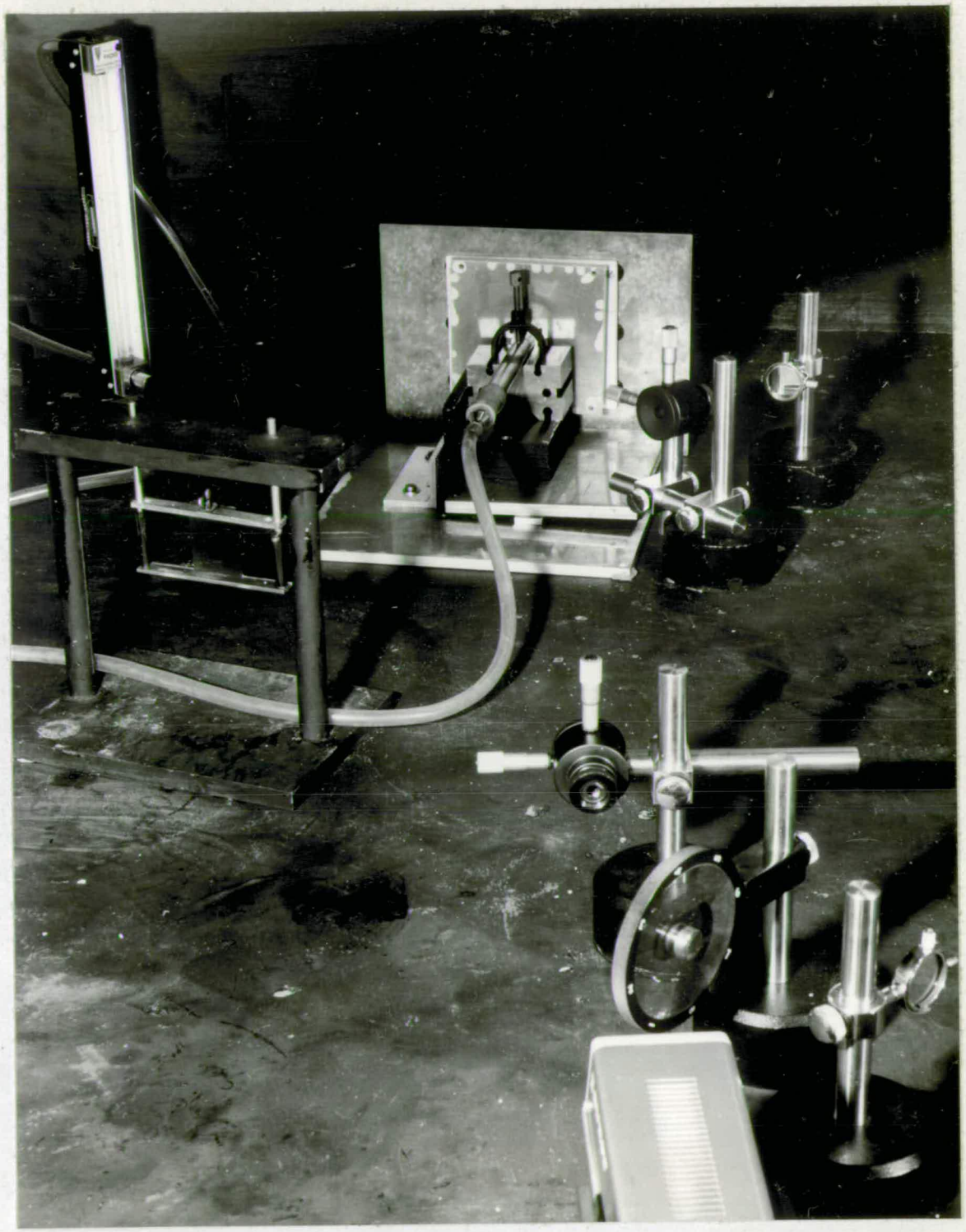

Fig.95. The airflow apparatus in position on the optical table.

7.2 Fringe Patterns

Eight series of photographs of fringe patterns are shown. Series 1-5 correspond to the five sizes of flow chamber. Series 'A' uses the same flow chamber as Series 1, but a different swelling agent. Series 'B' demonstrates the formation of wake patterns behind struts and imperfections, and Series 'C' shows the effect of natural convection and the improved fringe quality at high Re. No.'s, for comparison.

SERIES A:

Jet diam: 6.4 m.m. Plate separation: 0.5 m.m.

Swelling agent: iso-butyl benzoate. Airflow: 37.5 ml/min.

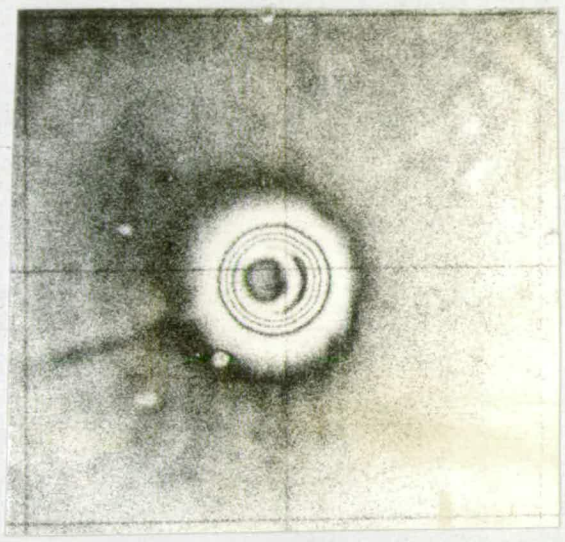

Fig. 96. Holo. 1. 19 min.

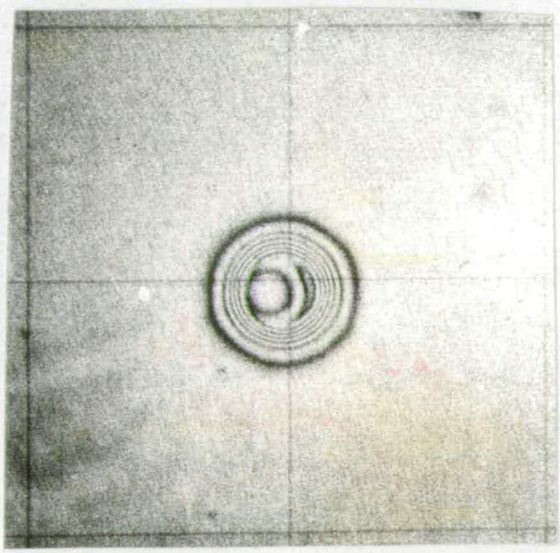

Fig. 97. Holo. 2. 32 min.

SERIES 1.

Jet diam: 6.4 m.m. Plate separation: 0.5 m.m.

Swelling agent: methyl salicylate. Airflow: 37.5 ml/min.

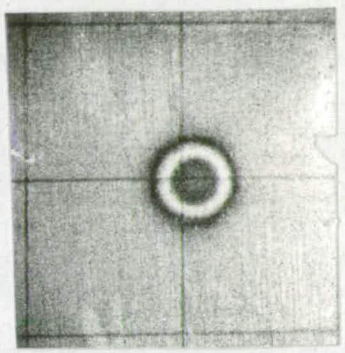

Fig. 98. Holo. 5. 1 min.

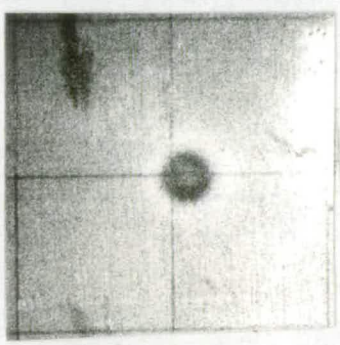

Fig. 99. Holo 6. 2 min.

SERIES 1 (cont.)

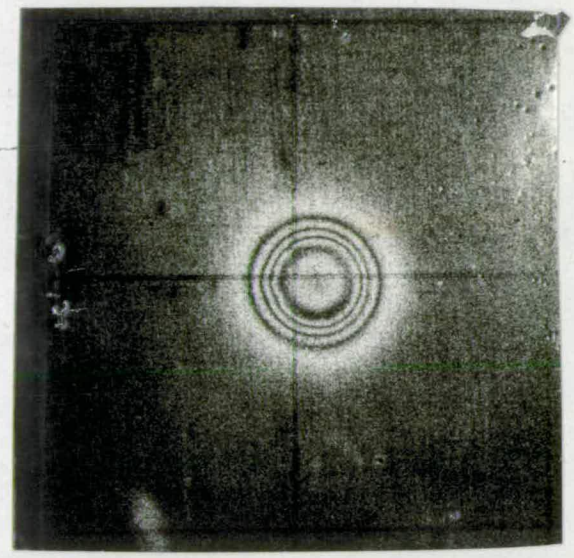

Fig. 100. Holo. 7. 5 min.

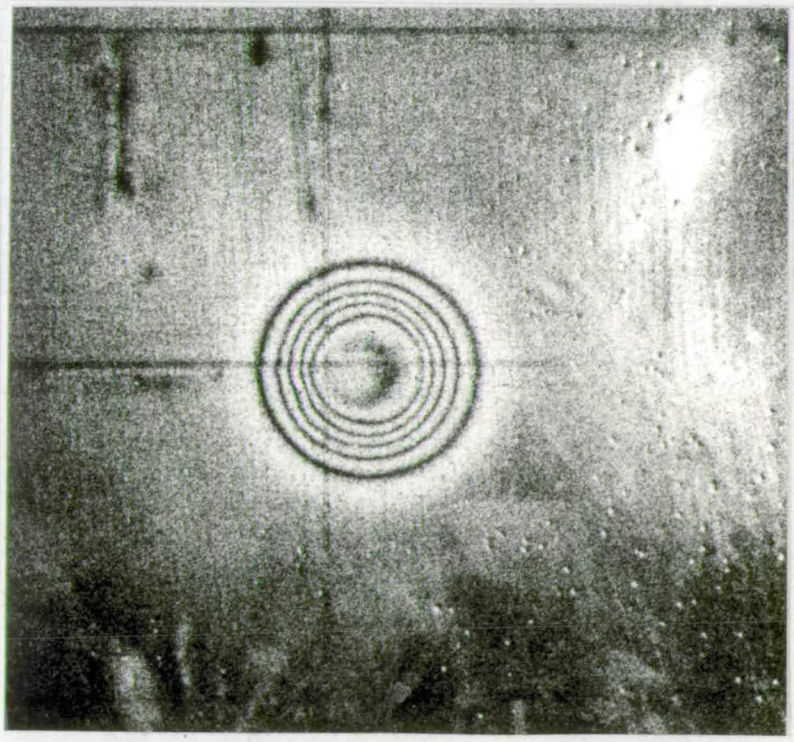

Fog. 101. Holo. 8. 10 min.

SERIES 1 (cont.)

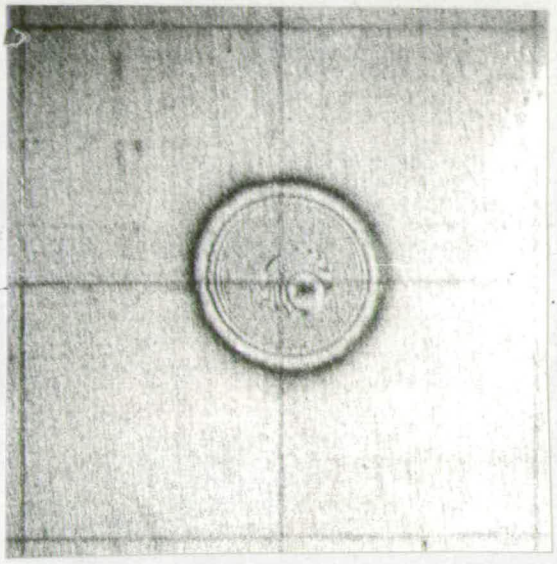

Fig. 102. Holo. 9. 25 min.

SERIES 2.

Jet diam: 8.5 m.m. Plate separation: 1.1 m.m.

Swelling agent: methyl salicylate. Airflow: 37.5 ml/min.

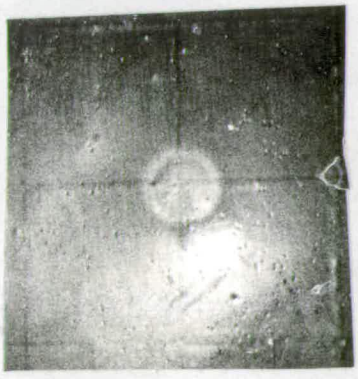

Fig. 103. Holo 10. 1 min.

SERIES 2 (cont.)

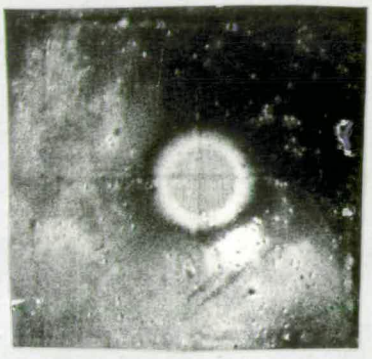

Fig. 104. Holo 11. 2 min.

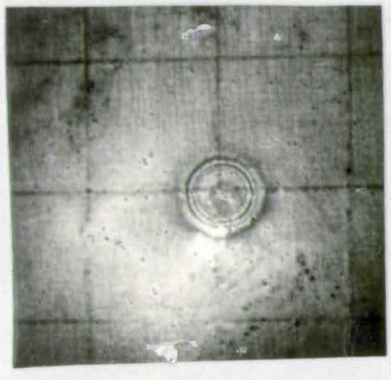

Fig. 105. Holo 12. 5 min.

SERIES 2 (cont.)

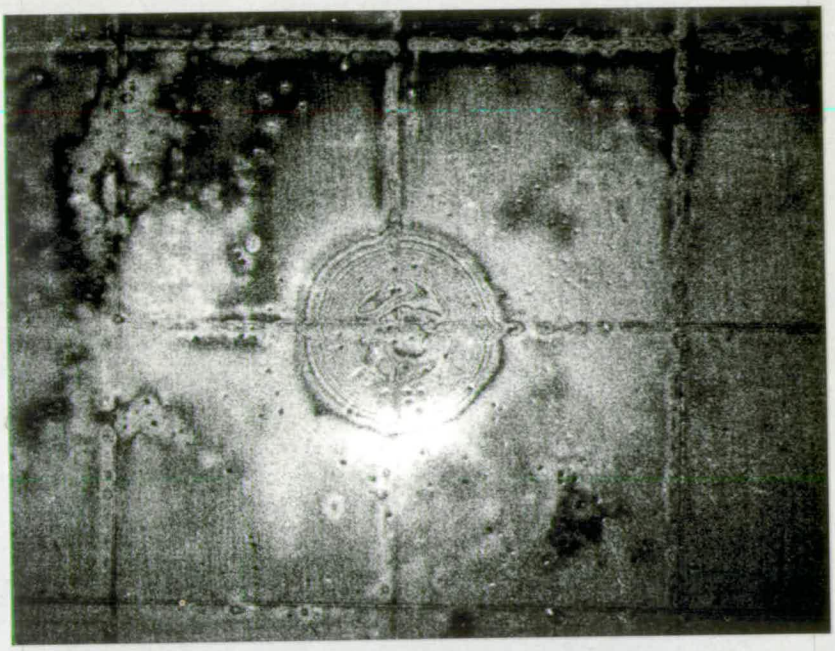

Fig 106. Holo. 13. 15 min.

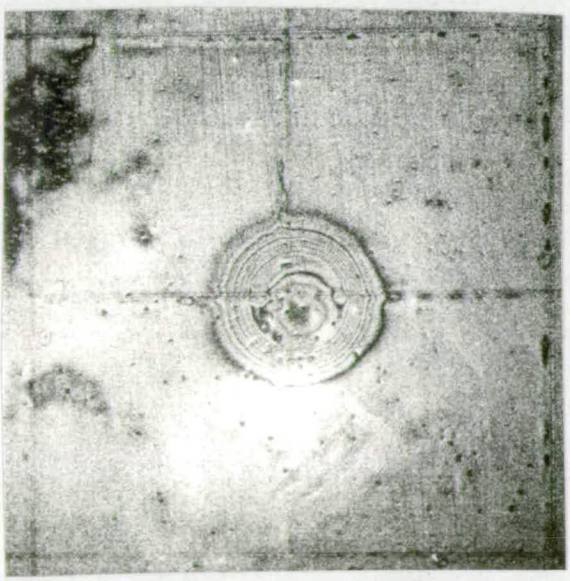

Fig. 107. Holo. 14. 25 min.

SERIES 3.

Jet diam: 13.3 m.m. Plate separation: 1.65 m.m.

Swelling agent: methyl salicylate. Airflow: 37.5 ml/min.

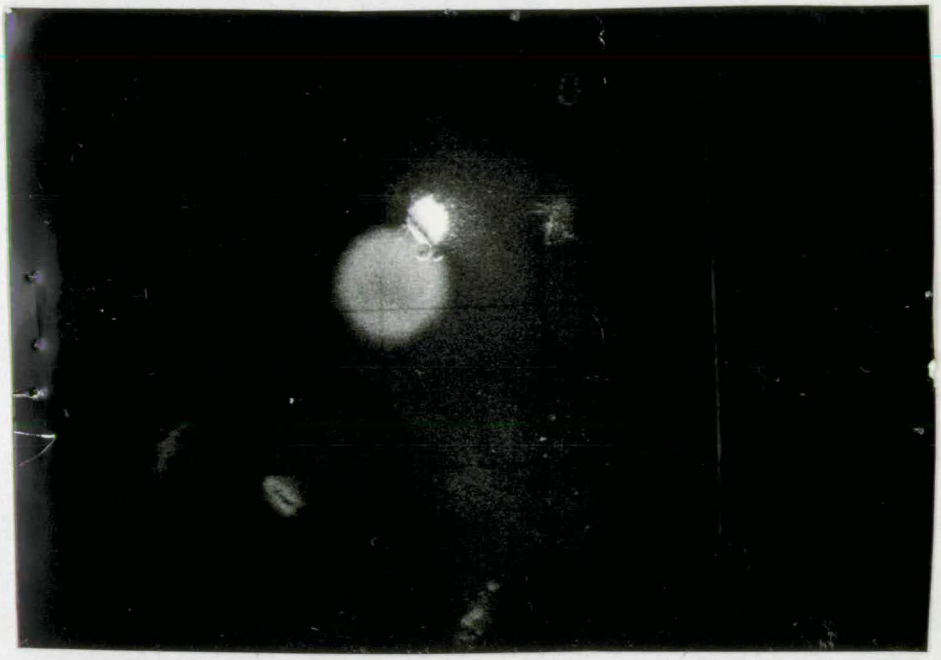

Fig. 108. Holo. 18. 2 min.

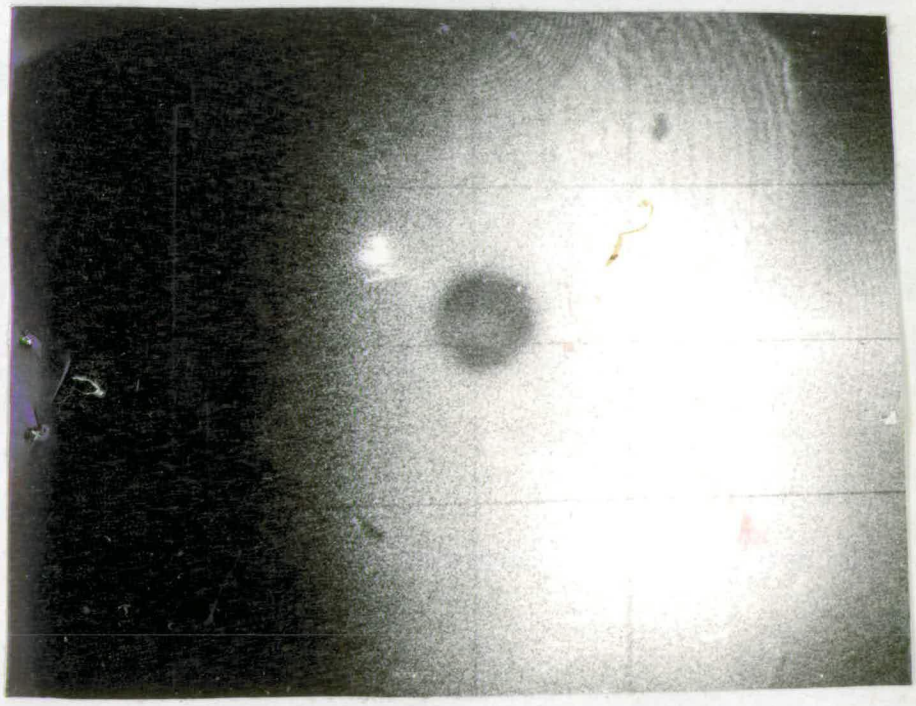

Fig. 109. This photograph of Holo. 18. is taken with the camera a few degrees off centre. This non-localisation is most pronounced with low order fringes.

SERIES 3 (cont.)

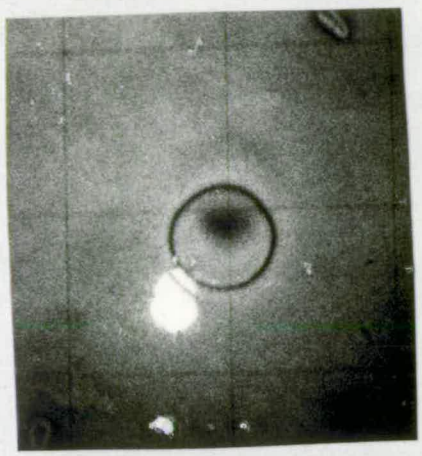

Fig. 110. Holo. 19. 6 min.

Fig. 111. Holo. 20. 8 min.

SERIES 3 (cont.)

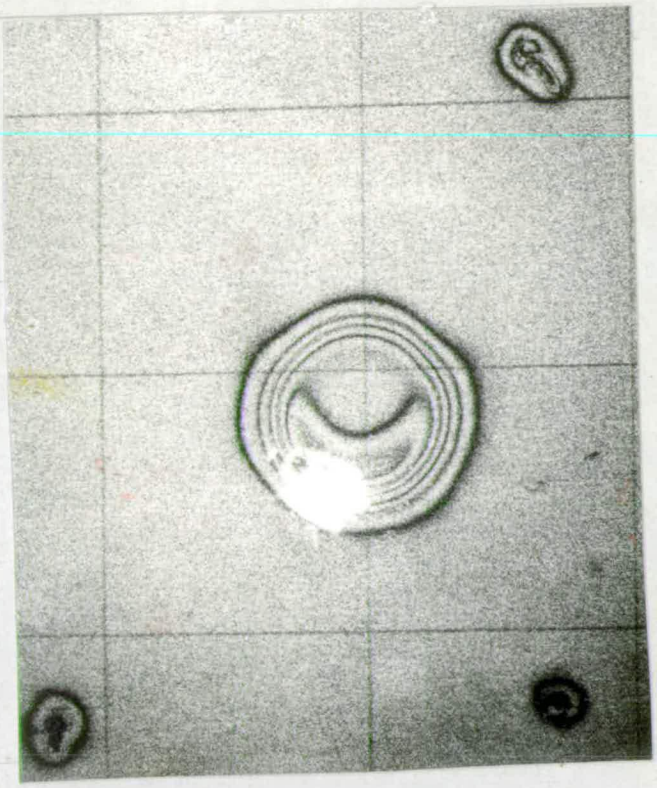

Fig. 112. Holo 21. 26 min.

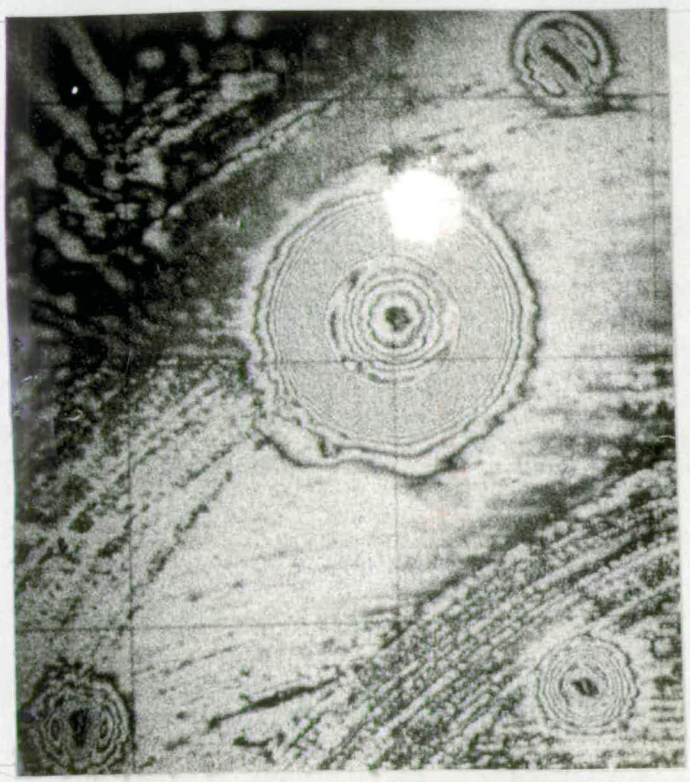

Fig. 113. Holo. 15. 119 min.

SERIES 3 (cont.)

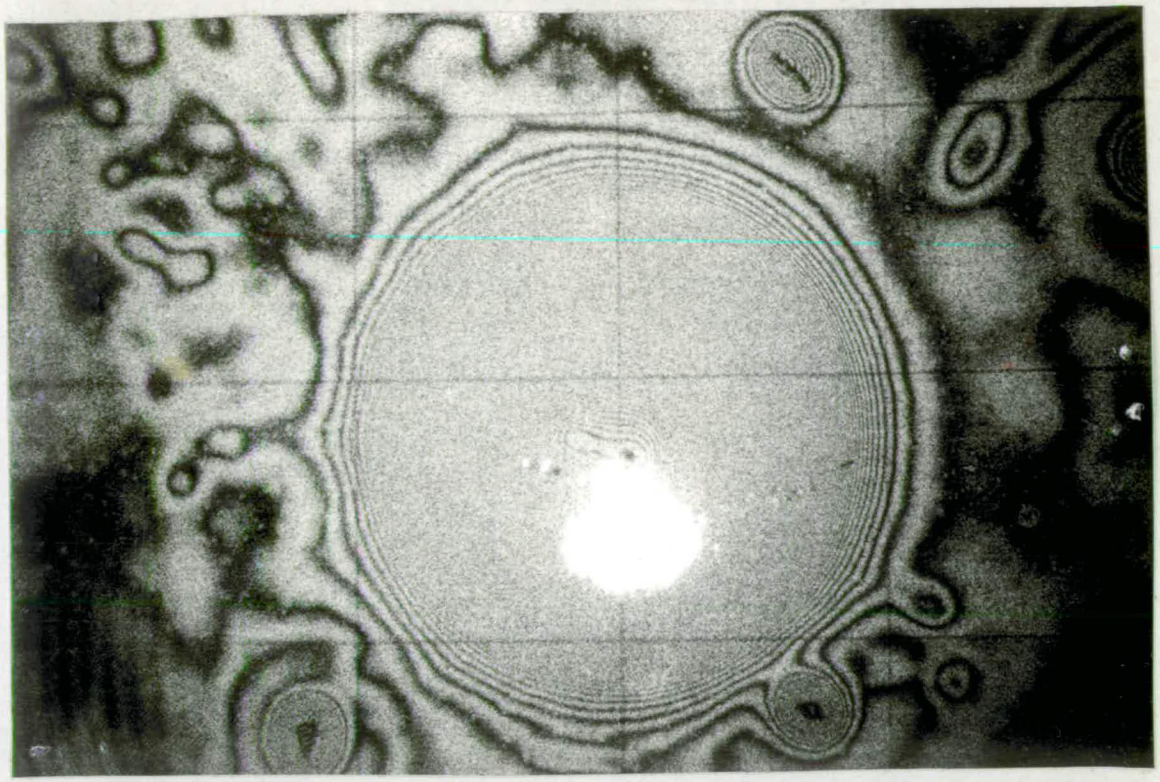

Fig. 114. Holo. 23. 41 hr. 32 min.

SERIES 4.

Jet diam: 15.5 m.m. Plate separation: 3.7 m.m.

Swelling agent: methyl salicylate. Airflow: 37.5 ml/min.

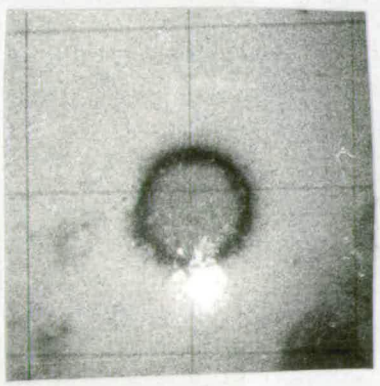

Fig. 115. Holo. 29. 7 min.

SERIES 4 (cont.)

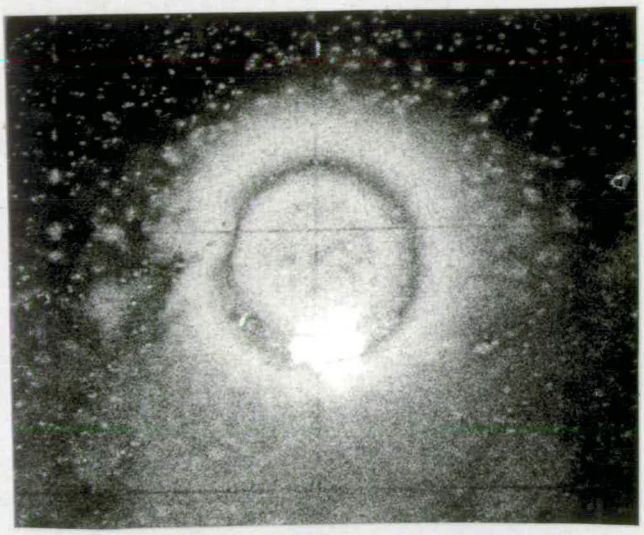

Fig. 116. Holo 30. 15 min.

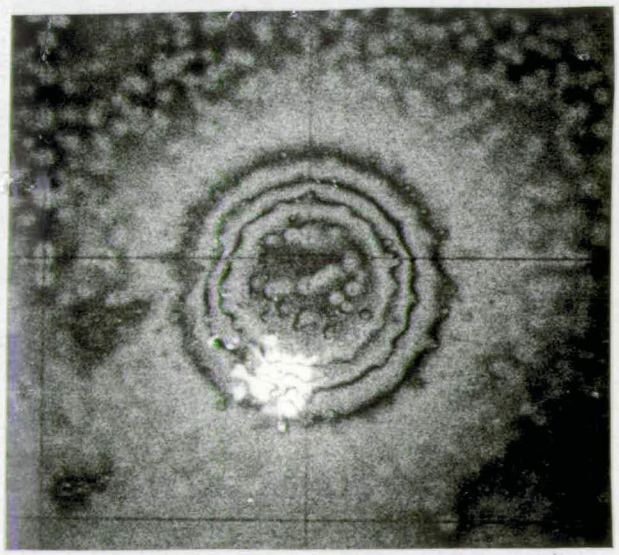

Fig. 117. Holo. 31. 37 min.

SERIES 4 (cont.)

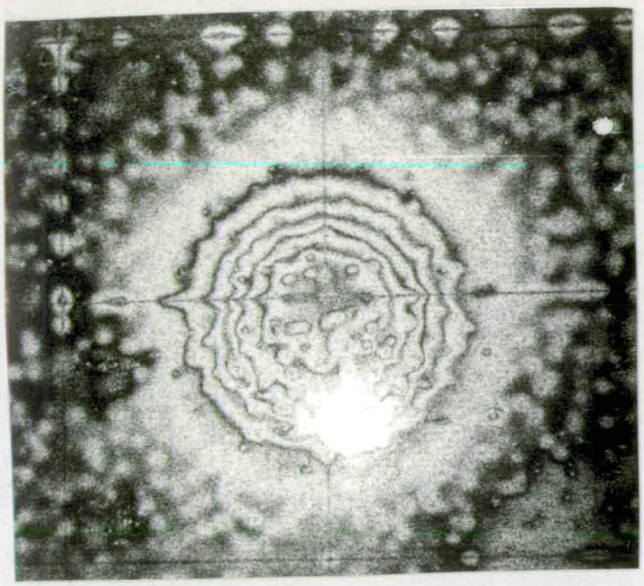

Fig. 118. Holo. 32. 55 min.

SERIES 5.

Jet diam: 15.5 m.m. Plate separation: 10.1 m.m.

Swelling agent: methyl salicylate. Airflow: 37.5 ml/min.

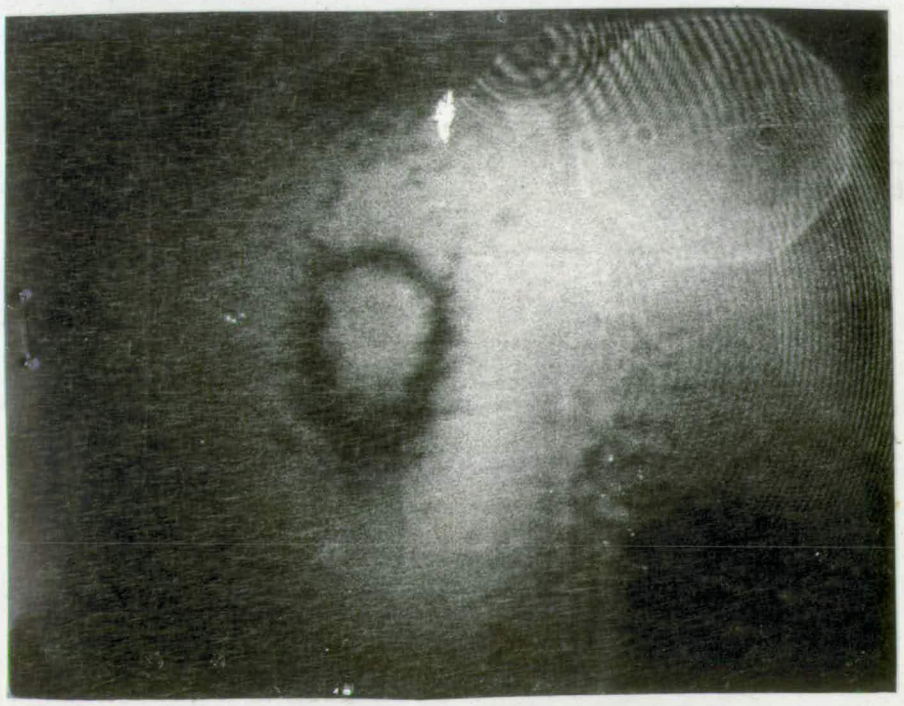

Fig. 119. Holo. 34. 39 min.

SERIES 5 (cont.)

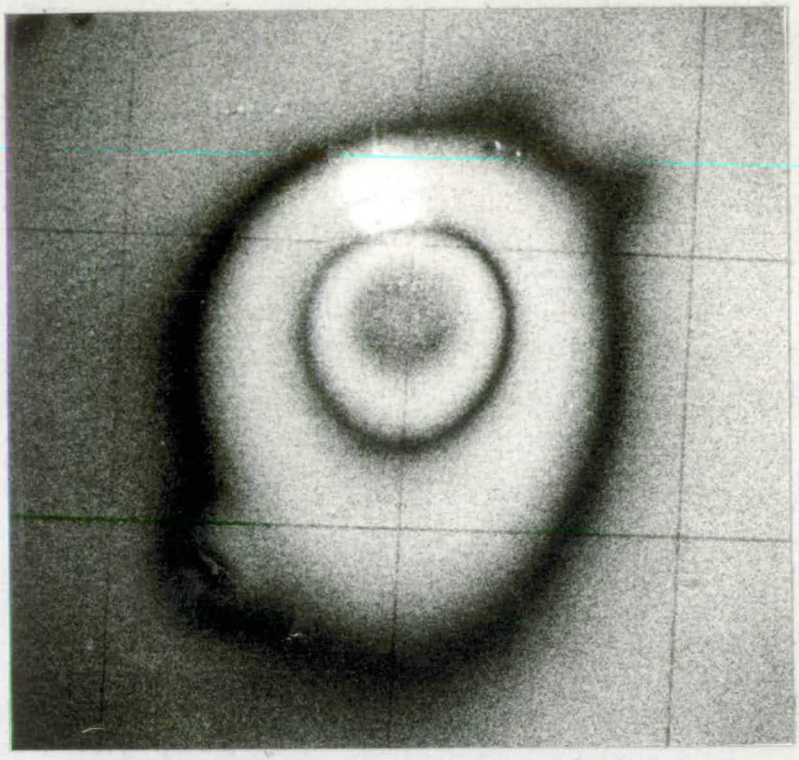

Fig. 120. Holo. 40. 56 min.

SERIES 5 (cont.)

Fig. 121. Holo. 38. 3 hr. 25 min.

SERIES 5 (cont.)

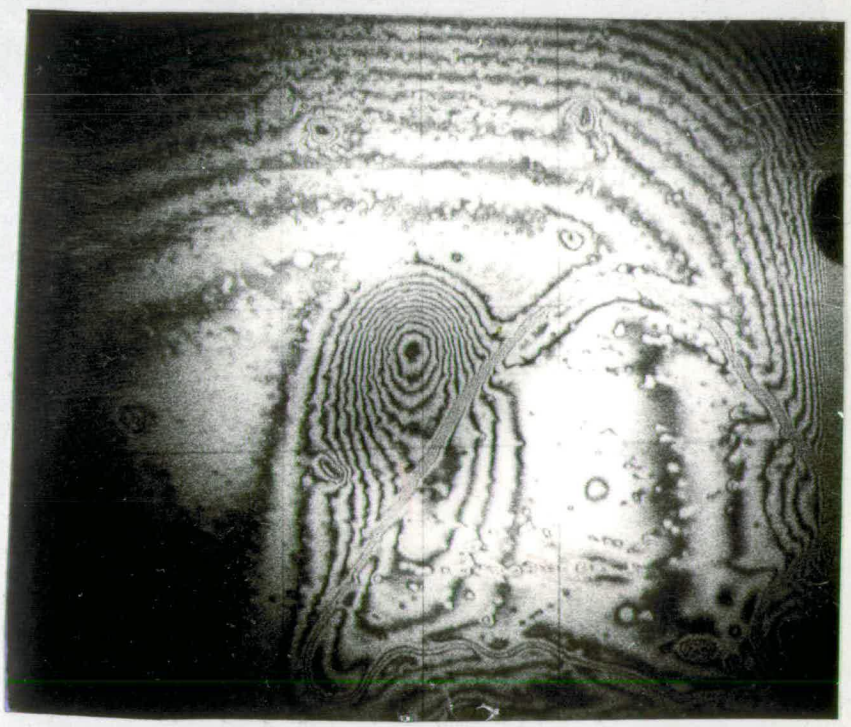

Fig. 122. Holo. 36. 4 hr. 55 min.

SERIES 5 (cont.)

Fig. 123. Holo. 37. 14 hr. 52 min.

SERIES B. Swelling agent: methyl salicylate.

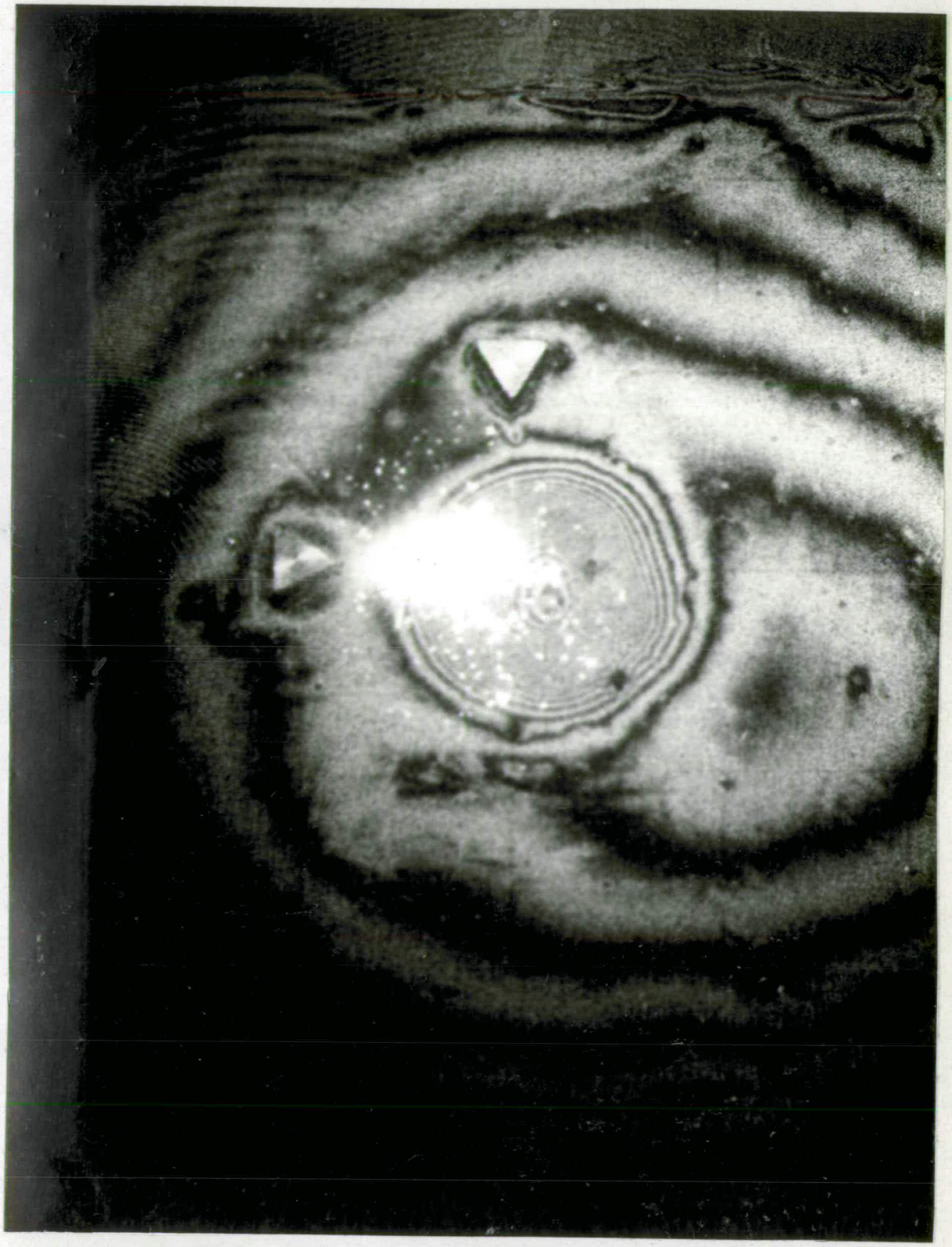

Fig. 124. Holo. 35. 3 hr. 45 min.

Jet diam: 15.5 m.m. Plate separation: 3 m.m. Airflow 37.5 ml/min.

SERIES B (cont.)

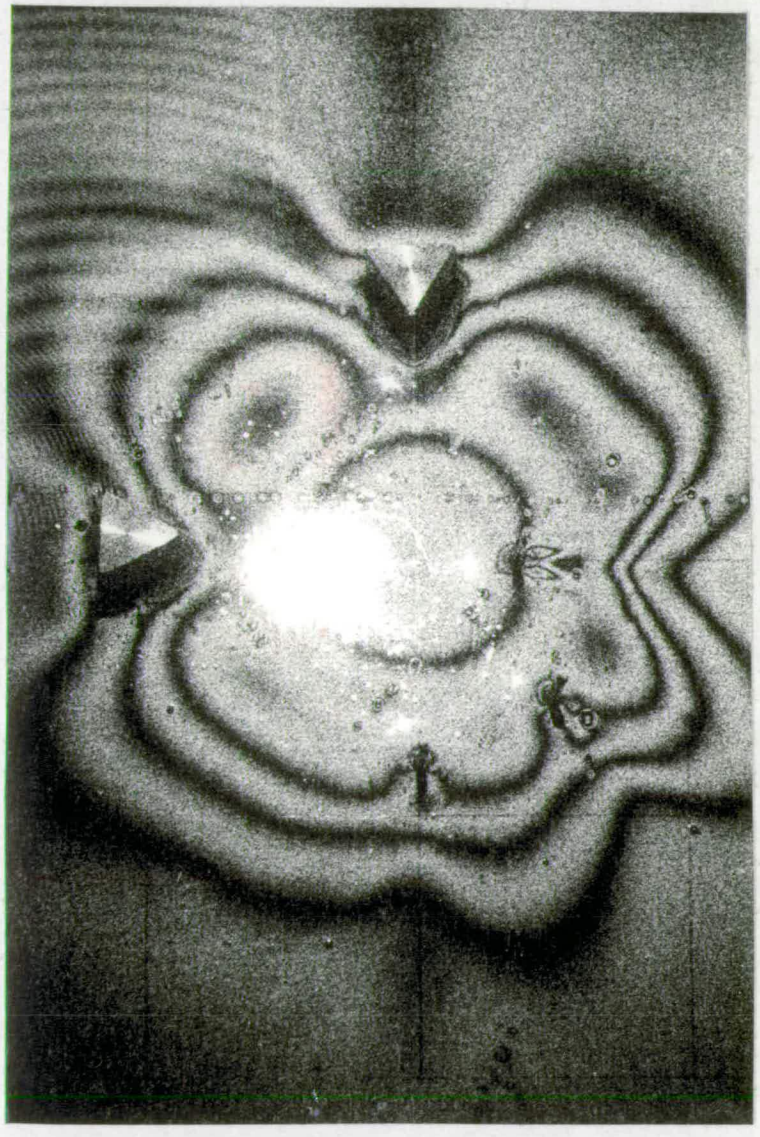

Fig. 125. Holo. 25. 2 min.

Jet diam 13.3 m.m. Plate separation 10.1 m.m. Airflow 75 L /min.

SERIES B (cont.)

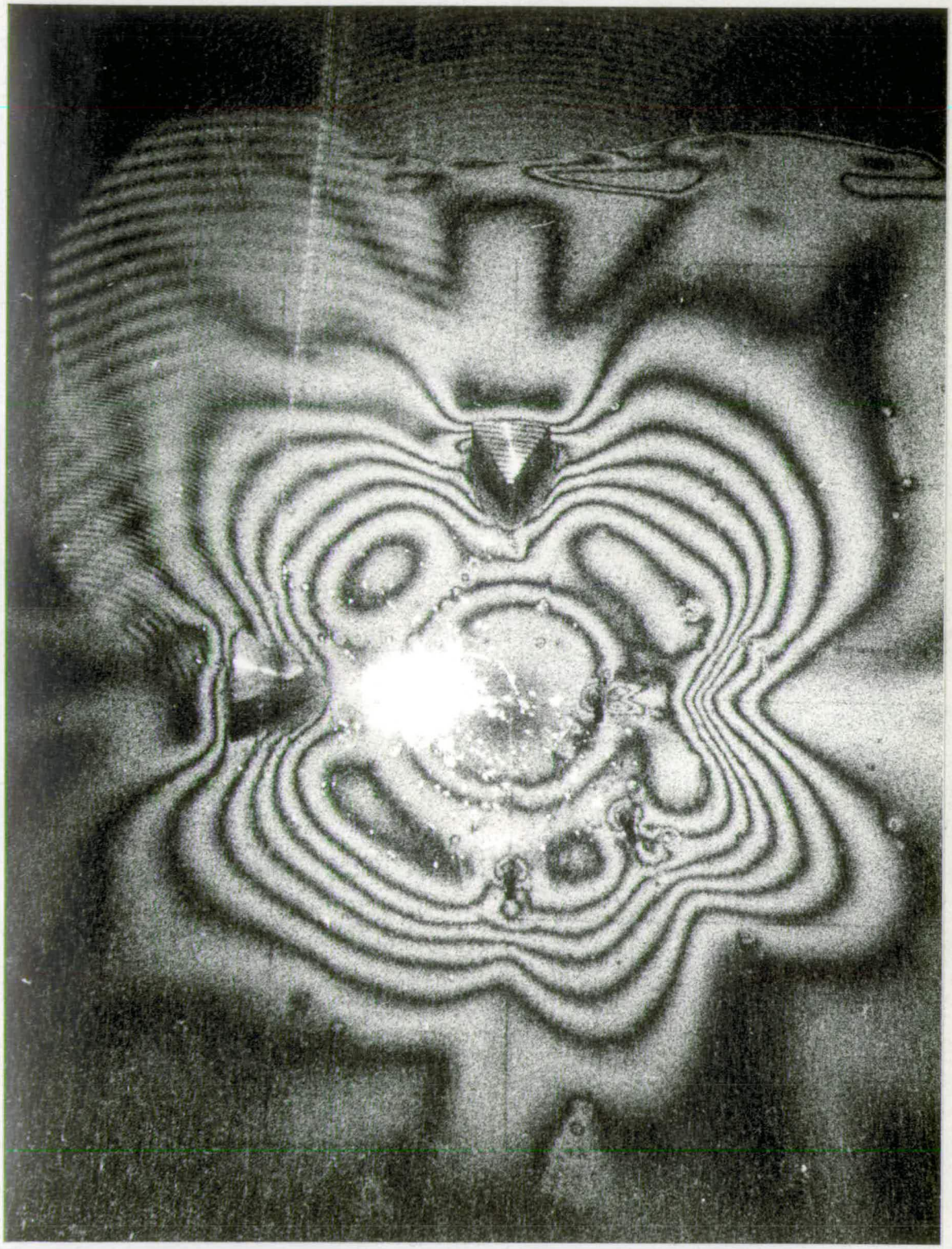

Fig. 126. Holo. 27. 5 min.

Jet diam 13.3 m.m. Plate separation 10.1 m.m. Airflow 75L /min.

SERIES B (cont.)

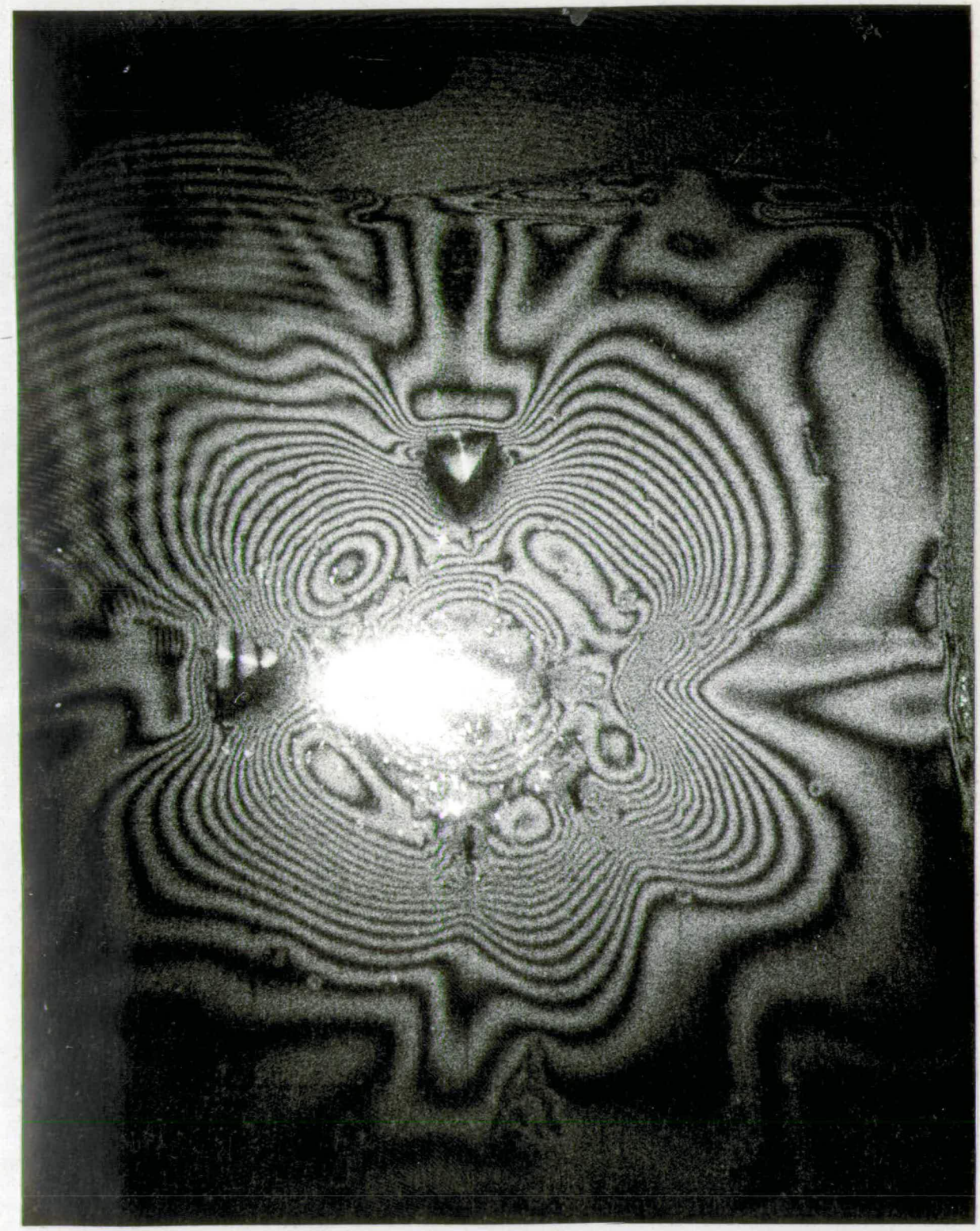

Fig. 127. Holo. 26. 11 min.

Jet diam 13.3 m.m. Plate separation 10.1 m.m. Airflow 75l/min.

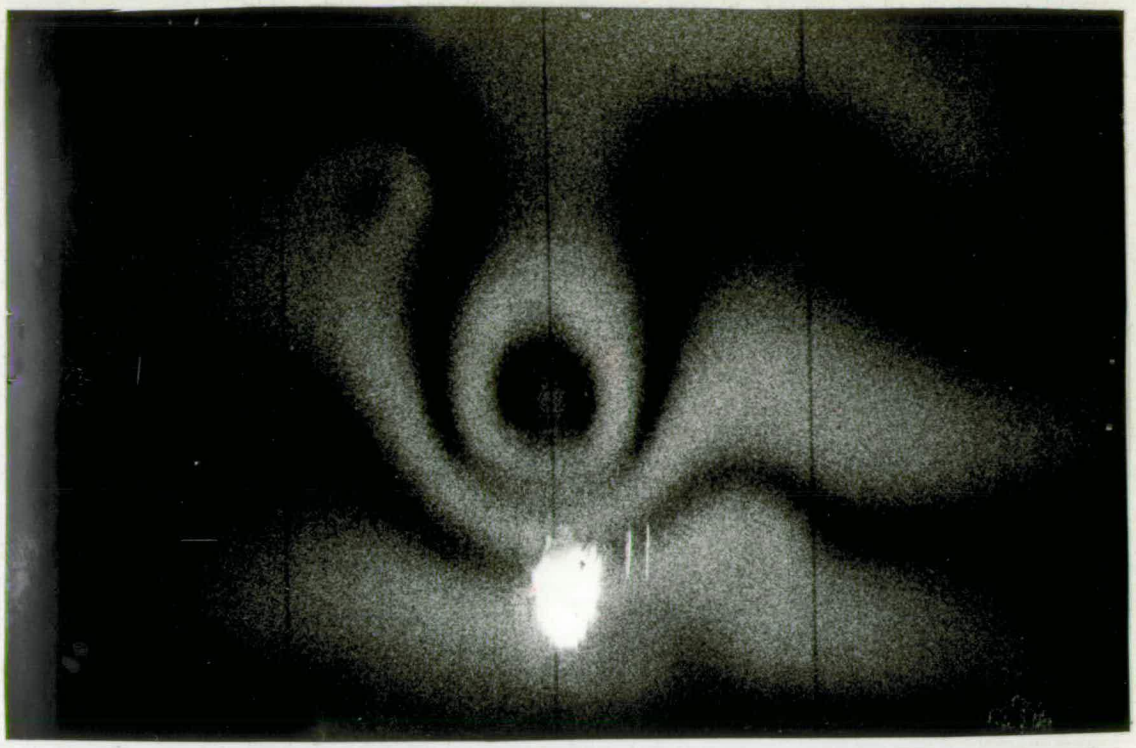

Fig. 128. Holo. 41. 4 hr. 22 min.

Natural convection from single vertical plate. Swelling agent: methyl salicylate. Plate was not reswollen after Holo. 40.

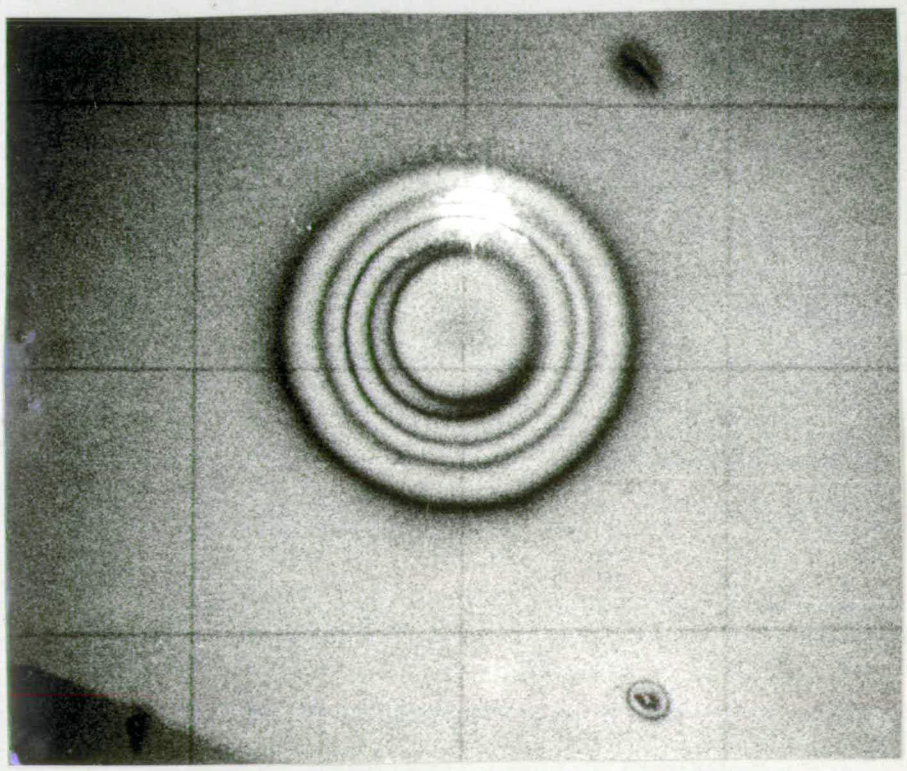

Fig. 129. Holo. 16. 10 min.

Superior clarity of fringes at high Re. No. Jet diam 13.3 m.m. Plate separation 1.65 m.m. Airflow 155 ml/min. Swelling agent: methyl salicylate.

7.3 Fringe Interpretation.

The shape of the recession crater can be deduced by similar reasoning to that used for the convex disc. Referring to Fig. 130, wide fringes are seen where the gradient of the crater surface is small, due to the gradual change from completely constructive to completely destructive interference. In these experiments, the fringe pattern of the form shown in Fig. 131, indicating a rounded crater, as opposed to a sharp crater as in Fig. 83. Wide fringes are not necessarily low-order fringes, although this is often the case in general, since small gradients obtain in the initial stages of mass transfer. Our fringe patterns cannot be interpreted as a "bumped" crater of the type shown in Fig. 132, but they could correspond to the "bumped" crater in Fig. 133. However, if this was the case, the first fringe to appear in the shorter experiments would consist of a black circular line rather than the black circular area obtained; therefore in these experiments, the crater is smooth-sided, without a central hump.

The fringe order will be established by comparing two or more experiments of different duration, the recession being proportional to the duration.

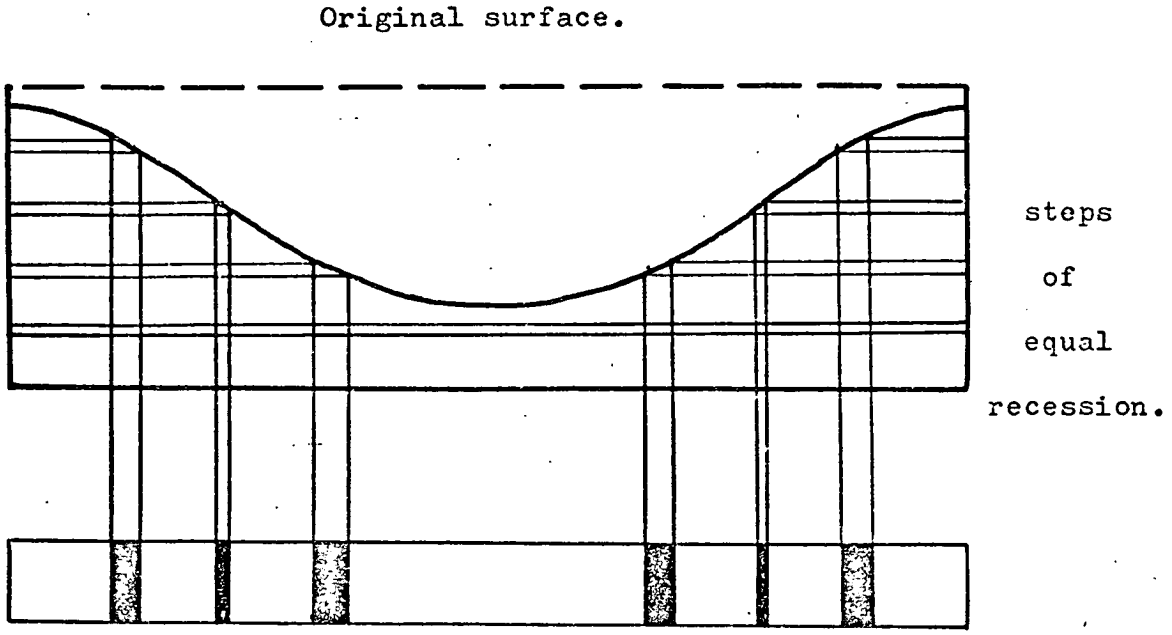

Fig. 130. Recession crater and fringe pattern.

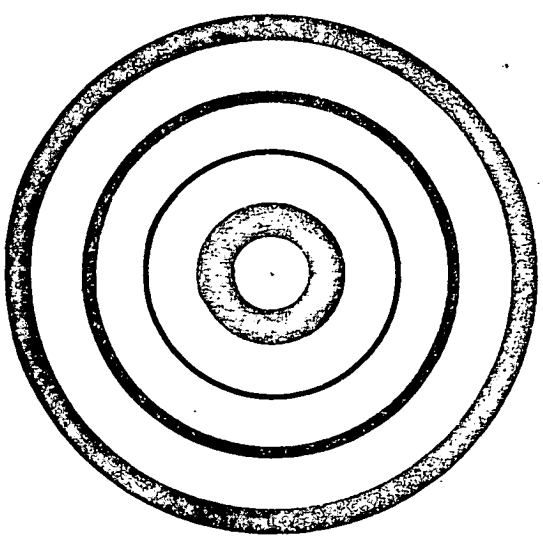

Fig. 131. Fringe pattern.

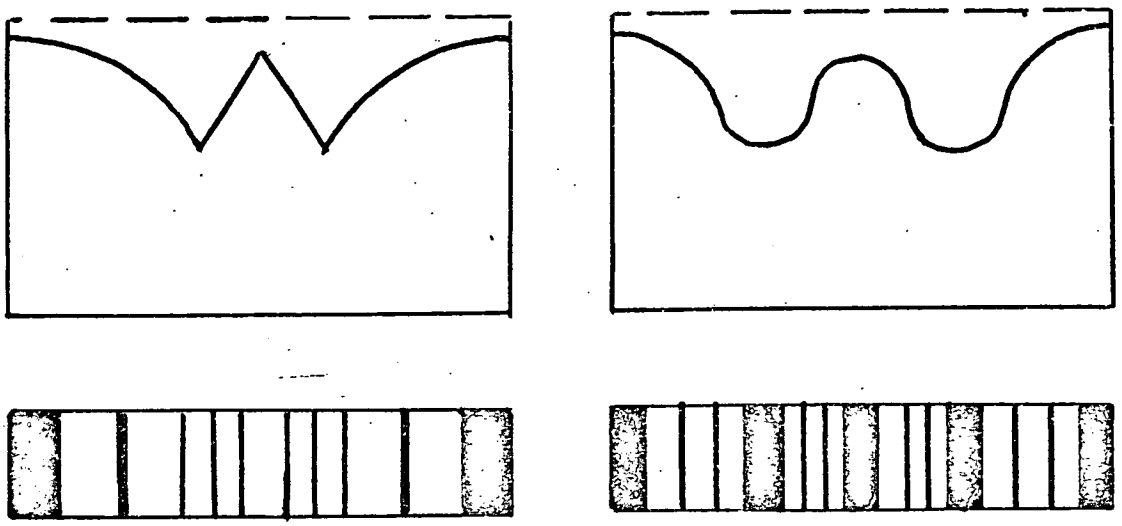

Fig. 132. "Bumped" recession craters and fringe patterns.

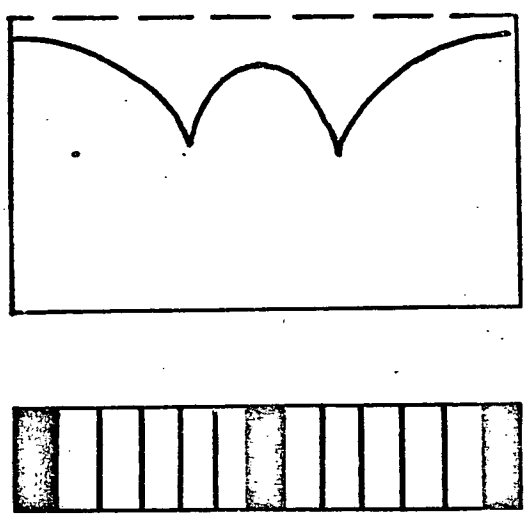

Fig. 133. "Bumped" recession crater and fringe pattern.

7.4 Fringe analysis and calculation of K.

The equation for the optical path length change is:

$$\frac{N\lambda}{2} = \delta\left[\sqrt{\eta^2 + \cos^2 i_1 - 1} + \sqrt{\eta^2 + \cos^2 i_2 - 1} - (\cos i_1 + \cos i_2)\right]$$

$$= \delta . f.$$

$i_1 = 15^\circ$ incident; $i_2 = 5^\circ$ reflected; measured on optical table.

Refractive index of RTV602 Polymer and Methyl Salicylate = 1.419.

$f = .8489.$

Data for RTV602 and Methyl Salicylate (from Ref. 105).

$\rho_{RTV602} = .98 \times 10^3$ kg./m^3 Diffusivity M.S. in air = 5.74×10^{-6} m^2/sec.

$\rho_{m.s.} = 1.18 \times 10^3$ kg/m^3. Sc. No. = 2.573.

% equilibrium volume swelling = 10.5%

$\rho_{SWOLLEN\ POLYMER}$ = 1.001 (by proportion)

Air temperature = 23.5°C.

Mol. wt. methyl salicylate = 152.

P_s = vapour pressure = .1225 m.m. Hg. at 23.5°C.

$$C_s = \frac{m.w. \times 760 \times P_s}{22{,}400 \times T_k} \times 10^3 \text{ kg./m}^3$$

$\lambda = 6.33 \times 10^{-7}$m.

$$K.Cs.t = \left(\rho_{SWOLLEN\ POLYMER}\right). \delta$$

$$K = \frac{\rho . N' . \lambda}{2 . f . Cs . t.}$$

$$= \frac{.3706\ N'}{t} \text{ m/sec., t is duration in secs.}$$

Calculation of K

To establish the fringe order, values of $\frac{N'}{t}$ for each duration

in a Series are plotted for various N values. On the basis that $\frac{N'}{t}$ should be constant between experiments, the N value selected as correct is that which gives a best fit by graphical trial and error.

SERIES 1. ANALYSIS. TABLE 10.

	Fringe Number	x	Best-fit N value	Fringe No. per 1 min.
holo.5	N+2	0-1.43		5.0
1 min.	N+1	2.26	3	4.0
	N	>10		3.0
holo.6	N+4	0-1.43		4.5
2 min.	N+2	2.38	5	3.5
	N+1	>10		3.0
	N+9	0		4.8
	N+8	1.23		4.6
holo.7	N+6	1.73		4.2
5 min.	N+4	2.02	15	3.8
	N+2	2.45		3.4
	N+1	2.89		3.2
	N	>3.5		3.0
	N+13	0		4.6
	N+12	.85		4.5
	N+10	1.56		4.3
	N+8	1.85		4.1
holo.8	N+6	2.13	33	3.9
10 min.	N+4	2.49		3.7
	N+2	3.06		3.5
	N+1	3.61		3.4
	N	>4.5		3.3
	N+8	2.67		
	N+6	2.77		
holo.9	N+4	2.99		
25 min.	N+2	3.70		
	N+1	>10		

The curves for the best-fit N valves, for the 4 holograms are shown in Fig134.

SERIES 2. ANALYSIS. TABLE 11.

	Fringe Number	x	Best-fit N value	Fringe No. per 1 min.
holo.10	N+2	0-1.67	1	3
1 min.	N+1	2.02		2
	N+2	0-1.91		2.5
holo.11	N+1	2.5	3	2.0
2 min.	N	>3		1.5
	N+6	0-1.96		2.6
holo.12	N+4	2.24	7	2.2
5 min.	N+2	2.80		1.8
	N	3.64		1.4
holo.13	N+4	2.84	21	1.67
15 min.	N+2	3.13		1.53
	N	3.56		1.40
holo.14	N+4	2.53		1.72
25 min	N+2	2.83	39	1.64
	N	3.42		1.56

The curves for the best-fit N values, for the five holograms, are shown in Fig. 135.

SERIES 3. ANALYSIS. TABLE 12.

	Fringe Number	x	Best-fit N value	Fringe No. per 2 min.
holo.18	N+1	0-3.18	1	2
2 min.	N	>3.18		1
holo.19	N+2	0-1.81	5	2.33
6 min.	N	2.95		1.60
	N+4	0-1.40		2.25
holo.20	N+2	2.94	5	1.75
8 min.	N+1	3.50		1.50
	N	>4.48		1.25
	N+8	2.56		1.92
holo.21	N+6	2.90		1.77
26 min.	N+4	3.24	17	1.62
	N+2	3.59		1.46
	N	4.28		1.31

The curves for the best-fit N values, for the four holograms, are shown in Fig. 136.

SERIES 4. ANALYSIS. TABLE 13.

	Fringe Number	x	Best-fit N value	Fringe No. per 7 min.
holo.29 7 min.	N+2	3.10	1	3
	N+1	>3.40		2
holo.30 15 min.	N+3	0	3	2.80
	N+2	3.503		2.33
	N+1	4.383		1.87
	N	>4.80		1.40
holo.31 37 min.	N+8	0-2.38	7	3.22
	N+6	3.08		2.84
	N+4	3.92		2.46
	N+2	4.90		2.08
	N+1	6.53		1.89
	N	>6.53		1.70
holo.32 55 min.	N+10	2.38	13	2.93
	N+8	2.80		2.67
	N+6	3.64		2.42
	N+4	4.20		2.16
	N+2	5.04		1.91
	N+1	6.48		1.78
	N	>6.48		1.66

The curves for the best-fit N values, for the four holograms, are shown in Fig. 137.

SERIES 5. ANALYSIS. TABLE 14.

	Fringe Number	x	Best-fit N value	Fringe No. per 39 min.
holo.34	N+2	2.35	1	3
39 min.	N+1	4.70		2
holo.39	N+4	0-1.35		4.88
56 min.	N+2	3.36	3	3.48
	N	7.01		2.09
	N+17	0		4.95
	N+16	.70		4.76
	N+14	1.54		4.38
holo.38	N+12	2.24	9	4.00
205min.	N+10	2.80		3.62
	N+8	3.36		3.23
	N+6	3.92		2.85
	N+4	4.55		2.47
	N+2	5.46		2.09
	N	7.01		1.71
	N+21	0		4.76
	N+20	1.19		4.63
holo.36	N+16	1.85	15	4.10
295min.	N+12	2.91		3.57
	N+8	3.84		3.04
	N+4	4.76		2.51
	N	6.35		1.98

The curves for the best-fit N value are shown in Fig.138.

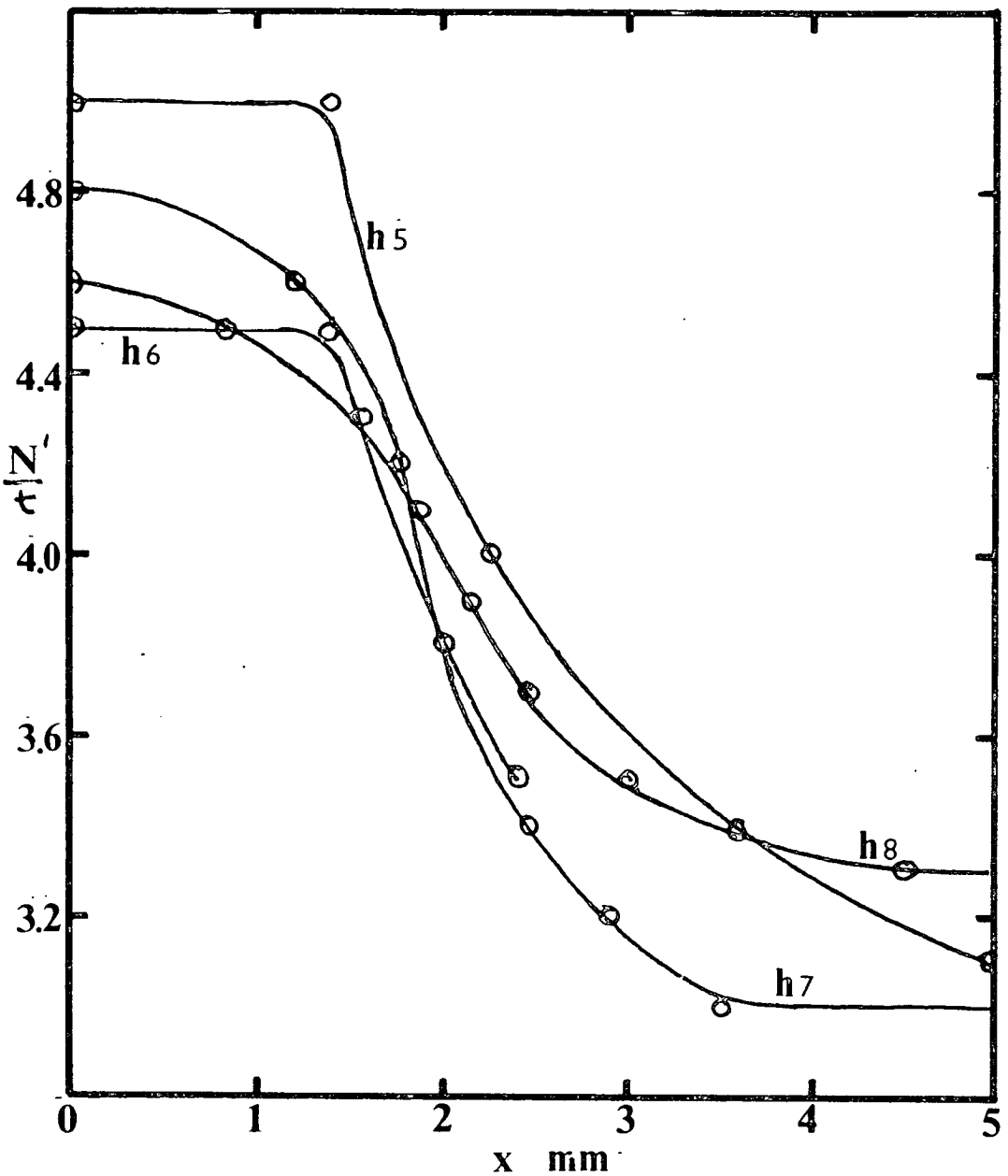

Fig. 134. Series 1. Fringe Number/time interval V. diam.

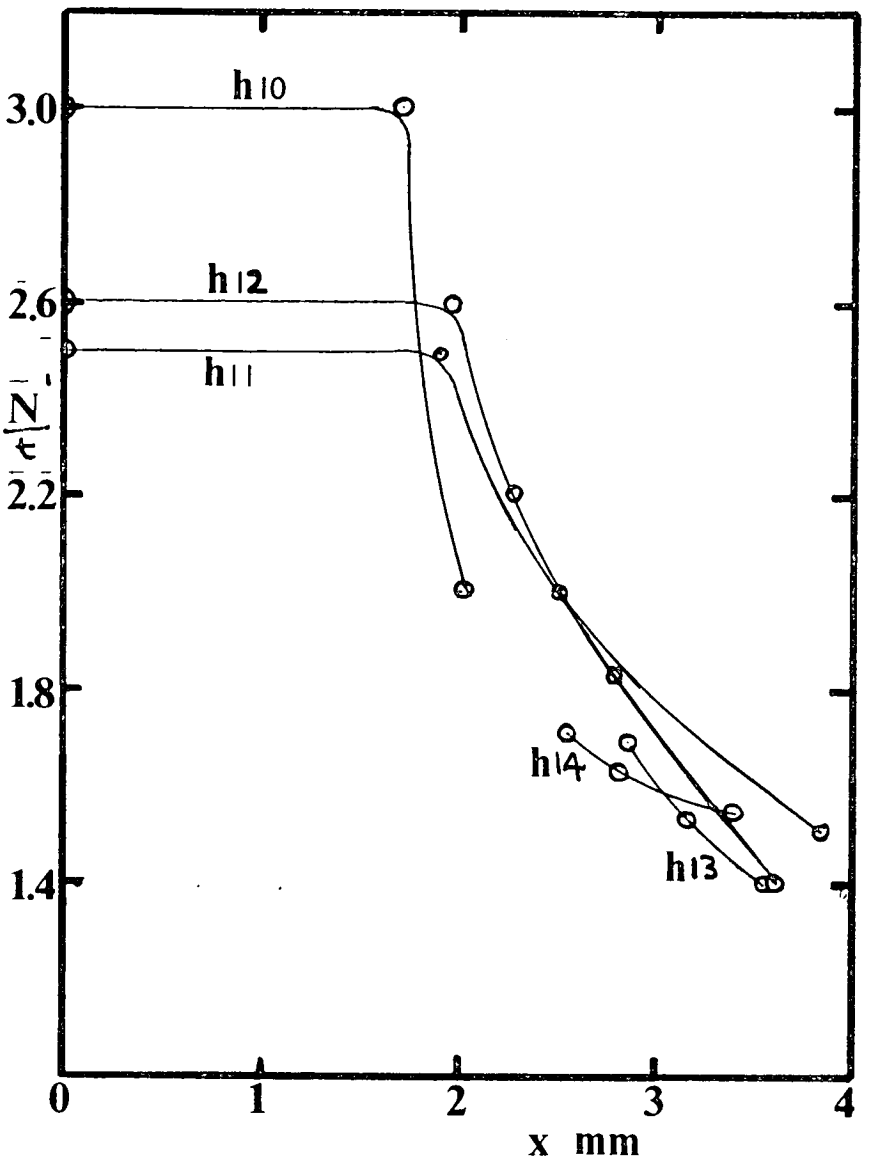

Fig. 135. Series 2. Fringe Number/time interval V. diam.

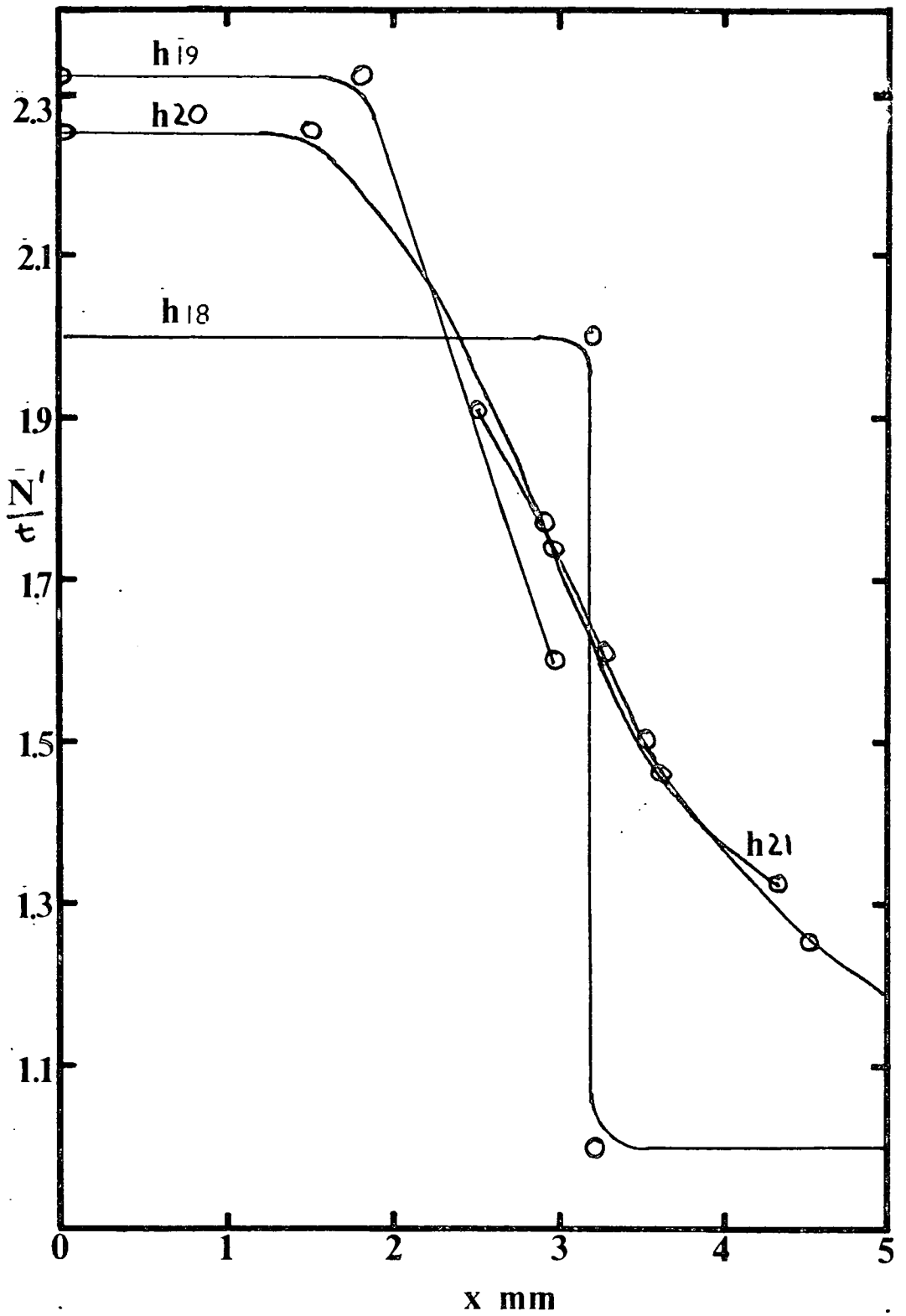

Fig. 136. Series 3. Fringe Number/time interval V. diam.

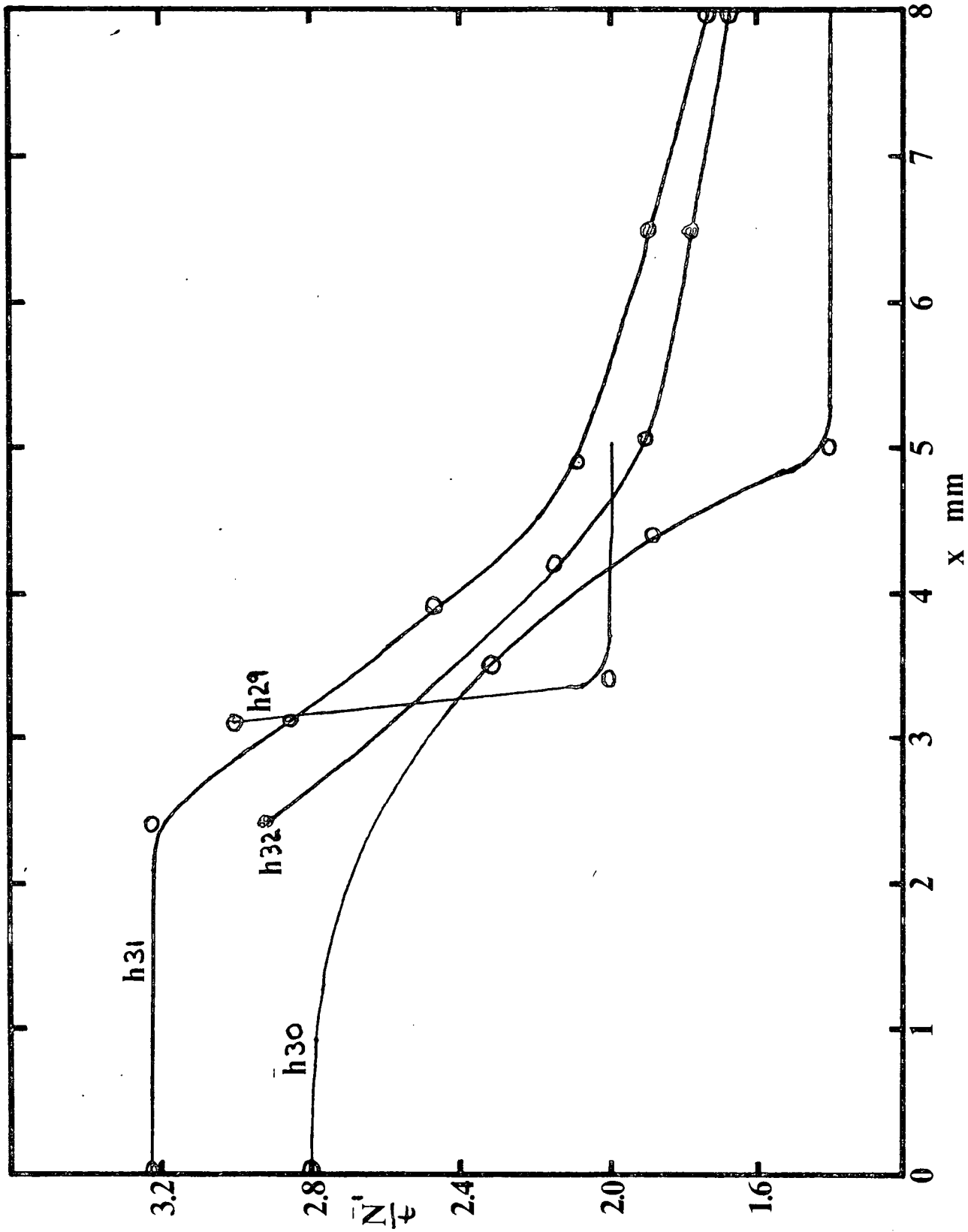

Fig. 137. Series 4. Fringe Number/time interval V. diam.

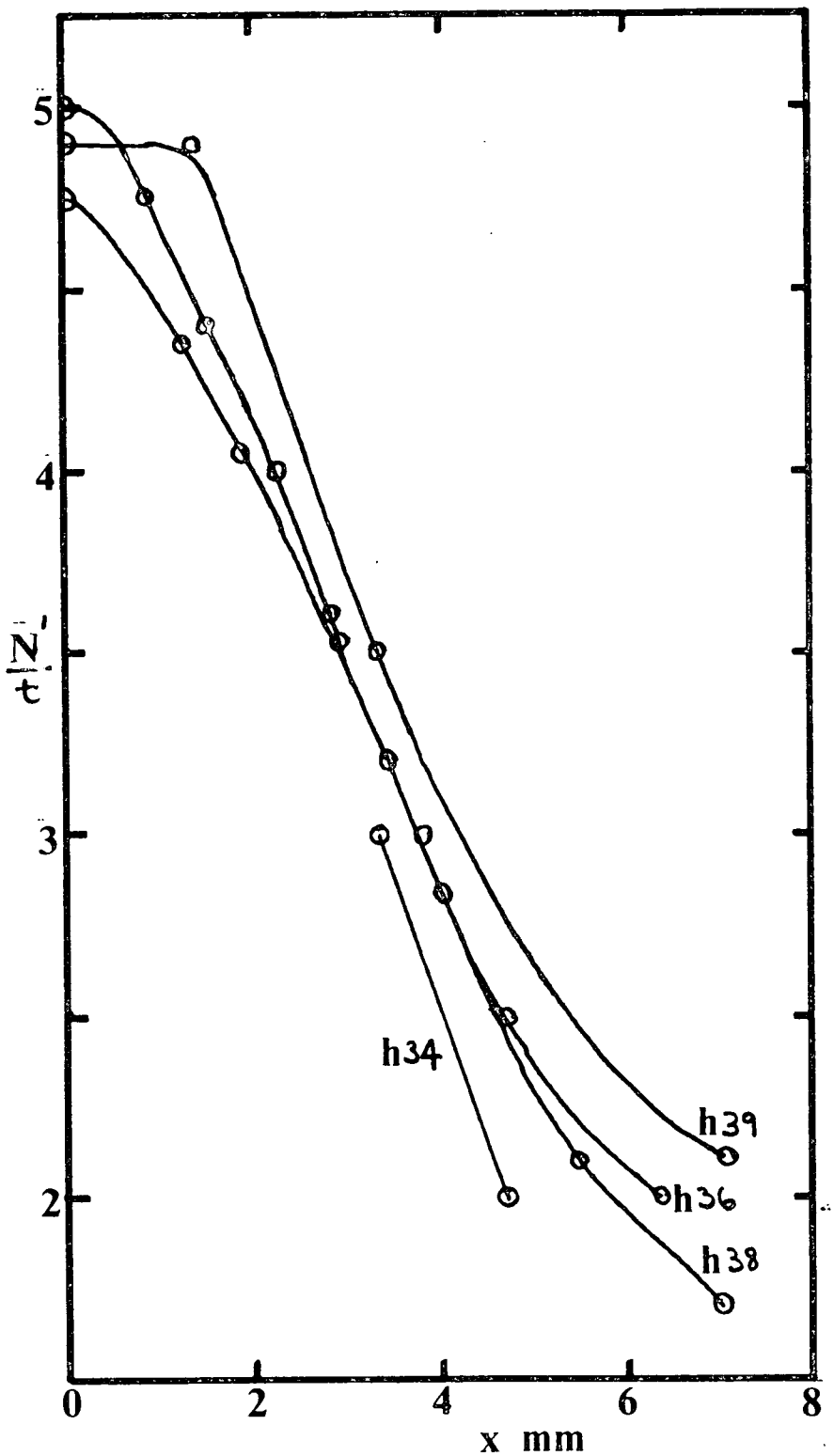

Fig. 138. Series 5. Fringe Number/time interval V. diam.

TABLE 15.

	SERIES 1.		SERIES 2.		SERIES 3.	
x	Fringe No. per 1 min.	K x10 m/sec.	Fringe No. per 1 min.	K x10 m/sec.	Fringe No. per 2 min.	K x10 m/sec
0	4.72	29.2	2.72	16.8	2.20	6.79
1.0	4.65	28.7	2.72	16.8	2.20	6.79
1.5	4.41	27.2	2.68	16.6	2.20	6.79
2.0	4.00	24.7	2.30	14.2	2.15	6.64
2.5	3.67	22.7	1.85	11.4	2.01	6.21
3.0	3.46	21.4	1.62	10.0	1.78	5.50
3.5	3.28	20.3	1.47	9.1	1.42	4.39
4.0	3.17	19.6			1.26	3.89
4.5	3.10	19.1			1.20	3.71
5.0	3.08	19.0				

The table is continued on the next page. For each series, the fringe No. per time interval is the mean of the curves shown in each of Figs. 134-138. The calculated K values are shown in Figs. 139-143; the area between the double curves covers the variation of the calculated recession values for all the holograms in a series. The K values listed above lie at the mean of the double curves.

wbc = white blood cell

TABLE 15. (cont.)

SERIES 4.		SERIES 5.		
Fringe No. per 7 min.	K x10 m/sec.	Fringe No. per 39 min.	K x10 m/sec.	x
3.02	2.66	4.86	.770	0
3.02	2.66	4.78	.757	1.0
3.02	2.66	4.60	.729	1.5
2.99	2.64	4.25	.673	2.0
2.90	2.56	3.86	.611	2.5
2.68	2.36	3.58	.567	3.0
2.39	2.11	3.16	.500	3.5
2.14	1.89	2.86	.453	4.0
1.97	1.74	2.55	.404	4.5
1.84	1.62	2.30	.364	5.0
1.76	1.55	2.16	.342	5.5
1.72	1.52	2.04	.323	6.0
1.66	1.46	1.92	.304	6.5
1.64	1.45	1.86	.295	7.0
1.60	1.41			8.0

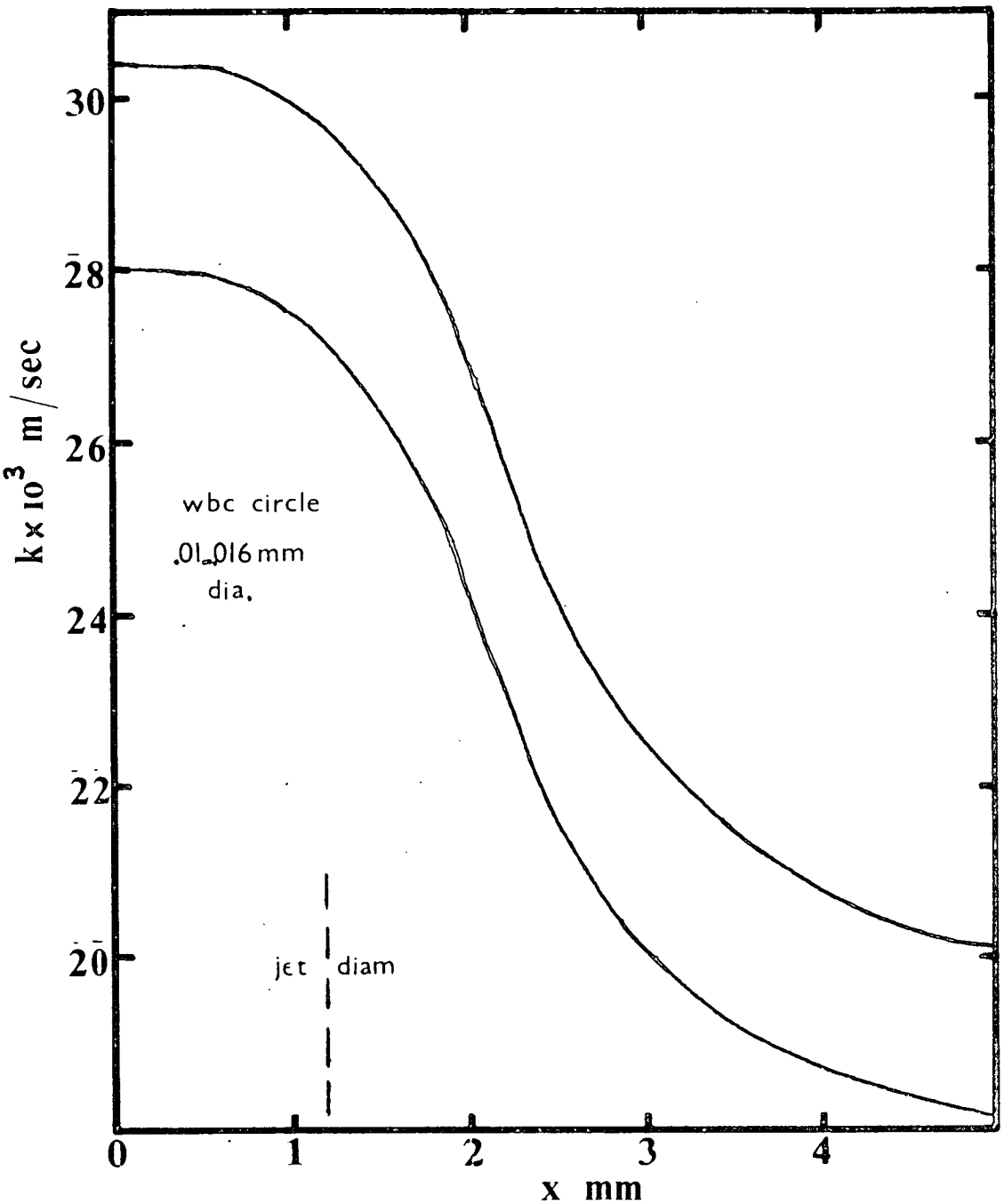

Fig. 139 Series 1. Mass transfer coeff. V. diam.

Re. No. 8·3

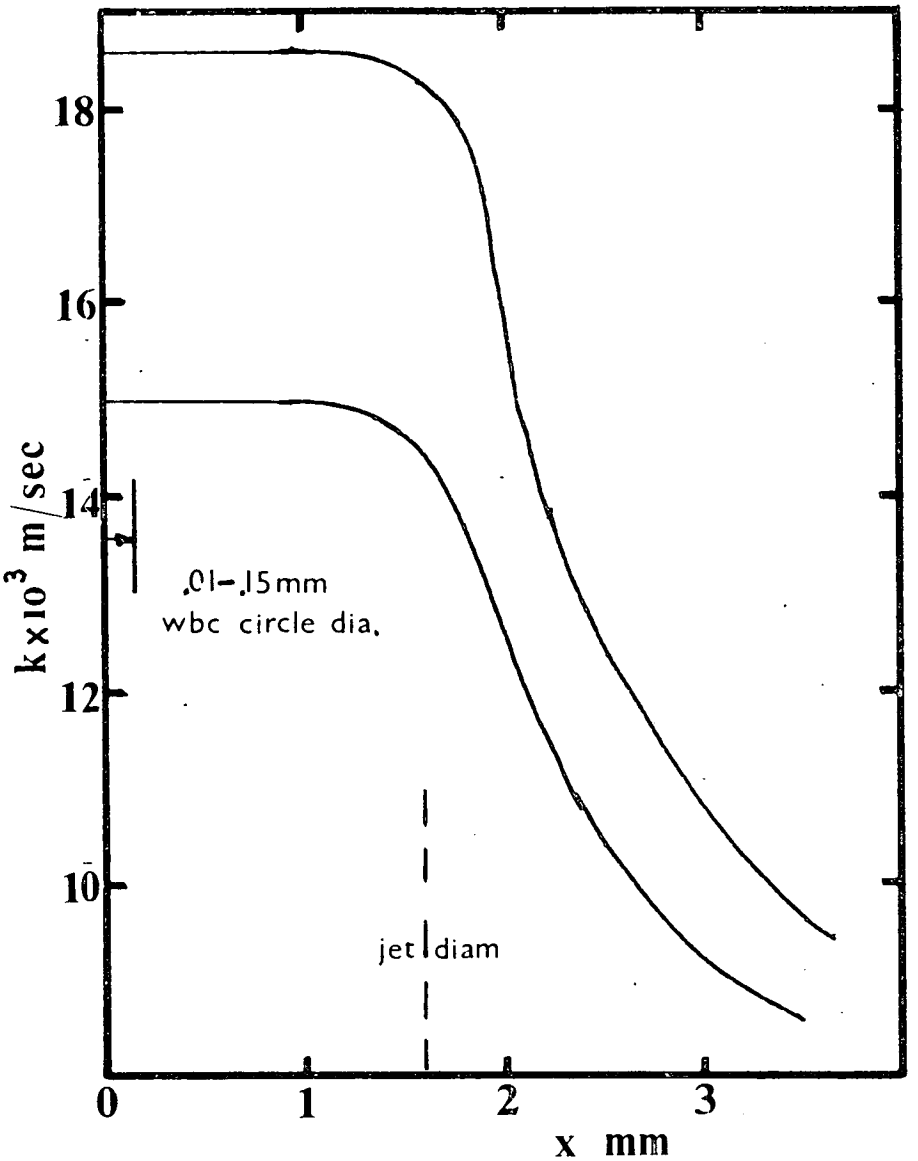

Fig. 140. Series 2. Mass transfer coeff. V. diam.

Re. No. 6.2

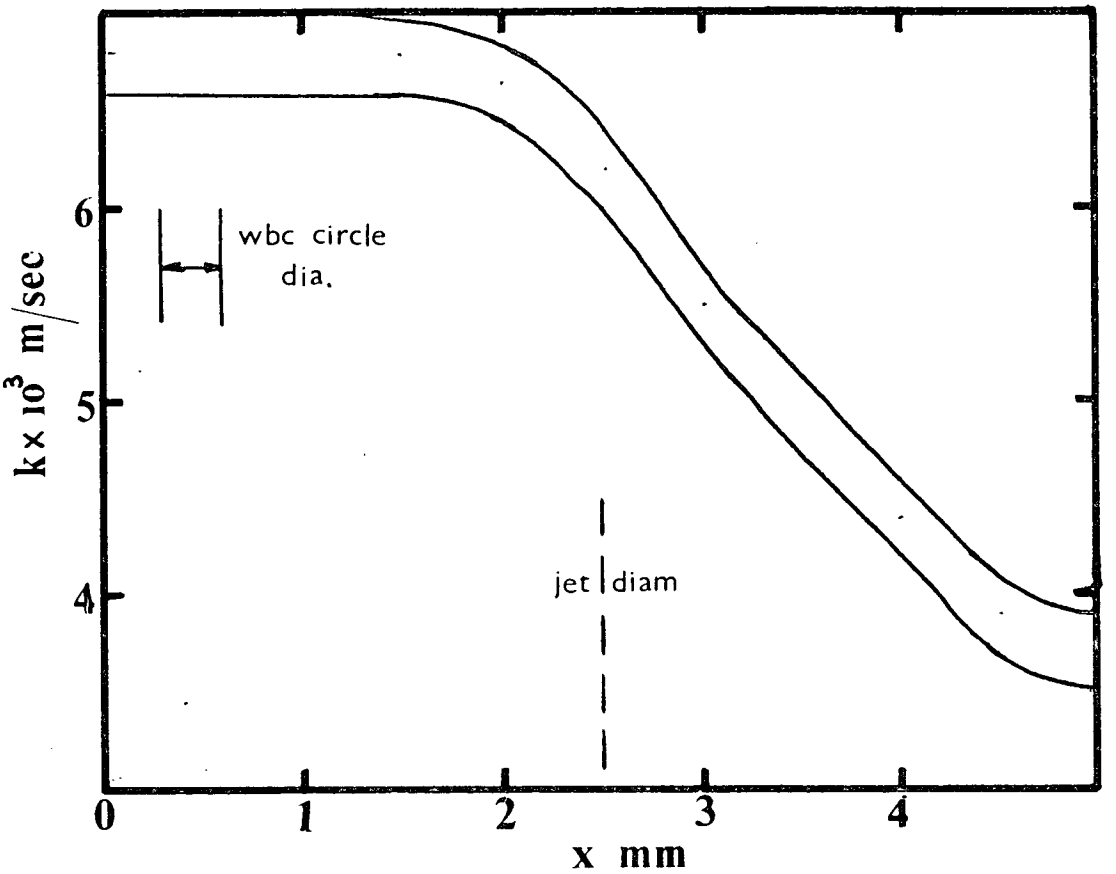

Fig. 141. Series 3. Mass transfer coeff. V. diam.

Re. No. 4.0

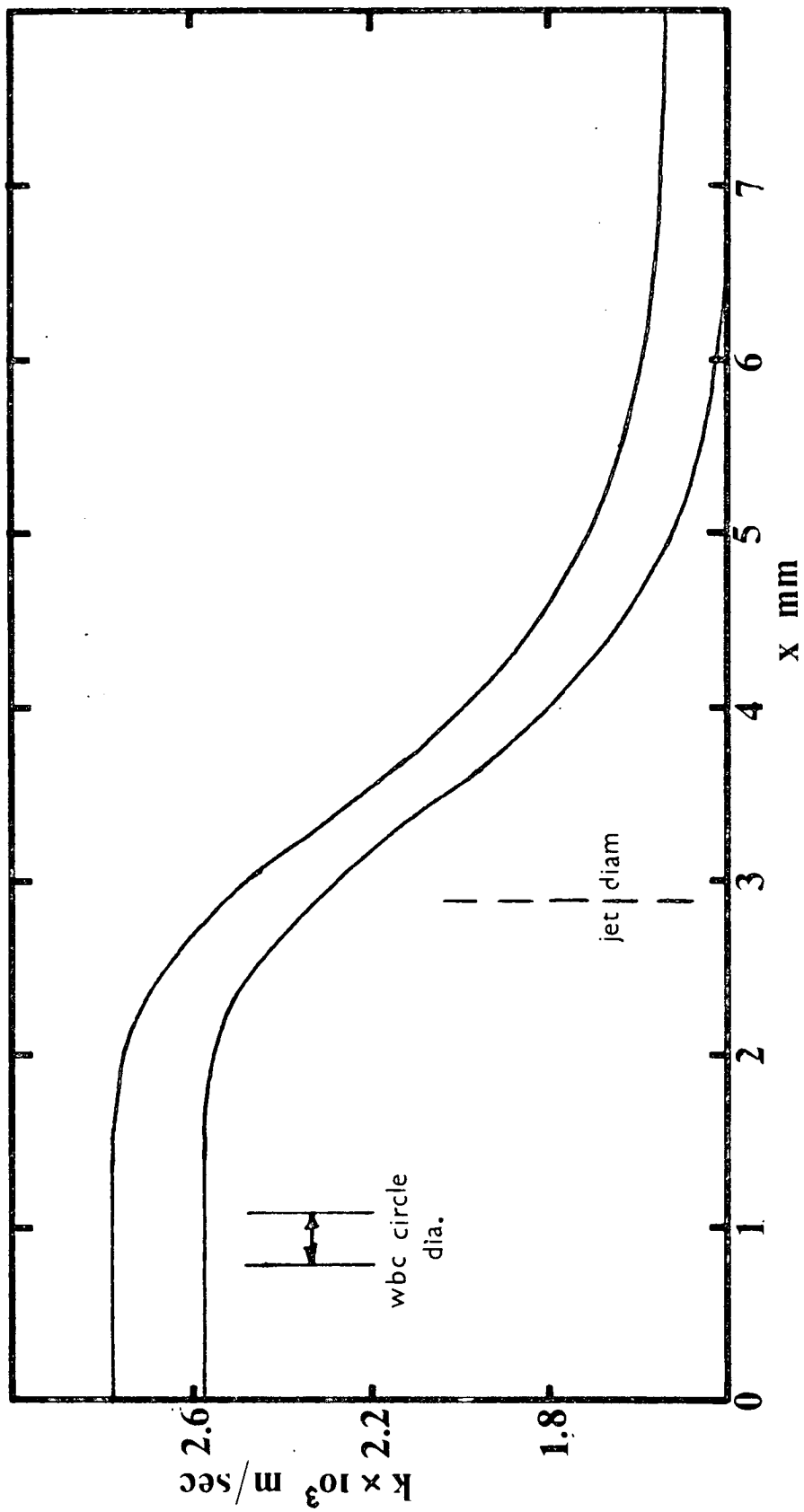

Fig. 142 Series 4. Mass transfer coeff. V. diam.

Re. No. 3·4

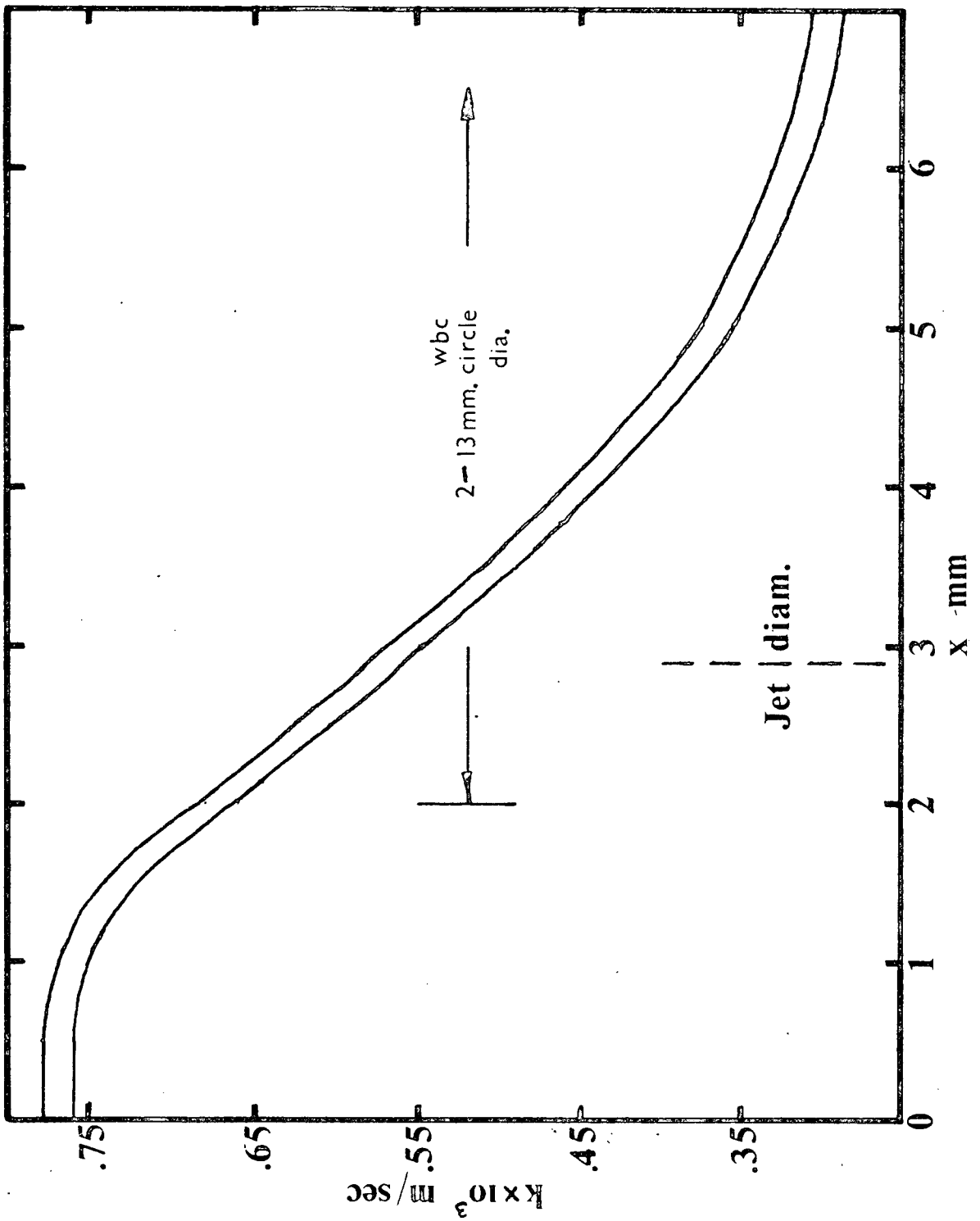

Fig. 143. Series 5. Mass transfer coeff. V. diam.

Re. No. 3·4

7.5 Sources of error.

The coincidence curves characteristically exhibit the patterns shown in Fig. 144.

Measurement errors on the optical table.

Unlike the case of the convex disc, the measurement of dimensions on the optical table does not need to be made to a high degree of accuracy, due to the localisation of the fringes and the large separation between components. Because the plate is not perpendicular to the illuminating beam and the holographic plate, there is a slight contraction of the fringe pattern in the horizontal direction. The effect is small, and was taken account of by averaging the horizontal and vertical diameters.

Timing errors.

Such errors are indicated by type (a) curves, which show a constant relative error in the value of recession/time, so that the curves diverge near x=0. When N is manipulated to obtain a better fit for an (a) type pattern, the residual discrepancy appears as a type (b) pattern.

Error in measurement of the position of the fringes.

This error appears as a type (c) pattern, and occurs with the very wide fringes encountered in the short duration experiments. The interferometry technique is inherently inaccurate when the recessions to be measured are rounded, as opposed to sharp, craters.

Superposition of natural convection.

This appears most noticeably in the longer duration experiments, with the largest hole site and plate separation, as a series of

horizontal parallel fringes curving downwards at the edges of the plate, and a vertical elongation of the "circular" fringes (Fig. 121). Fig. 128 shows the fringe pattern obtained from natural convection from a single vertical plate. In this experiment, the expected pattern is distorted in the central region, presumably due to the fact that the polymer was not reswollen after the previous long duration experiments.

Plate misalignment.

The apparatus was tested for sensitivity to plate misalignment, and was found to be very insensitive, as demonstrated by the symmetry of the fringe pattern.

Extraneous fringe patterns.

The small, isolated fringe bunches which can be seen in Series 3 photographs correspond to accidental chipping of the polymer layer. The cause of the eccentric and crescent shaped fringes in the centre of some patterns is not known (Fig. 96,97,102,112,113).

7.6 Conclusions.

(1) Relation between mass transfer coefficient and white cell circle diameter.

These experiments indicate (See Figs. 139-143) that there is no direct relation between mass transfer coefficient and white cell circle diameter.

(2) Relation between mass transfer coefficient and wedge-shaped thrombi.

Fig. 124 shows no fringe wake patterns representing flow disturbance and increased mass transfer coefficients behind either

the triangular struts or the simulated surface imperfections, despite the fact that the experiment was conducted with reduced plate separation (3 m.m. instead of 10 m.m.) to increase the flow velocity and exaggerate any wake effect. For comparison, Series B shows, as expected, the highly disturbed region behind the struts and imperfections at greatly elevated Re. No's.

(3) Relation between shear stress and white cell circle diameter.

The experiments confirm Petschek's assertion that white cell circle diameter is shear limited, as far as the area within the jet is concerned, on the basis of the Chilton-Colburn analogy.

$$\frac{K}{u_m} \cdot f(Sc.) = \frac{\tau}{\rho u_m^2}$$

where τ = surface shear stress.

u_m = bulk flow velocity.

K = mass transfer coefficient.

ρ = density

Sc = Schmidt No.

Here, u_m increases linearly with radius; therefore if τ does indeed increase with radius as Petschek maintains, K would remain constant. This is found to be the case roughly as far as the jet radius. (Figs. 139-143). However, the experiments confirm, as predicted from the theory discussed in 1.3, that the shear stress does not continue to increase outside the jet diameter, as indicated by the reducing K-value.

(4) The holographic interferometry technique in this flow situations.

(a) Low Re. No.

At very low Re. No., natural convection distorts the fringe

pattern. This might be overcome by using a swelling agent of lower vapour pressure, but this would result in inconveniently long run times. Probably the effect of natural convection would have to be separately measured and subtracted from the superposed recession patterns. As demonstrated in Fig. 129, the clarity of the fringes is superior at high Re. No.

(b) Fringe position measurement.

In cases where the fringes are very wide, a more accurate position can be obtained by printing the photographs on normal contrast paper, instead of the high constrast paper used in this case, and measuring the tone-density by some optical technique, to find the maximum points of brightness and darkness.

(c) Method of coincidences for establishing fringe order.

As in the convex disc case, the technique has proved accurate to $\pm$ 5% approx.

(d) Use of small holographic plates.

No observable difference in the fringe contrast or clarity was found between plates of 6x4½ cm. and plates of 2¼x1½ cm.; the use of larger plates is thus undesirable in view of their high cost.

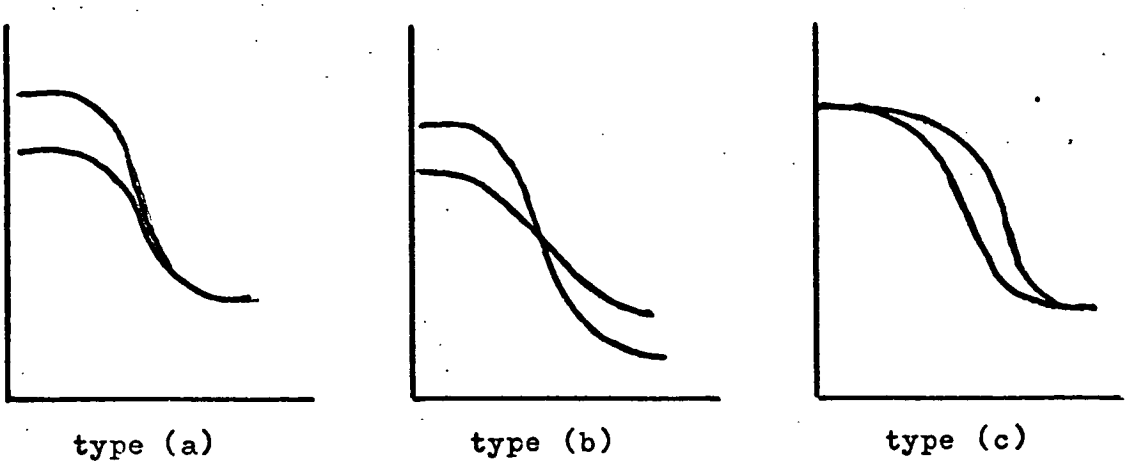

Fig. 144. Characteristic recession curves.

CHAPTER 8

Conclusions and recommendations.

The conclusions will be considered under four headings: The relation between mass transfer coefficient and blood clotting propensity; The technique of mass transfer measurement by holographic interferometry; The hydrydynamical application of the mass transfer results obtained; and, The suitability of this project as a three-year Ph.D research programme.

Blood clotting and mass transfer.

The experiments with the prototype Edinburgh Heart Valves failed to realise any blood clot data; the reason being the design of the valve was improved more successfully and quickly than anticipated, and the expected clotting problems did not arise. The mass transfer coefficient distribution was measured over the convex disc surface, but unexpectedly, no blood clot data became available over the corresponding surface of the valve occluder; and so this part of the project is inconclusive. The experiments with the stagnation point flow chamber demonstrated that there is no direct relationship between mass transfer coefficient and blood clotting propensity, as far as white cell deposition can be taken to be representative of blood clotting. The lack of highly disturbed wake patterns behind the supporting struts and simulated surface imperfections in those flow situations that give rise to blood clotting in those regions again indicate no relation between clotting and mass transfer. The possibility of a correlation cannot, however, be dismissed; because the conclusions in this thesis are based on the interpretation of a limited amount of blood clot data. Before this line of approach can be investigated further, it is necessary to acquire blood clot data

on a variety of surfaces. The technique of holographic interferometry for measurement of mass transfer coefficients is now sufficiently developed to provide data for the small surfaces likely to be used experimentally to obtain blood clot data.

Holographic interferometry for mass transfer measurement.

The technique has been extended considerably, from the case of large flat surfaces to small curved surfaces. The difficulties which have been overcome to allow this are threefold:

(a) experimental difficulties, due to the miniaturisation.

(b) difficulty in the qualitative interpretation of fringe patterns, arising when the shape of the recession crater cannot be inferred from other considerations.

(c) difficulty in the quantitative analysis of fringe patterns, arising when the surface under study is curved and close to the recording camera.

In addition, the determination of the fringe order, the difficulty of which is the most serious drawback of the method, has been established from the information on a single hologram, without recourse to any separate measuring device to provide recession values on a limited region of the surface.

Hydrodynamical data from mass transfer coefficients.

The values of the mass transfer coefficients on the convex disc and within the central area of the impinging jet in the parallel plate experiments have not previously been measured, as far as is known by the author. Such information is itself of definite, if limited,

hydrodynamical interest.

The suitability of this project for a Ph.D research programme.

The particular project has proved in many ways unsuited for study in a three-year Ph.D course, for the following reasons.

(a) the behaviour of blood is a notoriously difficult topic to make progress in, and is apt to confront the researcher engaging on his first research project with a bewildering and discouraging variety of unsolved problems.

(b) the acquisition of data from animal experiments is at best a slow and unreliable procedure, and was particularly so in this case where the experiments were performed under circumstances outwith our control within a severely limited budget, leading to delays, failed experiments, and the necessity to attempt interpreting data from a single animal instead of from a series of animals. These experiments were carried out by one surgeon, one technician and one medically-untrained engineer; a unit in Nymegen, Holland, for example, uses for similar research two surgeons, six technicians and one anaesthetist. In this project the animals used were often diseased and aged; in contrast the Dutch unit used purpose-bred animals. In consequence of this and other delaying circumstances, two years were effectively wasted in acquiring a miniscale amount of meaningful information from animal experiments.

(c) holographic interferometry is extraordinarily difficult experimentally, requiring several months to acquire even

the basic skills. Such a technique does of itself put substantial difficulties in the way of the initially inexperienced research student undertaking a project of limited duration. The difficulty is formidably compounded in this case by his need at the same time to acquire surgical and after-care technique for live animal experimentation.

APPENDICES

1. The correspondence equations for the flat plate.

2. Derivation of the mapping equation for the horizontal equator of the convex disc.

3. The mapping equation connecting any point on the disc with its photographic image.

4. The change in optical path length due to recession at a point of a curved polymer-coated surface.

5. The derivation of the incidence and reflection angles on the convex disc.

APPENDIX 1

The correspondence equations for the flat plate in Section 4.2.2, in polar coordinates are:

$$r = v \sqrt{\frac{x'^2}{(f' \cos\gamma - x' \sin\gamma)^2}\left(1 + \frac{y'^2}{(f'^2 + x'^2)}\right) + \frac{y'^2}{f'^2 + x'^2}}$$

$$\tan\theta = \frac{y'}{x'}\sqrt{\frac{(f' \cos\gamma - x' \sin\gamma)^2 + x'^2}{(f'^2 + x'^2)}}$$

And for the purpose of drawing the demonstration diagram in Fig. 39, the equations are rearranged thus:

$$x' = \frac{f' \cos\gamma}{\sin\gamma + \frac{v}{r\cos\theta}}$$

$$y' = \frac{f' \sin\theta}{(\cos\theta \sin\gamma + \frac{v}{r})}\sqrt{1 + \left(\frac{2\sin\gamma}{\frac{r}{v}\cos\theta + \frac{v}{r\cos\theta}}\right)}$$

APPENDIX 2

Derivation of the mapping equation for the horizontal equator of the convex disc (See Section 4.3)

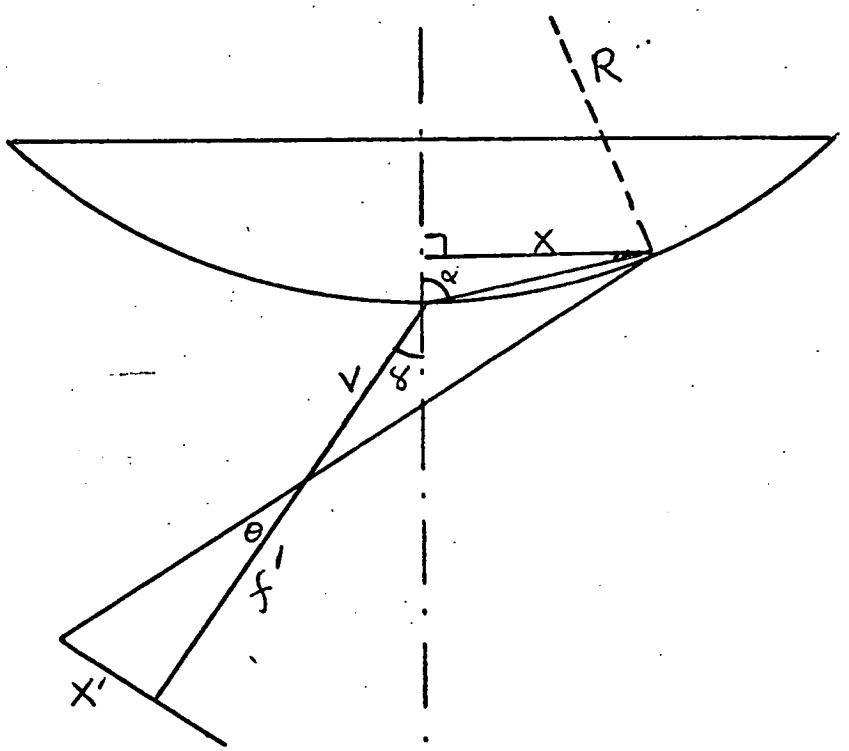

from the diagram,

let $Q = \left(R - \sqrt{R^2 - x^2}\right)$

then, $\tan\alpha = \dfrac{x}{Q}$; $\cos\alpha = \sqrt{\dfrac{Q}{2R}}$

also, $\dfrac{v}{\sin(\alpha - \theta - \gamma)} = \dfrac{\sqrt{2RQ}}{\sin\theta}$

and $\tan\theta = \dfrac{x'}{f'}$

eliminating α and θ

$$v = \frac{f'(x\cos\gamma - Q\sin\gamma) - Q\cos\gamma - x\sin\gamma}{x'}$$

putting $K = \left(\dfrac{f'\sin\gamma + \cos\gamma}{x'}\right)$ and $M = \left(\dfrac{f'\cos\gamma - \sin\gamma}{x'}\right)$

$$x = \frac{M(KR + v) + \sqrt{M^2(KR + v)^2 - (M^2 + K^2)[(KR + v)^2 - K^2R^2]}}{M^2 + K^2}$$

The negative root is ignored to give the value of x positive from the disc centre outwards.

When the camera is held head-on, i.e. $\gamma = 0$, this equation reduces to equation 4 given in Section 4.3.

APPENDIX 3

The mapping equation connecting any point on the disc with its photographic image.

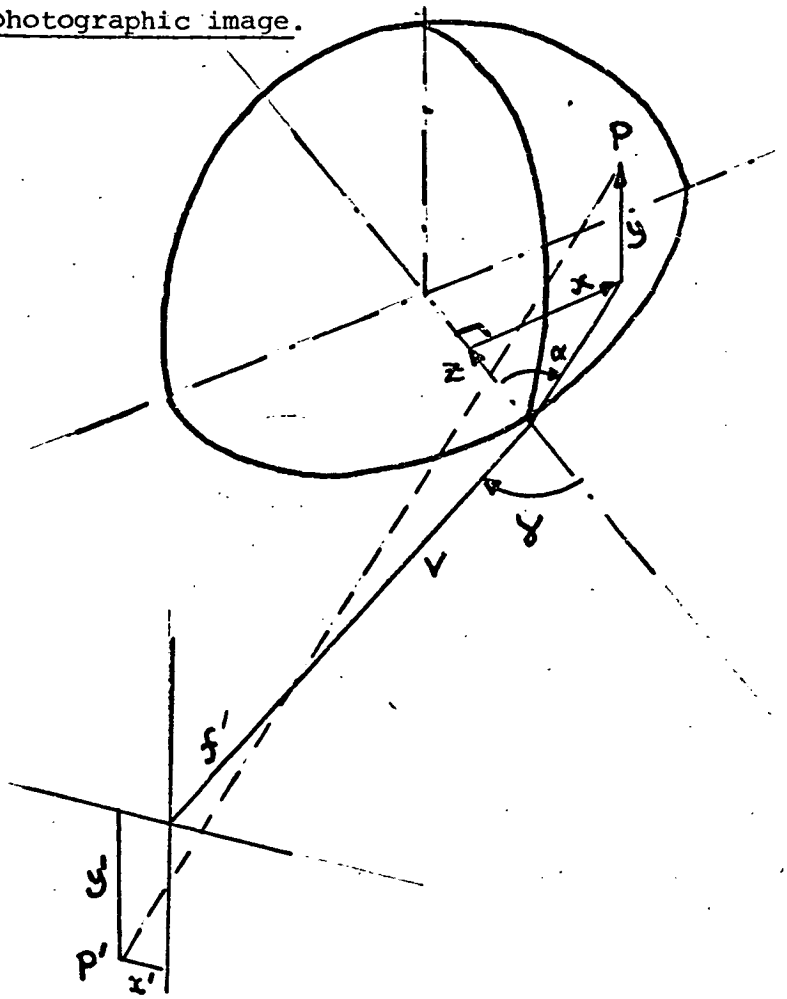

The disc surface is given by:

$$x^2 + y^2 + (R - z)^2 = R^2$$

By a similar analysis to Appendix 2, the mapping equations are:

$$x' = \frac{f'}{v}(x \cos \gamma - z \sin \gamma)$$

$$y' = y \sqrt{\frac{f'^2 + x'^2}{v^2 + x^2 + z^2 + 2f'(x \sin \gamma + z \cos \gamma)}}$$

Attempts to make x or y the subjects of these equations result in sixth-degree equations, impossible to solve analytically. No suitable approximation, such as arranging the high-power terms to be small, was found to simplify the equations. Three alternative coordinate systems were tried without success.

APPENDIX 4

The change in optical path length due to recession at a point of a curved polymer-coated surface.

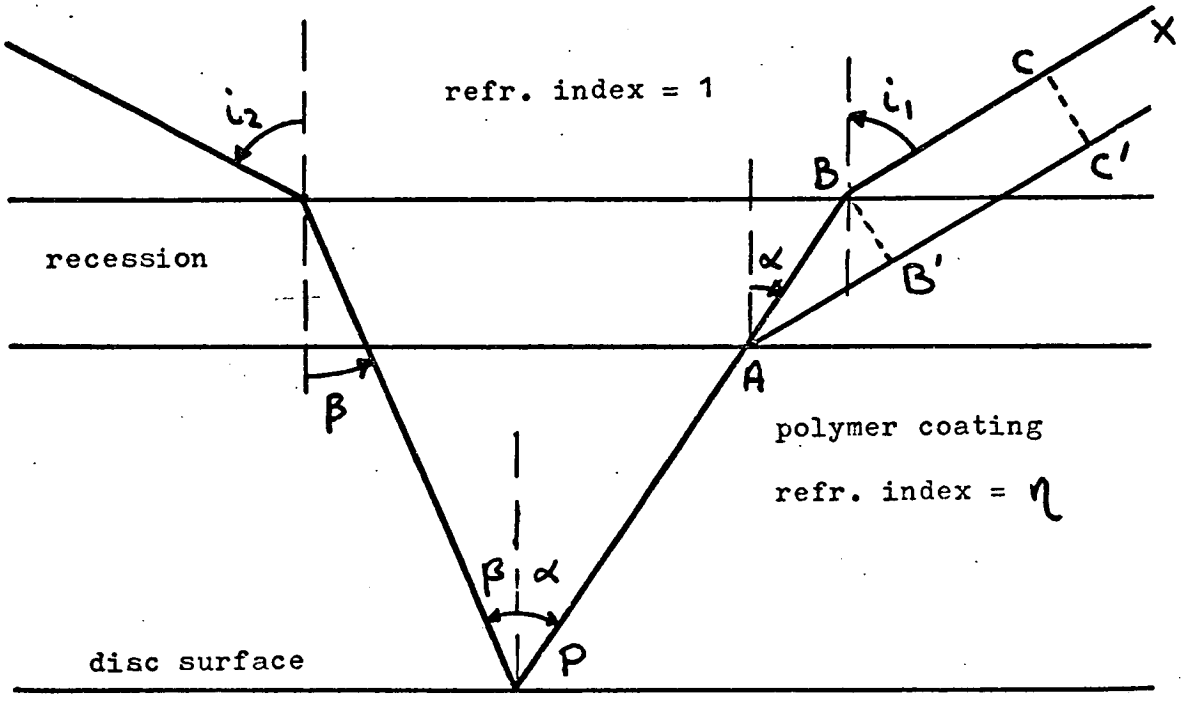

The incoming beam path length before recession is:

$$XC + CB + \eta.(BA + AP)$$

$$= XC + (C'A - B'A) + \eta.(BA + AP)$$

and after recession is

$$XC' + C'A + \eta.AP$$

therefore the change in path length is:

$$-B'A + \eta.BA$$

$$= BA\,[-\cos(i_1 - \alpha) + \eta]$$

$$= \frac{\delta}{\cos\alpha}\,[\eta - \cos(i_1 - \alpha)]$$

and similarly for the change in the path length of the outgoing beam, which is:

$$\frac{\delta}{\cos\beta}\,[\eta - \cos(i_2 - \beta)]$$

The total path length change at the point P, which equals $\frac{N\lambda}{2}$ if there is a fringe at P, is:

$$\frac{\delta}{\cos\alpha} \cdot [\eta - \cos(i_1 - \alpha)] + \frac{\alpha}{\cos\beta} \cdot [\eta - \cos(i_2 - \beta)]$$

where $\frac{\sin i_1}{\sin\alpha} = \frac{\sin i_2}{\sin\beta} = \eta$

This expression can be rearranged to give:

$$\frac{N\lambda}{2} = \delta \left[\sqrt{\eta^2 + \cos^2 i_1 - 1} + \sqrt{\eta^2 + \cos^2 i_2 - 1} - (\cos i_1 + \cos i_2)\right]$$

Equation 7

APPENDIX 5

The derivation of the incidence and reflection angles on the convex disc.

In the derivation, each quadrant will be considered in turn, the azimuth and altitude angles defined to be positive in all cases. In the diagram in fig. 50,

P is any point on the disc surface,

R is the radius of curvature,

α is the altitude angle,

θ is the azimuth angle.

Considering the geometry,

$$OA^2 = (R + S')^2 + q^2$$

$$\sin \hat{GOA} = \frac{q}{OA} \quad ; \cos \hat{GOA} = \frac{R + S'}{OA}$$

$$OE = R \cos \alpha$$

$$\hat{OEA} = \theta + \hat{GOA}$$

$$EA^2 = EO^2 + OA^2 - 2EO.OA. \cos \hat{OEA}$$

$$\cos \hat{OEA} = \cos (\theta + \hat{GOA})$$

therefore,

$$EA^2 = R^2 \cos\alpha + (R + S')^2 + q^2 - 2R \cos\alpha.[(R + S').\cos\theta = q.\sin\theta]$$

Now $PA^2 = PE^2 + EA^2$

$$= R^2 + (R + S')^2 + q^2 - 2R \cos\alpha.[(R + S') \cos\theta - q \sin\theta]$$

and $\cos i = -\cos \hat{APO}$

$$= \frac{OA^2 - OP^2 - PA^2}{2.OP.PA}$$

$$\cos i = \frac{\cos\alpha\,[(R + S').\cos\theta - q.\sin\theta] - R}{\sqrt{R^2 + (R + S')^2 + q^2 - 2R\cos\alpha[(R + S').\cos\theta - q.\sin\theta]}}$$

Equation 5

This expression gives values of i_1 and i_2 to substitute in the path length change equation. For the horizontally opposite quadrant, the sign of the q term is changed. For the vertically opposite quadrant, there is no change in the equation because of symmetry.

REFERENCES

1. BEN-ZVI, J., HILDNER, F.J., CHANDRARATNA, P.A., SAMET, P.
"Thrombosis on Bjork-Shiley Aortic Valve Prosthesis",
Am. J. Cardiol. 34: 538-544, 1974.

2. GRAY, L.A., FULTON, R.L., TRIBENI, N.S., FLOWERS, N.C.
"Surgical Treatment of Thrombosed Bjork-Shiley Aortic Valve Prosthesis",
J. Thoracic and Cardiovascular Surgery 71: 429-432, 1976.

3. ROBERTS, W.C., HAMMER, W.J.
'Cardiac Pathology after Valve Replacement with a Tilting-Disc Prosthesis",
Am. J. Cardiol. 37: 1024-1033, 1976.

4. AKBARIAN, M., AUSTEN, W.G., YURCHAK, P.M., SCANNEL, J.G.
"Thrombo embolic Complications of Prosthetic Heart Valves",
Circulation 37: 826-831, 1968.

5. ROBERTS, W.C., MORROW, A.G.
"Late Postoperative Pathological Findings after Cardiac Valve Replacement",
Circulation, Supp. 1 to vols. 35/36, 48-62, 1967.

6. WUKASCH, D.C., UNGER, F., REVL, G.J. SANDIFORD, F.M., KYGER, E.R., HALL, R.J., NORMAN, J.C., COOLEY, D.A.
"Long-Term Results in Cardiac Valve Replacements",
Proc. of the 2nd Henry Ford Hospital Int. Symp. on Cardiac Surgery, Detroit, U.S.A., Oct. 1975.

7. WILLIAMS, W.J.,
"Mechanism of Blood Coagulation",
from "Hematology" Section 6, McGraw-Hill, New York, 1972.

8. BIGGS, R.

"Human Blood Coagulation, Haemostasis, and Thrombosis",

2nd edition, Blackwell Scientific, Oxford, 1972.

9. BAUGH, R.F., HOUGIE, C.

"Biochemistry of Blood Coagulation",

from "Recent Advances in Blood Coagulation" No. 2.

ed. L. POLLER, Chap. 1, Churchill Livingstone, Edinburgh.

10. DAVIE, E.W., FUJIKAWA, K.

"Basic Mechanisms in Blood Coagulation",

Annual Rev. Biochem. 44: 799-829, 1975.

11. BENNETT, B., RATNOFF, O.D.

"The Normal Coagulation Mechanism",

Medical Clinics of North America 56: 95-104, 1972.

12. MERENDINO, K.A.

"Panel Discussion: Clinical Problems in Prosthetic Valves",

Chapter 62, ed. L.A. BREWER, Thomas; Illinois, U.S.A.

13. ARRIGONI, M.G., DANIELSON, G.K., MANKIN, H.T., PLUTH, J.R.

"Aortic Valve Replacement with Cloth-Covered Composite-Seat Starr-Edwards Prosthesis",

J. Thorac. Cardiovasc. Surg. 65: 376-380, 1973.

14. HODAM, R., ANDERSON, R., STARR, A., WOOD, J., DOBBS, J., RAIBLE, D.

"Further Evaluation of the Composite-Seat Cloth-Covered Prosthesis",

Ann. Thorac. Surg. 12: 621-638, 1971.

15. ISOM, O.W., WILLIAMS, C.A., FALK, E.A., GLASSMAN, E., SPENCER, F.C.

"Long term Evaluation of Cloth-Covered Metallic Ball Prostheses",

J. Thorac. Cardiovasc. Surg. 64_ 354-67, 1972.

16. BJORK, V.O., HENZE, A., HOLMGREN, A.
"Five Years Experience with the Bjork-Shiley Tilting Disc Valve in Isolated Aortic Valvular Disease",
J. Thorac. Cardiovas. Surg. 68: 393-404, 1974.

17. STANFORD, W., LINDBERG, E.F., ARMSTRONG, R.G.
"Implantation of Heart Valve Prostheses without Anticoagulants",
J. Thorac. Cardiovasc. Surg. 63: 648-651, 1972.

18. CLELAND, J., MOLLOY, P.J.
"Thrombo embolic Complications of the Cloth-Covered Starr-Edwards Prostheses",
Thorax 28: 41-47, 1973.

19. VIDNE, B., ERDMAN, S., LEVY, M.J.
"Thromboembolism Following Heart Valve Replacement by Prosthesis",
Chest 63: 713-717, 1973.

20. COHN, L.H., SANDERS, J.H., COLLINS, J.J.
"Aortic Valve Replacement with the Hancock Porcine Xenograft",
Ann. Thorac. Surg. 22: 221-227, 1976.

21. CLEVESE, P.G., GALLUCCI, V., MOREA, M. VOLTA, S.D., FASOLI, G., CASAROTTO, D.
"Heart Valve Replacement with the Hancock Bioprosthesis",
Cardiovasc. Surg. Supp. 2, Circulation 56: 111-116, 1977.

22. LURIE, A.J., MILLER, R.R., KEVIN, S., MAXWELL, B.S., GREHL, T.M., VISMARA, L.A., HURLEY, E.J., MASON, D.T.
"Hemodynamic Assessment of the Glutaraldehyde-Preserved Porcine Heterograft in the Aortic and Mitral Positions",
Cardiovasc. Surg, Supp. 2, Circulation 56: 104-110, 1976.

23. ZUHDI, N.
"The Porcine Aortic Valve Prosthesis: A Significant Alternative",
Ann. Thorac. Surg. 21: 573-575, 1976.

24. STINSON, E.B., GRIEPP, R.B., DYER, P.E., SHUMWAY, N.E.
"Long-Term experience with Porcine Aortic Valve Xenografts",
J. Thorac. and Cardiovas. Surg. 73: 54-63, 1977.

25. PIPKIN, R.D., BUCH, W.S., FOGARTY, T.J.
"Evaluation of aortic valve replacement with a porcine xenograft without long-term anticoagulation",
J. Thorac. and Cardiovasc. Surg. 71: 179-186, 1976.

26. BRITISH MEDICAL JOURNAL,
"Obituary for Fascia-Lata Heart Valves",
editorial 17, January 1976.

27. ANGELL, W.W., SHUMWAY, N.E.
"The Homograft Prosthesis",
from "Prosthetic Heart Valves",
Chapter 55, (ibid)

28. GOTT, V.L., WHIFFEN, J.D., LEININGER, R.I., FALB, R.D., VALIATHAN, S.M.
"Thrombo-resistant Surfaces",
Bibl. Haematologica 29: 863-872, 1968.

29. GOTT, V.L., AMELI, M.M., WHIFFTEN, J.D., LEININGER, R.I. FALB, R.D.
"Newer Thrombo-resistant Surfaces",
Surgical Clinics of North America 47: 1443-1452, 1967.

30. GHIDONI, J.J., LIOTTA, D., HALL, C.W., O'NEAL, R.M., DE BAKEY, M.E.
"Production of Cellular Linings in Impermeable Velour-lined Cardiovascular Prostheses",
Surgery 65: 70-77, 1969.

31. GOTT, V.L., FURUSE, A.
"Antithrombogenic Surfaces, Classification and In Vivo Evaluation",
Federation Proc. (USA) 30: 1679-1697, 1971.

32. ROOHK, H.V., NAKAMURA, M., HILL, R.L., HUNG, E.K., BARTLETT, R.H.
"A Thrombogenic Index for Blood Contact Materials",
Trans. Am. Soc. Artif. Int. Organs 23: 152-161, 1977.

33. SALZMAN, E.W.
"Surface Effects in Hemostasis and Thrombosis",
from "The Chemistry of Biosurfaces",
Vol. 2. ed. M. HAIR, Mariel Dekker Inc. USA, 1972.

34. KUSSEROW, B., LAWWOW, R., NICHOLS, J.
"Observations Concerning Prosthesis-induced Thromboembolic Phenomena Made with an In Vivo Embolus Test System",
Trans. Am. Soc. Artif. Int. Organs 16: 58-62, 1970.

35. BAIER, R.E., DUTTON, R.C., GOTT, V.L.
"Surface Chemical Features of Blood Vessel Walls and of Synthetic Materials Exhibiting Thrombo-resistance"
from "Surface Chemistry of Biological Systems",
Plenum Press, 1970.

36. EFFLER, D.B., "Do Prosthetic Heart Valves Really Make Clots?" J. Thorac. and Cardiovasc. Surg. 69: 664-666, 1975.

37. GLOVER, C.J., McINTIRE, L.V., LEVERETT, L.B., HELLUMS, J.D., BROWN, C.H., NATELSON, E.A.
"Effect of Shear Stress on Clot Structure Formation", Trans. Am. Soc. Artif. Inter. Organs 20: 463-468, 1974.

38. SPAETH, E.E., ROBERTS, G.W., YADWADKAR, S.R., NG, P.K., JACKSON, C.M.
"The Influence of Fluid Shear on the Kinetics of Blood Coagulation Reactions", Trans. Am. Soc. Artif. Int. Organs 19: 179-187, 1973.

39. ROSCHKE, E.J., HARRISON, E.C.
"Fluid Shear Stress Studies in Prosthetic Heart Valves", J. Biomechanics 10: 299-311, 1977.

40. GOLDSMITH, H.L.
"The Effects of Flow and Fluid Mechanical Stress on Red Cells and Platelets", Trans. Am. Soc. Artif. Int. Organs 20: 21-26, 1974.

41. GLOVER, C.J., McINTIRE, L.V., BROWN, C.H., NATELSON, E.A.
"Mechanical Trauma Effect on Clot Structure Formation", Thrombosis Research 10: 11-25, 1977.

42. GOLDSMITH, H.L., KARINO, T.
"Platelets in a Region of Disturbed Flow", Trans. Am. Soc. Artif. Int. Organs 23: 632-638, 1977.

43. MORTON, W.A., PARMENTIER, E.M., PETSCHEK, H.E.
"Study of Aggregate Formation in Region of Separated Blood Flow", Thromb. Diathes. Haemorrh 34: 840-847, 1975.

44. STEIN, P.D., SABBAH, H.N.
"Measured Turbulence and its Effect on Thrombus Formation",
Circulation Research 35: 608-614, 1974.

45. SHIONOYA, T.
"Studies in Experimental Extracorporeal Thrombosis",
J. Exp. Med. 46: 19-26, 1927.

46. FRY, F.J., EGGLETON, R.C., KELLY, E., FRY, W.J.
"Properties of the Blood Interface Essential to Successful Artificial Heart Function",
Trans. Am. Soc. Artif. Int. Organs 11: 307-312, 1965.

47. BLACKSHEAR, P.L., FORSTROM, R.J., LORBERBAUM, M., GOTT, V.L., SOVILJ, R.
"A Role of Flow Separation and Recirculation in Thrombus Formation on Prosthetic Surfaces",
Paper 71-103, 9th Aerospace Sciences Meeting, A.I.A.A., New York, 1971.

48. NYILAS, E., MORTON, W.A., LEDERMAN, D.M., CHIU, T.H., CUMMING, R.D.
"Interdependence of Hemodynamic and Surface Parameters in Thrombosis",
Trans. Am. Soc. Artif. Int. Organs 21: 55-70, 1975.

49. KNIGHT, C.J., MACLEOD, N., TAYLOR, D.E.M.
"Physical Principles of the Edinburgh Prosthetic Heart Valve",
Med. and Biol. Eng. and Comput. 15: 264-272, 1977.

50. MACLEOD, N., TURINA, M., WADE, J.D., WRIGHT, J.T.M., RIEMERSMAA, R.,
"Further Developments of the Edinburgh Prosthetic Heart Valve",
Proc. Eur. Soc. Artif. Org. (LONDON), 1976.

51. VORHAUER, B.W.

Ph.D. Thesis, 1968, West Virginia University, Morgantown, W. Va, U.S.A.

52. MADRAS, P.N., MORTON, W.A., PETSCHEK, H.E.

"Dynamics of Thrombus Formation",
Fed. Proc. (USA) 30: 1665-1676, 1971.

53. STORMORKEN, H.

"Platelets, Thrombosis, and Hemolysis",
Fed. Proc. (USA) 30: 1551-1555, 1971.

54. NANJAPPA, B.N., CHANG, H.K., GLOMSKI, C.A.

"Trauma of the Erythrocyte Membrane Associated with Low Shear Stress",
Biophys. J. 13: 1212-1222, 1973.

55. SUTERA, S.P., CROCE, P.A., MEHRJARDI, M.

"Hemolysis and Subhemolytic Alterations of Human RBC Induced by Turbulent Shear Flow",
Trans. Am. Soc. Artif. Int. Organs 18: 335-341.

56. INDEGLIA, R.A., SHEA, M.A., FORSTROM, R., BERNSTEIN, E.F.

"Influence of Mechanical Factors on Erythrocyte Sublethal Damage",
Trans. Am. Soc. Artif. Int. Organs 14: 264-271, 1968.

57. PIERCE, E.C., TAMARI, Y., GOETTER, W.E., BALLENTINE, M.B., KENT, B.

"An Attempt to Assess Occult RBC Damage by a Standard Shear Test",
Trans. Am. Soc. Artif. Int. Organs 18: 342-347, 1972.

58. LEVERITT, L.B., HELLUMS, J.D., ALFREY, C.P., LYNCH, E.C.
"RBC Damage by Shear Stress",
Biophysical J. 12: 257-273, 1972.

59. BERNSTEIN, E.F., BLACKSHEAR, P.L., KELLER, K.H.
"Factors Influencing Erythrocyte Destruction in Artificial Organs",
Am. J. of Surgery 114: 126-138, 1967.

60. NEVERIL, C.G., HELLUMS, J.D., ALFREY, C.P., LYNCH, E.C.
"Physical Effects in RBC Trauma",
A.I.Ch.E. Journal 15: 707-711, 1969.

61. BLACKSHEAR, P.L.
"Mechanical Hemolysis in Flowing Blood",
from "Biomechanics", Chapter 19,
ed. Y.C. Fung et.al. Prentice-Hall Inc. USA, 1972.

62. INDEGLIA, R.A., SHEA, M.A., VARCO, R.L., BERNSTEIN, E.F.
"Erythrocyte Destruction by Prosthetic Heart Valves",
Supp. 2 to Circulation Vols 37/38, 86-93, 1968.

63. GEORGE, J.N., WEED, R.I., REED, C.F.
"Adhesion of Human Erythrocytes to Glass",
J. Cell. Physiol. 77: 51-60, 1971.

64. HOCHMUTH, R.M., MOHANDAS, N., SPAETH, E.E., WILLIAMSON, J.R., BLACKSHEAR, P.L., JOHNSON, D.W.
"Surface Adhesion, Deformation and Detachment at Low Shear of Red Cells and White Cells",
Trans. Am. Soc. Artif. Int. Organs 18: 325-333, 1972.

65. BLACKSHEAR, P.L., DORMAN, F.D., STEINBACH, J.H.
"Some Mechanical Effects that Influence Hemolysis",
Trans. Am. Soc. Artif. Int. Organs 11: 112-117, 1965.

66. BLACKSHEAR, P.L., DORMAN, F.D., STEINBACH, E.J.,
MAYBACH, E.J., SINGH, A., COLLINGHAM, R.E.
"Shear, Wall Interaction and Hemolysis",
Trans. Am. Soc. Artif. Int. Organs 12: 113-119, 1966.

67. BLACKSHEAR, P.L.
"Hemolysis at Prosthetic Surfaces"
from "The Chemistry of Biosurfaces",
Vol. 2, Chap. 11. ed. M. Hair, Marcel Dekker Inc. USA, 1972.

68. FRIEDMAN, L.I., LEONARD, E.F.
"Platelet Adhesion to Artificial Surfaces",
Fed. Proc. (USA) 30: 1641-1648, 1971.

69. BRAIN, M.C.
"Microangiopathic Hemolytic anemia",
New Eng. J. Med. 281: 833-5, 1969.

70. CHANDLER, A.B.
"In vitro thrombotic coagulation of the blood",
Laboratory Investigation 7: 110-114, 1958.

71. HUCKABA, C.E., HAHN, A.W.
"A Generalized Approach to the Modelling of Arterial Blood Flow",
Bulletin of Math. Phys. 30: 645-662, 1968.

72. COTTON.
Ph.D. Thesis, 1960, London University.

73. WESTERHOF, N., BOSMAN, F., DE VRIES, C.J., NOORDERGRAAF, A.
"Analog Studies of the Human Systemic Arterial Tree", J. Biomechanics 2: 121-143, 1969.

74. MRAVA, G.L.
"Mock Circulation Systems for Artificial Hearts", from "Cardiac Engineering", Chap. 6, ed. Y. Nose, Interscience Publ. 1970.

75. KLAIN, M.
"Comparative Testing of Artificial Hearts and Heart Valves in a Mock Circulation", from "Cardiac Engineering", Chap. 7.

76. WESTERHOF, N., ELZINGA, G., SIPKEMA, P.
"An Artificial Arterial System for Pumping Hearts", J. App. Physiol. 31: 776-781, 1971.

77. MILLS, C.J., GABE, I.T., GAULT, J.H., MASON, D.T., ROSS, J., BRAUNWALD, E., SHILLINGFORD, J.P.
"Pressure-flow Relationships and Vascular Impedance in Man", Cardiovasc. Research 4: 405-417, 1970.

78. O'ROURKE, M.F., TAYLOR, M.G.
"Input Impedance of the Systemic Circulation", Circulation Research 20: 365-381, 1967.

79. ALAMI, M.A.
Ph. D. Thesis, 1975, Edinburgh University.

80. ALAMI, M.A., MACLEOD, N.,
"Some Aspects of Hemolysis in Pulsatile Pumps", from "Biocompatability of Implant Materials", Chap. 25, ed. D. Williams, Sector Publishing, London 1976.

81. KNIGHT, C.J., JULIAN, D.G., MACLEOD, N., TAYLOR, D.E.M., WADE, D.
"An Artificial Heart with Independently Variable Pulse Parameters",
Trans. Am. Soc. Artif. Int. Organs 17: 433-436, 1971.

82. WEITING, D.W.
Ph.D. Thesis, 1969, University of Texas at Austin.

83. WELLS, P.N.T.
"Physical Principles of Ultrasonic Diagnosis",
Academic Press, N.Y., 1969.

84. FEIGENBAUM, H.
"Echocardiography",
Lea & Febiger, Philadelphia, 1972.

85. HURST, J.W.
"Laboratory Procedures used in the evaluation of the cardiovascular system-echocardiography",
from "The Heart, Arteries, and Veins",
McGraw-Hill, Tokyo, 3rd ed., 1974.

86. FRIEDMAN, N.J.
"Echocardiographic Studies of Mitral Valve Motion",
Am. Heart J. 80: 177-187, 1970.

87. ABRAMS, H.L.
"Cine fluorographic Equipment", from "Angiography",
Little Brown & Co., Boston, 2nd ed. 1971.

88. FILSHIE, J.H., MCGEE, I.J.
"A Hybrid Thin-Film Multi-Channel Bio Telemetry Transmitter",
I.E.R.E. Conf. Proc. 1975, 31: 49-56.

89. STARR, A., EDWARDS, M.L.
"Mitral Replacement: The Shielded Ball Valve Prosthesis",
J. Thorac. Cardiovasc. Surg. 42: 673-682, 1961.

90. MACLEOD, N., TURINA, M., WADE, J.D., WHEATLEY, D.J.
"The Principles and in-vivo performance of the Edinburgh pivoted aerofoil-disc prosthetic heart valve",
Trans. Am. Soc. Artif. Int. Organs 23: 80-88, 1977.

91. LEHMAN, M.
"Holography, Technique and Practice",
from "The Engineering Uses of Holography, Proc. of Conf. at Strathclyde Univ",
Ed. E.R. Robertson and J.M. Harvey, Cambridge Univ. Press, 1970.

92. NASSENSTEIN, H., BUSCHMANN, H.T., DEDDEN, H., MOISAR, E., RIECK, H.
"An investigation of the properties of photographic materials for Holography",
idid "The Eng. Uses of Holography".

93. BRADFORD, W.R.
"Holographic Measuring Techniques",
ibid "The Eng. Uses of Holography",

94. ABRAMSON, N.
"The Holo-Diagram",
ibid "The Eng. Uses of Holography",

95. GIVENS, M.P.
"Introduction to Holography",
Am. J. Phys. 35: 1053-1064, 1967.

96. WILLIAMS, G.T., OWEN, T.C.
"Do-it-yourself Holography",
Phys. Ed. 2: 1967.

97. DANDLIKER, R., MAROM, E., MOTTIER, F.M.
"Two-Reference-Beam holographic Interferometry",
J. Opt. Soc. Am 66: 23-30, 1976.

98. KAPUR, D.N., MACLEOD, N.
"The Determination of Local Mass Transfer Coefficients by holographic interferometry",
Int. J. Heat Mass Transfer 17: 1151-1162, 1974.

99. KAPUR, D.N., MACLEOD, N.
"The use of holographic interferometry for the measurement of local mass transfer coefficients",
J. Photographic Science 23: No. 2, 1975.

100. KAPUR, D.N., MACLEOD, N.
"Determiniation of local mass transfer coefficients by holography",
Nature Physical Science 237: 57-59, 1972.

101. MACLEOD, N., STEWART, G.
"An experimental method for determining local mass transfer rates at a solid surface",
Chem. Eng. Sci. 12: 142-146, 1960.

102. MACLEOD N., COX, M.D., TODD, R.B.
"A profilometric technique for determining local mass transfer rates",
Chem. Eng. Sci. 17: 923;935, 1962.

103. MACLEOD, N., TODD, R.B.
"The experimental determination of wall-fluid mass transfer coefficients using plasticized polymer surface coatings", Int. J. Heat Mass Transfer 16: 485-504, 1973.

104. MACLEOD, N., KAPUR, D.N.
"A kinematically designed mount for the precise location of specimens for holographic interferometry", J. Physics E. 6: 423-424, 1973.

105. KAPUR, D.N.
Ph.D. Thesis, Edinburgh University, 1973.

106. ABRAMSON, N.
"The Holo-diagram: a practical device for making and evaluating holograms", App. Optics 8: 1235-1240, 1969.

107. JENKINS, F.A., WHITE, H.E.
"Fundamentals of Optics", McGraw-Hill, Tokyo, 3rd ed. 1957.

108. HORDER, A.
"Ilford Manual of Photography", Focal Press, London 6th Ed, 1972.

109. ENGEL, C.E.
"Photography for the Scientist", Academic Press, London 1968.

110. COX, A.
"Optics: The techniques of definition", Focal Press, London 1956.

111. MACLEOD, N., KAPUR, D.N.
"The Estimation of local heart transfer coefficients for 2-D surface roughness elements by holographic interferometry",
from "The Engineering Uses of Coherent Optics, Proc. of Conf. at Strathclyde University 1975",
ed. E.R. Robertson, Cambridge University Press, 1976.

112. TSURUTA, T., SHIOTAKE, N., ITOH, Y.
"Formation and localisation of holographically produced interference fringes",
Optica Acta 16: 723-733, 1969.

113. STETSON, K.A.
"A rogorous treatment of the fringes of hologram interferometry",
Optik 29: 386-400, 1969.

114. HILDEBRAND, B.P., HAINES, K.A.
"Surface deformation measurements using the wavefront reconstruction technique",
Appl. Optics 5: 595-602, 1966.

115. ALEKSANDROV, F.B., BONCH-BRUEVICH, A.M.
"Investigation of surface strains by the hologram technique",
Soviet Physics (Technical Physics) 12: 258-265, 1967.

116. ABRAMSON, N.
"The Holodiagram 2: A practical device for information retrieval in hologram-interferometry",
App. Op. 9: 1970.

117. ABRAMSON, N.
"The Holodiagram 3: A practical device for predicting fringe patterns in hologram interferometry",
App. Op. 9: 2311-2320, 1970.

118. BOONE, P.M.
"Measurement of displacement, strain and stress by holography",
ibid "The engineering uses of coherent optics",
81-98, 1975.

119. MATSUMOTO, T., IWATA, K., NAGATA, R.
"Measurement of Deformation in a Cylindrical Sheet by holographic interferometry",
App. Op. 13: 1080-1084, 1974.

120. SHIBAYAMA, K., UCHIYAMA, H.
"Measurement of three-dimensional displacements by hologram interferometry",
App. Op. 10: 2150-2154, 1971.

121. PASTOR, J.
"Hologram Interferometry and Optical Technology",
App. Op. 8: 525-531, 1969.

122. SOLLID, J.E.
"Holographic Interferometry applied to measurements of small-static displacements of diffusely reflecting surfaces",
App. Op. 8: 1587-1595, 1969.

123. ABRAMSON, N.
"Sandwich Hologram Interferometry: A new dimension in holographic comparison",
App. Op. 13: 2019-2025, 1974.

124. VIENOT, J. Ch., FROEHLY, C., MONNERET, J., PASTEUR, J., "Hologram interferometry: surface displacement fringe analysis as an approach to the study of mechanical strains", ibid "The Engineering uses of Holography", 133-150, 1970.

125. GATES, J.W.C. "Measurement of displacements in three dimensions from a single hologram", Symposium: "Applications de l'Holographie", Besancon, 1970.

126. HANSCHE, B.D., MURPHY, C.G. "Hologram interferogram analysisfrom a single view", App. Op. 13: 630-635, 1974.

127. LIU, H.K., KURTZ, R.L. "A practical method for holographic interference fringe assessment", Op. Eng. 16: 176-186, 1977.

128. WALLES, S. "Visibility and localisation of fringes in holographic interferometry for diffusely reflecting surfaces". Institute of Optical Research, Communication 156, Stockholm.

129. WELFORD, W.T. "Fringe visibility and localisation in hologram interferometry", Op. Comm. 1: 123-125, 1969.

130. WELFORD, W.T. "Fringe visibility and localisation in hologram interferometry with parallel displacement", Op. Comm. 1: 311-314, 1970.

131. WELFORD, W.T.
"Geometrical optics treatment of fringe localisation in two-beam hologram interferometry",
ibid Symposium, Besancon, 1970.

132. LEROY, J.
"Localisation des Franges en interferometrie holographique",
Nouv. Rev. Optique 6: 329-337, 1975.

133. WALL, M.R.
"Zero-motion Fringe identification
ibid Symposium, Besancon, 1970.

134. PETSCHEK, H., ADAMIS, D., KANTROWITZ, A.R.
"Stagnation flow thrombus formation",
Trans. Amer. Soc. Artif. Int. Organs 14: 256-260, 1968.

135. GRABOWSKI, E.F., DIDISHEIM, P., LEWIS, J.C., FRANTA, J.T., STROPP, J.Q.
"Platelet Adhesion to foreign surfaces under controlled conditions of whole blood flow",
Trans. Am. Soc. Artif. Int. Organs 23: 141-151, 1977.

136. TURITTO, V.T., LEONARD, E.F.
"Platelet adhesion to a spinning surface",
Trans. Am. Soc. Artif. Organs 18: 348-354, 1972.

137. VROMAN, L., ADAMS, A.L.
"Peculiar behaviour of blood at solid interfaces",
J. Polymer Sci. Part C 34: 159-165, 1971.

138. HLADOVEC, J., RIHA, P.
"The model of thrombosis and thrombolysis in vitro",
Thrombosis Research 7: 743-752, 1975.

139. SALZMAN, E.W.
"Role of Platelets in blood-surface interactions",
Fed. Proc. (USA) 30: 1503-1509, 1971.

140. LEDERMAN, D.M., CUMMING, R.D., PETSCHEK, H.E., CHIU, T.H., NYILAS, E., SALZMAN, E., COLLINS, R.E.C., COE, N.P.
"The intravascular magnetic suspension of a test device for in vivo hemocompatibility evaluation of materials",
Trans. Am. Soc. Artif. Organs 22: 545-553, 1976.

141. DUTTON, R.C., BAIER, R.E., DEDRICK, R.L., BOWMAN, R.L.
"Initial thrombus formation on foreign surfaces"
Trans. Am. Soc. Artif. Int. Organs 14: 57-62, 1968.

142. BAIER, R.E.
"The organisation of blood components near interfaces"
in "The behaviour of blood and its components at interfaces"
ed. L. Vroman and E.F. Leonard. Conf. Proc., The New York Academy of Sciences, 1977.

143. VIRCHOW, R.L.K.
"Thrombose und embolie"
Beitr. exp. Path. 2: 227-380 1846.

144. SCHOLTZ, M.T., TRASS, O.
"Mass transfer in the laminar radial wall jet".
A.I.Ch.E.Jn. 9: 548-554, 1963.

145. SCHLICHTING, H.
"Boundary Layer Theory",
McGraw-Hill, New York, p.78, 1960.

146. GLAUERT, M.B.
"The wall jet",
Jn. Fluid Mechs. 1: 625-643, 1956.